WILEY ONLINE LIBRARY

Early View publication on wileyonlinelibrary.com
(issue and page numbers not yet assigned;
citable using Digital Object Identifier – DOI)

Ann. Phys. (Berlin) 00, No. 0, A1–A2 (2013) / DOI 10.1002/andp.201300729

annalen der physik

EDITORIAL

Precision experiments and fundamental physics at low energies – Part I

Klaus Blaum, Holger Müller, and Nathal Severijns

Precision measurements probing nature's fundamental interactions help physicists to address the great challenges they face now, such as finding and verifying a theory beyond the Standard Model of particle physics that might, ultimately, unify gravity and quantum mechanics. While the energy scale of such theories might be out of reach of all but the largest colliders, or even beyond the reach of any experiment, it is possible to probe for suppressed effects at low energy scales in experiments of outstanding precision. Such experiments, e.g., probe the value of fundamental constants and set limits on their time dependence, try to understand the dominance of matter over antimatter, or search for new types of interactions. Precision measurements have been playing a central role in the shifts of paradigms in physics in the twentieth century and will very likely continue to do so.

In two volumes of *Annalen der Physik* a series of articles will address current precision efforts investigating fundamental interactions and their properties at lowest energies. Both volumes will contain review articles with broad or more focused topical overviews, as well as a series of original papers reporting on new experimental or technical progress from recent and ongoing experiments.

Review articles in this volume focus mainly on fundamental constants and symmetry tests. The last decade has witnessed significant progress in the precision of the unitarity test of the Cabibbo-Kobayashi-Maskawa quark-mixing matrix. The precision of both the V_{ud} and V_{us} matrix elements has improved due to new and more precise measurements as well as important theoretical progress in nuclear and kaon decays, respectively. Further improvements, leading to a gain of another factor of about two in the unitarity test might be possible in the foreseeable future, thereby further improving the sensitivity to new physics, not included in the Standard Model (J. Hardy, I. S. Towner, pp. 443–451). Penning traps will continue to play an important role in this respect as is illustrated by recent results with the TITAN Penning trap mass spectrometer (A. A. Kwiatkowski *et al.*, pp. 529–537).

Among the fundamental constants of Nature the fine structure constant, α, has a particular status, being the corner stone of quantum electrodynamics but also as a keystone for the determination of other fundamental physical constants. State of the art atomic physics methods to determine the fine structure constant are reviewed and discussed, together with the opportunity to provide a precise value of the ratio h/m_u between the Planck constant and the atomic mass constant (R. Bouchendira *et al.*, pp. 484–492). New quantum-mechanical calculations show that microwave and sub-millimeter molecular transition frequencies for a number of molecules which are usually observed in astronomical sources exhibit a very high sensitivity to the value of the fine structure constant, but also to the electron-to-proton mass ratio (M. G. Kozlov and S. A. Levshakov, pp. 452–471). This offers unique possibilities to test space- and time-invariance of fundamental constants by comparing precise laboratory measurements of the molecular rest frequencies and their astronomical counterparts, which could lead to astrophysical tests of Einstein's Equivalence Principle at an unprecedented level of sensitivity. Another unique laboratory to investigate the fine structure constant, as well as other fundamental quantities such as, e.g., the atomic mass of the electron are highly charged ions, and in particular the simple systems formed by hydrogen-like ions (S. G. Karshenboim, pp. 472–483). In these, the bound electrons are subjected to extreme fields which generate a number of interesting features. High precision is achieved by confinement of the ions in Penning

traps allowing specific manipulation and measurement techniques to be applied (M. Vogel and W. Quint, pp. 505–513). Finally, an improved determination of two other fundamental constants, i.e. the Rydberg constant and the 1S Lamb shift, is now possible through the precise determination of the 1S-3S and 1S-3D two-photon transitions in atomic hydrogen, which is reported using direct frequency-comb spectroscopy in a Doppler-free arrangement (E. Peters *et al.*, pp. L29-L34). In addition, this could shed light on the current discrepancy in the determination of the proton charge radius.

Over the last few years experiments with antimatter at the AD facility at CERN have provided important new physics results. These allow for different new tests of the symmetry of the Standard Model under the combined CPT operation (Charge conjugation, Parity and Time reversal) through comparisons of properties of particles and corresponding antiparticles, such as the magnetic moment of the proton and the antiproton, or the hydrogen and anti-hydrogen ground state hyperfine splitting (Y. Yamazaki and S. Ulmer, pp. 493–504). In the context of tests of very general and basic principles, experimental sensitivity, systematic effects and initial data searching for a long-range coupling between rubidium nuclear spins and the mass of the Earth are finally reported as well (D. F. Jackson Kimball *et al.*, pp. 514–528).

In the second volume additional reviews and results from dedicated efforts to study fundamental constants, to test basic symmetries of the Standard Model and search for new physics, will be reported: e.g. nuclear beta decay and neutron decay provide unique opportunities to search for new weak interactions providing results that are complementary to and compete in sensitivity with direct searches for new bosons at the LHC. Also neutrinos constitute unique probes to study different fundamental physics aspects via either laboratory or oscillation experiments or even via neutrino astronomy. Finally, many experiments are focusing lately on testing either the parity or CP symmetry of the weak interaction in atomic systems or via electric dipole moment searches, as well as CPT symmetry or Lorentz invariance.

Klaus Blaum graduated in 2000 at the University in Mainz. After a postdoctoral position at GSI, Darmstadt, he went to CERN to lead the ISOLTRAP experiment. In 2004 he became head of a Helmholtz Research Group in Mainz. Since 2007 he is director at the Max-Planck Institute for Nuclear Physics in Heidelberg and head of the Cooled and Stored Ions Division. His main research focus is on precision measurements of atomic and nuclear ground state properties as well as tests of fundamental symmetries using Penning traps.

Holger Müller graduated in 2004 at Humboldt-University, Berlin and was a postdoc with Steven Chu at Stanford. Since July 2009, he has been assistant professor of physics at the University of California, Berkeley. His work is focused on atom interferometers and precision measurements, for example determining the fine structure constant, inertial sensing, and testing general relativity

Nathal Severijns graduated in 1989 at the Katholieke Universiteit Leuven (KU Leuven). After two years of postdoctoral studies at the Université Catholique de Louvain-la-Neuve (U.C.L.) he became an assistant professor and later full professor of physics at KU Leuven. His work focuses on low energy weak interaction studies, testing symmetries of the standard model and searching for new physics beyond this model in nuclear beta decay and neutron decay, and the search for an electric dipole moment of the neutron.

Klaus Blaum
Max-Planck-Institute for Nuclear Physics,
Stored and Cooled Ions Devision,
Heidelberg, Germany
E-mail: klaus.blaum@mpi-hd.mpg.de

Holger Müller
Department of Physics, University of
California, Berkeley, CA, USA
E-mail: hm@berkeley.edu

Nathal Severijns
Nuclear and Radiation Physics Section,
Leuven, Belgium
E-mail: Nathal.Severijns@fys.kuleuven.be

Ann. Phys. (Berlin) **525**, No. 7, A104–A107 (2013) / DOI 10.1002/andp.201370073

annalen der physik

Contents

Full text on our homepage at www.ann-phys.org

WILEY ONLINE LIBRARY

COVER PICTURE

Volume **525** | **2013** | **No. 7**

SPECIAL ISSUE

Precision Experiments and Fundamental Physics at Low Energies – Part I

edited by Klaus Blaum, Holger Müller and Nathal Severijns

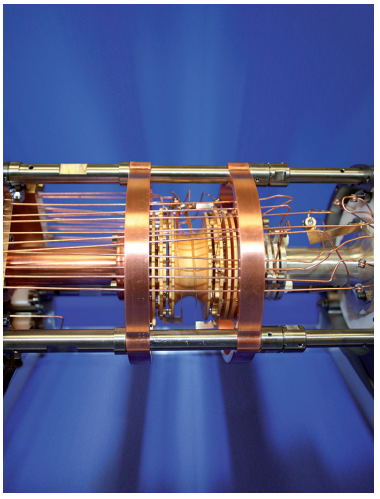

Precision measurements probing nature's fundamental interactions help physicists to address the great challenges they face, such as finding and verifying a theory beyond the Standard Model of particle physics that might, ultimately, unify gravity and quantum mechanics. In two volumes of *Annalen der Physik* a series of articles will address current precision efforts investigating fundamental interactions and their properties at lowest energies. The cover picture shows an example of an ion trap, here in particular a Penning trap that can be employed to measure the mass of exotic isotopes to high precision.
Photo: The TITAN mass measurements trap (with permission from M. Hapke, TRIUMF).

Page A109 — **Advisory Board**

Page A111–A112 — *K. Blaum, H. Müller and N. Severijns* — **Precision experiments and fundamental physics at low energies – Part I** — **EDITORIAL**

PHYSICS FORUM

Page A113–A115 — *W. Ubachs, W. Vassen, E. J. Salumbides, K. S. E. Eikema* — **Precision metrology on the hydrogen atom in search for new physics** — **EXPERT OPINION**

Volume 525 | 2013 | No. 7

annalen der physik

REVIEW ARTICLES

Page 443–451

J. C. Hardy, I. S. Towner

CKM unitarity normalization tests, present and future

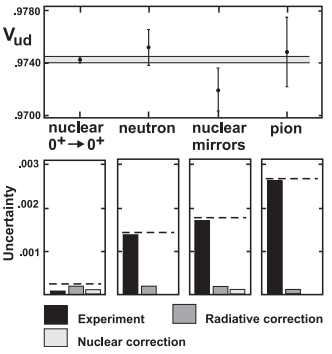

The Cabibbo-Kobayashi-Maskawa quark-mixing matrix is a central pillar of the Electroweak Standard Model. The elements of the matrix must be determined from experiment, but the Model requires the matrix itself to be unitary. Any deviation from unitarity would signal the presence of "new physics" beyond the Standard Model. This work overviews the status of the normalization tests and speculates on likely future improvements.

Page 452–471

M. G. Kozlov and S. A. Levshakov

Microwave and submillimeter molecular transitions and their dependence on fundamental constants

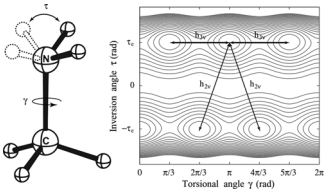

Microwave and submillimeter molecular transition frequencies between nearly degenerated rotational levels, tunneling transitions, and mixed tunneling-rotational transitions show an extremely high sensitivity to the values of the fine-structure constant, α, and the electron-to-proton mass ratio, μ. This review summarizes the theoretical background on quantum-mechanical calculations of the sensitivity coefficients of such transitions to tiny changes in α and μ for a number of molecules.

Page 472–483

S. G. Karshenboim

Recent progress in determination of fundamental constants and fundamental physics at low energies

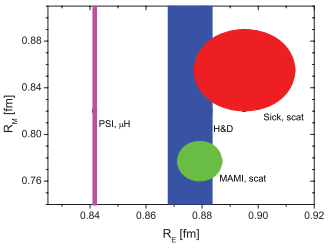

A brief overview on determination of the values of fundamental constants by means of atomic physics is given. Recommended values of CODATA-2010 least square adjustment are discussed as well as the related input data.

Page 484–492

R. Bouchendira, P. Cladé, S. Guellati-Khélifa, F. Nez, and F. Biraben

State of the art in the determination of the fine structure constant: test of Quantum Electrodynamics and determination of h/m_u

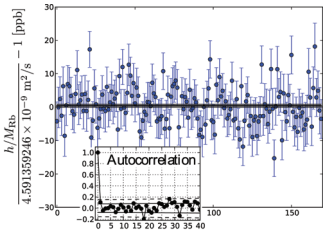

The fine structure constant α is a keystone for the determination of other fundamental physical constants, especially the ones involved in the framework of the future International System of units. This paper presents the Paris experiment, where the fine structure constant is determined by measuring the recoil velocity of a rubidium atom when it absorbs a photon.

annalen der physik

Full text on our homepage at www.ann-phys.org

Page 493–504

Y. Yamazaki and S. Ulmer

CPT symmetry tests with cold $\overline{\mathrm{p}}$ and antihydrogen

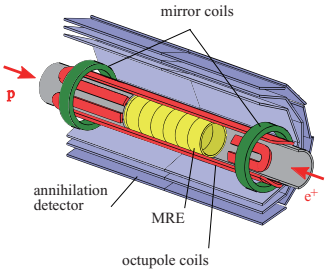

Precision comparisons of the properties of particles and corresponding antiparticles are highly relevant because the Standard Model of elementary particle physics, a local, Lorentz-invariant field theory, is necessarily symmetric with respect to the combined CPT operation. This symmetry defines exact equality between the fundamental properties of particles and their anti-images. Here, recent results of different CPT-tests are summarized.

ORIGINAL PAPERS

Page 505–513

M. Vogel and W. Quint

Aspects of fundamental physics in precision spectroscopy of highly charged ions in Penning traps

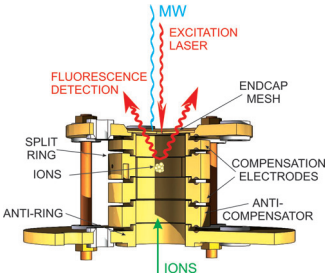

Highly charged ions, in particular hydrogen-like ions, are simple systems which allow to observe a number of fundamental processes and quantities within physics at low energies. High precision is achieved by ion confinement in Penning traps where cooling of the ion motion and trap-specific manipulation and measurement techniques can be applied. This work reports on spectroscopy experiments for precision studies of highly charged ions in Penning traps and their connection to fundamental symmetries and constants.

Page 514–528

D. F. Jackson Kimball, I. Lacey, J. Valdez, J. Swiatlowski, C. Rios, R. Peregrina-Ramirez, C. Montcrieffe, J. Kremer, J. Dudley, and C. Sanchez

A dual-isotope rubidium comagnetometer to search for anomalous long-range spin-mass (spin-gravity) couplings of the proton

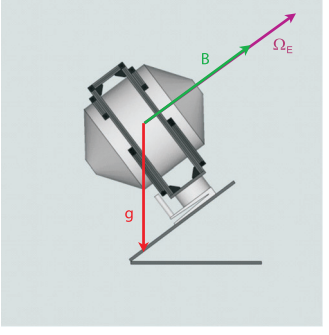

The experimental concept of a search for a long-range coupling between rubidium nuclear spins and the mass of the Earth is described. The experiment is based on simultaneous measurement of the spin precession frequencies for overlapping ensembles of ^{85}Rb and ^{87}Rb atoms contained within an evacuated, antirelaxation-coated vapor cell.

Volume 525 | 2013 | No. 7

annalen der physik

Page 529–537

A. A. Kwiatkowski, A. Chaudhuri, U. Chowdhury, A. T. Gallant, T. D. Macdonald, B. E. Schultz, M. C. Simon, and J. Dilling

Mass measurements of singly and highly charged radioactive Ions at TITAN: A new Q_{EC}-value measurement of ^{10}C

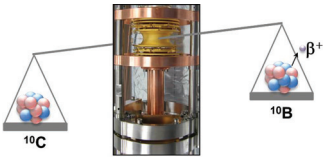

Superallowed β-decay strengths or corrected $\mathcal{F}$t values provide some of the most stringent limits for physics beyond the standard three-quark model. For this reason, the Q_{EC}-value ^{10}C has been measured and found to be 3468.31(51) keV with the TITAN Penning trap mass spectrometer. An overview of the TITAN facility and recent highlights are presented alongside the new Q_{EC}-value determination of ^{10}C.

RAPID RESEARCH LETTER

Page L29–L34

E. Peters, D. C. Yost, A. Matveev, T. W. Hänsch, and T. Udem

Frequency-Comb spectroscopy of the hydrogen 1S-3S and 1S-3D transitions

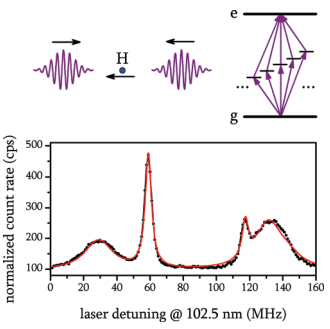

An observation of the 1S-3S and 1S-3D two-photon transition in an atomic hydrogen beam using direct frequency-comb spectroscopy in a Doppler-free arrangement is reported. The measurements of these transition frequencies may be used for an improved determination of the Rydberg constant and the 1S Lamb shift and could shed light on the current discrepancy in the determination of the proton charge radius.

Annalen der Physik is indexed in Chemical Abstracts Service/SciFinder, COMPENDEX, Current Contents®/Physical, Chemical & Earth Sciences, FIZ Karlsruhe Databases, INIS: International Nuclear Information System Database, INSPEC, Journal Citation Reports/Science Edition, Science Citation Index Expanded™, Science Citation Index®, SCOPUS, Statistical Theory & Method Abstracts, VINITI, Web of Science® , Zentralblatt MATH/Mathematics Abstracts

Recognized by the European Physical Society

WILEY ONLINE LIBRARY

Early View publication on wileyonlinelibrary.com
(issue and page numbers not yet assigned;
citable using Digital Object Identifier – DOI)

Ann. Phys. (Berlin), 1–9 (2013) / DOI 10.1002/andp.201300004

annalen der physik

Review Article

CKM unitarity normalization tests, present and future

J. C. Hardy and I. S. Towner*

Received 8 January 2013, revised 11 February 2013, accepted 5 March 2013
Published online 10 April 2013

The Cabibbo-Kobayashi-Maskawa (CKM) quark-mixing matrix is a central pillar of the Electroweak Standard Model. The elements of the matrix must be determined from experiment, but the Model requires the matrix itself to be unitary. Any deviation from unitarity would signal the presence of "new physics" beyond the Standard Model, so tests of CKM unitarity have attracted considerable attention. Currently the most precise test is of the normalization of the top row, which has now reached a precision of 0.06% based on measurements of superallowed $0^+ \rightarrow 0^+$ nuclear β decay and of kaon semileptonic and leptonic decays. This work overviews the status of the normalization tests and speculates on likely future improvements.

1 Introduction

The Cabibbo-Kobayashi-Maskawa (CKM) matrix is a central pillar of the Electroweak Standard Model. Its origins are with the pioneering 1963 work of Cabibbo [1], who reconciled the concept of vector-current universality with the recently observed difference between strangeness changing and strangeness non-changing weak decays by proposing that universality was manifest only if one considered the total strength of both the strangeness changing and non-changing decays. In modern terminology we would say that he was the first to realize that there was mixing between the first two generation of quarks. Ten years later, Kobayashi and Maskawa [2], who were faced with the puzzle of CP violation, demonstrated that it could only be explained by the existence of a third generation of quarks with many more mixing possibilities. They argued that the quark-mass eigenstates are not the same as the weak-interaction eigenstates, but are related by a 3×3 unitary rotation matrix – the CKM matrix.

By convention, the three quarks with charge 2/3 (u, c and t) are unmixed and all the mixing is expressed in terms of the CKM matrix operating on the quarks with charge -1/3 (d, s and b):

$$\begin{pmatrix} d' \\ s' \\ b' \end{pmatrix} = \begin{pmatrix} V_{ud} & V_{us} & V_{ub} \\ V_{cd} & V_{cs} & V_{cb} \\ V_{td} & V_{ts} & V_{tb} \end{pmatrix} \begin{pmatrix} d \\ s \\ b \end{pmatrix}. \quad (1)$$

The Standard Model itself does not prescribe the elements of the CKM matrix – they have to be determined experimentally – but the Standard Model does insist that the matrix be unitary. This requirement can be tested if the elements of the matrix can be individually measured with sufficient precision. Should the result violate the matrix's unitarity, then that would be very exciting. It would indicate that the Standard Model is flawed, or approximate, and that some "new physics" must be injected. To date there is no evidence for this. Nevertheless unitarity tests continue to be pursued with ever-increasing precision since they provide limits on any possible new physics, and these limits themselves yield interesting conclusions.

There are two types of tests for CKM unitarity:

- Test the orthogonality of rows and columns:

$$\sum_k V_{ik} V_{kj}^\dagger = \sum_k V_{ik}^\dagger V_{kj} = 0 \quad i \neq j. \quad (2)$$

  It is difficult to achieve high precision with this type of test since six elements are involved, from all three quark generations. Though it is currently a very active field of research, the results cannot yet match the precision achieved by normalization tests. We will not pursue such tests any further here.
- Test the normalization of rows and columns:

$$\sum_k V_{ik} V_{ki}^\dagger = \sum_k |V_{ik}|^2 = 1,$$
$$\sum_i V_{ki}^\dagger V_{ik} = \sum_i |V_{ik}|^2 = 1. \quad (3)$$

* Corresponding author E-mail: hardy@comp.tamu.edu
Cyclotron Institute, Texas A&M University, College Station, Texas 77845-3366, USA

For the first row or first column, this normalization test is made much easier by the realization that the contribution from the third-generation member is negligibly small, so only two matrix elements must be determined precisely. To date, the best precision is obtained in the top-row test

$$|V_{ud}|^2 + |V_{us}|^2 + |V_{ub}|^2 = 1. \quad (4)$$

In this article, we will concentrate on the top-row normalization test beginning with a discussion of the determination of V_{ud} from nuclear beta decay.

2 Measurements of superallowed β decay

For the past decade at least, the most precise value for the top left element of the CKM matrix, V_{ud}, has been obtained from measurements of β-decay between nuclear states with $(J^\pi, T) = (0^+, 1)$. This type of "superallowed" transition offers a powerful simplicity: Because the axial current cannot contribute to transitions between spin-0 states, only the vector current is involved. Consequently, the measured strength of the transition – its "*ft* value" – relates directly to the fundamental vector coupling constant G_V; so, according to the Conserved Vector Current (CVC) hypothesis, the measured *ft* values should be the same for all such transitions regardless of their specific host nuclei.

In practice, the expression for the *ft* value of a superallowed transition must incorporate several small correction terms, which account for radiative and isospin symmetry-breaking effects, both to be discussed in more detail in the next section. It is convenient to combine some of these terms with the *ft* value and define a "corrected" $\mathcal{F}t$ value, which we write [3]

$$\mathcal{F}t \equiv ft(1+\delta'_R)(1+\delta_{NS}-\delta_C) = \frac{K}{2G_V^2(1+\Delta_R^V)}, \quad (5)$$

where $K/(\hbar c)^6 = 2\pi^3\hbar \ln 2/(m_e c^2)^5 = 8120.2787(11) \times 10^{-10}$ GeV^{-4}s, δ_C is the isospin-symmetry-breaking correction and Δ_R^V is the transition-independent part of the radiative correction. The terms δ'_R and δ_{NS} comprise the transition-dependent part of the radiative correction, the former being a function only of the electron's energy and the Z of the daughter nucleus, while the latter, like δ_C, depends in its evaluation on the details of the nuclear structure of the parent and daughter states. All these correction terms are small, of order 1% or less, with uncertainties at least an order of magnitude smaller than that, so equation (5) provides an experimental method for determining G_V to better than a part in a thousand. This result can then yield a value for V_{ud} with the same precision since $V_{ud} = G_V/G_F$, where G_F is the well known [4] weak-interaction constant for purely leptonic muon decay.

Experimentally, the *ft* value that characterizes a superallowed transition – or any β transition for that matter – is determined from three measured quantities: the total transition energy, Q_{EC}, the half-life, $t_{1/2}$, of the parent state, and the branching ratio, R, for the particular transition of interest. The Q_{EC}-value is required to determine the phase-space integral, f, while the half-life and branching ratio combine to yield the partial half-life, t. In a 2009 survey of world data [3], the *ft* values of thirteen superallowed transitions in nuclei ranging from ^{10}C to ^{74}Rb were obtained with high precision. Although some more measurements have been published since that time, the overall outcome is unchanged.

The 2009 survey included the results from more than 150 independent measurements with comparable precision of the three properties, Q_{EC}, $t_{1/2}$ and R, for all thirteen superallowed transitions. Thus, on average, each quantity has been independently determined four times. This is a very robust data set. An overview of the results is presented in Fig. 1, where the three measured properties for each transition appear in the top three panels, and the corresponding *ft* and $\mathcal{F}t$ values are in the bottom two panels. They are plotted against the Z values of the daughter nuclei. The *ft* and $\mathcal{F}t$ values also appear numerically in Table 1. It is striking to see in the figure that the three experimental quantities change over orders of magnitude in the span from $Z = 5$ to $Z = 36$, yet the *ft* values change by less than 3%, and the final corrected $\mathcal{F}t$ values are all consistent with a single constant having $\pm 0.03\%$ precision. This, in itself, is convincing proof that CVC is satisfied and that G_V can be reliably extracted from the data.

As will be explained in the next section, the correction terms applied to obtain $\mathcal{F}t$ are based on criteria that are completely independent of these results so, in addition to confirming CVC, the results in Fig. 1 strongly support the validity of these correction terms since their presence in the $\mathcal{F}t$ values completely removes the vestigial transition-to-transition variations evident in the *ft* values.

3 Theoretical corrections to superallowed β decay

3.1 Radiative corrections

In a beta-decay half-life experiment, the rate measured includes not only the bare decay but also radiative decay processes, in which for example the beta particle emits

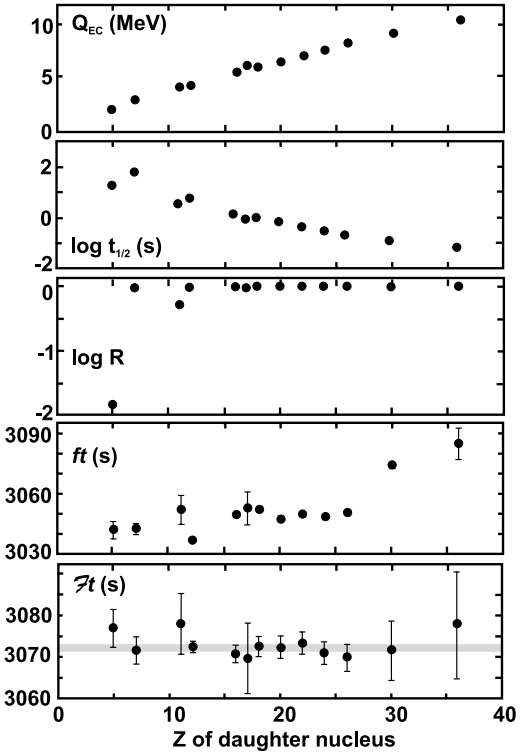

Figure 1 Results from the recent survey [3] of 13 precisely measured superallowed β transitions between $(J^\pi, T) = (0^+, 1)$ states. The parents of these transitions, from left to right, are ^{10}C, ^{14}O, ^{22}Mg, ^{26}Al^m, ^{34}Cl, ^{34}Ar, ^{38}K^m, ^{42}Sc, ^{46}V, ^{50}Mn, ^{54}Co, ^{62}Ga and ^{74}Rb. The top three panels present the average of measured Q_{EC}, log $t_{1/2}$ and log R values for each transition. The bottom two panels give the corresponding ft and $\mathcal{F}t$ values. The shaded horizontal line in the bottom panel represents the overall average $\overline{\mathcal{F}t}$ value for all transitions. All error bars are shown: in the cases where none are visible, they are smaller than the data point.

a bremsstrahlung photon. Since it is just the half-life for the bare beta-decay process that is required for the ft value, the measured result needs to be amended with a calculated radiative correction, RC:

$$t \to t(1 + RC). \tag{6}$$

In such a calculation it is necessary to consider not just bremsstrahlung but also the exchange of virtual photons and Z-bosons. To order α, the fine-structure constant, the principal graphs are one-photon bremsstrahlung, the γW-box and ZW-box diagrams. At low energies there is an infrared divergence in the bremsstrahlung process that is cancelled by a corresponding divergence in the γW-box graph. For these reasons it is convenient to separate the contributions from these graphs into contributions at low energies (long distances) from those at high

Table 1 Experimentally determined ft values and corresponding derived $\mathcal{F}t$ values. From ref. [3].

Nucleus	ft (s)	$\mathcal{F}t$ (s)
^{10}C	3041.7(43)	3076.7(46)
^{14}O	3042.3(27)	3071.5(33)
^{22}Mg	3052.0(72)	3078.0(74)
^{26}Al^m	3036.9(9)	3072.4(14)
^{34}Cl	3049.4(12)	3070.6(21)
^{34}Ar	3052.7(82)	3069.6(85)
^{38}K^m	3051.9(10)	3072.5(24)
^{42}Sc	3047.7(14)	3072.4(27)
^{46}V	3049.5(9)	3073.3(27)
^{50}Mn	3048.4(12)	3070.9(28)
^{54}Co	3050.8(15)	3069.9(33)
^{62}Ga	3074.1(15)	3071.5(72)
^{74}Rb	3084.9(78)	3078(13)

energies (short distances):

$$(1 + RC) \to (1 + \delta_R)\left(1 + \Delta_{\mathrm{R}}^{\mathrm{V}}\right). \tag{7}$$

The short-distance correction, $\Delta_{\mathrm{R}}^{\mathrm{V}}$, includes the ZW-box and the high-energy part of the γW-box diagrams and is evaluated by ignoring the hadronic structure and using free-quark Lagrangians. This contribution therefore is universal, being independent of which nucleus is involved in the beta decay. The current value, from Marciano and Sirlin [5], is

$$\Delta_{\mathrm{R}}^{\mathrm{V}} = (2.361 \pm 0.038)\%. \tag{8}$$

The long-distance correction, δ_R, includes the bremsstrahlung and low-energy part of the γW-box diagram and requires a model calculation of the hadronic structure. Also included in δ_R are contributions of order $Z\alpha^2$ and $Z^2\alpha^3$ in which the electron in the γW-box and bremsstrahlung diagrams is allowed to interact with the Coulomb field of the nucleus. If in the evaluation of the box graphs, it is assumed that the γN-vertex and WN-vertex are both with the same nucleon N, then the box graph, like the bremsstrahlung graph, becomes proportional to the Fermi matrix element. This means these contributions are independent of nuclear structure, depending only trivially on the nucleus involved

Table 2 Calculated radiative corrections δ'_R and δ_{NS} in percent units. From ref. [6].

Nucleus	δ'_R (%)	δ_{NS} (%)
Neutron	1.4902(2)	0.0
^{10}C	1.679(4)	−0.345(35)
^{14}O	1.543(8)	−0.245(50)
^{22}Mg	1.466(17)	−0.225(20)
^{26}Al^m	1.478(20)	0.005(20)
^{34}Cl	1.443(32)	−0.085(15)
^{34}Ar	1.412(35)	−0.180(15)
^{38}K^m	1.440(39)	−0.100(15)
^{42}Sc	1.453(47)	0.035(20)
^{46}V	1.445(54)	−0.035(10)
^{50}Mn	1.445(62)	−0.040(10)
^{54}Co	1.443(71)	−0.035(10)
^{62}Ga	1.459(87)	−0.045(20)
^{74}Rb	1.50(12)	−0.075(30)

through its total charge Z and the energy of the electron emitted.

By contrast, in the γW-box graph, if the γ- and W-interactions are with different nucleons in the nucleus, then the evaluation involves two-nucleon operators, necessitating a nuclear-structure calculation. It is convenient therefore to separate δ_R into two pieces:

$$(1+\delta_R) \rightarrow (1+\delta'_R)(1+\delta_{NS}), \tag{9}$$

where δ'_R depends only trivially on the nucleus involved, while δ_{NS} requires a nuclear-structure calculation.

Further details on the calculation of δ'_R and δ_{NS} are given in ref. [6]. In Table 2 we give current values of δ'_R and δ_{NS} for the neutron and 13 superallowed transitions of interest.

3.2 Isospin-symmetry breaking

A central tenet of the Standard Model is the Conserved Vector Current (CVC) hypothesis. It asserts that the coupling constant governing the strength of a vector weak interaction is not renormalized by the hadronic environment. Thus, irrespective of which nucleus is under study with superallowed beta decay, the coupling constant G_V should remain the same. This tenet, however, is only true in the limit of isospin symmetry. In nuclei, the Coulomb interaction among protons, for example, breaks this symmetry. Thus to be able to test, or use, the constancy of G_V it is necessary first to have an estimate of the degree of isospin-symmetry breaking that occurs in the nuclei under study. The symmetry breaking is characterized as a reduction in the square of the Fermi matrix element

$$|M_F|^2 = \left|M_F^0\right|^2(1-\delta_C), \tag{10}$$

where $|M_F^0|^2$ is the symmetry-limit value of the Fermi matrix element squared, and δ_C is the correction to it.

Over the years there have been many computations of δ_C by various authors using a diverse set of nuclear models [3, 6–14]. We have selected five sets from these works to display in Table 3. Two of the sets use the nuclear shell model to account for configuration mixing, and a mean field – taken to be either a phenomenological Woods-Saxon potential (SM-WS) or a Hartree-Fock computed potential (SM-HF) – to account for the radial

Table 3 Five recent sets of δ_C calculations from model approaches labelled DFT, RHF-RPA, RH-RPA, SM-HF and SM-WS (see text). Also given is the chi square per degree of freedom, χ^2/n_d, from the confidence test proposed in Ref. [15].

	δ_C(%)				
Nucleus	DFT	RHF-RPA	RH-RPA	SM-HF	SM-WS
^{10}C	0.462(65)	0.082	0.150	0.225(36)	0.175(18)
^{14}O	0.480(48)	0.114	0.197	0.310(36)	0.330(25)
^{22}Mg	0.432(49)			0.260(56)	0.380(22)
^{26}Al^m	0.307(62)	0.139	0.198	0.440(51)	0.310(18)
^{34}Cl		0.234	0.307	0.695(56)	0.650(46)
^{34}Ar	1.08(42)	0.268	0.376	0.540(61)	0.665(56)
^{38}K^m		0.278	0.371	0.745(63)	0.655(59)
^{42}Sc	0.70(32)	0.333	0.448	0.640(56)	0.665(56)
^{46}V	0.375(96)			0.600(63)	0.620(63)
^{50}Mn	0.39(13)			0.620(59)	0.655(54)
^{54}Co	0.51(20)	0.319	0.393	0.685(63)	0.770(67)
^{62}Ga				1.21(17)	1.48(21)
^{74}Rb	0.90(22)	1.088	1.258	1.42(17)	1.63(31)
χ^2/n_d	1.9	2.7	2.1	2.2	0.4

mismatch of proton and neutron single-particle wave functions caused by Coulomb polarization. These results by Towner and Hardy [3, 6] are considered to be semi-phenomenological in that a number of isospin-specific nuclear properties have been fitted in their derivation: *viz.*, the different proton and neutron separation energies in the parents and daughters respectively, and the *b*- and *c*-coefficients in the isobaric multiplet mass equation (IMME) for each T=1 multiplet that includes a parent and daughter state.

Alternative models do not lend themselves to local phenomenological constraints. One, by Sagawa et al. [9] and improved upon by Liang et al. [10], treats the even-even nucleus of the parent-daughter pair as a core, and the analog odd-odd nucleus as a particle-hole excitation built on that core. The particle-hole calculation is carried out in the charge-exchange random-phase approximation (RPA). The more recent work [10] replaces zero-range interactions with finite-range meson-exchange potentials and a relativistic rather than nonrelativistic treatment (RHF-RPA) is used. In a variation of this approach, density-dependent meson-nucleon vertices were introduced in a Hartree (only) computation with nonlocal interactions (RH-RPA).

Most recently, Satula et al. [14] used an isospin- and angular-momentum-projected density functional theory (DFT). This method accounts for spontaneous symmetry breaking, configuration mixing and the long-range Coulomb polarization effects.

The five sets of δ_C values in Table 3 show a wide variation. It would be useful if some yardstick were available to distinguish the quality of one set relative to another. Towner and Hardy [15] proposed such a test using the premise that the CVC hypothesis is valid. The requirement is that a calculated set of δ_C values should produce a statistically consistent set of $\mathcal{F}t$ values, the average of which we can write as $\overline{\mathcal{F}t}$. Then Eq. (5) can be written for each individual transition in the set as

$$\delta_C = 1 + \delta_{NS} - \frac{\overline{\mathcal{F}t}}{ft\left(1+\delta'_R\right)}. \tag{11}$$

For any set of corrections to be acceptable, the calculated value of δ_C for each superallowed transition must satisfy this equation where ft is the measured result for that transition and $\overline{\mathcal{F}t}$ has the same value for all of them. Thus to test a set of δ_C values for n superallowed transitions, one can treat $\overline{\mathcal{F}t}$ as a single adjustable parameter and use it to bring the n results for the right hand side of Eq. (11), which are based predominantly on experiment, into the best possible agreement with the corresponding n calculated values of δ_C. The normalized χ^2, minimized by this process, then provides a figure of merit for that set of calculations, The χ^2 for each fit, expressed as χ^2/n_d, where $n_d = n-1$ is the number of degrees of freedom, is given in the last row of Table 3.

The most obvious outcome of this analysis is that the model, SM-WS, has a χ^2 smaller by a factor of five than the other four cases cited. For this reason the SM-WS δ_C values are used in the determination of the CKM matrix element, V_{ud}. However, the other cases can be used for establishing an error assignment on this analysis.

4 Results for V_{ud}

The consistency of the $\mathcal{F}t$ values (and consequently G_V) obtained from the 13 measured superallowed $0^+ \rightarrow 0^+$ β transitions (see Sec. 2) is a crucially important result. Without consistency, there is no coupling "constant" and there can be no justification for extracting a value of V_{ud}. With consistency demonstrated, however, V_{ud} can be reliably obtained from the following equation [16]:

$$|V_{ud}|^2 = \frac{K}{2G_F^2\left(1+\Delta_R^V\right)\overline{\mathcal{F}t}} = \frac{2915.64 \pm 1.08}{\overline{\mathcal{F}t}}, \tag{12}$$

where $G_F/(\hbar c)^3 = 1.1663787(6) \times 10^{-5}$ GeV^{-2} [4] and $\overline{\mathcal{F}t}$ is the average measured $\mathcal{F}t$ value. Taking $\overline{\mathcal{F}t} =$ 3071.81(83) s from the 2009 survey [3], we arrive at $|V_{ud}|$ = 0.97425(22), a value with 0.02% precision.

This result is certainly the most precise current determination of V_{ud}, but superallowed $0^+ \rightarrow 0^+$ β decay is not the only experimental approach to V_{ud}. Neutron decay, nuclear $T = 1/2$ mirror decays, and pion beta decay have all been used for this purpose. Though these other methods cannot as yet compete with $0^+ \rightarrow 0^+$ decays for precision, they can lend useful confirmation to the more precise result.

Neutron β decay has one important advantage to offer: Its analysis does not require the application of corrections for isospin-symmetry breaking (δ_C) or for nuclear-structure-dependent radiative effects (δ_{NS}). But it also has big disadvantages: neutrons are notoriously difficult to confine; and their decay is not restricted to the vector weak interaction, as are the $0^+ \rightarrow 0^+$ decays. The axial-vector current is also present so, in addition to its ft value, some other parameter, usually the β asymmetry from the decay of polarized neutrons, must be measured to determine the ratio of the vector to axial-vector contributions. These experimental challenges have so far limited the achievable precision and, indeed, have at times led to completely inconsistent results. Even as of 2012, when the world average value for the neutron lifetime is

$\tau = 880.4(10)$ s [4, 17] and for $\lambda \equiv g_A/g_V$ is $-1.2731(20)$ [4, 18, 19], both have normalized χ^2 values well above unity, 2.7 for the former and 4.1 for the latter, which have caused their uncertainties to be enlarged. Together, these results yield a value for $|V_{ud}|$ of 0.97520(140), which agrees with the superallowed result but has an uncertainty more than six times larger.

The nuclear $T = 1/2$ mirror decays, like neutron decay, also require an additional correlation measurement to sort the weak vector contribution from the axial-vector one. However, unlike neutron decay, they provide no simplification in avoiding the nuclear-structure-dependent corrections, δ_C and δ_{NS}. A recent analysis of the five measured mirror transitions [20], which incorporated δ_C and δ_{NS} corrections, yielded $|V_{ud}| = 0.97190(170)$, a result that is only slightly less precise that the neutron result and is consistent within 1.2 combined standard deviations with the value obtained from the superallowed $0^+ \rightarrow 0^+$ decays.

Finally, pion β decay should, in principle, be the best way to determine V_{ud}. It is a pure vector decay between two spin-zero members of an isospin triplet and is therefore analogous to the superallowed decays, but is uncontaminated by nuclear-structure uncertainties. Unfortunately, in practice the branching ratio is very small ($\sim 10^{-8}$) and difficult to measure with sufficient precision. The most recent, and best, measurement is by the PIBETA group [21], whose result corresponds to a value for $|V_{ud}|$ of 0.97420(260) [16].

The results from all four types of measurement are plotted in Fig. 2. Obviously they are consistent with one another but, because the nuclear $0^+ \rightarrow 0^+$ value is so much more precise, it dominates the average. Furthermore, it is the most secure result, its value having changed little in the past two decades except for a steady (and significant) improvement in its uncertainty (see Fig. 6 in Ref. [3]). Thus we continue our practice [16] of adopting the $0^+ \rightarrow 0^+$ result as the recommended value, namely

$$|V_{ud}| = 0.97425(22), \tag{13}$$

while noting that the results from the other measurement techniques are entirely consistent with this value.

5 V_{us} and V_{ub}

The top row CKM matrix element V_{us} is best determined from kaon semi-leptonic decays, $K_{\ell 3}$, of both charged and neutral kaons, and from the purely leptonic decay of the kaon, the most important mode being $K^+ \rightarrow \mu^+ \nu$. Other determinations from hyperon decays and hadronic tau decays do not have the precision at the present time to challenge the results from kaon decays and therefore will not be considered here.

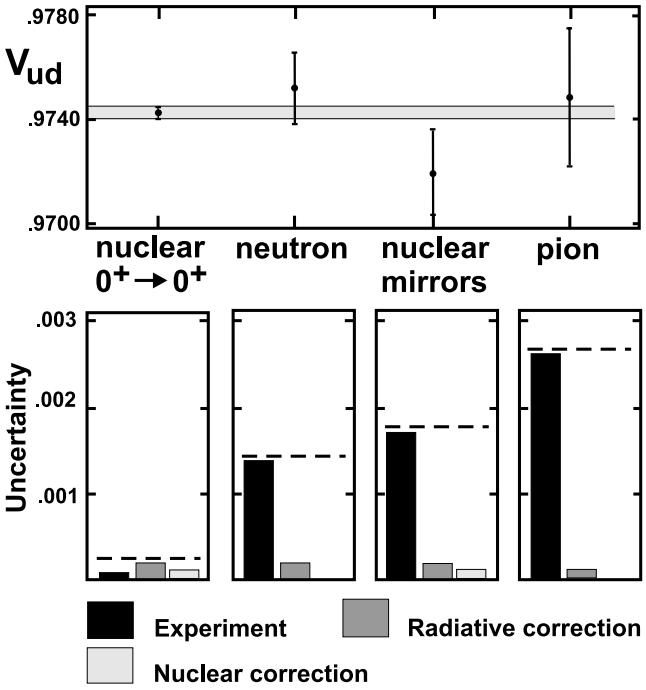

Figure 2 The four values for V_{ud} discussed in the text are shown in the top panel, the grey band being the average value. The four panels at the bottom of the figure show the error budgets for each result. The three contributors to the uncertainties – experiment, radiative correction and nuclear correction – are separately identified.

The experimental inputs for the determination of V_{us} are the rates – lifetimes and branching ratios – and the form factors required for the phase space integration. The best current value, presented at the CIPANP12 workshop [22] is

$$f_+(0)|V_{us}| = 0.2163(5). \tag{14}$$

Here $f_+(0)$ is the semi-leptonic decay form factor at zero-momentum transfer. Its value is close to unity. In fact, the CVC hypothesis in the exact SU(3) symmetry limit establishes its value to be exactly one. But SU(3) symmetry is broken to some extent and a theoretical calculation is required to estimate the departure of $f_+(0)$ from unity. Today, lattice QCD calculations are used for this purpose, replacing the former semi-analytic approaches based on chiral perturbation theory. Two groups working on the classification and averaging of results from lattice QCD [23, 24] have joined their efforts, forming the

Flavor Lattice Average Group (FLAG-2) to provide recommended values for these form factors [25]. For $f_+(0)$ their recommended value, after symmetrizing the uncertainty, is $f_+(0) = 0.959(5)$, yielding

$$|V_{us}| = 0.2254(13). \tag{15}$$

An independent determination of V_{us} can be obtained from the purely leptonic decay of the kaon. Further, if it is considered as a ratio with the leptonic decay of the pion, $\pi^+ \to \mu^+\nu$, the hadronic uncertainties can be minimized and the result yields the ratio of the CKM matrix elements $|V_{us}|/|V_{ud}|$. In the analysis of the FlaviaNet group [26], the current result is

$$\frac{|V_{us}|}{|V_{ud}|} \times \frac{f_K}{f_\pi} = 0.2758(5). \tag{16}$$

The most recent FLAG-2 average of the four published determinations of the decay constants f_K/f_π in lattice QCD is $f_K/f_\pi = 1.193(5)$ [25]. More significant is a new calculation of a correction to the ratio of experimentally determined decay rates, $\Gamma(K^\pm_{\mu 2})/\Gamma(\pi^\pm_{\mu 2})$ for isospin-symmetry breaking [27] that nearly doubles the formerly-used correction. The resulting value for $|V_{us}|/|V_{ud}|$ reported at the CIPANP12 workshop [22] is

$$\frac{|V_{us}|}{|V_{ud}|} = 0.2317(11). \tag{17}$$

Thus, we now have three pieces of data – $|V_{ud}|$ from nuclear decays, Eq. (13), $|V_{us}|$ from $K_{\ell 3}$ decays, Eq. (15), and the ratio $|V_{us}|/|V_{ud}|$ from $K_{\ell 2}$ decays, Eq. (17) – from which to determine two parameters $|V_{ud}|$ and $|V_{us}|$. An unconstrained fit does not change the input value of $|V_{ud}|$ and yields for $|V_{us}|$ our final selection

$$|V_{us}| = 0.2256(8). \tag{18}$$

The third element of the top row of the CKM matrix, V_{ub}, is very small and hardly impacts on the unitarity test at all. Its value from the 2012 PDG compliation [4] is

$$|V_{ub}| = (4.15 \pm 0.49) \times 10^{-3}. \tag{19}$$

6 CKM unitarity tests

We can test the unitarity of the CKM matrix by evaluating the sum of squares of the measured elements in any one of the rows or columns of the matrix, and then comparing the result with unity. We have set the stage for testing the top row elements by individually examining the results for V_{ud}, V_{us} and V_{ub}. Now, combining the results from Eqs. (13), (18) and (19), we obtain the result

$$|V_{ud}|^2 + |V_{us}|^2 + |V_{ub}|^2 = 1.00008 \pm 0.00056, \tag{20}$$

a result that shows unitarity to be fully satisfied to a precision of 0.06%. Only V_{us} and V_{ud} contribute perceptibly to the uncertainty and their contributions to it are almost equal. This may seem surprising since V_{ud} is known to much higher relative precision than V_{us}, but it follows from the fact that $|V_{ud}|^2$ contributes 95% to the unitarity sum itself.

No other row or column approaches this precision on a unitarity test. The first column comes closest, with $|V_{ud}|^2 + |V_{cd}|^2 + |V_{td}|^2 = 1.0021(51)$ [4], but this is a factor of ten less precise than the top-row sum. The corresponding sums for the second row and second column are another order of magnitude less precise. Without question the top row sum provides the most demanding test of CKM unitarity, V_{ud} is its dominant contributor, and superallowed $0^+ \to 0^+$ β decay is effectively the sole experimental source for the value of V_{ud}.

7 Outcome from unitarity tests

The unitarity sum established in Eq. (20) can be used to set limits on new physics beyond the Standard Model in two ways: *(i)* directly, via a new semi-leptonic interaction (e.g. right-hand currents) and *(ii)* indirectly, via loop-graph contributions to the radiative correction (e.g. extra Z-bosons). One example of each type is discussed in some detail in Sect. 9 of Ref. [16]. Here we just update the results given there for the current unitarity sum.

First, for right-hand currents, we write

$$1.00008 \pm 0.00056 = 1 + 2\overline{a}_{LR}$$
$$\overline{a}_{LR} = 0.00004 \pm 0.00028. \tag{21}$$

Here $\overline{a}_{LR}$ is the amplitude for a semi-leptonic weak interaction with left-hand couplings in the lepton sector and right-hand couplings in the hadron sector. Clearly, the result in Eq. (21) is consistent with no right-hand currents.

Second, for extra Z-bosons, we write

$$1.00008 \pm 0.00056 = 1 - \Delta, \tag{22}$$

yielding the one-standard deviation limits on Δ of

$$-0.00064 \le \Delta \le +0.00048. \tag{23}$$

Marciano and Sirlin [28] relate Δ to the mass of the extra Z boson via

$$\Delta = -0.00455\frac{\ln x}{x-1}$$
$$x = m_{Z_\chi}^2/m_W^2. \quad (24)$$

Here m_{Z_χ} is the mass of the extra Z-boson contributing to the radiative correction and m_W the W-boson mass. Noting that the correction Δ is negative, we obtain from the lower limit in Eq. (23)

$$\frac{\ln x}{x-1} \leq 0.14, \quad (25)$$

and

$$m_{Z_\chi} > 390\,\text{GeV}. \quad (26)$$

The confidence level is 68%. This limit is slightly weaker than the limit of 460 GeV given in [15] as the lower limit on Δ in Eq. (23) has been increased slightly through a more recent revision in the V_{us} value (see Section 5). Impressive though this limit remains, somewhat higher limits have been obtained in direct searches at proton and electron colliders, as described in the survey of Erler and Langacker [29] in the 2012 PDG listings.

8 Future prospects

The CKM unitarity sum tests a key premise of the Standard Model so the limits of its uncertainty set boundaries on the scope of possible new physics that may exist beyond the Standard Model. The opportunity to expose new physics, or to further limit the possible scope of new physics, together provide ample motivation to push for still tighter uncertainties on the unitarity sum. What are the prospects for achieving that goal?

As of 2012, after a concentrated effort, the measurements on $K_{\ell 3}$ decays have arrived at the value for $|V_{us}|\,f_+(0)$ in Eq. (14), which has a relative uncertainty of about $\pm 0.2\%$. However, the lattice QCD estimate for the form factor, $f_+(0)$, has a much larger $\pm 0.5\%$ uncertainty, so it dominates the uncertainty on $|V_{us}|$. While little improvement in the experimental result is anticipated in the near future [22], Van de Water [30] predicts that the uncertainty on the lattice calculation will be decreased to 0.2% in 2014 and to 0.1% by 2020. Thus, we can anticipate an improvement in the uncertainty of $|V_{us}|$ by a factor of 2 in the near future and perhaps by a bit more in five or ten years.

The error budget for the determination of $|V_{ud}|$ is similarly dominated by uncertainties in the theoretical correction terms. Of the total 0.023% uncertainty on $|V_{ud}|$ as derived from the superallowed $0^+ \rightarrow 0^+$ decays, 0.018% is contributed by the uncertainty associated with the radiative correction Δ_R^V and 0.010% comes from the nuclear-structure-dependent corrections, $\delta_C - \delta_{NS}$. Only 0.008% can be considered experimental in origin. This error budget is illustrated in the lower left panel of Fig. 2.

It is also instructive to observe that the Δ_R^V uncertainty is the same size in the middle two lower panels of Fig. 2 as well. Thus, even if the experimental uncertainties can be reduced dramatically for neutron decay or for the mirror decays, the overall uncertainty on $|V_{ud}|$ will be limited to about the same value by Δ_R^V. For pion decay, in the bottom right panel, the uncertainty in Δ_R^V is less than for the other types of measurement, but there is no apparent path to experimental error bars that are reduced by the factor of 20 needed for the result to have an impact on $|V_{ud}|$.

Any improvement in Δ_R^V is a problem for theory and, unfortunately, we are not aware of any attempts currently underway to reduce its uncertainty.

In the meantime some small improvement in $|V_{ud}|$ can be obtained from a reduction in the uncertainty associated with the nuclear-structure-dependent corrections, $\delta_C - \delta_{NS}$. As already discussed in Sec. 3.2, there is considerable activity in this area on the theoretical side. However, experiment can also play an important role too: Every set of nuclear-structure-dependent corrections can be tested by being applied to the uncorrected experimental ft values to obtain a set of $\mathcal{F}t$ values, which can then be evaluated for the consistency required by CVC (see Eq. (11) and Table 3). The more precisely the ft values have been measured, the more discriminating this test can be; and if new superallowed transitions with larger predicted nuclear corrections can be measured, the test will be improved still more.

Measurements with reduced uncertainties are regularly being reported for the thirteen previously measured transitions, which are listed in Tables 2 and 3. Additionally, it is to be anticipated that at least three new superallowed $0^+ \rightarrow 0^+$ transitions – from ^{26}Si, ^{34}Ar and ^{38}Ca – which all have relatively large predicted nuclear corrections, will be fully characterized within two or three years. Together, these improvements and additions should serve to reduce the overall uncertainty attributed to $|V_{ud}|$ by 15%.

Considering anticipated improvements to both V_{ud} and V_{us}, the uncertainty on the unitarity sum will likely be dropped from ± 0.00060 to ± 0.00040 in the next few years. If the uncertainty on Δ_R^V could also be reduced by,

say, a factor of two, then the unitarity uncertainty would become even less, ± 0.00030. This reduction would of course improve the limits given in Section 7: for example, with the limits $-0.00030 \leq \Delta \leq +0.00030$, the limit on the extra Z boson mass would become $m_{Z_\chi} > 650$ GeV, which is comparable to the limits from direct searches.

This is likely the extent of improvements for the foreseeable future.

Acknowledgements. This work was supported by the U.S. Department of Energy under Grant No. DE-FG03-93ER40773 and by the Robert A. Welch Foundation under Grant No. A-1397.

Key words. PACS numbers: 23.40.Bw, 12.15.Hh, 12.60.-i.

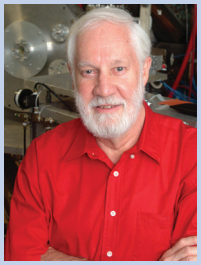

John Hardy received his Ph.D. degree in nuclear physics from McGill University (Montréal) in 1965. He was a postdoctoral fellow at Oxford University and a Miller Fellow at the University of California in Berkeley before joining the Chalk River Nuclear Labs of Atomic Energy of Canada in 1970. In 1997, he joined the Texas A&M University where he is now a Distinguished Professor. In 2006, he shared the Bonner Prize with Ian Towner from the American Physical Society.

Ian Towner is a retired professor of physics from the Queen's University, Canada and an adjunct professor of physics at the Texas A&M University. Together with John Hardy, he won the American Physical Society's Bonner Prize in 2006.

References

[1] N. Cabibbo, Phys. Rev. Lett. **10**, 531 (1963).
[2] M. Kobayashi and T. Maskawa, Prog. Theor. Phys. **49**, 652 (1973).
[3] J. C. Hardy and I. S. Towner, Phys. Rev. C **79**, 055502 (2009).
[4] J. Beringer et al., (Particle Data Group), Phys. Rev D **86**, 010001 (2012).
[5] W. J. Marciano and A. Sirlin, Phys. Rev. Lett. **96**, 032002 (2006).
[6] I. S. Towner and J. C. Hardy, Phys. Rev. C **77**, 025501 (2008).
[7] J. Damgaard, Nucl. Phys. A **130**, 233 (1969).
[8] W. E. Ormand and B. A. Brown, Phys. Rev. C **52**, 2455 (1995); Phys. Rev. Lett. **62**, 866 (1989); Nucl. Phys. A **440**, 274 (1985).
[9] H. Sagawa, N. van Giai, and T. Suzuki, Phys. Rev. C **53**, 2163 (1986).
[10] H. Liang, N. van Giai, and J. Meng, Phys. Rev. C **79**, 064316 (2009).
[11] N. Auerbach, Phys. Rev. C **79**, 035502 (2009).
[12] G. A. Miller, and A. Schwenk, Phys. Rev. C **80**, 064319 (2009); Phys. Rev. C **78**, 035501 (2008).
[13] G. F. Grinyer, C. E. Svensson, and B. A. Brown, Nucl. Instrum. Methods Phys. Res. Sect. A **622**, 236 (2010).
[14] W. Satula, J. Dobaczewski, W. Nazarewicz and T. R. Werner, Phys. Rev. C **86**, 054316 (2012).
[15] I. S. Towner and J.C. Hardy, Phys. Rev. C **82**, 065501 (2010).
[16] I. S. Towner and J. C. Hardy, Rep. Prog. Phys. **73**, 046301 (2010).
[17] A. Steyerl et al. Phys. Rev. C **85**, 065503 (2012).
[18] M. P. Mendenhall et al., arXiv:1210.7048v2 [nucl-ex] (2012).
[19] D. Mund et al., arXiv:1204.0013v1 [hep-ex] (2012).
[20] O. Naviliat-Cuncic and N. Severijns, Phys. Rev. Lett. **102**, 142302 (2009).
[21] D. Počanić et al., Phys. Rev. Lett. **93**, 181803 (2004).
[22] M. Moulson, arXiv:1209.3426 (2012).
[23] G. Colangelo et al., (FLAG Working Group), Eur. Phys. J. C **71**, 1695 (2011).
[24] J. Laiho, E. Lunghi, and R. Van de Water, Phys. Rev. D **81**, 034503 (2010).
[25] G. Colangelo, talk at Lattice '12 conference, Cairns, Australia (2012): quoted in [22].
[26] M. Antonelli et al., (FlaviaNet Kaon Working Group), Eur. Phys. J. C **69**, 399 (2010).
[27] V. Cirigliano and H. Neufeld, Phys. Lett. B **700**, 7 (2011).
[28] W. J. Marciano and A. Sirlin, Phys. Rev. D **35**, 1672 (1987).
[29] J. Erler and P. Langacker, mini-review in PDG12 [16].
[30] R. Van de Water, talk at CIPANP 2012 conference, St. Petersburg, FL, USA, (2012).

WILEY ONLINE LIBRARY

Early View publication on wileyonlinelibrary.com
(issue and page numbers not yet assigned;
citable using Digital Object Identifier – DOI)

Ann. Phys. (Berlin), 1–20 (2013) / DOI 10.1002/andp.201300010

annalen der physik

Review Article

Microwave and submillimeter molecular transitions and their dependence on fundamental constants

Mikhail G. Kozlov[1,2] *and Sergei A. Levshakov*[2,3,*]

Received 22 January 2013, revised 26 February 2013, accepted 18 March 2013
Published online 30 April 2013

Microwave and submillimeter molecular transition frequencies between nearly degenerated rotational levels, tunneling transitions, and mixed tunneling-rotational transitions show an extremely high sensitivity to the values of the fine-structure constant, α, and the electron-to-proton mass ratio, μ. This review summarizes the theoretical background on quantum-mechanical calculations of the sensitivity coefficients of such transitions to tiny changes in α and μ for a number of molecules which are usually observed in Galactic and extragalactic sources, and discusses the possibility of testing the space- and time-invariance of fundamental constants through comparison between precise laboratory measurements of the molecular rest frequencies and their astronomical counterparts. In particular, diatomic radicals CH, OH, NH^+, and a linear polyatomic radical C_3H in Π electronic ground state, polyatomic molecules NH_3, ND_3, NH_2D, NHD_2, H_2O_2, H_3O^+, CH_3OH, and CH_3NH_2 in their tunneling and tunneling-rotational modes are considered. It is shown that sensitivity coefficients strongly depend on the quantum numbers of the corresponding transitions. This can be used for astrophysical tests of Einstein's Equivalence Principle all over the Universe at an unprecedented level of sensitivity of $\sim 10^{-9}$, which is a limit three to two orders of magnitude lower as compared to the current constraints on cosmological variations of α and μ: $\Delta\alpha/\alpha < 10^{-6}$, $\Delta\mu/\mu < 10^{-7}$.

1 Introduction

The fundamental laws of particle physics, in our current understanding, depend on 28 constants including the gravitational constant, G, the mass, m_e, and charge, e, of the electron, the masses of six quarks, m_u, m_d, m_c, m_s, m_t, and m_b, the Planck constant, $\hbar$, the Sommerfeld constant α, the coupling constants of the weak, g_w, and strong, g_s, interactions, etc. The numerical values of these constants are not calculated within the Standard Model and remain, as Feynman wrote about the fine structure constant α in 1985, "one of the greatest mysteries of physics" [1]. However, it is natural to ask whether these constants are really constants, or whether they vary with the age of the universe, or over astronomical distances.

The idea that the fundamental constants may vary on the cosmological time scale has been discussing in different forms since 1937, when Milne and Dirac argued about possible variations of the Newton constant G during the lifetime of the universe [2, 3]. Over the past few decades, there have been extensive searches for persuasive evidences of the variation of physical constants. So far, there was found no one of them. The current limits for dimensionless constants such as the fine structure constant, $\alpha = e^2/\hbar c$, and the electron to proton mass ratio, $\mu = m_e/m_p$, obtained in laboratory experiments and from the Oklo natural reactor are on the order of one part in $10^{15} - 10^{17}$ [4–6] and one part in $10^{14} - 10^{16}$ [7–9] per year, respectively. The detailed discussion of ideas behind laboratory experiments can be found in a review [10].

Assuming that the constants are linearly dependent on the cosmic time, the same order of magnitude constraints on the fractional changes in $\Delta\alpha/\alpha = (\alpha_{obs} - \alpha_{lab})/\alpha_{lab}$ and in $\Delta\mu/\mu = (\mu_{obs} - \mu_{lab})/\mu_{lab}$ are stemming from astronomical observations of extragalactic objects at redshifts $z \sim 1 - 5$ [11–15]. Less stringent constraints at a percent level have been obtained from the cosmic microwave background (CMB) at $z \sim 10^3$ [16–18] and big bang nucleosynthesis (BBN) at $z \sim 10^{10}$

* Corresponding author E-mail: lev@astro.ioffe.rssi.ru
[1] Petersburg Nuclear Physics Institute, 188300 Gatchina
[2] St. Petersburg Electrotechnical University "LETI", Prof. Popov Str. 5, 197376 St. Petersburg
[3] Ioffe Physical-Technical Institute, Polytekhnicheskaya Str. 26, 194021 St. Petersburg

[19,20]. We note that space and/or time dependence of α based on optical spectra of quasars and discussed in the literature [21, and references therein] is still controversial and probably caused by systematic effects since independent radio-astronomical observations, which are more sensitive, show only null results for both $\Delta\alpha/\alpha$ and $\Delta\mu/\mu$ [22,23].

Surprisingly, it looks as if the Einstein heuristic principle of local position invariance (LPI) — *the outcome of any local non-gravitational experiment is independent of where and when in the universe it is performed* — is valid all over the universe, i.e., at the level of $\sim 10^{-6}$ neither α no μ deviate from their terrestrial values for the passed 10^{10} yr. In the Milky Way, it was also found no statistically significant deviations of $\Delta\mu/\mu$ from zero at even more deeper level of $\sim 10^{-8}$ [24–26].

However, the violation of the LPI was predicted in some theoretical models such as, for example, the theory of superstrings which considers time variations of α, $g_{\rm w}$, and the QCD scale $\Lambda_{\rm QCD}$ (i.e., μ since $m_{\rm p} \propto \Lambda_{\rm QCD}$) and thereby opening a new window on physics beyond the Standard Model [27, and references therein]. If the fundamental constants are found to be changing in space and time, then they are not absolute but dynamical quantities which follow some deeper physical laws that have to be understood. Already present upper limits on the variation of the fundamental constants put very strong constraints on the theories beyond the Standard Model [28, and references therein]. This motivates the need for more precise laboratory and astronomical tests of the LPI. Of course, there are also other attempts to look for the new physics. For example the electric dipole moments (EDMs) of the elementary particles are very sensitive to the different extensions of the Standard Model. Present limit on the EDM of the electron significantly constrains supersymmetrical models and other theories [29,30].

In this review we will consider tests of LPI which are based on the analysis of microwave and submillimeter[1] astronomical spectra and which are essentially more sensitive to small variations in α and μ than the test based on optical spectral observations of quasars.

[1] The frequency range 1 GHz $\leq \nu \leq$ 300 GHz is usually referred to as a microwave range. Molecular transitions below 1 GHz (wavelength $\lambda > 30$ cm) are from a low-frequency range which is restricted by the ionospheric cut-off at 10 MHz ($\lambda = 30$ m).

2 Differential measurements of $\Delta\alpha/\alpha$ and $\Delta\mu/\mu$ from atomic and molecular spectra of cosmic objects

Speaking about stable matter, as, for example, atoms and molecules, we have only seven physical constants that describe their spectra [31]:

$$G,\ \Lambda_{\rm QCD},\ \alpha,\ m_{\rm e},\ m_{\rm u},\ m_{\rm d},\ m_{\rm s}.$$

The QCD scale parameter $\Lambda_{\rm QCD}$ and the masses of the light quarks u, d, and s contribute to the nucleon mass $m_{\rm p}$ (with $\Lambda_{\rm QCD} \gg m_{\rm u} + m_{\rm d} + m_{\rm s}$) and, thus, the electron-to-proton mass ratio μ is a physical constant characterizing the strength of electroweak interaction in terms of the strong interaction.

In the nonrelativistic limit and for an infinitely heavy pointlike nucleus all atomic transition frequencies are proportional to the Rydberg constant, R, and the ratios of atomic frequencies do not depend on any fundamental constants. Relativistic effects cause corrections to atomic energy, which can be expanded in powers of α^2 and $\alpha^2 Z^2$, the leading term being $\alpha^2 Z^2 R$, where Z is atomic number. Corrections accounting for the finite nuclear mass are proportional to $R\mu/Z$, but for atoms they are much smaller than relativistic corrections.

Astronomical differential measurements of the dimensionless constants α and μ are based on the comparison of the line centers in the absorption/emission spectra of cosmic objects and the corresponding laboratory values. It follows that the uncertainties of the laboratory rest frequencies and the line centers in astronomical spectra are the prime concern of such measurements. It is easy to estimate the natural bounds set by these uncertainties on the values of $\Delta\alpha/\alpha$ and $\Delta\mu/\mu$.

Consider the dependence of an atomic frequency ω on α in the comoving reference frame of a distant object located at redshift z [32,33]:

$$\omega_z = \omega + qx + O(x^2), \quad x \equiv (\alpha_z/\alpha)^2 - 1. \tag{1}$$

Here ω and ω_z are the frequencies corresponding to the present-day value of α and to a change $\alpha \to \alpha_z$ at a redshift z. In this relation, the so-called q factor is an individual parameter for each atomic transition.

If $\alpha_z \neq \alpha$, the quantity x in (1) differs from zero and the corresponding frequency shift $\Delta\omega = \omega_z - \omega$ is given by

$$\frac{\Delta\omega}{\omega} = Q\frac{\Delta\alpha}{\alpha}, \tag{2}$$

where $Q = 2q/\omega$ is the dimensionless sensitivity coefficient and $\Delta\alpha = (\alpha_z - \alpha)/\alpha$ is the fractional change in α. Here we assume that $|\Delta\alpha/\alpha| \ll 1$. The condition $\alpha_z \neq \alpha$ leads to a change in the apparent redshift of the distant object $\Delta z = \tilde{z} - z$:

$$\frac{\Delta\omega}{\omega} = -\frac{\Delta z}{1+z} \equiv \frac{\Delta v}{c}\,, \tag{3}$$

where Δv is the Doppler radial velocity shift.

If ω' is the observed frequency from the distant object, then the true redshift is given by

$$1 + z = \frac{\omega_z}{\omega'}\,, \tag{4}$$

whereas the shifted (apparent) value is

$$1 + \tilde{z} = \frac{\omega}{\omega'}\,. \tag{5}$$

Now, if we have two lines of the same element with the apparent redshifts $\tilde{z}_1$ and $\tilde{z}_2$ and the corresponding sensitivity coefficients Q_1 and Q_2, then

$$\Delta Q\frac{\Delta\alpha}{\alpha} = \frac{\tilde{z}_1 - \tilde{z}_2}{1+z} = \frac{\Delta v}{c}\,. \tag{6}$$

Here $\Delta v = v_1 - v_2$ is the difference of the measured radial velocities of these lines, and $\Delta Q = Q_2 - Q_1$ is the corresponding difference between their sensitivity coefficients. By comparing the apparent redshifts of two lines with different sensitivity coefficients Q we can study variation of α on a cosmological timescale.

Unfortunately, optical and UV transitions of atoms and molecules are not very sensitive to changes in α and μ. The sensitivity coefficients of atomic resonance transitions of usually observed in quasar spectra chemical elements (C, N, O, Na, Mg, Al, Si, S, Ca, Ti, Cr, Mn, Fe, Co, Ni, Zn) are very small, $Q \sim (\alpha Z)^2 \ll 1$ [34]. The same order of magnitude sensitivity coefficients to μ variations have been calculated for the UV transitions in the Lyman and Werner bands of molecular hydrogen H_2 [35–37], and for the UV transitions in the $4th$ positive band system $A^1\Pi - X^1\Sigma^+$ of carbon monoxide CO [38].

Small values of Q and ΔQ put tough constraints on optical methods to probe $\Delta\alpha/\alpha$ and $\Delta\mu/\mu$. Let us consider an example of Fe II lines arising from the ground state $3d^6(^5D)4s$. In quasar spectra we observe 7 resonance transitions ranging from 1608 Å to 2600 Å with both signs sensitivity coefficients: $Q_{\lambda 1608} = -0.0322$, $Q_{\lambda 1611} = +0.0502$, and $Q \simeq +0.08$ for transitions with $\lambda > 2000$ Å [39, note a factor of two difference in the definition of the coefficients Q with the present work]. This gives us the maximum value of $\Delta Q \simeq 0.11$ which is known with an error of ∼30%. From (6) it follows that a variance of $\Delta\alpha/\alpha \sim 10^{-5}$ would induce a velocity offset $\Delta v \simeq 0.3$ km s^{-1} between the 1608 Å line and any of the line with $\lambda > 2000$ Å. We may neglect uncertainties of the rest frame wavelengths since they are ∼0.02 km s^{-1} [40]. If both iron line centers are measured in quasar spectra with the same error σ_v, then the error of the offset Δv is $\sigma_{\Delta v} = \sqrt{2}\sigma_v$. The error $\sigma_{\Delta v}$ is a statistical estimate of the uncertainty of Δv, and, hence, it should be less than the absolute value of Δv. This gives us the following inequality to adjust parameters of spectral observations required to probe $\Delta\alpha/\alpha$ at a given level:

$$\sigma_v < \frac{\Delta Q}{\sqrt{2}}\frac{\Delta\alpha}{\alpha}c\,. \tag{7}$$

At $\Delta\alpha/\alpha \sim 10^{-5}$, the required position accuracy should be $\sigma_v \lesssim 0.25$ km s^{-1}. A typical error of the line center of an unsaturated absorption line in quasar spectra is about $1/10th$ of the pixel size (the wavelength interval between pixels) [41]. Current observations with the UV-Visual Echelle Spectrograph (UVES) at the ESO Very Large Telescope (VLT) provide a pixel size $\Delta\lambda_{\rm pix} \sim 0.05 - 0.06$ Å, i.e., at $\lambda \sim 5000$ Å the expected error σ_v should be ∼0.3 km s^{-1}, which is comparable to the velocity offset due to a fractional change in α at the level of 10^{-5}. Such a critical relationship between the 'signal' (expected velocity offset Δv) and the error σ_v hampers measuring $\Delta\alpha/\alpha$ at the level of $\sim 10^{-5}$ from any absorption system taking into account all imperfections of the spectrograph and the data reduction procedure. Systematic errors exceeding 0.5 km s^{-1} are known to be typical for the wavelength calibration in both the VLT/UVES and Keck/HIRES spectrographs [12,42–44]. At this level of the systematic errors an estimate of $\Delta\alpha/\alpha$ from any individual absorption-line system must be considered as an *upper limit* but not a 'signal'. Otherwise, a formal statistical analysis of such values may lead to unphysical results (examples can be found in the literature).

The UV molecular spectra of H_2 and CO observed at high redshifts in the optical wavelength band encounter with similar difficulties and restrictions. The maximum difference between the sensitivity coefficients in case of H_2 is $\Delta Q \sim 0.06$, the rest frame wavelength uncertainties are negligible, $\sim 5 \times 10^{-9}$ [45], and with the current spectral facilities at giant telescopes it is hard to get estimates of $\Delta\mu/\mu$ at a level deeper than 10^{-5}. For carbon monoxide such measurements have not been done so far but the expected limit on $\Delta\mu/\mu$ should be $\gtrsim 10^{-5}$ since CO lines are much weaker than H_2 [46] and therefore their line centers are less certain. The analogue of Eq. (6) for

the μ-estimation from a pair of molecular lines is [47]:

$$\frac{\Delta\mu}{\mu} = \frac{\Delta v}{c\Delta Q} = \frac{v_1 - v_2}{c(Q_2 - Q_1)}\,, \tag{8}$$

and for a given level of $\Delta\mu/\mu$, molecular line centers should be measured with an error

$$\sigma_v < \frac{\Delta Q}{\sqrt{2}}\frac{\Delta\mu}{\mu}c\,. \tag{9}$$

This means that at $\Delta\mu/\mu \sim 10^{-5}$, the required position accuracy should be $\sigma_v \lesssim 0.13$ km s^{-1}, or the pixel size $\Delta\lambda_{\rm pix} \lesssim 0.017$ Å at 4000 Å. This requirement was realized in the VLT/UVES observations of the quasar Q0347–383 [48] where a limit on $\Delta\mu/\mu$ of $(4.3 \pm 7.2) \times 10^{-6}$ was set.

At present the only way to probe variation of the fundamental constants on the cosmological timescale at a level deeper than 10^{-5} is to switch from optical to far infrared and microwave bands. In the microwave, or submillimeter range there are a good deal of molecular transitions arising in Galactic and extragalactic sources. Electronic, vibrational, and rotational energies in molecular spectra are scaled as $E_{\rm el} : E_{\rm vib} : E_{\rm rot} = 1 : \mu^{1/2} : \mu$. In other words, the sensitivity coefficients for pure vibrational and rotational transitions are equal to $Q_\mu = 0.5$ and $Q_\mu = 1$, respectively. Besides, molecules have fine and hyperfine structures, Λ-doubling, hindered rotation, accidental degeneracy between narrow close-lying levels of different types, which have a specific dependence on the physical constants. The advantage of radio observations is that some of these molecular transitions are approximately 100–1000 times more sensitive to variations of μ and/or α than optical and UV transitions.

In the far infrared waveband also lie atomic fine-structure transitions, which have sensitivity to α-variation $Q_\alpha \approx 2$ [49]. We can combine observations of these lines and rotational molecular transitions to probe a combination $F = \alpha^2/\mu$ [50]. Besides, radio-astronomical observations allow us to measure emission lines from molecular clouds in the Milky Way with an extremely high spectral resolution (channel width $\sim$0.02 km s^{-1}) leading to stringent constraints at the level of $\sim 10^{-9}$ [24]. The level 10^{-9} is a natural limit for radio-astronomical observations since it requires the rest frequencies of molecular transitions to be known with an accuracy better than 100 Hz. At the moment only ammonia inversion transitions and 18 cm OH Λ-doublet transitions have been measured in the laboratory with such a high accuracy [51, 52].

In the next sections we consider in more detail the sensitivities of different types of molecular transitions to changes in α and μ. We are mainly dealing with molecular lines observed in microwave and submillimeter ranges in the interstellar medium, but a few low-frequency transitions with high sensitivities are also included in our analysis just to extend the list of possible targets for future studies at the next generation of large telescopes for low-frequency radio astronomy.

3 Diatomic radicals in the Π ground state: CH, OH, and NH^+

We start our analysis of the microwave spectra of molecules from the simplest systems — diatomic molecules with nonzero projection of the electronic angular momentum $\boldsymbol{L}$ on the molecular axis. Several such molecules are observed in the interstellar medium. Here we will mostly focus on the two most abundant species — CH and OH. Recently it was realized that Λ-doublet transitions in these molecules have high sensitivity to the variation of both α and μ [53–55]. There are also several relatively low frequency transitions between rotational levels of the ground state doublet $\Pi_{1/2}$ and $\Pi_{3/2}$ with sensitivities, which are significantly different from the typical rotational ones [56]. Then we will briefly discuss the NH^+ radical[2], which is interesting because it has very low lying excited electronic state $^4\Sigma^-$. This leads to an additional enhancement of the dimensionless sensitivity coefficients Q [58]. The latter are defined as follows:

$$\frac{\Delta\omega}{\omega} = Q_\alpha\frac{\Delta\alpha}{\alpha} + Q_\mu\frac{\Delta\mu}{\mu}\,. \tag{10}$$

3.1 Λ-doubling and Ω-doubling

Consider electronic state with nonzero projection Λ of the orbital angular momentum on the molecular axis. The spin-orbit interaction couples electron spin $\boldsymbol{S}$ to the molecular axis, its projection being Σ. To a first approximation the spin-orbit interaction is reduced to the form $H_{so} = A\Lambda\Sigma$. Total electronic angular momentum $\boldsymbol{J}_e = \boldsymbol{L} + \boldsymbol{S}$ has projection Ω on the axis, $\Omega = \Lambda + \Sigma$. For a particular case of $\Lambda = 1$ and $S = \frac{1}{2}$ we have two states $\Pi_{1/2}$ and $\Pi_{3/2}$ and the energy difference between them is: $E(\Pi_{3/2}) - E(\Pi_{1/2}) = A$.

Rotational energy of the molecule is described by the Hamiltonian:

[2] NH^+ has not yet been detected in space, its fractional abundance in star-forming regions is estimated $N(NH^+)/N(H_2) \lesssim 4 \times 10^{-10}$ [57].

$$H_{\rm rot} = B(\boldsymbol{J} - \boldsymbol{J}_e)^2 \tag{11a}$$

$$= B\boldsymbol{J}^2 - 2B(\boldsymbol{J}\boldsymbol{J}_e) + B\boldsymbol{J}_e^2\,, \tag{11b}$$

where B is the rotational constant and $\boldsymbol{J}$ is the total angular momentum of the molecule. The first term in expression (11b) describes conventional rotational spectrum. The last term is constant for a given electronic state and can be added to the electronic energy.[3] The second term describes Ω-doubling and is known as the Coriolis interaction $H_{\rm Cor}$.

If we neglect the Coriolis interaction, the eigenvectors of Hamiltonian (11) have definite projections M and Ω of the molecular angular momentum $\boldsymbol{J}$ on the laboratory axis and on the molecular axis respectively. In this approximation the states $|J, M, \Lambda, \Sigma, \Omega\rangle$ and $|J, M, -\Lambda, -\Sigma, -\Omega\rangle$ are degenerate, $E_{J,\pm\Omega} = BJ(J+1)$. The Coriolis interaction couples these states and removes degeneracy. New eigenstates are the states of definite parity $p = \pm 1$ [59]:

$$|J, M, \Omega, p\rangle = (|J, M, \Omega\rangle + p(-1)^{J-S}|J, M, -\Omega\rangle)/\sqrt{2}. \tag{12}$$

The operator $H_{\rm Cor}$ can only change quantum number Ω by one, so the coupling of states $|\Omega\rangle$ and $|-\Omega\rangle$ takes place in the 2Ω order of the perturbation theory in $H_{\rm Cor}$.

The Ω-doubling for the state $\Pi_{1/2}$ happens already in the first order in the Coriolis interaction, but has additional smallness from the spin-orbit mixing. The operator $H_{\rm Cor}$ can not directly mix degenerate $|\Lambda, \Sigma, \Omega\rangle$ states $|1, -\frac{1}{2}, \frac{1}{2}\rangle$ and $|-1, \frac{1}{2}, -\frac{1}{2}\rangle$ because it requires changing Λ by two. Therefore, we need to consider spin-orbit mixing of the Π and Σ states:

$$\left|\Omega = \frac{1}{2}\right\rangle = \left|1, -\frac{1}{2}, \frac{1}{2}\right\rangle + \zeta \left|0, \frac{1}{2}, \frac{1}{2}\right\rangle, \tag{13}$$

where

$$\zeta \sim A/(E_\Pi - E_\Sigma), \tag{14}$$

and then

$$\left\langle \Omega = \frac{1}{2}\middle| H_{\rm Cor}\middle|\Omega = -\frac{1}{2}\right\rangle = 2\zeta B\left(J + \frac{1}{2}\right)\langle \Lambda = 1|L_x|\Lambda = 0\rangle. \tag{15}$$

[3] Note that this term contributes to the separation between the states $\Pi_{1/2}$ and $\Pi_{3/2}$. This becomes particularly important for light molecules, where the constant A is small.

Note that ζ depends on the non-diagonal matrix element (ME) of the spin-orbit interaction and Eq. (14) is only an order of magnitude estimate. It is important, though, that non-diagonal and diagonal MEs have similar dependence on fundamental constants. We conclude that Ω-splitting for the $\Pi_{1/2}$ level must scale as $ABJ/(E_\Pi - E_\Sigma)$. The Ω-doubling for $\Pi_{3/2}$ state takes place in the third order in the Coriolis interaction. Here $H_{\rm Cor}$ has to mix first states $\Pi_{3/2}$ with $\Pi_{1/2}$ and $\Pi_{-3/2}$ with $\Pi_{-1/2}$ before ME (15) can be used. Therefore, the splitting scales as $B^3J^3/[A(E_\Pi - E_\Sigma)]$.

The above consideration corresponds to the coupling case *a*, when $|A| \gg B$. In the opposite limit the states $\Pi_{1/2}$ and $\Pi_{3/2}$ are strongly mixed by the Coriolis interaction and spin $\boldsymbol{S}$ decouples from the molecular axis (coupling case *b*). As a result, the quantum numbers Σ and Ω are not defined and we only have one quantum number $\Lambda = \pm 1$. The Λ-splitting takes place now in the second order in the Coriolis interaction via intermediate Σ states. The scaling here is obviously of the form $B^2J^2/(E_\Pi - E_\Sigma)$. Note that in contrast to the previous case $|A| \gg B$, the splitting here is independent on A.

We can now use found scalings of the Λ- and Ω-doublings to determine sensitivity coefficients (10). We only need to recall that in atomic units $A \propto \alpha^2$ and $B \propto \mu$. We conclude that for the case *a* the Ω-doubling spectrum has following sensitivity coefficients:

$$\text{State } {}^2\Pi_{1/2}: \quad Q_\alpha = 2\,, \quad Q_\mu = 1\,, \tag{16a}$$

$$\text{State } {}^2\Pi_{3/2}: \quad Q_\alpha = -2\,, \quad Q_\mu = 3\,. \tag{16b}$$

For the case *b*, when $\boldsymbol{S}$ is completely decoupled from the axis, the Λ-doubling spectrum has following sensitivity coefficients:

$$\text{State } \Pi: \quad Q_\alpha = 0\,, \quad Q_\mu = 2\,. \tag{16c}$$

When constant A is slightly larger than B, the spin $\boldsymbol{S}$ is coupled to the axis only for lower rotational levels. As rotational energy grows with J and becomes larger than the splitting between states $\Pi_{1/2}$ and $\Pi_{3/2}$, the spin decouples from the axis. Consequently, the Ω-doubling is transformed into Λ-doubling. Equations (16) show that this can cause significant changes in sensitivity coefficients. The spin-orbit constant A can be either positive (CH molecule), or negative (OH). The sign of the Ω-doubling depends on the sign of A, while Λ-doubling does not depend on A at all. Therefore, decoupling of the spin can change the sign of the splitting. In Sec. 3.2 we will see that this can lead to a dramatic enhancement of the sensitivity to the variation of fundamental constants.

3.2 Intermediate coupling

The Λ-doubling for the intermediate coupling was studied in detail in many papers, including [63–65] (see also the book [59]). Here we use the effective Hamiltonian $H_{\rm eff}$ from [63] in the subspace of the levels $\Pi^{\pm}_{1/2}$ and $\Pi^{\pm}_{3/2}$, where upper sign corresponds to the parity p in Eq. (12). The operator $H_{\rm eff}$ includes spin-rotational and hyperfine parts

$$H_{\rm eff} = H_{\rm sr} + H_{\rm hf}\,. \tag{17}$$

Neglecting third order terms in the Coriolis and spin-orbit interactions, we get the following simplified form of the spin-rotational part:

$$\langle \Pi_{1/2},\, J,\, p|\, H_{\rm sr}|\Pi_{1/2},\, J,\, p\rangle = -\frac{1}{2}A + B\left(J+\frac{1}{2}\right)^2 + p(S_1+S_2)(2J+1)\,, \tag{18a}$$

$$\langle \Pi_{3/2},\, J,\, p|\, H_{\rm sr}|\Pi_{3/2},\, J,\, p\rangle = +\frac{1}{2}A + B\left(J+\frac{1}{2}\right)^2 - 2B\,, \tag{18b}$$

$$\langle \Pi_{3/2},\, J,\, p|\, H_{\rm sr}|\Pi_{1/2},\, J,\, p\rangle = \left[B + pS_2\left(J+\frac{1}{2}\right)\right] \times \sqrt{\left(J-\frac{1}{2}\right)\left(J+\frac{3}{2}\right)}\,. \tag{18c}$$

Here in addition to the parameters A and B we have two parameters which appear in the second order of perturbation theory via intermediate state(s) $\Sigma_{1/2}$. The parameter S_1 corresponds to the cross term of the perturbation theory in the spin-orbit and Coriolis interactions, while the parameter S_2 is quadratic in the Coriolis interaction. Because of this S_1 scales as $\alpha^2\mu$ and S_2 scales as μ^2. It is easy to see that the Hamiltonian $H_{\rm sr}$ describes limiting cases $|A| \gg B$ and $|A| \ll B$ considered in Sec. 3.1.

The hyperfine part of the effective Hamiltonian is defined in the lowest order of perturbation theory and has the form:

$$\langle \Pi_{1/2},\, J,\, p|H_{\rm hf}|\Pi_{1/2},\, J,\, p\rangle = C_F[2a - b - c + p(2J+1)d], \tag{19a}$$

$$\langle \Pi_{3/2},\, J,\, p|H_{\rm hf}|\Pi_{3/2},\, J,\, p\rangle = 3C_F\,[2a + b + c]\,, \tag{19b}$$

$$\langle \Pi_{3/2},\, J,\, p|\, H_{\rm hf}|\Pi_{1/2},\, J,\, p\rangle = -C_F\sqrt{(2J-1)(2J+3)}\,b, \tag{19c}$$

$$C_F \equiv [F(F+1) - J(J+1) - I(I+1)][8J(J+1)]^{-1}\,.$$

Here we assume that only one nucleus has spin and include only magnetic dipole hyperfine interaction.

The effective Hamiltonian described by Eqs. (18, 19) has 8 parameters. We use NIST values [60] for the fine structure splitting A, rotational constant B, and magnetic hyperfine constants a, b, c, d. Remaining two parameters S_1 and S_2 are found by minimizing the *rms* deviation between theoretical and experimental Λ-doubling spectra.

In order to find sensitivity coefficients Q_α we calculate transition frequencies for two values of $\alpha = \alpha_0 \pm \delta$ near its physical value $\alpha_0 = 1/137.035999679(94)$. The similar procedure is applied to Q_μ at the physical value of the electron-to-proton mass ratio, $\mu_0 = 1/1836.15267247(80)$. We use scaling rules discussed above to recalculate parameters of the effective Hamiltonian for different values of fundamental constants. Then we use numerical differentiation to find respective sensitivity coefficient.

3.3 Sensitivity coefficients for Λ-doublet transitions in CH and OH

In Ref. [55], the method described in the previous section was applied to ^{16}OH, ^{12}CH, ^{7}Li^{16}O, ^{14}N^{16}O, and ^{15}N^{16}O. The molecules CH and NO have ground state $^2\Pi_{1/2}$ ($A > 0$), while OH and LiO have ground state $^2\Pi_{3/2}$ ($A < 0$). The ratio $|A/B|$ changes from 2 for CH molecule [66], to 7 for OH [67], and to almost a hundred for LiO and NO. Therefore, LiO and NO definitely belong to the coupling case *a*. For OH molecule we can expect transition from case *a* for lower rotational states to case *b* for higher ones. Finally, for CH we expect intermediate coupling for lower rotational states and coupling case *b* for higher states.

Let us see how this scheme works in practice for the effective Hamiltonian (18, 19). Figure 1 demonstrates J-dependence of the sensitivity coefficients for CH and OH molecules. Both of them have only one nuclear spin $I = \frac{1}{2}$. For a given quantum number J, each Λ-doublet transition has four hyperfine components: two strong transitions with $\Delta F = 0$ and $F = J \pm \frac{1}{2}$ (for $J = \frac{1}{2}$ there is only one transition with $F = 1$) and two weaker transitions with $\Delta F = \pm 1$. The hyperfine structure for OH and CH molecules is rather small and sensitivity coefficients for all hyperfine components are very close. Because of

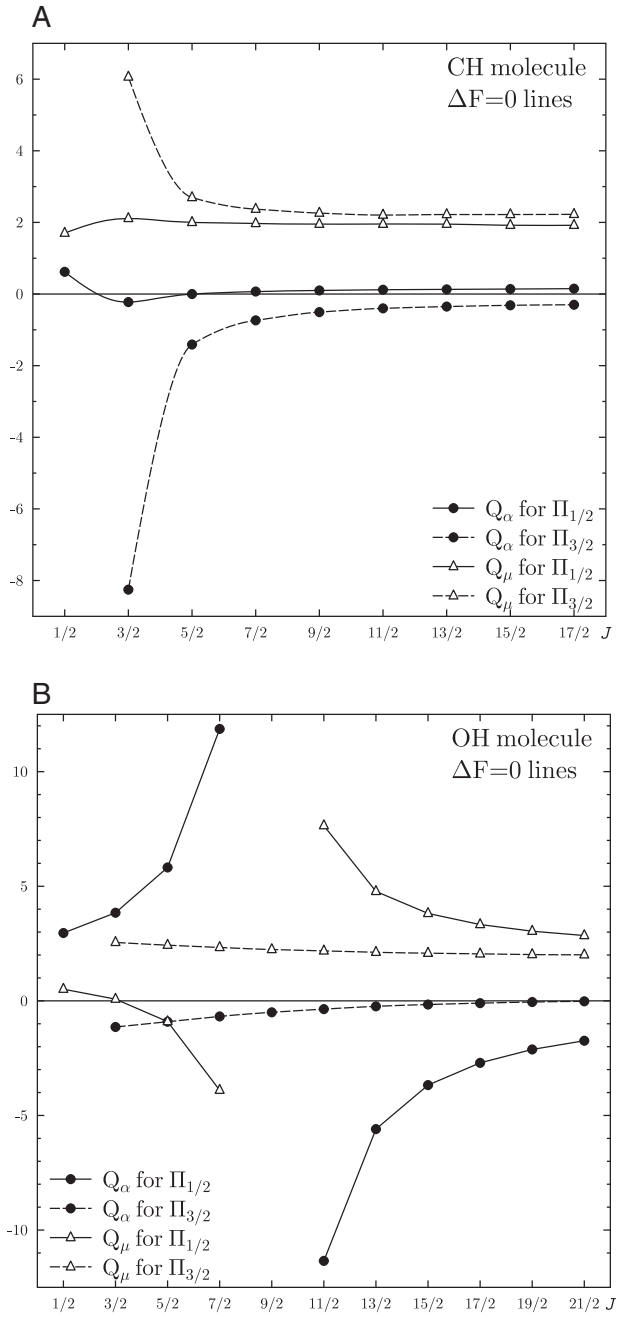

Figure 1 Sensitivity coefficients Q_α and Q_μ for Λ-doublet lines with $\Delta F = 0$ in CH and OH. The difference between lines with $F = J + \frac{1}{2}$ and $F = J - \frac{1}{2}$ is too small to be seen. For the state $\Pi_{3/2}$ of OH the values for $J = \frac{9}{2}$ are too large to be shown on the plot. They are listed in Table 1.

that Fig. 1 presents only averaged values for strong transitions with $\Delta F = 0$.

We see that for large values of J the sensitivity coefficients for both molecules approach limit (16c) of the coupling case *b*. The opposite limits (16a, 16b) are not reached for either molecule even for smallest values of J. So, we conclude that the coupling case *a* is not realized. It is interesting that in Fig. 1 the curves for the lower states are smooth, while for upper states there are singularities. For CH molecule this singularity takes place for the state $\Pi_{3/2}$ near the lowest possible value $J = 3/2$. A singularity for OH molecule takes place for the state $\Pi_{1/2}$ near $J = 9/2$.

These singularities appear because Λ-splitting turns to zero. As we saw above, the sign of the splitting for the coupling case *a* depends on the sign of the constant A. The same sign determines which state $\Pi_{1/2}$, or $\Pi_{3/2}$ lies higher. As a result, for the lower state the sign of the splitting is the same for both limiting cases, but decoupling of the electron spin S for the upper state leads to the change of sign of the splitting. Of course, these singularities are most interesting for our purposes, as they lead to large sensitivity coefficients which strongly depend on the quantum numbers. Note, that when the frequency of the transition is small, it becomes sensitive to the hyperfine part of the Hamiltonian and the sensitivity coefficients for hyperfine components may differ significantly. The sensitivity coefficients of all hyperfine components of such Λ-lines are given in Table 1. We can see that near the singularities all sensitivity coefficients are enhanced.

In addition to Λ-doublet transitions and purely rotational transitions there are also mixed transitions between rotational states of $\Pi_{1/2}$ and $\Pi_{3/2}$ states. The transition energy here includes the rotational and the fine structure parts. Because of that, such transitions may have different sensitivities to the variation of fundamental constants [56]. As an example, Fig. 2 shows mixed transitions in CH molecule. The sensitivity coefficients are given in Table 2. The isotopologue CD has mixed transitions of lower frequencies and higher sensitivities [56]. Similar picture takes place for OH molecule.

The molecule NH^+ is isoelectronic to CH and also has ground state $^2\Pi_{1/2}$. However, there is an important difference: for NH^+ the first excited state $^4\Sigma^-$ lies only 340 cm^{-1} above the ground state [68, 69]. The spin-orbit interaction between these states leads to strong perturbations of the rotational structure and of the Λ-doublet splittings and to an additional enhancement of the sensitivity coefficients [58]. The spectrum of NH^+ is shown in Fig. 3. The effective Hamiltonian is similar to the one considered above with two additional terms describing interaction between the $^2\Pi$ and $^4\Sigma$ states [68]:

$$\langle {}^2\Pi_{3/2},\, J,\, p|\, H_{\rm so}|\, {}^4\Sigma^-_{3/2},\, J,\, p\rangle = -\frac{1}{2}\zeta_{3/2}\,, \tag{20a}$$

$$\langle {}^2\Pi_{1/2},\, J,\, p|H_{\rm so}|\, {}^4\Sigma^-_{1/2},\, J,\, p\rangle = -\frac{1}{2\sqrt{3}}\zeta_{1/2}\,. \tag{20b}$$

Table 1 Frequencies (in MHz) and sensitivity coefficients for hyperfine components $(J, F \to J, F')$ of Λ-doublet lines in CH and OH molecules. Recommended frequencies and their uncertainties are taken from [60–62].

					ω (MHz)					
Molecule	Level	J	F	F'	Recom.	Uncert.	Theory	Diff.	Q_α	Q_μ
^{12}CH	$^2\Pi_{1/2}$	0.5	0	1	3263.795	0.003	3269.40	− 5.61	0.59	1.71
		0.5	1	1	3335.481	0.001	3340.77	− 5.29	0.62	1.70
		0.5	1	0	3349.194	0.003	3354.11	− 4.92	0.63	1.69
		1.5	1	2	7275.004	0.001	7262.25	12.75	− 0.24	2.12
		1.5	1	1	7325.203	0.001	7312.02	13.18	− 0.23	2.11
		1.5	2	2	7348.419	0.001	7335.30	13.12	− 0.22	2.11
		1.5	2	1	7398.618	0.001	7385.08	13.54	− 0.20	2.10
^{12}CH	$^2\Pi_{3/2}$	1.5	2	2	701.68	0.01	682.96	18.72	− 8.44	6.15
		1.5	1	2	703.97	0.03	679.83	24.14	− 8.66	6.32
		1.5	2	1	722.30	0.03	702.98	19.52	− 8.37	6.17
		1.5	1	1	724.79	0.01	699.85	24.94	− 8.07	5.97
^{16}OH	$^2\Pi_{3/2}$	1.5	1	2	1612.2310	0.0002	1595.42	16.81	− 1.27	2.61
		1.5	1	1	1665.4018	0.0002	1648.93	16.47	− 1.14	2.55
		1.5	2	2	1667.3590	0.0002	1650.66	16.70	− 1.14	2.55
		1.5	2	1	1720.5300	0.0002	1704.17	16.36	− 1.02	2.49
^{16}OH	$^2\Pi_{1/2}$	0.5	0	1	4660.2420	0.0030	4638.98	21.26	2.98	0.50
		0.5	1	1	4750.6560	0.0030	4729.51	21.15	2.96	0.51
		0.5	1	0	4765.5620	0.0030	4744.50	21.06	2.96	0.51
		4.5	5	4	88.9504	0.0011	64.34	24.61	− 921.58	459.86
		4.5	5	5	117.1495	0.0011	92.35	24.80	− 699.65	349.59
		4.5	4	4	164.7960	0.0011	141.20	23.60	− 496.67	248.77
		4.5	4	5	192.9957	0.0011	169.22	23.78	− 424.05	212.68

Obviously, the parameters $\zeta_{1/2}$ and $\zeta_{3/2}$ scale as α^2. As mentioned above, for the NH^+ molecule the splitting between Σ and Π states $\Delta E_{\Sigma\Pi}$ is only about 340 cm^{-1}. This splitting includes three contributions: the non-relativistic electronic energy difference, the relativistic corrections ($\sim\alpha^2 Z^2$) and the difference in the zero point vibrational energies for the two states ($\sim\mu^{1/2}$). Note that the accidental degeneracy of these levels for NH^+ means that the first contribution is anomalously small. Because of that, the other two contributions can not be neglected and modify the scaling of $\Delta E_{\Sigma\Pi}$ with fundamental constants. This effect has to be taken into account in the calculations of the sensitivity coefficients [58].

4 Linear polyatomic radicals in the Π ground state: C_3H

The linear form of the molecule C_3H (l-C_3H) is similar to the molecule NH^+: it also has the ground state $^2\Pi_{1/2}$ and two closely lying states $^2\Pi_{3/2}$ and $^2\Sigma^+_{1/2}$. Here the quasi

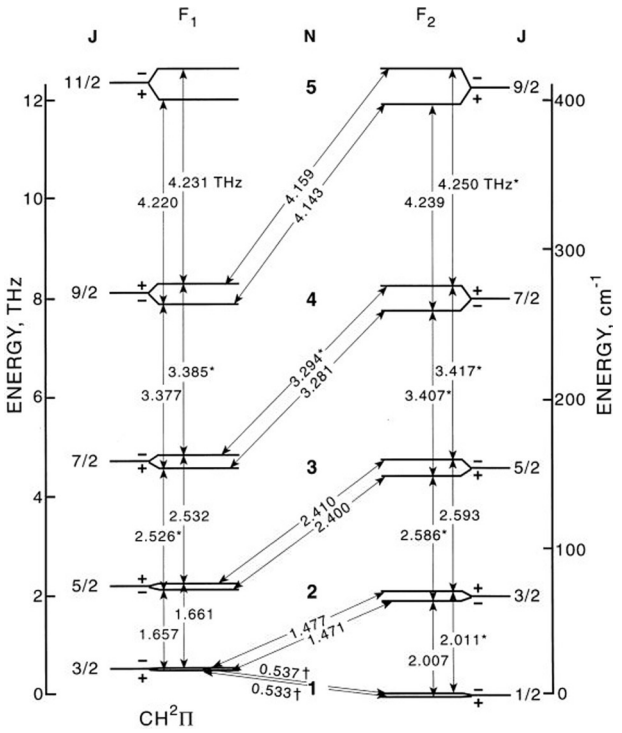

Figure 2 Rotational spectrum of CH from [66]. Vertical and diagonal arrows correspond to pure rotational and mixed transitions, respectively. Λ-doubling is not to scale.

Table 2 Frequencies (GHz) and sensitivities of the rotational and mixed transitions in CH.

N, J, p	N', J', p'	ν_{theor}	ν_{expt} [62]	Q_α	Q_μ
$1, \frac{3}{2}, +$	$1, \frac{1}{2}, -$	533.9	532.7	1.59	0.20
$1, \frac{3}{2}, -$	$1, \frac{1}{2}, +$	537.9	536.8	1.57	0.22
$2, \frac{3}{2}, +$	$1, \frac{3}{2}, -$	1477.2	1477.4	0.00	1.00
$2, \frac{3}{2}, -$	$1, \frac{3}{2}, +$	1470.6	1470.7	−0.01	1.00
$2, \frac{5}{2}, +$	$1, \frac{3}{2}, -$	1663.0	1661.1	0.00	1.00
$2, \frac{5}{2}, -$	$1, \frac{3}{2}, +$	1658.8	1657.0	0.00	1.00
$2, \frac{3}{2}, +$	$1, \frac{1}{2}, -$	2011.8	2010.8	0.42	0.79
$2, \frac{3}{2}, -$	$1, \frac{1}{2}, +$	2007.8	2006.8	0.42	0.79
$2, \frac{5}{2}, +$	$2, \frac{3}{2}, -$	193.1	191.1	0.01	1.03
$2, \frac{5}{2}, -$	$2, \frac{3}{2}, +$	180.9	178.9	0.06	0.94

degeneracy of the Π and Σ states is not accidental, but is caused by the Renner-Teller interaction. In the following section we briefly recall the theory of the Renner-Teller effect in polyatomic linear molecules [70, 71].

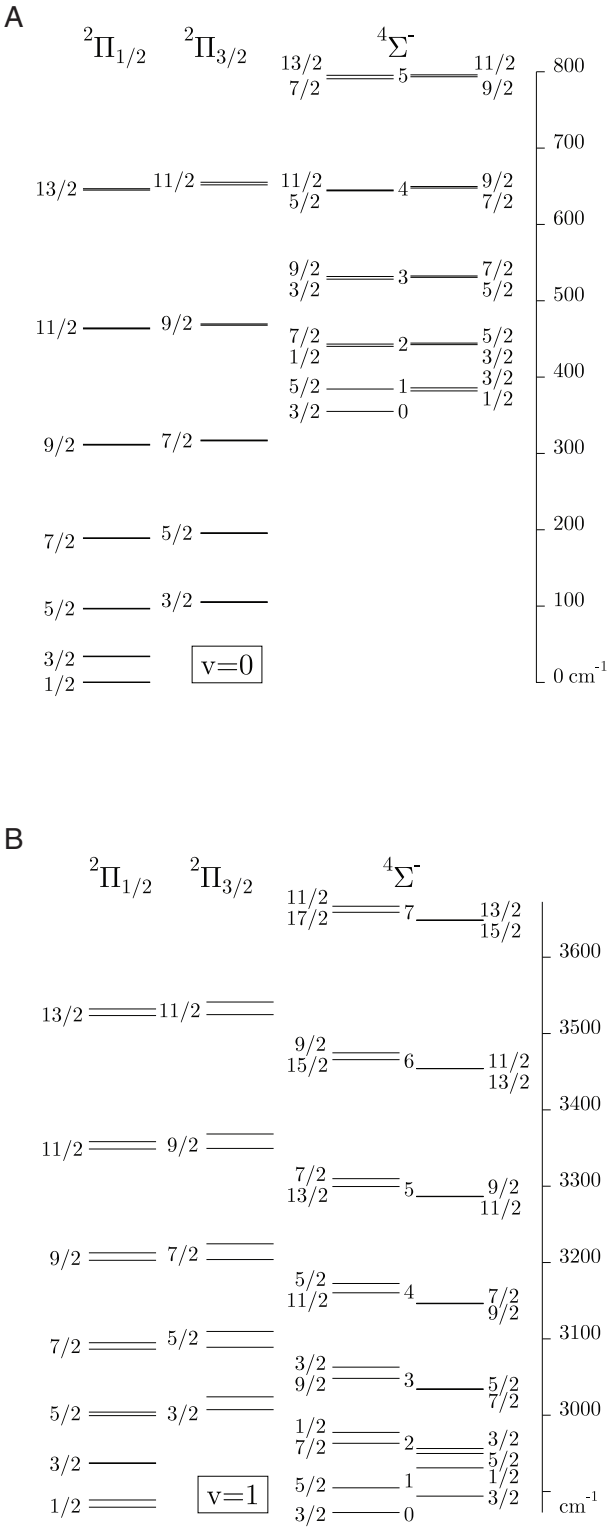

Figure 3 Spin-rotational levels of the three lowest electronic states of the molecule NH^+. Panels (A) and (B) correspond to vibrational states $v = 0$ and $v = 1$ respectively. The energy levels are labeled with the quantum number J for the Π states and with J and N for the Σ state.

4.1 Renner-Teller effect

The total molecular angular momentum of the polyatomic molecule $\boldsymbol{J}$ includes the vibrational angular momentum $\boldsymbol{G}$ associated with the twofold degenerate bending vibration mode(s): $\boldsymbol{J} = \boldsymbol{N} + \boldsymbol{S} = \boldsymbol{R} + \boldsymbol{G} + \boldsymbol{L} + \boldsymbol{S}$, where $\boldsymbol{R}$ describes rotation of the molecule as a whole and is perpendicular to the molecular axis ζ. Other momenta have nonzero ζ-projections: $\langle G_\zeta \rangle = l$, $\langle L_\zeta \rangle = \Lambda$, $\langle N_\zeta \rangle = K = l + \Lambda$, and $\langle J_\zeta \rangle = \Omega$.

Suppose we have Π electronic state $|\Lambda = \pm 1\rangle$ and $v = 1$ vibrational state of a bending mode $|l = \pm 1\rangle$. All together there are 4 states $|\Lambda = \pm 1\rangle|l = \pm 1\rangle$. We can rewrite them as one doublet Δ state $|K = \pm 2\rangle$ and states Σ^+ and Σ^-. In the adiabatic approximation all four states are degenerate. Renner [70] showed that the states with the same quantum number $K = l + \Lambda$ strongly interact, so the Σ^+ and Σ^- states repel each other, while the Δ doublet in the first approximation remains unperturbed. We are particularly interested in the case when one of the Σ levels is pushed close to the ground state $v = 0$. This is what takes place in the l-C_3H molecule [74–76].

Consider a linear polyatomic molecule with the unpaired electron in the π_ξ state in the molecular frame ξ, η, ζ. Obviously, the bending energy is different for bendings in $\xi\zeta$ and in $\eta\zeta$ planes: $V_\pm = \frac{1}{2} k_\pm \chi^2$ (here χ is the supplement to the bond angle). That means that the electronic energy depends on the angle ϕ between the electron and nuclear planes:

$$H' = V' \cos 2\phi \,, \tag{21}$$

where $2V' = V_+ - V_- = k'\chi^2$. There is no reason for V' to be small, so $k' \sim k_\pm \sim 1$ a.u. and to a first approximation k' does not depend on α and μ.

As long as interaction (21) depends on the relative angle between the electron and the vibrational planes, it changes the angular quantum numbers as follows: $\Delta\Lambda = -\Delta l = \pm 2$ and $\Delta K = 0$. This is exactly what is required to produce splitting between the Σ^+ and Σ^- states with $v = 1$ as discussed above.

Interaction (21) also mixes different vibrational levels with $\Delta v = \pm 2, \pm 4, \ldots$. Thus, we have, for example, the nonzero ME $\langle 0, 0, 1, 1|H'|2, 2, -1, 1\rangle$ between states $|v, l, \Lambda, K\rangle$. Such mixings reduce effective value of the quantum number Λ and, therefore, reduce the spin-orbital splitting between the $\Pi_{1/2}$ and $\Pi_{3/2}$ states [73],

$$H_{\rm so} \equiv A_{\rm eff} \Lambda \Sigma \,, \quad A_{\rm eff} = A\Lambda_{\rm eff}/\Lambda \,. \tag{22}$$

Let us define the model more accurately. Following [73] we write the Hamiltonian as:

$$H = H_e + T_v + A L_\zeta S_\zeta \,. \tag{23}$$

Here the "electronic" part H_e includes all degrees of freedom except for the bending vibrational mode and spin. For l-C_3H there are two bending modes, but for simplicity we include the second bending mode in H_e too. Electronic MEs in the $|\Lambda\rangle$ basis have the form:

$$\langle \pm 1|H_e|\pm 1\rangle = \frac{V_+ + V_-}{2} = \frac{k}{2}\chi^2 \,, \tag{24a}$$

$$\langle \pm 1|H_e|\mp 1\rangle = \frac{k'}{2}\chi^2 \exp(\mp 2i\phi) \,. \tag{24b}$$

Here χ and ϕ are the vibrational coordinates for the bending mode. Kinetic energy in these coordinates has the form:

$$T_v = -\frac{1}{2MR^2}\left(\frac{\partial^2}{\partial\chi^2} + \frac{1}{\chi}\frac{\partial}{\partial\chi} + \frac{1}{\chi^2}\frac{\partial^2}{\partial\phi^2}\right) . \tag{25}$$

We can use the basis set of 2D harmonic functions in polar coordinates $\rho = \chi R$ and ϕ for the mass M and the force constant k:

$$\psi_{v,l}(\rho, \phi) = R_{v,l}(\rho)\frac{1}{\sqrt{2\pi}}\exp(il\phi) \,. \tag{26}$$

It is important that the radial functions are orthogonal only for the same l:

$$\langle R_{v',l}|R_{v,l}\rangle = \delta_{v',v} \,. \tag{27}$$

This allows for the nonzero MEs between states with different quantum number l. By averaging operator (23) over vibrational functions we get:

$$\langle v', l'|H_e + T_v|v, l\rangle = \left[\omega_v(v+1) + A\Lambda S_\zeta\right]\delta_{v',v}\delta_{l',l} + \frac{1}{2}\langle R_{v'l'}|k'\chi^2|R_{vl}\rangle \exp(\mp 2i\phi)\delta_{l',l\pm 2} . \tag{28}$$

The exponent here ensures the selection rule $\Lambda' = \Lambda \mp 2$ for the quantum number Λ when we calculate MEs for the rotating molecule.

4.2 Molecule l-C_3H

We solve the eigenvalue problem for Hamiltonian (23) using the basis set of the 2D-harmonic oscillator. Our model Hamiltonian has only 3 parameters, namely ω_v, A, and the dimensionless Renner-Teller parameter $\mathcal{E}$:

Table 3 Low lying energy levels for the bending mode $\omega_\nu = 589\ \mathrm{cm}^{-1}$ of l-C_3H molecule and their sensitivities q_α and q_μ to the variation of α and μ respectively. Δ is the distance from the ground state. All values are in cm^{-1}.

						Δ			
v_{nom}	$\langle v\rangle$	K	Ω	$\langle\Lambda\rangle$	E	[72]	[73]	q_μ	q_α
0	1.22	1	0.5	0.50	367.9	0.0	0.0	187.8	−14.6
0	1.35	1	1.5	0.46	381.9	13.9	14.0	187.8	13.3
1	2.32	0	0.5	−0.01	394.2	26.3	27.0	197.3	−0.4
1	3.57	2	1.5	0.21	597.7	229.7	226.0	300.3	−6.1
1	3.65	2	2.5	0.19	603.5	235.5	232.0	300.3	5.5

Table 4 l-C_3H sensitivity coefficients for the transitions between states from Table 3 and for parameters A_{eff} and $\Delta E_{\Sigma\Pi}$ defined by (22) and (29) respectively. Frequencies are in cm^{-1}.

				Fit to [73]			Fit to [76]		
K	Ω	K'	Ω'	ω	Q_μ	Q_α	ω	Q_μ	Q_α
1	0.5	1	1.5	13.9	0.00	2.00	14.4	0.00	2.00
1	1.5	0	0.5	12.4	0.78	−1.11	13.3	0.77	−1.07
0	0.5	2	1.5	203.5	0.51	−0.03	204.4	0.51	−0.03
2	1.5	2	2.5	5.8	0.00	2.00	6.0	0.00	2.00
	A_{eff}			13.9	0.00	2.00	14.4	0.00	2.00
	$\Delta E_{\Sigma\Pi}$			19.4	0.50	0.00	20.5	0.50	0.00

$k' = \mathcal{E}k$. The values for ω_ν and A for l-C_3H are given in [73]. We varied the Renner-Teller parameter $\mathcal{E}$ to fit five lowest levels for the given bending mode: $\Pi_{1/2}$, $\Pi_{3/2}$, $\Sigma_{1/2}$, $\Delta_{3/2}$, and $\Delta_{5/2}$. The optimal value appeared to be $\mathcal{E} = 0.788$. The results are presented in Table 3. The first two columns give nominal vibrational quantum number v and its actual average value. We see that the Renner-Teller term in (28) strongly mixes vibrational states. This mixing also affects $\langle\Lambda\rangle$ and decreases spin-orbital splittings as explained by Eq. (22).

The last two columns in Table 3 give dimensional sensitivity coefficients q_μ and q_α in cm^{-1}:

$$\Delta E = q_\alpha \frac{\Delta\alpha}{\alpha} + q_\mu \frac{\Delta\mu}{\mu}\,.$$

To estimate them we assumed that the parameters scale in a following way: $\omega_\nu \sim \mu^{1/2}$, $A \sim \alpha^2$, and $\mathcal{E}$ does not depend on α and μ. The dimensionless sensitivity coefficients (10) for the transitions $\omega_{i,k} = E_k - E_i$ can be found as:

$$Q_{i,k} = (q_k - q_i)/\omega_{i,k}\,.$$

In Table 4 these coefficients are calculated for the same set of parameters as in Table 3 and for the slightly different parameters which better fit experimental frequencies from [76]. We see that the sensitivity coefficients are practically the same for both sets.

For the two fine structure transitions, $\Pi_{1/2} \longrightarrow \Pi_{3/2}$ and $\Delta_{3/2} \longrightarrow \Delta_{5/2}$, we get sensitivities $Q_\mu = 0$ and $Q_\alpha = 2$. This may seem strange as the fine structure is significantly reduced by the Renner-Teller mixing: the fine-structure parameter is 29 cm^{-1} and the splitting between $\Pi_{1/2}$ and $\Pi_{3/2}$ is only 13.9 cm^{-1}. According to (22) the mixing reduces the splitting. However, this effect depends on the dimensionless Renner-Teller parameter $\mathcal{E}$ and does not depend on μ and α. Consequently, *the effective parameter A_{eff} depends on fundamental constants in the same way as initial parameter A.*

For the high frequency transition $\Sigma_{1/2} \longrightarrow \Delta_{3/2}$, where the spin-orbital energy can be neglected, we get $Q_\mu = 0.5$ and $Q_\alpha = 0$. These results are expected, because our model has only two dimensional parameters: vibrational frequency, which is proportional to $\mu^{1/2}$ and the fine structure parameter A, which scales as α^2. Even though our vibrational spectrum is far from that of a simple harmonic oscillator, the non-diagonal MEs (28) of the Hamiltonian (23) still scale as $\mu^{1/2}$. Therefore, if we neglect spin-orbital splittings, we get $Q_\mu = 1/2$ for all transitions. The only transition in Table 4 where the spin-orbital energy and vibrational energy are close to each other is the $\Pi_{3/2} \longrightarrow \Sigma_{1/2}$ transition. The resultant frequency is roughly half of the vibrational energy difference between the Π and Σ states. This leads to $Q_\mu \approx 1$ and $Q_\alpha \approx -1$.

The spectrum of the l-C_3H molecule is shown on Fig. 4. The effective Hamiltonian for the rotating molecule is similar to that of the NH^+ molecule. It includes the effective fine-structure parameter A_{eff} and the energy difference between the Σ and Π states,

$$\Delta E_{\Sigma\Pi} = E(\Sigma^+) - \frac{E(\Pi_{1/2}) + E(\Pi_{3/2})}{2}\,. \tag{29}$$

Numerical values for these parameter are obtained from the fit to the experimental transition frequencies. Here we only need to determine the dependence of these parameters on fundamental constants. Table 4 shows that $A_{\mathrm{eff}} \sim \alpha^2$ and $\Delta E_{\Sigma\Pi} \sim \mu^{1/2}$. Once again, this is because

the Renner-Teller mixing depends on the dimensionless parameter $\mathcal{E}$ and *does not* depend on α and μ. Calculated sensitivity coefficients for the K-doublet transitions of the l-C_3H molecule are listed in Tables 5 and 6. The results for the mixed transitions can be found in [72].

5 Tunneling modes in polyatomic molecules

In this section we consider non linear and non planar polyatomic molecules. Such molecules generally have more than one equivalent potential minimum. If the barriers between these minima are not too high the molecule can tunnel between them. Ammonia (NH_3) is the best known textbook example of a nonrigid molecule (see Fig. 5). Interestingly, this molecule is also one of the most abundoned polyatomic molecules in the interstellar medium. Other important for astrophysics molecules with tunneling include hydronium (H_3O^+), peroxide (H_2O_2), methanol (CH_3OH), and methylamine (CH_3NH_2). We will briefly discuss all of them below. All these molecules include only light atoms with $Z \leq 8$ and have singlet electronic ground states. Thus we can neglect relativistic corrections and assume that all discussed transitions have $Q_\alpha = 0$.

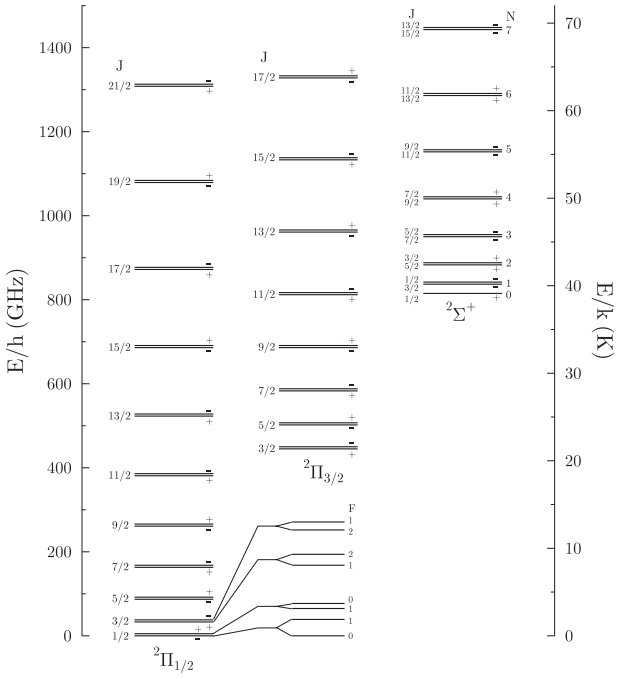

Figure 4 Spin-rotational levels of the three lowest vibronic states of the molecule l-C_3H. K-doubling is indicated schematically, hyperfine structure is shown only for the two lowest K-doublets. Due to a strong Renner-Teller effect the component $^2\Sigma^+$ of the excited bending state ν_4(CCH bending) is shifted towards lower energies, $\sim$29 cm^{-1} above the zero-level of the ground state $^2\Pi_{1/2}$.

Table 5 Frequencies (MHz), sensitivity coefficients, and reduced MEs (a.u.) for some K-doubling transitions in $\Pi_{1/2}$ state of the l-C_3H molecule.

J $F'p'$, Fp	ω	Q_α	Q_μ	$\|\|D\|\|^2$
$\frac{1}{2}$ 1+, 0−	52.37	0.66(2)	1.7(2)	0.333
$\frac{1}{2}$ 0+, 1−	39.12	0.20(2)	1.9(2)	0.333
$\frac{1}{2}$ 1+, 1−	34.93	−0.02(2)	2.0(2)	0.667
$\frac{3}{2}$ 1−, 1+	85.55	0.65(2)	1.7(1)	0.166
$\frac{3}{2}$ 2−, 1+	78.60	0.55(2)	1.7(1)	0.033
$\frac{3}{2}$ 1−, 2+	75.23	0.43(2)	1.8(1)	0.033
$\frac{3}{2}$ 2−, 2+	68.29	0.30(2)	1.8(1)	0.299
$\frac{5}{2}$ 2+, 2−	107.19	0.95(2)	1.5(1)	0.132
$\frac{5}{2}$ 3+, 2−	98.97	0.89(2)	1.5(1)	0.009
$\frac{5}{2}$ 2+, 3−	98.83	0.82(2)	1.6(1)	0.009
$\frac{5}{2}$ 3+, 3−	90.61	0.75(2)	1.6(1)	0.188
$\frac{7}{2}$ 3−, 3+	112.38	1.63(2)	1.2(1)	0.105
$\frac{7}{2}$ 4−, 4+	96.07	1.56(2)	1.2(1)	0.136
$\frac{9}{2}$ 4+, 4−	95.75	3.22(4)	0.36(7)	0.086
$\frac{9}{2}$ 5+, 5−	79.63	3.45(4)	0.23(7)	0.105
$\frac{11}{2}$ 5−, 5+	52.81	9.1 (6)	−2.6 (3)	0.072
$\frac{11}{2}$ 6−, 6+	36.85	12.1 (6)	−4.1 (3)	0.085
$\frac{13}{2}$ 6−, 6+	20.25	− 34. (2)	19. (2)	0.062
$\frac{13}{2}$ 7−, 7+	36.06	− 18. (2)	11. (2)	0.071
$\frac{15}{2}$ 7+, 7−	126.59	−7.6 (2)	5.8 (4)	0.054
$\frac{15}{2}$ 8+, 8−	142.24	−6.5 (2)	5.3 (4)	0.061
$\frac{17}{2}$ 8−, 8+	268.76	−4.7 (1)	4.4(3)	0.047
$\frac{17}{2}$ 9−, 9+	284.25	−4.3 (1)	4.2(3)	0.053
$\frac{19}{2}$ 9+, 9−	448.75	−3.59(7)	3.8(3)	0.042
$\frac{19}{2}$ 10+, 10−	464.07	−3.39(7)	3.7(3)	0.046
$\frac{21}{2}$ 10−, 10+	668.02	−2.97(6)	3.5 (3)	0.038
$\frac{21}{2}$ 11−, 11+	683.18	−2.85(6)	3.4 (3)	0.041

It is clear that tunneling frequencies should strongly depend on the nuclear masses, and we can expect large sensitivity coefficients $Q_{\mu,\mathrm{tun}}$. They can be found using

Table 6 Frequencies (MHz), sensitivity coefficients, and reduced MEs (a.u.) for some K-doubling transitions in $\Pi_{3/2}$ state of the l-C_3H molecule.

$J\ F'p', Fp$	ω	Q_α	Q_μ	$\|\|D\|\|^2$
$\frac{3}{2}\ 1-, 1+$	5.61	−2.63(8)	3.2 (2)	1.493
$\frac{3}{2}\ 2-, 1+$	18.50	0.49(8)	1.7 (2)	0.299
$\frac{3}{2}\ 1-, 2+$	−7.30	5.28(8)	−0.6 (2)	0.299
$\frac{3}{2}\ 2-, 2+$	5.58	−2.63(8)	3.2 (2)	2.688
$\frac{5}{2}\ 2+, 2-$	22.24	−2.60(8)	3.2 (2)	1.186
$\frac{5}{2}\ 3+, 2-$	31.50	−1.35(8)	2.6 (2)	0.085
$\frac{5}{2}\ 2+, 3-$	12.88	−5.67(8)	4.6 (2)	0.085
$\frac{5}{2}\ 3+, 3-$	22.15	−2.60(8)	3.2 (2)	1.694
$\frac{7}{2}\ 3-, 3+$	54.92	−2.57(8)	3.2 (2)	0.943
$\frac{7}{2}\ 4-, 4+$	54.76	−2.57(8)	3.2 (2)	1.223
$\frac{9}{2}\ +-$	108.13	−2.50(8)	3.1 (2)	1.230
$\frac{11}{2}\ -+$	185.99	−2.46(8)	3.1 (2)	1.007
$\frac{39}{2}\ -+$	4266.17	−2.9 (1)	2.53(8)	0.224
$\frac{41}{2}\ +-$	4553.04	−3.5 (1)	2.42(5)	0.208
$\frac{43}{2}\ -+$	4663.43	−4.6 (2)	2.2 (1)	0.192
$\frac{45}{2}\ +-$	4377.16	−7.5 (2)	1.4 (3)	0.174
$\frac{47}{2}\ -+$	3097.96	−19.0 (4)	−2.3 (9)	0.149
$\frac{49}{2}\ -+$	909.06	132. (2)	53.(8)	0.103
$\frac{51}{2}\ -+$	19813.69	−3.11(5)	−1.6 (4)	0.116

the semi-classical Wentzel-Kramers-Brillouin (WKB) approximation. Following [77] we can write the ground state tunneling frequency in atomic units ($\hbar = |e| = m_e = 1$) as:

$$\omega_{\rm tun} \approx \frac{2E_0}{\pi}\, e^{-S}, \tag{30}$$

where S is the action over classically forbidden region and E_0 is the ground state vibrational energy calculated from the bottom of the well $U_{\rm min}$. If the barrier is high enough the harmonic approximation gives $2E_0 = \omega_v$, where ω_v is the observed vibrational frequency. In this case Eq. (30) allows to find action S from experimentally known frequencies $\omega_{\rm tun}$ and ω_v. For lower barriers we need to know the shape of the potential to estimate E_0. The examples of these two limiting cases are ammonia and hydronium, where tunneling frequencies are 0.8 $\rm cm^{-1}$ and 55 $\rm cm^{-1}$ respectively.

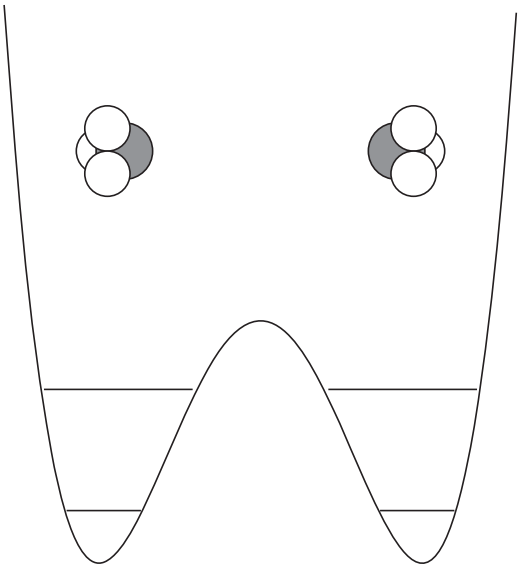

Figure 5 Potential for the tunneling (umbrella) mode of the NH_3 molecule. Two lowest vibrational levels lie below the barrier.

The action S depends on the tunneling mass, which in atomic units is proportional to μ^{-1}. Differentiating (30) over μ we get [78, 79]

$$Q_{\mu,\rm tun} \approx \frac{1+S}{2} + \frac{S\,E_0}{2(\Delta U - E_0)}\,, \tag{31}$$

where $\Delta U = U_{\rm max} - U_{\rm min}$ is the barrier hight. Numerical solution of the Schrödinger equation for realistic potentials agrees with this WKB expression within few percent for all molecules considered so far.

5.1 Ammonia

Equations (30), (31) show that sensitivity coefficient logarithmically depends on the tunneling frequency. For example, for the symmetric isotopologues of ammonia we get:

$$NH_3: \qquad \omega_{\rm tun} = 24\,{\rm GHz}, \quad Q_{\mu,\rm tun} = 4.5\,, \tag{32a}$$

$$ND_3: \qquad \omega_{\rm tun} = 1.6\,{\rm GHz}, \quad Q_{\mu,\rm tun} = 5.7\,. \tag{32b}$$

Such a weak dependence on the tunneling frequency limits possible values of the sensitivity coefficients for tunneling transitions in the microwave range: $Q_{\mu,\rm tun} \lesssim 8$. This is quite good, compared to the rotational sensitivity $Q_{\mu,\rm rot} \approx 1$, but smaller than the best sensitivities in linear molecules considered above.

Let us consider mixed tunneling-rotational transitions, where tunneling goes along with the change of the rotational quantum numbers. If we neglect interaction between tunneling and rotational degrees of freedom we can write approximate expressions for the frequency and the sensitivity of the mixed inversion-rotational transition:

$$\omega_{\rm mix} = \omega_r \pm \omega_{\rm tun}\,, \tag{33a}$$

$$Q_{\mu,{\rm mix}} = \frac{\omega_r}{\omega_{\rm mix}} \pm Q_{\mu,{\rm tun}}\frac{\omega_{\rm tun}}{\omega_{\rm mix}}\,. \tag{33b}$$

We are particularly interested in the case when the minus sign in (33) is realized and $\omega_{\rm mix} \ll \omega_{\rm tun}$. For this case the tunneling sensitivity is enhanced by the factor $\omega_{\rm tun}/\omega_{\rm mix} \gg 1$ and resultant sensitivity of the mixed transition is inversely proportional to the transition frequency $\omega_{\rm mix}$. Therefore, *for the mixed transitions we can have much higher sensitivities in the observable frequency range, then for the purely tunneling transitions.*

Another important advantage of the mixed transitions is that there are usually many of them each having different sensitivity. This means that we can have very good control on possible systematics and reliably estimate the accuracy of the results for μ-variation.

The mixed transitions can not be observed in the symmetric isotopologues of ammonia (32), but they are observed in the partly deuterated species NH_2D and NHD_2. Unfortunately, for both of them the tunneling frequency is much smaller then all rotational frequencies and sensitivities (33b) are not large [80]:

$$\begin{aligned} &NH_2D: && 0.10 \le Q_{\mu,{\rm mix}} \le 1.61\,,\\ &NHD_2: && 0.27 \le Q_{\mu,{\rm mix}} \le 1.54\,. \end{aligned} \tag{34}$$

Relatively small sensitivity coefficients for deuterated isotopologues of ammonia (34) and their low abundance does not allow to get strong limits on μ-variation, so we need to use tunneling ammonia line (32a). It was observed from the several objects with the redshifts about unity. Measuring radial velocities for rotational lines and for the ammonia tunneling line we have $\Delta Q = 3.5$ in Eq. (8), which is two orders of magnitude larger than for optical lines. Because of that the ammonia method allowed to place more stringent bounds on μ-variation than bounds, which follow from the optical spectra of the hydrogen molecule. However, recent observations of the molecules with mixed tunneling-rotational transitions provide even higher sensitivity to μ-variation.

5.2 Mixed tunneling-rotational transitions and effective Hamiltonians

Equations (33) show that high sensitivity mixed transitions are possible when tunneling frequency is of the same order of magnitude as rotational constants. However, in this case tunneling and rotational degrees of freedom start to interact and the accuracy of approximation (33) decreases. A much better approximation can be reached with the help of the effective Hamiltonians, which describe rotational and tunneling degrees of freedom and their interactions with each other. At present the state of the art effective Hamiltonians can include on the order of hundred parameters. These parameters are fitted to the experimentally known transitions and provide an accuracy on the ppm scale, or better.

When such Hamiltonians are used to find sensitivity coefficients Q_μ we need to know how all the parameters depend on μ. It was shown in [25] that this can usually be done only within an accuracy of a few percent. The final accuracy for the large Q-factors is somewhat lower because of the instability of Eq. (33b). Because of that we need not complex effective Hamiltonians but their simplified versions with considerably smaller numbers of fitting parameters can be used instead.

5.3 Hydronium and peroxide

Let us start with hydronium molecule H_3O^+ [81]. This molecule is a symmetric top. It is similar to ammonia, but flatter. Tunneling frequency is almost 50 times larger and comparable to rotational intervals. The tunneling umbrella mode does not change the symmetry and does not contribute to the angular momentum of the molecule. Because of that the tunneling-rotational interaction is reduced to the centrifugal corrections to the tunneling frequency [82].

The tunneling-rotational spectrum of hydronium is shown in Fig. 6. It consists of the J ladders for each quantum number K, where K is projection of the angular momentum on the molecular axis. Due to the tunneling each rotational level is split in two states with different parity p. For $K = 0$ the permutation symmetry of the hydrogen nuclei allows only one of these levels, while for $K > 0$ both levels are present.

In Fig. 6 we see four mixed transitions with frequencies around 300 GHz, which is few times smaller than the tunneling frequency that is about 1.6 THz. Table 7 shows that these transitions have enhanced sensitivity to μ variation ($Q_{\mu,{\rm tun}} = 2.0 \pm 0.1$). Those transitions, whose

frequencies decrease when tunneling frequency increases have negative sensitivity coefficients Q_μ. We conclude that hydronium has several mixed transitions with sensitivities of both signs and the maximum ΔQ_μ is around 10. Other isotopologues of hydronium have even higher sensitivities [79], but up to now they have not been observed in the interstellar medium.

Another molecule where tunneling frequency is comparable to rotational constants, but tunneling-rotational interaction is rather weak, is peroxide H_2O_2 [83, 84]. In equilibrium geometry H_2O_2 is not flat; the angle 2γ between two HOO planes is close to 113°. Two flat configurations correspond to local maxima of potential energy; the potential barrier for *trans* configuration ($2\gamma = \pi$) is significantly lower, than for *cis* configuration ($\gamma = 0$): $U_\pi \approx 400$ cm^{-1} and $U_0 \approx 2500$ cm^{-1}. To a first approximation one can neglect the tunneling through the higher barrier. In this model peroxide is described by a slightly asymmetric oblate top with inversion tunneling mode, similar to ammonia and hydronium.

The sensitivity coefficients for the mixed transitions in peroxide were calculated in [86]. Results of these calculations are shown in Table 8. Molecular states are labeled with the rotational quantum numbers J, K_A, and K_C and the tunneling quantum number τ [83]. Transitions with the frequencies below 100 GHz were found to

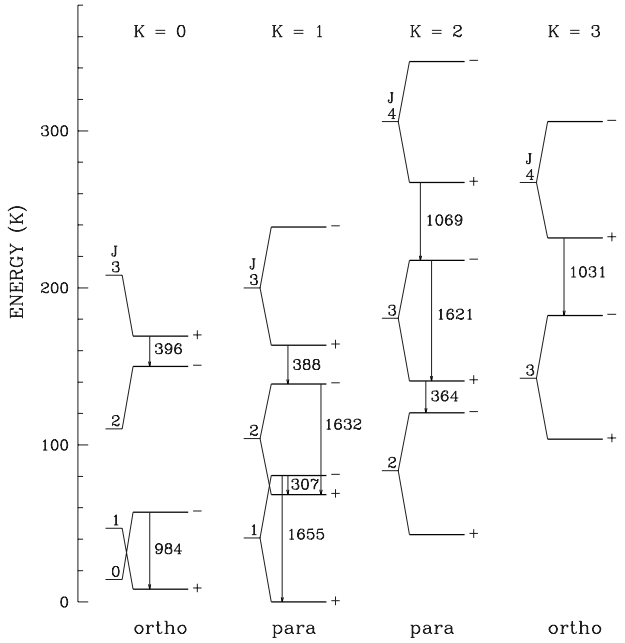

Figure 6 Tunneling-rotational spectrum of H_3O^+ molecule. Several low-frequency tunneling and mixed transitions are marked with vertical arrows. Their frequencies are shown in GHz.

Table 7 Sensitivities of the low frequency mixed inversion-rotational transitions in hydronium H_3O^+. Molecular states are labeled with quantum numbers J^p_K.

Transition		Frequency (MHz)		
Upper	Lower	Theory	Exper.	Q_μ
1^-_1	2^+_1	307072	307192.4	6.4(5)
3^+_2	2^-_2	365046	364797.4	−3.5(5)
3^+_1	2^-_1	389160	388458.6	−3.1(4)
3^+_0	2^-_0	397198	396272.4	−3.0(4)
0^-_0	1^+_0	984690	984711.9	2.7(2)
4^+_3	3^-_3	1031664	1031293.7	−0.6(2)
4^+_2	3^-_2	1071154	1069826.6	−0.5(2)
3^-_2	3^+_2	1621326	1621739.0	2.0(1)
2^-_1	2^+_1	1631880	1632091.0	2.0(1)
1^-_1	1^+_1	1655832	1655833.9	2.0(1)

Table 8 Numerical calculation of the Q-factors for low frequency mixed transitions in peroxide H_2O_2 using effective Hamiltonian. Experimental frequencies are taken from JPL Catalogue [61]. $E_{\rm up}$ is upper state energy in Kelvin.

$J_{K_A,K_C}(\tau)$			ω (MHz)		
upper	lower	$E_{\rm up}$ (K)	theory	exper.	Q_μ
Transitions below 100 GHz					
$0_{0,0}(3)$	$1_{1,0}(1)$	17	14818.8	14829.1	+36.5(2.9)
$2_{1,1}(1)$	$1_{0,1}(3)$	21	37537.0	37518.28	−13.0(1.2)
$1_{0,1}(3)$	$1_{1,1}(1)$	19	67234.5	67245.7	+8.8(6)
$2_{0,2}(3)$	$2_{1,2}(1)$	24	68365.3	68385.0	+8.7(6)
$3_{0,3}(3)$	$3_{1,3}(1)$	31	70057.4	70090.2	+8.5(6)
$4_{0,4}(3)$	$4_{1,4}(1)$	41	72306.0	72356.4	+8.3(6)
$5_{0,5}(3)$	$5_{1,5}(1)$	53	75104.6	75177.4	+8.0(6)
$6_{0,6}(3)$	$6_{1,6}(1)$	68	78444.7	78545.4	+7.7(6)
$3_{1,2}(1)$	$2_{0,2}(3)$	28	90399.8	90365.51	−4.8(5)
Transitions observed from ISM in [85]					
$3_{0,3}(3)$	$2_{1,1}(1)$	31	219163.2	219166.9	+3.4(2)
$6_{1,5}(1)$	$5_{0,5}(3)$	66	252063.6	251914.68	−1.1(2)
$4_{0,4}(3)$	$3_{1,2}(1)$	41	268963.7	268961.2	+3.0(2)
$5_{0,5}(3)$	$4_{1,3}(1)$	53	318237.7	318222.5	+2.7(1)

have rather high sensitivities of both signs. Several transitions of peroxide were recently observed from interstellar medium (ISM) in [85]. These transitions have higher frequencies and smaller sensitivities to μ-variation. Nevertheless, even for these transitions the maximum value of ΔQ_μ is about 4.5.

5.4 Molecules with hindered rotation: methanol and methylamine

Hindered rotation is one of the examples of the large amplitude internal motions in non rigid molecules. In the discussion of the peroxide molecule in the previous subsection, we neglected the tunneling through the higher *cis* barrier. For the excited vibrational states tunneling through both barriers can take place leading to the hindered rotation of one HO group in respect to another. Many molecules which include CH_3 group have three equivalent minima at 120° to each other. Hindered rotation in such molecules can take place already for the ground vibrational state. When the tunneling frequencies are comparable to the rotational ones, such molecules have very rich microwave spectra with a large number of mixed transitions. Another distinctive feature of these molecules is strong interaction between the internal (hindered) and overall rotations. One of the simplest molecules of this type is methanol CH_3OH.

The basic theory of the non-rigid tops with internal rotation was established in the 1950s [87, 88] and the main features of the methanol spectrum were explained. Later on the theory was refined many times and currently there is a very impressive agreement between the theory and experiment [89–92].

The sensitivity coefficients to the μ-variation for methanol microwave transitions were calculated independently in [93, 94] and in [25]. The first group used the state of the art effective Hamiltonian [91], which included 120 fitting parameters. The second group used a much simpler model [95]. The rotational part $H_{\rm rot}$ was that of the slightly asymmetric top and included the rotational constants A, B, and C ($A \approx B$). The hindered rotation was described by the Hamiltonian

$$H_{\rm hr} = -F\frac{{\rm d}^2}{{\rm d}\omega^2} + \frac{V_3}{2}\,(1-\cos 3\omega)\ , \qquad (35)$$

where the kinetic coefficient F was proportional to μ and the electronic potential V_3 was independent on μ. The angle ω described position of the OH group in respect to the CH_3 top. This model did not include centrifugal distortions. The interaction of the internal rotation with the overall rotation was described by a single parameter D, which scaled linearly with μ [87]. Altogether this model had 6 parameters.

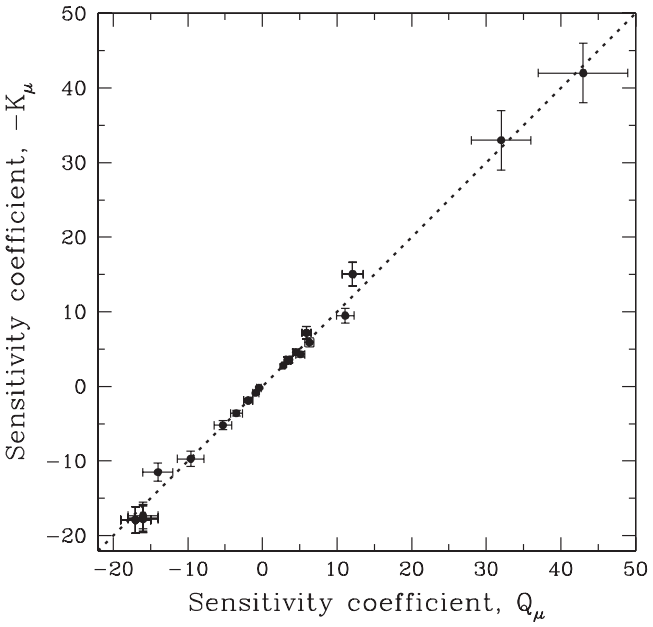

Figure 7 Comparison of the sensitivity coefficients for CH_3OH from [93] and [25]. The former used the sensitivity coefficients K_μ defined as $K_\mu = -Q_\mu$. This corresponds to the different definition of the mass ratio: $m_{\rm p}/m_{\rm e}$ instead of $m_{\rm e}/m_{\rm p}$, which is used in the present review.

Both effective Hamiltonians were diagonalized for several sets of parameters, which correspond to an increased and decreased μ and the sensitivity coefficients were found by the numerical differentiation. The comparison of the two calculations is given in Fig. 7. We see that in spite of a significant difference in complexity of the models the results are in good agreement and of the comparable accuracy. As we discussed above, the latter is mostly determined by ambiguity in the μ-scaling of model parameters.

The sensitivity coefficients for the mixed transitions in methanol span from −17 to +43, which corresponds to $|\Delta Q_\mu| \sim 60$. This is more than an order of magnitude larger than in ammonia method. Moreover, in methanol we have a large number of strong lines with different sensitivities and can effectively control possible systematic effects. Until very recently methanol was observed only at small redshifts, but in 2011 it was first detected in the microwave survey towards the object PKS 1830-211 at redshift $z = 0.89$ [96]. This means that at present methanol can be used as a very

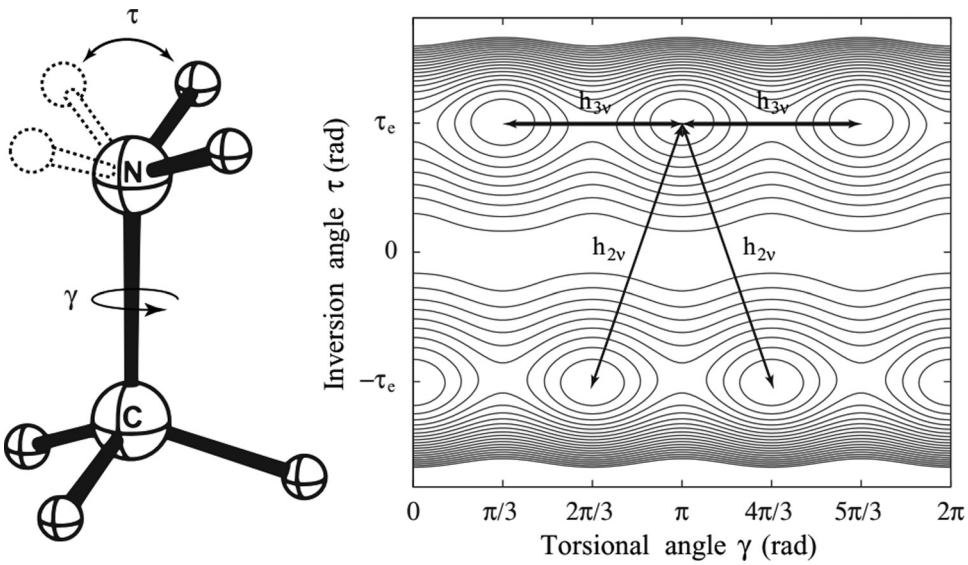

Figure 8 Schematic representation of methylamine and variation of the potential energy of methylamine as function of the relative rotation γ of the CH_3 group with respect to the amine group about the CN bond and the angle τ of the two hydrogen atoms of the NH_2 group with respect to the CN bond. The two large amplitude motions, corresponding to inversion h_{2v} and hindered rotation h_{3v} are schematically indicated by the arrows. Note that inversion of the NH_2 group is accompanied by a $\pi/3$ rotation about the CN bond of the CH_3 group with respect to the amine group.

sensitive tool to probe μ-variation on a cosmological timescale [23, 97].

In the same survey [96], a large number of rather complex molecules were detected for the first time at high redshift. In particular, the list includes methylamine — yet another molecule with tunneling motion. In contrast to all previously discussed molecules, methylamine has two tunneling modes. First is hindered rotation of the NH_2 around CH_3 top, which is similar to that in methanol. Second is a wagging mode when the NH_2 group flips over to the other side (see Fig. 8). Both modes contribute to the angular momentum of the molecule and, therefore, strongly interact with the overall rotation.

The spectrum of methylamine is also very rich. The effective Hamiltonian must include both tunneling motions and their interactions with each other and with the overall rotation. Therefore, even the simplest form of this Hamiltonian is quite complex and we will not discuss it here. Calculations of the sensitivity coefficients were recently done in [98]. It was found that they lie in the range $-24 \leq Q_\mu \leq 19$. However, the lines, which were observed in [96] at $z = 0.89$ have sensitivities close to 1. Up to now neither of the more sensitive lines of methylamine has been observed at high redshifts.

There are several other molecules with mixed tunneling-rotational spectra, for example N_2H_4 and CH_3SH. The former has three tunneling modes which strongly interact with rotation. Thus, we should expect very complex spectrum. This molecule is predicted to form in Jupiter's and Titan's atmospheres [99, 100]. The latter is similar to methanol and exhibits hindered rotation and complex spectrum [101]. Effective Hamiltonians for many of these molecules are known, but no other calculations of the sensitivity coefficients have been done so far (preliminary results for CH_3SH show that there are transitions with high sensitivities of both signs). If any new sufficiently low frequency mixed transitions are observed from the interstellar medium, it is possible to calculate respective sensitivity coefficients using the methods outlined in this section.

6 Summary and conclusions

As we discussed in the previous sections the constraints on the possible variation of fundamental constants are an efficient method of testing the equivalence principle which is a basic assumption of General Relativity. These constraints can be derived from a wide variety of atomic and molecular transitions observed in laboratory, solar and extra solar systems, and at very early cosmological epochs up to a redshift of order $z \sim 5 - 6$ where molecular and atomic transitions have been recently detected and observed with a sufficiently high spectral resolution [14, 15]. Radio astronomical observations of the NH_3 molecule in two distant galaxies provide tight constraints

at the $\Delta\mu/\mu < 1 \times 10^{-6}$ level at $z = 0.89$ [102] and $z = 0.69$ [13]. Even deeper bounds were deduced from observations of the CH_3OH molecule in the $z = 0.89$ galaxy: $\Delta\mu/\mu < 3 \times 10^{-7}$ [97], and $\Delta\mu/\mu < 1 \times 10^{-7}$ [23].

To probe α and μ at the level of 10^{-8} or 10^{-9}, at least two main requirements should be fulfilled: (*i*) increasing precision of the laboratory measurements of the rest frame frequencies of the most sensitive molecular transitions discussed in this review, and (*ii*) increasing sensitivity and spectral resolution of astronomical observations.

The most promising molecular transitions are those of a mixed nature, where there are two, or more, competing contributions to the transition energy. We get strong enhancement of the sensitivity to the variation of the fundamental constants when the resultant transition frequency is much smaller than individual contributions. This happens, for example, for some mixed tunneling-rotational transitions. Diatomic radicals give another example, where spin-orbit interaction is competing with Coriolis interaction. As a result we have strong enhancement of the sensitivity coefficients for the Λ-doublet transitions. There are other known examples, which are more relevant for the laboratory experiments [103,104]. It is possible that more examples will be found both for the laboratory and astrophysical studies. The methods described in this review allow us to calculate sensitivity coefficients for any microwave and submillimeter molecular transitions of interest.

Mikhail G. Kozlov received his Ph.D. degree in Physics 1982 from the Petersburg Nuclear Physics Institute (PNPI) in Russia where he is currently a Leading Research Scientist. He is also a Professor of Physics at St. Petersburg Electrotechnical University. Kozlov's research interests include atomic and molecular theory, fundamental symmetries, and fundamental constants.

Sergei A. Levshakov received his Ph.D. degree in Physics 1982 from the Physical-Technical Institute (PTI), St. Petersburg (Russia) where he is currently a Leading Research Scientist. He is also a Professor of Physics at St. Petersburg Electrotechnical University. Levshakov's research interests include astrophysics and space science, atomic and molecular spectroscopy, chemical evolution and the origin of the elements, and data analysis.

References

[1] R. P. Feynman, QED: the Strange Theory of Light and Matter (Princeton, NJ, Princeton Univ. Press, 1985), p. 129.
[2] E. A. Milne, Proc. Roy. Soc. A. **158**, 324 (1937).
[3] P. A. M. Dirac, Nature **139**, 323 (1937).
[4] A. Cingöz et al., Phys. Rev. Lett. **98**, 040801 (2007).
[5] Yu. V. Petrov et al., Phys. Rev. C **74**, 064610 (2006).
[6] T. Rosenband et al., Science **319**, 1808 (2008).
[7] A. Shelkovnikov, R. J. Butcher, C. Chardonnet, and A. Ami-Klein, Phys. Rev. Lett. **100**, 150801 (2008).
[8] S. Blatt et al., Phys. Rev. Lett. **100**, 140801 (2008).
[9] M. C. Ferreira, M. D. Julião, C. J. A. P. Martins, and A. M. R. V. L. Monteiro, Phys. Rev. D **86**, 125025 (2012).
[10] V. V. Flambaum, Int. J. Mod. Phys. A **22**, 4937 (2007).
[11] P. Molaro, D. Reimers, I. I. Agafonova, and S. A. Levshakov, Eur. Phys. J. Special Topics **163**, 173 (2008).
[12] I. I. Agafonova, P. Molaro, S. A. Levshakov, and J. L. Hou, Astron. Astrophys. **529**, A28 (2011).
[13] N. Kanekar, Astrophys. J. **728**, L12 (2011).
[14] S. A. Levshakov et al., Astron. Astrophys. **540**, L9 (2012).
[15] L. Lentati et al., Mon. Not. R. Astron. Soc. **430**, 2454 (2013).
[16] S. J. Landau, M. E. Mosquera, C. G. Scóccola, and H. Vucetich, Phys. Rev. D **78**, 083527 (2008).
[17] C. J. A. P. Martins et al., Phys. Rev. D **82**, 023532 (2010).
[18] M. Nakashima, K. Ichikawa, R. Nagata, and J. Yokoyama, J. Cos. Astropart. Phys. **01**, 030 (2010).
[19] V. V. Flambaum and E. V. Shuryak, Phys. Rev. D **65**, 103503 (2002).
[20] A. Coc et al., Phys. Rev. D **86**, 043529 (2012).

[21] J. K. Webb et al., Phys. Rev. Lett. **107**, 191101 (2011).
[22] H. Rahmani et al., 2012, Mon. Not. R. Aastron. Soc. **425**, 556 (2012).
[23] J. Bagdonaite et al., Science **339**, 46 (2013).
[24] S. A. Levshakov et al., 2010, Astron. Astrophys. **512**, A44 (2010).
[25] S. A. Levshakov, M. G. Kozlov, and D. Reimers, Astrophys. J. **738**, 26 (2011).
[26] S. Ellingsen, M. Voronkov, and S. Breen, Phys. Rev. Lett. **107**, 270801 (2011).
[27] T. Damour, 2012, Class. Quant. Gravity **29**, 184001 (2012).
[28] J.-P. Uzan, Living Reviews in Relativity **14**, 2 (2011).
[29] M. Raidal et al., Eur. Phys. J. C **57**, 13 (2008).
[30] T. Fukuyama, Int. J. Mod. Phys. A **27**, 30015 (2012).
[31] V. V. Fritzsch, Uspekhi Fiz. Nauk **52**, 359 (2009).
[32] V. A. Dzuba, V. V. Flambaum, and J. K. Webb, Phys. Rev. Lett. **82**, 888 (1999).
[33] V. A. Dzuba, V. V. Flambaum, and J. K. Webb, Phys. Rev. A **59**, 230 (1999).
[34] J. C. Berengut et al., in: From Varying Couplings to Fundamental Physics, edited by C. Martins and P. Molaro (Springer-Verlag, Berlin, 2011), p. 9.
[35] D. A. Varshalovich and S. A. Levshakov, J. Exp. Theor. Phys. **58**, 231 (1993).
[36] V. V. Meshkov, A. V. Stolyarov, A. V. Ivanchik, and D. A. Varshalovich, J. Exper. Theor. Phys. Lett. **83**, 303 (2006).
[37] W. Ubachs, R. Buning, K. Eikema, and E. Reinhold, J. Mol. Spectrosc. **241**, 155 (2007).
[38] E. J. Salumbides et al., Phys. Rev. A **86**, 022510 (2012).
[39] S. G. Porsev et al., Phys. Rev. A **76**, 052507 (2007).
[40] G. Nave and S. Johansson, Astrophys. J. Suppl. **204**, 1 (2013).
[41] S. A. Levshakov, M. Centurión, P. Molaro, and S. D'Odorico, Astron. Astrophys. **434**, 827 (2005).
[42] K. Griest et al., Astrophys. J. **708**, 158 (2010).
[43] J. B. Whitmore, M. T. Murphy, and K. Griest, Astrophys. J. **723**, 89 (2010).
[44] I. I. Agafonova et al., Astron. Astrophys. **552**, A83 (2013).
[45] E. J. Salumbides et al., Phys. Rev. Lett. **101**, 223001 (2008).
[46] P. Noterdaeme et al., Astron. Astrophys. **523**, A80 (2010).
[47] S. A. Levshakov, M. Dessauges-Zavadsky, S. D'Odorico, and P. Molaro, Mon. Not. R. Astron. Soc. **333**, 373 (2002).
[48] M. Wendt and P. Molaro, Astron. Astrophys. **541**, A69 (2012).
[49] M. G. Kozlov et al., Phys. Rev. A **77**, 032119 (2008).
[50] S. A. Levshakov et al., Astron. Astrophys. **479**, 719 (2008).
[51] S. G. Kukolich, Phys. Rev. **156**, 83 (1967).
[52] E. R. Hudson, H. J. Lewandowski, B. C. Sawyer, and J. Ye, Phys. Rev. Lett. **96**, 143004 (2006).
[53] J. N. Chengalur and N. Kanekar, Phys. Rev. Lett. **91**, 241302 (2003).
[54] J. Darling, Phys. Rev. Lett. **91**, 011301 (2003).
[55] M. G. Kozlov, Phys. Rev. A **80**, 022118 (2009).
[56] A. J. de Nijs, W. Ubachs, W., and H. L. Bethlem, Phys. Rev. A **86**, 032501 (2012).
[57] C. M. Persson et al., Astron. Astrophys. **543**, A145 (2012).
[58] K. Beloy et al., Phys. Rev. A **83**, 062514 (2011).
[59] J. M. Brown and A. Carrington, Rotational Spectroscopy of Diatomic Molecules (Cambridge University Press, Cabmridge, 2003).
[60] F. J. Lovas et al., Diatomic Spectral Database (2005) (http://www.physics.nist.gov/PhysRefData/ MolSpec/Diatomic/index.html)
[61] H. M. Pickett et al., J. Quant. Spectrosc. Rad. Transfer **60**, 883 (1998) (http://spec.jpl.nasa.gov).
[62] H. S. P. Müller, F. Schlöder, J. Stutzki, and Winnewisser, J. Mol. Struct. **742**, 215 (2005) (http://www.astro.uni-koeln.de/site/vorhersagen).
[63] W. L. Meerts and A. Dymanus, J. Mol. Spec. **44**, 320 (1972).
[64] J. M. Brown, G. A. Colbourn, J. K. G. Watson, and F. D. Wayne, J. Mol. Spec. **74**, 294 (1979).
[65] J. M. Brown and A. J. Merer, J. Mol. Spec. **74**, 488 (1979).
[66] S. Davidson, K. M. Evenson, and J. M. Brown, Astrophys. J. **546**, 330 (2001).
[67] M. A. Martin-Drumel et al., Chem. Phys. Lett. **550**, 8 (2012).
[68] K. Kawaguchi and T. Amano, J. Chem. Phys. **88**, 4584 (1988).
[69] H. Hübers, K. M. Evenson, C. Hill, and J. M. Brown, J. Chem. Phys. **131**, 034311 (2009).
[70] R. Renner, Zeitschrift für Physik **92**, 172 (1934).
[71] J. T. Hougen, J. Chem. Phys. **36**, 519 (1962).
[72] M. G. Kozlov, Phys. Rev. A **87**, 032104 (2013).
[73] M. Perić, M. Mladenović, K. Tomić, and C. M. Marian, J. Chem. Phys. **118**, 4444 (2003).
[74] S. Yamamoto et al., Astrophys. J. **348**, 363 (1990).
[75] M. Kanada, S. Yamamoto, S. Saito, and Y. Osamura, J. Chem. Phys. **104**, 2192 (1996).
[76] M. Caris et al., J. Mol. Spect. **253**, 99 (2009).
[77] L. D. Landau and E. M. Lifshitz, Quantum mechanics (Oxford, Pergamon, 1977).
[78] V. V. Flambaum and M. G. Kozlov, Phys. Rev. Lett. **98**, 240801 (2007).
[79] M. G. Kozlov, S. G. Porsev, and D. Reimers, Phys. Rev. A **83**, 052123 (2011).
[80] M. G. Kozlov, A. V. Lapinov, and S. A. Levshakov, J. Phys. B **43**, 074003 (2010).
[81] M. G. Kozlov and S. A. Levshakov, Astrophys. J. **726**, 65 (2011).
[82] S. Yu, B. J. Drouin, J. C. Pearson, and H. M. Pickett, Astrophys. J. Suppl. **180**, 119 (2009).
[83] J. T. Hougen, Canadian J. Phys. **62**, 1392 (1984).
[84] F. Masset et al., J. Phys. France **49**, 1901 (1988).
[85] P. Bergman et al., Astron. Astrophys. **531**, L8 (2011).
[86] M. G. Kozlov, Phys. Rev. A **84**, 042120 (2011).
[87] C. C. Lin and J. D. Swalen, Rev. Mod. Phys. **31**, 841 (1959).
[88] D. R. Herschbach, J. Chem. Phys. **31**, 91 (1959).

[89] T. Anderson, F. De Lucia, and E. Herbst, Astrophys. J. Suppl. **72**, 797 (1990).
[90] H. S. P. Müller, L. H. Xu, and F. van der Tak, J. Mol. Struc. **795**, 114 (2006).
[91] L. Xu et al., J. Mol. Spec. **251**, 305 (2008).
[92] I. Kleiner, J. Mol. Spec. **260**, 1 (2010).
[93] P. Jansen et al., Phys. Rev. Lett. **106**, 100801 (2011).
[94] P. Jansen et al., Phys. Rev. A **84**, 062505 (2011).
[95] D. Rabli and D. R. Flower, Mon. Not. R. Astron. Soc. **403**, 2033 (2010).
[96] S. Muller et al., Astron. Astrophys. **535**, A103 (2011).
[97] S. P. Ellingsen, M. A. Voronkov, S. L. Breen, and J. E. J. Lovell, Astrophys. J. **747**, 7 (2012).
[98] V. V. Ilyushin et al., Phys. Rev. A **85**, 032505 (2012).
[99] J. I. Moses, A. D. Sperier, and T. C. Keane, Bull. Am. Astron. Soc. **40**, 459 (2008).
[100] G. P. Smith, Bull. Am. Astron. Soc. **42**, 970 (2010).
[101] F. L. Bettens et al., Astrophys. J. **510**, 789 (1999).
[102] C. Henkel et al., Astron. Astrophys. **500**, 725 (2009).
[103] C. Chin, V. V. Flambaum, and M. G. Kozlov, New J. Phys. **11**, 055048 (2009).
[104] H. L. Bethlem and W. Ubachs, Faraday Discussions **142**, 25 (2009).

www.ann-phys.org

adp

annalen der physik

WILEY-VCH

WILEY ONLINE LIBRARY
Early View publication on wileyonlinelibrary.com
(issue and page numbers not yet assigned;
citable using Digital Object Identifier – DOI)

Ann. Phys. (Berlin), 1–15 (2013) / DOI 10.1002/andp.201300036

annalen der physik

Original Paper

A dual-isotope rubidium comagnetometer to search for anomalous long-range spin-mass (spin-gravity) couplings of the proton

Derek F. Jackson Kimball, Ian Lacey, Julian Valdez, Jerlyn Swiatlowski, Cesar Rios, Rodrigo Peregrina-Ramirez, Caitlin Montcrieffe, Jackie Kremer, Jordan Dudley, and C. Sanchez*

Received 28 February 2013, revised 16 April 2013, accepted 22 April 2013
Published online 17 May 2013

The experimental concept of a search for a long-range coupling between rubidium (Rb) nuclear spins and the mass of the Earth is described. The experiment is based on simultaneous measurement of the spin precession frequencies for overlapping ensembles of ^{85}Rb and ^{87}Rb atoms contained within an evacuated, antirelaxation-coated vapor cell. Rubidium atoms are spin-polarized in the presence of an applied magnetic field by synchronous optical pumping with circularly polarized laser light. Spin precession is probed by measuring optical rotation of far-off-resonant, linearly polarized laser light. Simultaneous measurement of ^{85}Rb and ^{87}Rb spin precession frequencies enables suppression of magnetic-field-related systematic effects. The nuclear structure of the Rb isotopes makes the experiment particularly sensitive to anomalous spin-dependent interactions of the proton. Experimental sensitivity and a variety of systematic effects are discussed, and initial data are presented.

1 Introduction

The connection between quantum theory and general relativity is one of the most important unsolved mysteries of modern physics, a mystery exacerbated by the dearth of experiments probing the rare intersections between these two theories. One intersection between quantum effects and gravity that does offer potential for experimental tests is the question of how intrinsic spins interact with gravitational fields (see, for example, the review [1]). According to general relativity, a purely tensor theory, the intrinsic spin of a particle is unaffected by the local gravitational field [2–6]. However, in extensions of general relativity based on a Riemann-Cartan spacetime instead of a Riemann geometry, the gravitational interaction is described by a torsion tensor which can generate heretofore undetected spin-mass and spin-spin interactions [7–10].

In terms of quantum field theory phenomenology, the torsion tensor describes new scalar-pseudoscalar and vector-pseudovector gravitational interactions, corresponding, respectively, to spin-0 and spin-1 gravitons in addition to the usual spin-2 graviton associated with the tensor nature of standard gravity [11–13]. New spin-1 and spin-0 partners of the usual spin-2 graviton also naturally arise in theoretical attempts to unify gravity and quantum mechanics, such as string theory and M-theory [14–16], especially in the context of supersymmetry [17]. It has recently been noted that a massless or nearly massless spin-0 component of gravity manifests as dark energy over cosmological distances [18–21]. The pseudoscalar component of such a field leads to an interaction that has the nonrelativistic form [21]:

$$H_g = k\frac{\hbar}{c}\boldsymbol{\sigma}\cdot\boldsymbol{g} \tag{1}$$

where k is a dimensionless parameter setting the scale of the new interaction, $\hbar$ is Planck's constant, $\boldsymbol{\sigma}$ is the intrinsic spin of the particle in units of $\hbar$, $\boldsymbol{g}$ is the Earth's gravitational field, and c is the speed of light. If the strength of the pseudoscalar coupling is the same as that of the tensor component of gravity, $k \approx 1$ [21].

The Hamiltonian H_g in Eq. (1) manifestly violates the equivalence principle for intrinsic spins, offering a

* Corresponding author E-mail: derek.jacksonkimball@csueastbay.edu
Department of Physics, California State University – East Bay, Hayward, California 94542-3084, USA

mechanism by which a gravitational field can be distinguished from an accelerating reference frame. Furthermore, if $H_g \neq 0$, gravity would violate parity (P) and time-reversal (T) symmetries, and the spin-gravity coupling would be a source of additional CP-violation that might explain the observed matter-antimatter asymmetry of the universe [22]. The possibility that gravity may violate discrete symmetries has led many authors over the past fifty years [3, 23–30] to consider the possibility of such an interaction, which would imply the existence of a gravitational dipole moment (GDM) $k\hbar\boldsymbol{\sigma}/c$ for elementary particles. One could envision a GDM as a separation between the center of inertial mass and the center of gravitational mass by a distance $k\hbar/mc$, where m is the particle mass. If the dimensionless coupling constant k is of order unity, then the separation between the centers of inertial mass and gravitational mass is on the order of the Compton wavelength. Generally, theoretical models of gravity that accommodate such an interaction predict that $k \lesssim 1$ [3, 23–30]. However, to date, the most sensitive searches [31, 32] for such a spin-gravity coupling have set limits $k \lesssim 10$, still an order of magnitude away from the most theoretically interesting region of parameter space. The central goal of the experiment described in the present paper is to probe spin-gravity interactions of the type described by Eq. (1) at the $k \sim 1$ level.

There are several experimental consequences of the existence of a GDM for an elementary particle. The interaction described by Eq. (1) leads to a gravity-induced splitting ΔE of the energy levels for spins oriented parallel and anti-parallel to $\boldsymbol{g}$:

$$\Delta E = 2k\frac{\hbar g}{c} \approx 4k \times 10^{-23}\text{eV}. \tag{2}$$

In addition, an interaction such as that described by Eq. (1) generates a torque on spins immersed in a gravitational field, leading to spin precession about the axis of the local gravitational field with a frequency

$$\frac{\Omega_g}{2\pi} = \frac{kg}{\pi c} \approx k \times 10^{-8}\text{Hz}. \tag{3}$$

This spin precession not associated with the magnetic moments of the particles is the signature of the P- and T-violating spin-gravity coupling that is being searched for in our present experiment.

In principle, the effect of a spin-gravity coupling is indistinguishable from the interactions resulting from any heretofore undiscovered force-mediating pseudoscalar or vector particle. In the literature, such new interactions are commonly parameterized using the Moody-Wilczek formalism for spin-0 particles [36], recently extended by Dobrescu and Mocioiu to include spin-1 particles [37]. In this context, the spin-gravity (or spin-mass) interaction searched for in our proposed experiment can be interpreted as a monopole-dipole coupling. In general, the monopole-dipole coupling strength can be different for different elementary particles—our proposed experiment is primarily sensitive to monopole-dipole couplings of the proton, whereas the previous best experimental limits are for neutron [31] and electron [32] couplings. Consequently, our experiment has the potential to improve experimental constraints on monopole-dipole couplings of the proton by orders of magnitude compared to the best previous limit [34].

Figure 1 presents a parameter exclusion plot showing existing direct experimental limits on monopole-dipole interactions of nucleons at various length scales, as well as astrophysical constraints inferred from the duration of the supernova SN 1987A neutrino burst in combination with data from searches for anomalous monopole-monopole forces [35]. (It should be noted that there are significant uncertainties related to dense nuclear matter effects in the analysis of the SN 1987A neutrino burst [38,39].) The blue horizontal line at the bottom of the plot shows the strength of the monopole-dipole interaction corresponding to $k \approx 1$. The dashed red curve shows the projected sensitivity of our experiment. Note that astrophysical limits for electron couplings, which are based on star cooling, are three orders of magnitude more restrictive than astrophysical limits on nucleon couplings. Thus the astrophysical limits for electrons just reach the $k \approx 1$ regime, and are comparable to the projected sensitivity of our experiment. Of interest are observations that the white-dwarf luminosity function fits better with a small amount of anomalous energy loss at a level that would correspond to a pseudoscalar interaction with coupling strength corresponding to $k \approx 1$ [40]. Furthermore, the observed period decrease of the pulsating white dwarf G117-B15A also favors some amount of extra cooling [41].

In the present work, we describe a dual-isotope rubidium (Rb) comagnetometer well-suited for searching for a long-range monopole-dipole coupling between proton spins and the mass of the earth. We show that the dual-isotope Rb comagnetometer as designed can achieve sufficient statistical sensitivity and rejection of known systematic errors so that present experimental limits on anomalous monopole-dipole couplings of the proton spin can be improved by orders of magnitude. The basic concept of our experiment is to use synchronous laser optical pumping to generate transverse spin polarization of Rb atoms contained in an antirelaxation-coated cell [42], and then employ

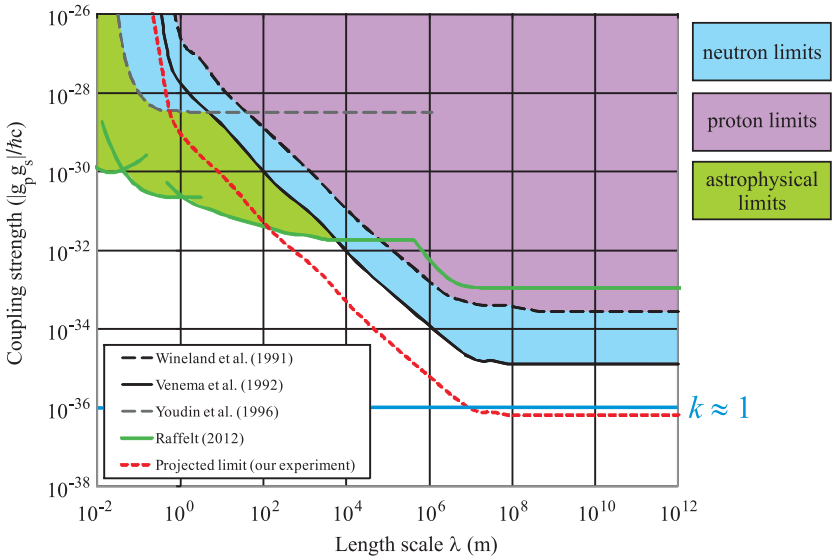

Figure 1 Existing experimental constraints (at the 2-σ level) on nucleon monopole-dipole (scalar-pseudoscalar) couplings $\left|g_p g_s\right|/\hbar c$ as a function of the range λ of the interaction (g_p and g_s are the pseudoscalar and scalar coupling constants, respectively). Direct experimental constraints for the neutron are from Youdin *et al.* (1996) [33] at the laboratory-scale range and from Venema *et al.* (1992) [31] for the earth-scale range (excluded parameter space shaded blue); constraints for the proton are from the experiment of Wineland *et al.* (1991) [34] (excluded parameter space shaded purple). Astrophysical constraints for baryon couplings (excluded parameter space shaded green) are from the recent analysis of Raffelt (2012) [35]. The nominal coupling strength for a scalar-tensor theory of gravity corresponding to $k \approx 1$ is represented by the blue line at the $\left|g_p g_s\right|/\hbar c \approx 10^{-36}$ level. Constraints on monopole-dipole couplings of the electron spin to the mass of the earth (obtained by the University of Washington torsion pendulum experiment [32], not shown) are similar to the constraints on the neutron spin from Ref. [31]. The potential sensitivity (dashed red line) of our proposed search could improve upon existing experimental limits on long-range ($\lambda \gtrsim 10^7\,\mathrm{m}$) monopole-dipole couplings in general by an order of magnitude and for the proton spin in particular by three orders of magnitude.

off-resonant laser light to simultaneously measure the spin precession frequencies of ^{85}Rb and ^{87}Rb atoms in the presence of a magnetic field **B**. The ratio of the difference between the Rb precession frequencies divided by their sum,

$$\mathcal{R} = \frac{\Omega_{87} - \Omega_{85}}{\Omega_{87} + \Omega_{85}}, \tag{4}$$

will be measured for a range of different magnetic fields. Measurement of the ratio $\mathcal{R}$ eliminates or reduces several common-mode sources of noise and systematic error. Taking the difference $\Delta\mathcal{R}$ between $\mathcal{R}$ for **B** parallel with $\boldsymbol{g}$ and anti-parallel with $\boldsymbol{g}$ yields a signal proportional to the spin precession frequency caused by non-magnetic interactions. In this configuration, the valence electron spin of the Rb atoms effectively serves as an accurate comagnetometer for the Rb nuclear spins.

Our early work on this experiment is described in Ref. [43]. In this early version of the experiment, a single linearly polarized laser beam, frequency-modulated at an integer multiple of the precession frequency, was used to measure nonlinear magneto-optical rotation (NMOR) induced by the spin precession of the Rb atoms [44–47]. While the NMOR measurements achieved our target statistical sensitivity to the Rb spin precession frequencies, a subtle systematic effect involving light shifts [43, 48] required us to modify our experimental approach. The effect, known as alignment-to-orientation conversion, arises from the combined action of the magnetic field and optical electric field. Alignment-to-orientation conversion evolves spin polarization aligned along the linear polarization axis into spin polarization oriented along the light propagation (magnetic field) direction. Atomic spins oriented along the light propagation direction generated ellipticity of the light field which in turn produced unacceptably large light-power- and magnetic-field-dependent shifts of the spin precession frequencies. Our present experiment circumvents these systematic effects by temporally separating pump and probe stages, using unmodulated probe light, and by a choice of experimental geometry where the probe beam

Table 1 Parameters determining gyro-gravitational ratios χ and gyromagnetic ratios $\gamma = g_F\mu_0$ for ^{85}Rb and ^{87}Rb in the ground-state hyperfine levels of interest.

Atom	Ground electronic state	Nuclear spin	Total angular momentum	g-factor	Proton state	$\chi_{\rm atom}$
^{85}Rb	$5s^2\,S_{1/2}$	$I = 5/2$	$F = 3$	$g_F = 1/3$	$4\,f_{5/2}$	$\frac{1}{6}\chi_e - \frac{5}{42}\chi_p$
^{87}Rb	$5s^2\,S_{1/2}$	$I = 3/2$	$F = 2$	$g_F = 1/2$	$3\,p_{3/2}$	$\frac{1}{4}\chi_e + \frac{1}{4}\chi_p$

propagates in a direction orthogonal to the magnetic field (Section 5).

2 Experimental concept

As noted in Section 1, a long-range spin-mass or spin-gravity interaction can be parameterized in terms of a GDM $\boldsymbol{\kappa}$ via $\boldsymbol{\kappa} = \chi\boldsymbol{\sigma}$, where $\chi = k\hbar/c$ is the "gyro-gravitational ratio" for the particle. The χ for Rb atoms can be calculated in terms of χ_e and χ_p, the gyro-gravitational ratios for the electron and proton, respectively, using the shell model to describe the nuclei. In a given ground-state hyperfine level with total angular momentum F, the atomic GDM $\boldsymbol{\kappa}_{\rm atom}(F)$ is

$$\begin{aligned}\boldsymbol{\kappa}_{\rm atom}(F) &= \chi_{atom}(F)\,\boldsymbol{F} \\ &= \frac{\langle \boldsymbol{S}_e\cdot\boldsymbol{F}\rangle}{F(F+1)}\langle\boldsymbol{F}\rangle\chi_e + \frac{\langle \boldsymbol{I}\cdot\boldsymbol{F}\rangle}{F(F+1)}\langle\boldsymbol{F}\rangle\chi_{\rm nucl},\end{aligned} \tag{5}$$

where $\boldsymbol{S}_e$ is the electron spin, $\boldsymbol{I}$ is the nuclear spin, and $\chi_{\rm nucl}$ is the nuclear gyro-gravitational ratio. In the nuclear shell model [49], both Rb isotopes have valence protons, and so the nuclear spin, magnetic moment, and nuclear GDM are, to a good approximation, due entirely to the proton. The nuclear GDM $\boldsymbol{\kappa}_{\rm nucl}$ is thus given by

$$\boldsymbol{\kappa}_{\rm nucl} = \chi_{\rm nucl}\,\boldsymbol{I} = \frac{\langle \boldsymbol{S}_p\cdot\boldsymbol{I}\rangle}{I(I+1)}\langle\boldsymbol{I}\rangle\chi_p, \tag{6}$$

where $\boldsymbol{S}_p$ is the proton spin and we have assumed, as do most theoretical models [3, 21, 23–30], that there is no contribution from orbital angular momentum. Relevant parameters based on the above considerations are presented for the two Rb isotopes in the probed ground-state hyperfine levels in Table 1.

Ignoring temporarily other causes of spin precession, the spin-precession frequencies for ^{85}Rb and ^{87}Rb in the presence of the magnetic field $\mathbf{B}$ and Earth's gravitational field $\boldsymbol{g}$ are

$$\Omega_{85} \approx \left|\gamma_{85}B + \left(\frac{1}{6}\chi_e - \frac{5}{42}\chi_p\right)g\cos\phi\right|, \tag{7}$$

$$\Omega_{87} \approx \left|\gamma_{87}B + \left(\frac{1}{4}\chi_e + \frac{1}{4}\chi_p\right)g\cos\phi\right|, \tag{8}$$

where ϕ is the angle between $\mathbf{B}$ and $\boldsymbol{g}$, γ_{85} and γ_{87} are the gyromagnetic ratios ($\gamma = g_F\mu_0$, where g_F is the Landé g-factor and μ_0 is the Bohr magneton) and the light propagation direction is along $\mathbf{B}$. In the above we neglect contributions to the spin-precession frequency second-order in g. To analyze the data, we construct the following ratio:

$$\mathcal{R} = \frac{\Omega_{87} - \Omega_{85}}{\Omega_{87} + \Omega_{85}}. \tag{9}$$

To first order assuming $\gamma B \gg \chi_e g, \chi_p g$ and neglecting the effects of the nuclear magnetic moments, we have

$$\mathcal{R}_\pm \approx \left(\frac{\gamma_{87} - \gamma_{85}}{\gamma_{87} + \gamma_{85}}\right)\left(1 \pm 2.06\frac{\chi_p g\cos\phi}{\mu_0 B}\right), \tag{10}$$

where $\mathcal{R}_+$ is for positive B and $\mathcal{R}_-$ is for negative B (relative to $\boldsymbol{g}$). There is first-order cancelation of the effects of an electron GDM in the ratio $\mathcal{R}$, and near unity sensitivity to the effects of a proton GDM. Measuring $\Delta\mathcal{R} = \mathcal{R}_+ - \mathcal{R}_-$ yields a signal proportional only to the proton GDM:

$$\Delta\mathcal{R} \approx 4.12\left(\frac{\gamma_{87} - \gamma_{85}}{\gamma_{87} + \gamma_{85}}\right)\left(\frac{\chi_p g\cos\phi}{\mu_0 B}\right). \tag{11}$$

The first-order cancelation of the electron GDM contribution to $\Delta\mathcal{R}$ is a result of the fact that we measure spin precession in the $F = I + 1/2$ ground state hyperfine level for both isotopes, so electron couplings contribute in nearly identical ways to the measured values of Ω_{85} and Ω_{87}.

3 Experimental setup

A schematic diagram of the experimental setup used to carry out simultaneous measurement of Ω_{85} and Ω_{87} is shown in Fig. 2. At the heart of the experiment is a natural isotopic mixture of Rb vapor (72.2% ^{85}Rb, 27.8%

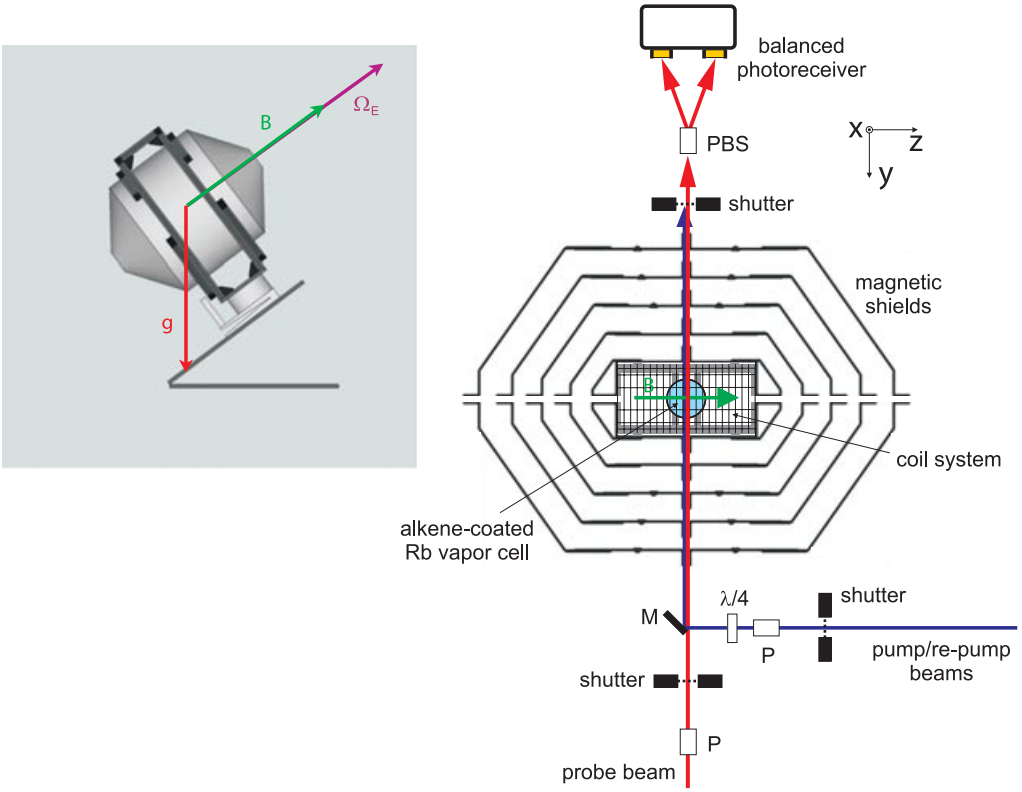

Figure 2 Right-hand side: schematic diagram of the experimental setup used to measure the spin precession frequencies of ^{85}Rb and ^{87}Rb and to search for a long-range spin-mass (spin-gravity) coupling (P = linear polarizer, M = mirror, PBS = polarizing beamsplitter, $\lambda/4$ = quarter wave plate). Picture, upper left: schematic of the apparatus used to align the magnetic shield system and magnetic field $\mathbf{B}$ along the Earth's rotation axis Ω_E, and geometrical relationship to the local gravitational field $\boldsymbol{g}$ (this geometry is chosen to control systematic errors related to the earth's rotation, see Section 5.2).

^{87}Rb) contained within an evacuated (residual pressure $\approx 10^{-6}$ torr) spherical alkene-coated glass cell (diameter = 5 cm). The alkene coating is 1-nonadecene $[CH_2 - CH(CH_2)_{16} - CH_2]$ and the cell was prepared according to procedures outlined in Ref. [42]. The particular cell we are using was measured to have longitudinal spin relaxation times $T_1 \approx 5$ s limited by exchange of atoms between the spherical bulb of the cell and the stem which contains the Rb reservoir. Under typical operating conditions, the spin relaxation rate due to wall collisions is significantly smaller than the relaxation rate due to spin-exchange collisions between the Rb atoms.

The vapor cell is mounted inside a frame manufactured of HDPE (High Density Polyethylene) which is fit inside the innermost layer of a five-layer magnetic shield (manufactured by Amuneal Inc.) made of a 1-mm thick high-permeability alloy, annealed in a hydrogen atmosphere. Each layer of the shield consists of a cylindrical center piece and two removable end caps. The outer layers of the shield are spaced by styrofoam (polymerized in place) and the innermost layer is spaced by melamine foam to reduce acoustic noise. Four ports for access to the inside of the shields are available on the cylindrical pieces and one port is available on each end cap. The shielding factor of the entire five-layer magnetic shield system was measured for a nearly identical design to be better than 10^7 [51]. The foam spacing between the shield layers provides thermal insulation in addition to mechanical support. The temperature of the innermost shield layer is stabilized at 30°C by a J-KEM Model 210 temperature controller using a T-type thermocouple attached to the inner surface of the shield layer for temperature measurement and resistive heating with a twisted pair of wires wrapped about the outside of the innermost shield layer. Stabilizing the shield temperature serves two functions: (1) it reduces temperature-related drifts of residual magnetic fields from the innermost shield and (2) it provides a stable, elevated temperature environment for the Rb cell yielding vapor densities of $\approx 2 \times 10^{10}$ atoms/cm^3.

A system of nine separate coils are wound in grooves cut into the frame mounted inside the innermost layer of

the shield. The system of coils was designed to provide, over the volume of the Rb vapor cell, uniform magnetic fields in three orthogonal directions (B_x, B_y, and B_z), linear magnetic field gradients in five directions (dB_x/dx, dB_z/dz, dB_x/dz, dB_y/dz, dB_y/dx), and a quadratic gradient along the shield axis (d^2B_z/dz^2). As a consequence of Maxwell's equations ($\nabla \cdot \mathbf{B} = 0$ and $\nabla \times \mathbf{B} = 0$), control over the five linear magnetic field gradients is sufficient to provide compensation of all nine possible linear gradients. Based on computer modeling (using the Amperes program from Integrated Engineering Software Inc.), the uniformity of the magnetic fields and linearity/quadracity of the field gradients generated by the coil system is at a part per thousand over the cell volume for typical applied currents. It should be noted that effects of uncompensated magnetic-field gradients are significantly reduced by motional averaging [50] (effects are quadratic in the the magnitude of the gradient). The coils are in series with a set of ultra-stable, low temperature coefficient (low TC) resistors (Caddock Type USF 200 Series, zero nominal TC with TC $\lesssim 2$ ppm/K). The voltage for the B_z coil is supplied by a precision DC voltage source (Krohn-Hite Model 523 calibrator, stability ± 1 ppm) and voltages for the coils controlling B_x, B_y, and field gradients are computer generated with a digital-to-analog-converter (DAC, National Instruments PCI-6733).

In order to measure Ω_{85} and Ω_{87}, a system of shutters (Stanford Research SR474) is used to implement a temporally separated pump/probe measurement scheme. During the optical pumping stage (duration = 1 s), Rb atoms are illuminated by two collinear, circularly polarized pump beams propagating along $-\hat{\mathbf{y}}$ (orthogonal to $\mathbf{B}$ which is along z), one tuned to the center of the Doppler-broadened ^{85}Rb D2 $F = 3 \rightarrow F'$ resonance and the other tuned to the center of the Doppler-broadened ^{87}Rb D1 $F = 2 \rightarrow F' = 1$ resonance (F, F' are the total atomic angular momenta of the ground and excited states, respectively). The 780-nm D2 pump beam is generated by a distributed feedback laser diode (EYP-DFB-0780-00080-1500-TOC03 from Eagleyard Photonics) and the 795-nm D1 pump beam is produced by a tunable external-cavity diode laser (Toptica DL100). The pump beams are amplitude-modulated at frequencies close to the respective Larmor frequencies of the isotopes using electro-optic modulators (EOMs, ThorLABs E0-AM-NR-C1, not shown in Fig. 2) placed between crossed calcite linear polarizers. The duty cycle for both pump beams is 20%; during the period when the EOMs transmit the pump light, the power of the D2 pump beam incident on the Rb atoms is ≈ 55 μW and the power of the D1 pump beam is ≈ 150 μW. These parameters were chosen to maximize the transverse spin polarization for both Rb isotopes. This synchronous optical pumping generates atomic spin polarization transverse to $\mathbf{B}$ in both isotopes precessing at their respective Larmor frequencies. A third, collinear, circularly polarized re-pump beam tuned to the center of the Doppler-broadened ^{87}Rb D2 $F = 1 \rightarrow F'$ resonance transfers ^{87}Rb atoms pumped into the unobserved $F = 1$ ground-state hyperfine level back into the $F = 2$ hyperfine level (which, taking into account natural isotopic abundances, yields approximately equal signals for both isotopes). The 780-nm re-pump beam is produced by tunable external-cavity diode laser (New Focus TLM 7000), with power $\approx$ 750 μW. The diameters of the pump and re-pump beams are $\approx$ 2mm.

During the optical probing stage (duration = 1 s), a shutter blocks the pump and re-pump beams, and shutters open to allow a linearly polarized probe laser beam to propagate along $-\hat{\mathbf{y}}$ through the vapor and into a polarimeter. The 780-nm D2 probe beam is produced by another tunable external-cavity diode laser (Toptica DL100). The ^{85}Rb and ^{87}Rb precession frequencies, Ω_{85} and Ω_{87}, are measured by observing optical rotation of the probe light. The frequency of the probe beam is tuned ≈ 3 GHz below the center frequency of the Doppler-broadened ^{87}Rb D2 $F = 2 \rightarrow F'$ resonance, the power is ≈ 200 μW, and the beam diameter is ≈ 2 mm. Prior to entering the vapor cell, the probe beam passes through an antireflection-coated Glan Thomson linear polarizer (calcite, extinction ratio $5 \times 10^5 : 1$). After exiting the vapor cell, the beam is analyzed by a polarimeter consisting of a Wollaston prism polarizing beamsplitter (calcite, extinction ratio $10^5 : 1$) whose output rays are detected with a balanced photoreceiver (New Focus Model 2307). The signal from the photoreceiver is sent to a preamplifier (Stanford Research Systems SR560) and then recorded on computer using an analog-to-digital converter (National Instruments PCIe-6361) using a routine written in LabVIEW. The time base for the data acquisition is provided by a 10 MHz signal from a Rb atomic frequency standard (Stanford Research Systems SIM940, short-term stability $\lesssim 2 \times 10^{-12}$ in 100 s) that is GPS-disciplined with a 1 PPS signal (from a Communication Navigation Surveillance Inc. CNS Clock II, with a long-term accuracy better than a part in $\approx 10^{12}$). The accurate time base ensures that Ω_{85} and Ω_{87} can be measured at the 10^{-8} Hz level over a long period of time for data averaging. The pump and re-pump lasers are frequency stabilized using dichroic atomic vapor laser locks (DAVLLs) [52, 53]. The probe, pump, and re-pump beam spectral purities are monitored with Fabry-Perot interferometers (ThorLABs SA200-5B) and the light powers of each beam transmitted through separate uncoated Rb

reference cells (natural isotopic mixture) are monitored to ensure that the lasers remain properly tuned. (The laser frequency locking and diagnostics setups are not shown in Fig. 2.)

The picture in the upper left corner of the experimental setup diagram (Fig. 2) depicts the magnetic shield mount used for mechanical alignment of the shield axis z along the Earth's rotation axis $\hat{\mathbf{\Omega}}_E$, which is important for control of a systematic error related to the Earth's rotation (Section 5.2). The outermost shield layer is held in place with an aluminum frame, which is bolted to precision tilt and rotation stages (Newport TGN160 and UTR120, respectively) attached to an optical breadboard tilted from horizontal by an angle approximately equal to the latitude of the laboratory (37°39′24″ N). By surveying the laboratory (using Google Earth as well as GPS signals) and using an alignment laser propagating along the shield axis (z) with a path length of $\approx$ 3m, we are able to mechanically align the shield axis with the Earth's rotation axis to within 0.3°. Prior to measurement of Ω_{85} and Ω_{87}, $\mathbf{B}$ is carefully aligned along the z-axis using a laser beam split off from the 780-nm probe beam by measuring NMOR with frequency modulated light [43,44,54,55]. The accuracy of the alignment of $\mathbf{B}$ along the light propagation direction $\mathbf{k}$ using NMOR [56] is much greater than the mechanical alignment accuracy of the shield axis, so the alignment of $\mathbf{B}$ parallel with $\hat{\mathbf{\Omega}}_E$ is achieved with an uncertainty of $\approx 0.3°$.

4 Initial data and projected statistical sensitivity

Sample data acquired during the probe sequence are shown in Fig. 3. The upper plot shows the optical rotation signal acquired in the time domain for an applied field of $B \approx 7.1443$ mG oriented in the $\hat{\mathbf{z}}$ direction, and the lower plot shows the absolute value of the Fourier transform of the data set (carried out using a data analysis routine written in Mathematica). In the frequency domain, distinct resonant peaks in the Fourier transform can be identified and correspond to Ω_{85} and Ω_{87}. The dominant contribution to these signals is from atoms in the resonantly pumped ^{85}Rb $F = 3$ ground state and the ^{87}Rb $F = 2$ ground state, since the pump and re-pump laser beam parameters are optimized for transverse spin polarization of these states and the probe beam is tuned closest to optical resonance with transitions from these states.

In the time domain a slow beating is observed in the optical rotation signal. The additional frequency

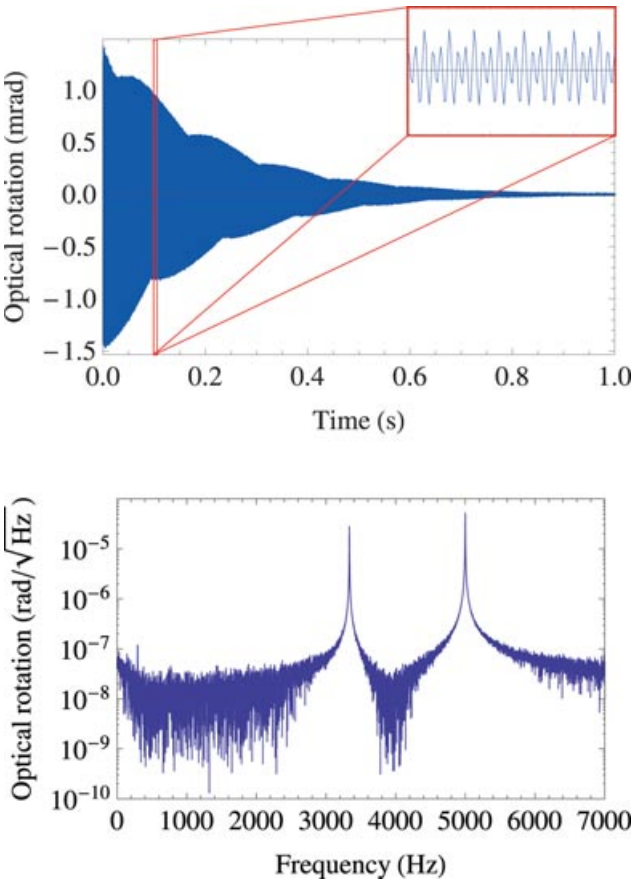

Figure 3 Upper plot: sample time-domain data from pump/probe measurement of Rb spin precession using optical rotation. Inset in upper right corner shows a subset of the data of total duration 10 ms (highlighted by the red box on the complete data set). In the inset, fast beating is observed between sinusoidal signals with frequencies Ω_{85} and Ω_{87}. The applied magnetic field corresponds to $|\mathbf{B}| \approx 7.1443$ mG. Slow beating can be observed in the main time-domain plot between a dominant signal from ^{85}Rb atoms in the $F = 3$ ground state hyperfine level and a smaller-amplitude signal from ^{85}Rb atoms in the $F = 2$ ground state hyperfine level (the absolute value of the Landé g-factors of the two ground state hyperfine levels differ due to the nuclear magnetic moments, see Section 5.3). Lower plot: Fourier transform of the time-domain data, showing resonances at Ω_{85} (lower-frequency peak) and Ω_{87} (higher-frequency peak).

component responsible for the beating arises from spin precession of ^{85}Rb atoms in the $F = 2$ ground state, which has a slightly different Landé g-factor magnitude than the $F = 3$ ground state because of the nuclear magnetic moment (this effect is discussed in detail in Section 5.3). The ^{85}Rb $F = 2$ ground state is slightly polarized by nearly synchronous re-population pumping: a fraction of the ^{85}Rb atoms optically pumped from the

$F = 3$ ground state spontaneously decay from the $5^2P_{3/2}$ excited state back to the $F = 2$ ground state; the absolute values of the Landé g-factors are close enough in value that for sufficiently small magnetic fields a detectable transverse spin polarization in the ^{85}Rb $F = 2$ ground state can be created during the pumping stage. (^{87}Rb atoms in the $F = 1$ ground state contribute a much smaller amplitude signal for a variety of reasons, discussed in Section 5.3.)

Data analysis is carried out by fitting subsets of the Fourier transformed optical rotation signal centered around Ω_{85} and Ω_{87} to a Lorentzian function $S(\omega)$:

$$S(\omega) = \sqrt{\left[\frac{\alpha}{1+\left(\frac{\omega-\Omega}{\Gamma}\right)^2}\right]^2 + \left[\frac{\beta(\omega-\Omega)/\Gamma}{1+\left(\frac{\omega-\Omega}{\Gamma}\right)^2}\right]^2}, \tag{12}$$

where α and β are the amplitudes of the imaginary and real components of the signal, respectively, ω is the frequency, Ω is the resonant spin-precession frequency, and Γ is the resonance width (corresponding to the spin relaxation rate). To account for spin precession of ^{85}Rb atoms in the $F = 2$ ground state, additional real and imaginary Lorentzian components of the signal can be included in the fitting function for Ω_{85}. Under typical operating conditions, $\Gamma/(2\pi) \approx 1$ Hz.

Fits to the data demonstrate a statistical sensitivity to the spin precession frequency Ω of

$$\frac{\delta\Omega}{2\pi} \approx 100\ \mu\text{Hz} \tag{13}$$

for a 1 s measurement. Ultimately, the shot-noise-limited (SNL) sensitivity $\delta\Omega_{\text{SNL}}$ of a spin-polarized atomic sample to precession frequencies is determined by the total number of atoms N and the relaxation rate Γ_{rel} of the atomic spin polarization (for measurement times $\tau \gg \Gamma_{\text{rel}}^{-1}$ [58–60]):

$$\delta\Omega_{\text{SNL}} \approx \sqrt{\frac{\Gamma_{\text{rel}}}{N\tau}}. \tag{14}$$

Under our experimental conditions, $N \approx 10^{12}$atoms and $\Gamma_{\text{rel}} \approx 2\pi \times 1$ Hz (limited by spin-exchange collisions), yielding $\delta\Omega_{\text{SNL}} \approx 2\pi \times 0.4\ \mu$Hz for $\tau = 1$ s. This suggests that the measurement is not presently shot-noise-limited, and further reduction in technical noise would permit even better statistical sensitivity.

We are in the process of making several modifications to the apparatus in order to improve the sensitivity. Noise from the balanced photoreceiver presently exceeds the photon-shot-noise limit by a factor of ≈ 5, and therefore we are upgrading the balanced photoreceiver in order to achieve photon-shot-noise-limited polarimetry. Optimization of the probe light power and detuning should enable further improvement in sensitivity, since the photon shot-noise limit presently exceeds the atomic shot-noise limit by over an order of magnitude.

Although comagnetometry significantly reduces magnetic-field-related noise and systematic effects from acquisition-to-acquisition, in our configuration it does not improve the statistical uncertainty for a single acquisition. Therefore magnetic field noise can degrade the sensitivity. In particular, magnetic field noise due to thermal Johnson currents in the innermost mu-metal shield is estimated to contribute noise at the 100 $\mu\text{Hz}/\sqrt{\text{Hz}}$ level [61–63]. We are in the process of replacing the innermost mu-metal shield with a nonconducting ferrite shield, which has been demonstrated to reduce thermal magnetic field noise [64].

We expect that these improvements to our apparatus should enable sensitivity to atomic spin precession at the 10 μHz level for a 1 s measurement. Collecting data for $\approx 10^6$ s would then yield a statistical sensitivity of $\approx 10^{-8}$ Hz to anomalous spin-precession, sufficient to search for a GDM signal corresponding to $k \sim 1$ (Eq. (3)).

5 Systematic effects

5.1 General considerations

For a general consideration of systematic errors, it is helpful to characterize the ways in which additional contributions to the spin-precession frequencies for ^{85}Rb and ^{87}Rb beyond Larmor precession can enter the expressions for Ω_{85} and Ω_{87}, and, crucially, the comagnetometer signal $\Delta\Re$ from which we will extract the GDM coupling.

One useful way to characterize systematic errors is to separate contributions to the spin precession frequencies into those that reverse sign when the direction of $\mathbf{B}$ is changed relative to $\boldsymbol{g}$ (B-odd terms, Ω_o) and those that do not reverse sign (B-even terms, Ω_e). Depending on the orientation of $\mathbf{B}$ relative to $\boldsymbol{g}$, for each isotope we obtain two different precession frequencies

$$\Omega_\pm = \Omega_L + \Omega_e \pm \Omega_o, \tag{15}$$

where Ω_L is the appropriate Larmor frequency. Somewhat counter-intuitively, any effect that causes spin precession in a fixed sense contributes a B-odd term. This is because reversal of $\mathbf{B}$ reverses the sense of Larmor precession, and it is the absolute value of the spin

precession frequency that is measured in the experiment. Thus spin-precession due to a GDM coupling is a B-odd term contributing to Ω_o, and consequently B-odd systematic errors are not suppressed in the comagnetometer signal $\Delta\mathcal{R}$. Assuming $\Omega_e = 0$ and a B-odd systematic effect adding to the ^{87}Rb precession frequency, we have

$$\Delta\mathcal{R} \approx 9.6\left(\frac{\gamma_{87}-\gamma_{85}}{\gamma_{87}+\gamma_{85}}\right)\frac{\Omega_o}{\mu_0 B}. \tag{16}$$

Therefore B-odd systematic effects must be suppressed or accounted for by other means.

In the case of perfect magnetic-field reversal, there is no contribution of B-even terms to $\Delta\mathcal{R}$. However, if magnetic-field reversal is imperfect by an amount δB, B-even systematic effects can lead to a nonzero $\Delta\mathcal{R}$. Assuming $\Omega_o = 0$ and a B-even systematic effect adding to the ^{87}Rb precession frequency, we have

$$\Delta\mathcal{R} \approx 4.8\left(\frac{\gamma_{87}-\gamma_{85}}{\gamma_{87}+\gamma_{85}}\right)\frac{\Omega_e}{\mu_0 B}\frac{\delta B}{B}. \tag{17}$$

Thus B-even systematic effects are suppressed relative to B-odd effects by a factor $\sim \delta B/B$ which in our experiment can be made $\lesssim 10^{-9}$ by taking advantage of the high sensitivity of the setup to magnetic fields (under typical experimental conditions, the applied magnetic field is ~ 10 mG and the magnetometric sensitivity of the apparatus is $\delta B \sim 10^{-11}$ G/$\sqrt{\text{Hz}}$).

Because our experiment employs a scalar measurement scheme (see, e.g., Refs. [59, 60]) where the dominant contribution to the spin precession frequency is from Larmor precession induced by the magnetic field **B**, we can also characterize spin precession in terms of contributions $\Omega_{||}$ that add linearly to Ω_L and contributions $\Omega_\perp$ that add in quadrature to Larmor precession:

$$\Omega = \sqrt{\left(\Omega_L + \Omega_{||}\right)^2 + (\Omega_\perp)^2}, \tag{18}$$

$$\approx \Omega_L + \Omega_{||} + \frac{\Omega_\perp^2}{2\Omega_L}, \tag{19}$$

where we have assumed that $\Omega_{||}, \Omega_\perp \ll \Omega_L$.

Certain systematic errors (such as light shifts) are suppressed by arranging the experimental geometry so that they contribute to Ω primarily as $\Omega_\perp$. Of course, imperfections in alignment inevitably mean that there is some contribution of such systematic errors to both $\Omega_{||}$ and $\Omega_\perp$:

$$\Omega_{||} = \Omega_{\text{err}} \sin\varphi \approx \varphi\Omega_{\text{err}}, \tag{20}$$

$$\Omega_\perp = \Omega_{\text{err}} \cos\varphi \approx \left(1 - \frac{\varphi^2}{2}\right)\Omega_{\text{err}}, \tag{21}$$

$$\Omega \approx \Omega_L + \varphi\Omega_{\text{err}} + \frac{\Omega_{\text{err}}^2}{2\Omega_L}, \tag{22}$$

where Ω_{err} is the amplitude of the systematic error and φ is the misalignment angle from perfect orthogonality to the leading field contribution. Experimentally, mechanical alignment of the system can in most cases achieve at best $\varphi \lesssim 5 \times 10^{-3}$ rad (0.3°). However, in the case of the alignment of **B** parallel with or orthogonal to the light propagation direction (represented by the wave vector **k**), much better results can be achieved by employing nonlinear magneto-optical effects that depend on the angle between **B** and **k** [56]: $\varphi \lesssim 10^{-5}$ rad can be achieved under typical operating conditions.

Other systematic errors cannot be sufficiently suppressed using the above experimental geometry (for example, the gyroscopic error introduced by rotation of the Earth [31, 32, 57]). In these cases, the experiment is arranged so that the error contributes to Ω primarily as $\Omega_{||}$:

$$\Omega_{||} = \Omega_{\text{err}} \cos\varphi \approx \left(1 - \frac{\varphi^2}{2}\right)\Omega_{\text{err}}, \tag{23}$$

$$\Omega_\perp = \Omega_{\text{err}} \sin\varphi \approx \varphi\Omega_{\text{err}}, \tag{24}$$

$$\Omega \approx \Omega_L + \left(1 - \frac{\varphi^2}{2}\right)\Omega_{\text{err}} + \frac{\varphi^2\Omega_{\text{err}}^2}{2\Omega_L}. \tag{25}$$

While this geometry offers no suppression Ω_{err}, the systematic uncertainty in the value of Ω_{err} due to apparatus misalignment is quadratically suppressed. If Ω_{err} is independently measured with sufficient accuracy, it can be subtracted from the data.

The various systematic effects considered in this section are summarized in Table 2, which lists their estimated contribution to $\Delta\mathcal{R}$. The most significant estimated source of systematic uncertainty in our experiment is the effect of light shifts due to the residual ellipticity of the nominally linearly polarized probe beam.

Table 2 Estimated contribution of various systematic errors to $\Delta\mathcal{R}$ for $|\mathbf{B}| = 7.1443$ mG. The atomic shot-noise-limited sensitivity of the setup under our experimental conditions, $N \approx 10^{12}$ atoms and $\Gamma_{\rm rel} \approx 2\pi \times 1$ Hz, is also listed for comparison, along with our anticipated experimental sensitivity (corresponding to $\delta\Omega = 2\pi \times 10$ μHz in 1 second of integration). An integration time of 10^6 seconds is assumed. For $k = 1$, $\chi_p = \hbar/c$, leading to a spin-gravity signal at the level $\Delta\mathcal{R} \approx 3 \times 10^{-13}$.

Description	$\Delta\mathcal{R}$
Atomic shot-noise limit	4×10^{-14}
Anticipated sensitivity	1×10^{-12}
Gyro-compass effect	2×10^{-14}
Nuclear magnetic moments	$< 10^{-16}$
Nonlinear Zeeman effect	negligible
Light shifts	$< 10^{-12}$
Spin-exchange collisions	2×10^{-18}
Magnetic field gradients & geometric phase	$< 10^{-16}$
Wall collisions	$< 10^{-16}$

5.2 Gyro-compass effect

Because the experimental apparatus is attached to the Earth, while the atomic spins are decoupled from Earth's rotation, the experimental signal is sensitive to the rotation rate of the Earth, $\Omega_E/(2\pi) \approx 11.6$ μHz. This effect, known as the gyro-compass effect [32] or the spin-rotation effect [1], can be understood as the result of viewing an inertial system, the atomic spins, from a non-inertial frame, the surface of the rotating Earth. Uncertainty in the magnitude of this B-odd systematic effect can be made quadratic in the misalignment of the experimental apparatus (Eq. (25)) by orienting $\mathbf{B}$ along the axis of Earth's rotation $\hat{\mathbf{\Omega}}_E$ [31]. This approach has been implemented as shown in the picture at the top left of the experimental setup diagram (Fig. 2).

Including the gyro-compass effect adds a B-odd spin-precession frequency ($\Omega_o = \Omega_E \cos\theta$) to Ω_{85} and Ω_{87}, where θ describes the misalignment between Earth's rotation axis $\hat{\mathbf{\Omega}}_E$ and $\mathbf{B}$. Based on Eq. (16):

$$\Delta\mathcal{R} \approx \left(\frac{\gamma_{87}-\gamma_{85}}{\gamma_{87}+\gamma_{85}}\right)\left[4.12\left(\frac{\chi_p g\cos\phi}{\mu_0 B}\right) - 2.4\left(\frac{\Omega_E\cos\theta}{\mu_0 B}\right)\right]. \tag{26}$$

The angle ϕ is now the resultant angle between $\boldsymbol{g}$ and $\hat{\mathbf{\Omega}}_E$ (ϕ equals 90° plus the latitude of the laboratory location, about 37°, so $\cos\phi \approx -0.6$). We can control the orientation of $\mathbf{B}$ with respect to an auxiliary laser beam propagating along $\hat{\mathbf{z}}$ to a level of better than 10^{-5} [56]. The long lever arm of the laser beam (in combination with GPS and aerial surveying) enables alignment of the auxiliary laser beam propagation direction with $\hat{\mathbf{\Omega}}_E$ to within $\approx 0.3^\circ \approx 5 \times 10^{-3}$ rad, so that systematic uncertainty in the gyro-compass effect due apparatus misalignment is at the 3×10^{-10} Hz level. Thus errors due to the Earth's rotation can be well-controlled at our proposed level of sensitivity.

5.3 Nuclear magnetic moments

Although nuclear magnetic moments are a thousand times smaller than μ_0, their effect on the observed spin precession frequencies is clearly evident in the sample data shown in Fig. 3, giving rise to a slow beating visible in the time-domain signal shown in the upper plot. The nuclear magnetic moment modifies the Landé factors for the alkali ground state hyperfine levels [65, 66]:

$$g_{F=I+\frac{1}{2}} = \frac{2}{2I+1} - g_I\frac{\mu_N}{\mu_0}\frac{2I}{2I+1}, \tag{27}$$

$$g_{F=I-\frac{1}{2}} = -\frac{2}{2I+1} - g_I\frac{\mu_N}{\mu_0}\frac{2(I+1)}{2I+1}, \tag{28}$$

where g_I is the nuclear Landé factor ($g_I \approx 0.539$ for ^{85}Rb, $g_I \approx 1.827$ for ^{87}Rb [67]) μ_N is the nuclear magneton, and $\mu_N/\mu_0 \approx 5 \times 10^{-4}$. This creates a difference in the Larmor frequencies for atoms in the two different ground state hyperfine levels

$$\begin{aligned}\Delta\Omega_{\rm nucl} &= \Omega_L\left(F = I+\frac{1}{2}\right) - \Omega_L\left(F = I-\frac{1}{2}\right)\\ &= -2g_I\mu_N B.\end{aligned} \tag{29}$$

For $B \approx 7.1443$ mG as in the data shown in Fig. 3, ^{85}Rb has $\Delta\Omega_{\rm nucl} \approx -2\pi \times 5.9$ Hz and ^{87}Rb has $\Delta\Omega_{\rm nucl} \approx -2\pi \times 19.9$ Hz. Off-resonant synchronous optical pumping for the ^{85}Rb $F = 2$ state is much more efficient than that for the ^{87}Rb $F = 1$ state because of the smaller $\Delta\Omega_{\rm nucl}$. The signal from the ^{87}Rb $F = 1$ state is additionally suppressed relative to the signal from the ^{85}Rb $F = 2$ state because the re-pump laser beam depletes the ^{87}Rb $F = 1$ state and the probe laser

light is farther detuned from the ^{87}Rb D2 $F = 1 \rightarrow F'$ resonance than from the ^{85}Rb D2 $F = 2 \rightarrow F'$ resonance. Consequently, only the dominant signals from the ^{85}Rb $F = 3$ and ^{87}Rb $F = 2$ states, along with a much smaller signal from the ^{85}Rb $F = 2$ state which leads to the slow beating observed in the time-domain signal in Fig. 3, are easily detectable in the data.

In our data analysis, the three observable resonances in the Fourier transformed optical rotation data are fit directly, and modeling demonstrates that neglecting the resonance associated with the ^{87}Rb $F = 1$ state in our fitting routine does not affect our analysis at the desired level of accuracy. Fortunately, any first-order systematic effect associated with the nuclear magnetic moments manifests as a B-even systematic that is suppressed by $\sim \delta B/B \sim 10^{-9}$ in the comagnetometer signal $\Delta\Re$ as discussed in Section. 5.1.

5.4 Nonlinear Zeeman effect

The magnetic field also mixes Zeeman sublevels in different ground state hyperfine levels, leading the Zeeman effect to acquire a nonlinear dependence on B. In our experiment, the nonlinear Zeeman effect manifests as a splitting of the Larmor resonances [68–71]. The splitting of the resonances is symmetric about the unperturbed Larmor frequency and smaller than the linewidth, therefore, to leading order, it does not contribute any systematic shift to the spin precession frequencies. The energy $E(F, M_F)$ of a particular ground state Zeeman sublevel (M_F is the projection of F along $\hat{\mathbf{z}}$) of an alkali atom is described by the Breit-Rabi formula [72]:

$$E(F = I \pm 1/2, M_F) = -\frac{\mathcal{A}_{\rm hfs}}{4} - g_I \mu_N B M_F \pm \frac{\mathcal{A}_{\rm hfs}}{4}(2I+1)\sqrt{1 + \frac{4M_F u}{2I+1} + u^2}, \tag{30}$$

where $\mathcal{A}_{\rm hfs}$ is the alkali atom's hyperfine structure constant and u is the perturbation parameter given by:

$$u \equiv \frac{g_J \mu_0 + g_I \mu_N}{2I+1}\frac{2B}{\mathcal{A}_{\rm hfs}} \approx \frac{4}{2I+1}\frac{\mu_0 B}{\mathcal{A}_{\rm hfs}}, \tag{31}$$

where $g_J \approx 2$ is the Landé g-factor for the electron. The Breit-Rabi formula (Eq. (30)) can be expanded to second order in u and the terms proportional to u^2 can be identified as the nonlinear Zeeman shifts $E_{\rm nlz}$:

$$E_{\rm nlz}(F = I \pm 1/2, M_F) = \pm u^2 \frac{\mathcal{A}_{\rm hfs}}{8}(2I+1)\left(1 - \frac{4M_F^2}{(2I+1)^2}\right). \tag{32}$$

The term in Eq. (32) proportional to M_F^2,

$$\approx \mp \frac{8}{(2I+1)^3}\frac{\mu_0^2 B^2}{\mathcal{A}_{\rm hfs}} M_F^2, \tag{33}$$

causes a nonlinear Zeeman shift of the Larmor frequencies that splits a single spin-precession resonance into multiple resonances. In the following we consider only the $F = I + 1/2$ ground state hyperfine levels and define the unperturbed Larmor frequency $\Omega_L^{(0)}$ as the term linear in B,

$$\Omega_L^{(0)} = \left(\frac{2}{2I+1}\mu_0 - g_I \mu_N \frac{2I}{2I+1}\right) B. \tag{34}$$

For the ^{85}Rb $F = 3$ state, there appear six resonance frequencies split symmetrically about $\Omega_L^{(0)}$:

$$\Omega_L^{(0)} \pm 5\frac{8}{(2I+1)^3}\frac{\mu_0^2 B^2}{\mathcal{A}_{\rm hfs}},$$
$$\Omega_L^{(0)} \pm 3\frac{8}{(2I+1)^3}\frac{\mu_0^2 B^2}{\mathcal{A}_{\rm hfs}},$$
$$\Omega_L^{(0)} \pm 1\frac{8}{(2I+1)^3}\frac{\mu_0^2 B^2}{\mathcal{A}_{\rm hfs}}.$$

(For the ^{87}Rb $F = 2$ state there are four resonance frequencies described by the latter four cases above.) For $B \approx 7.1443$ mG, as in the data shown in Fig. 3, the maximum splitting of the resonance frequencies is ≈ 0.2 Hz for the ^{85}Rb $F = 3$ state and ≈ 0.08 Hz for the ^{87}Rb $F = 2$ state, in both cases smaller than the resonance linewidth of ≈ 1 Hz. Any imbalance in the population of the Zeeman sublevels associated with the different resonances constitutes longitudinal spin polarization that does not contribute to the spin precession signal. Therefore, in some sense, the signal amplitudes for different resonances are naturally balanced. Thus the only apparent consequence of the nonlinear Zeeman effect under our experimental conditions is a slight broadening of the spin precession resonances. Nonetheless, measurements will be carried out at different magnetic fields to test for any magnetic-field-dependent systematic errors.

5.5 Light shifts

The ac Stark effect due to the optical electric field of the probe beam can cause light shifts of Zeeman sublevels, leading to shifts of the measured precession frequencies for ^{85}Rb and ^{87}Rb. In general, ac Stark shifts can be described in terms of scalar, vector, and tensor polarizabilities [66, 73]. The scalar and tensor polarizabilities are described by rank-zero and rank-two operators, and thus their effect on atoms can be modeled as a fictitious static electric field along the light polarization axis; the vector polarizability is described by a rank-one operator, and thus can be modeled as a fictitious static magnetic field along the light propagation direction $\hat{\mathbf{k}}$ [74–78].

For measurement of Ω_{85} and Ω_{87}, it is the vector light shift in particular that causes the most significant systematic effect. Although the probe beam is nominally linearly polarized and detuned far from the Doppler-broadened optical resonances, vector light shifts can still arise due to residual ellipticity ϵ induced in the beam due to birefringence of the vapor cell walls. Measurements of the probe beam polarization before and after the cell using a ThorLABs PAX720IR1-T polarimeter system show that ϵ can be made $\lesssim 0.01^\circ \approx 2 \times 10^{-4}$ rad.

The frequency shift $\Omega_{\rm ac}$ associated with the vector polarizability is a B-odd systematic effect, and thus is not suppressed in the comagnetometer signal $\Delta\mathcal{R}$. However, because $\mathbf{k}$ is orthogonal to $\mathbf{B}$, there is a geometric suppression according to Eq. (22). The quadratic correction term in Eq. (22) can be neglected in our case, and we have:

$$\Omega_{\rm ac} \approx \varphi \sin(2\epsilon)\Delta E_{\rm ac}/\hbar \approx 2\varphi\epsilon\Delta E_{\rm ac}/\hbar, \tag{35}$$

where $\Delta E_{\rm ac}$ is the vector light shift between adjacent Zeeman sublevels ($\Delta M_F = 1$) for left-circularly polarized light along the quantization axis. $\Delta E_{\rm ac}$ can be estimated, for example, based on the formula from Ref. [78]:

$$\Delta E_{\rm ac} \approx -\frac{|\langle 5S_{1/2}|er|5P_{1/2}\rangle|^2}{9\Delta\omega_{3/2}} g_F \langle|\mathcal{E}_0|^2\rangle, \tag{36}$$

where $\langle 5S_{1/2}|er|5P_{1/2}\rangle \approx 3ea_0$ is the transition dipole matrix element between the $5S_{1/2}$ and $5P_{1/2}$ states, a_0 is the Bohr radius, $\Delta\omega_{3/2}$ is the detuning of the probe beam from the D2 resonance, g_F is the ground state Landé factor, and $\langle|\mathcal{E}_0|^2\rangle$ is the average square of the optical electric field experienced by the atoms. In calculating $\langle|\mathcal{E}_0|^2\rangle$, one must take into account the fact that the effective optical electric field experienced by the atoms is diluted by the ratio of the volume within the cell illuminated by the probe light beam to the total volume of the cell (for our experiment, the ratio $\approx 2 \times 10^{-3}$) since the atoms spend only a small fraction of their time in the probe light during the precession time [70]. For our typical probe light power of 200 μW and detuning of ≈ 3 GHz below the center frequency of the Doppler-broadened ^{87}Rb D2 $F = 2 \rightarrow F'$ resonance, we estimate that the vector light shifts for ^{85}Rb and ^{87}Rb are given, respectively, by

$$\Delta E_{\rm ac}(85) \approx -2\pi\hbar \times (3\text{Hz}), \tag{37}$$

$$\Delta E_{\rm ac}(87) \approx -2\pi\hbar \times (1.3\text{Hz}). \tag{38}$$

Because sensitive nonlinear magneto-optical effects can be used to directly measure the angle between $\mathbf{k}$ and $\mathbf{B}$ [56], it is actually feasible in our setup to constrain $\varphi \lesssim 10^{-5}$ rad. Therefore, based on Eq. (35), $\Omega_{\rm ac} \lesssim 10^{-8}$ Hz, and consequently light shifts are not expected to prevent the experiment from reaching its sensitivity target. Nevertheless, data will be taken at different probe light powers to check for any systematic effects related to light shifts.

5.6 Spin-exchange collisions

The dual-isotope Rb comagnetometer relies on independent measurements of Ω_{85} and Ω_{87}, so coupling between the two isotopes through spin-exchange (SE) collisions can produce a systematic error. However, since the experiment is carried out in a bias field of $|\mathbf{B}| \sim 10$ mG and $\Omega_{85} \neq \Omega_{87}$, in the frame rotating with each isotope's precession frequency, the spin-polarization of the other isotope is time-averaged to nearly zero [79]. Nonetheless, there still appears a small SE frequency shift [80]. Spin-exchange collisions tend to pull the precession frequencies toward a weighted average: SE collisions that transfer atoms between ground state hyperfine levels of a single isotope reduce the measured spin precession frequency since the gyromagnetic ratios have opposite signs; SE collisions between Rb isotopes shift Ω_{85} to a higher frequency and Ω_{87} to a lower frequency (cross-isotope SE shifts do not cancel because of the larger statistical weights of the $F = I + 1/2$ hyperfine levels).

An estimate of the scale of the SE frequency shift $\Omega_{\rm se}$ can be obtained by considering SE collisions between ground state hyperfine levels of each individual isotope. Under our experimental conditions, where the SE

collision rate $\gamma_{se} \ll \Omega_L$, we have Ref. [80]:

$$\Omega_{se} \approx -\frac{\gamma_{se}^2}{18\Omega_L}\left(1-\frac{1}{(2I+1)^2}\right)\left(1-\frac{4}{(2I+1)^2}\right). \quad (39)$$

Under the experimental conditions for the data shown in Fig. 3 ($\gamma_{se} \approx 2\pi \times 1.3$ Hz, $\Omega_{85} \approx 2\pi \times 3334$ Hz, and $\Omega_{87} \approx 2\pi \times 5001$ Hz):

$$\Omega_{se}(85) \approx -2\pi \times 2.3 \times 10^{-5} \text{ Hz}, \quad (40)$$

$$\Omega_{se}(87) \approx -2\pi \times 1.3 \times 10^{-5} \text{ Hz}. \quad (41)$$

Crucially, SE frequency shifts are B-even and so their effect on the comagnetometer signal $\Delta\Re$ is described by Eq. (17), thus suppressing any SE collision-related systematic effects by $\sim \delta B/B \sim 10^{-9}$. Because of the suppression of Ω_{se} in $\Delta\Re$, systematic effects due to SE collisions between atoms are negligible in our experiment.

5.7 Other systematic effects

Another concern is the effect of magnetic field gradients which cause ^{85}Rb and ^{87}Rb atoms to, on a random basis, sample different magnetic fields, reducing the effectiveness of the comagnetometry scheme. Field gradients are nulled using auxiliary measurements to $\lesssim 10^{-7}$ G/cm in all directions [50]. Effects of gradients are further reduced due to motional averaging in the evacuated antirelaxation-coated cells: atoms typically bounce off of the cell walls $\gtrsim 10^5$ times between interactions with the laser beam [42]. For a sample of $\sim 10^{12}$ atoms, this creates uncertainty at the nHz/$\sqrt{\text{Hz}}$ level, well below our statistical sensitivity to spin precession. Furthermore, systematic frequency shifts related to the geometric (Berry's) phase [81] are proportional to gradients, and are estimated to be less than a nHz under typical experimental conditions based on the analysis of Ref. [82].

Wall collisions can produce quadrupolar splittings of spin precession frequencies due interaction of atomic spins with surface electric field gradients [31]. In our experiment, wall collisions should produce negligibly small shifts of Ω_{85} and Ω_{87} since the vapor cell employs an amorphous antirelaxation coating and is spherical in shape, so that, to a high precision, there is no preferred direction in the cell. We can estimate that in the worst-case scenario the contribution to a cell-related shift is on the order of the wall relaxation rate ($\sim 10^{-2}$ Hz) times the square of the ratio of the size of the opening to the stem that contains the alkali metal sample ($\approx 10^{-2}$ cm^2) to the inner surface area of the cell (≈ 80 cm^2): $\lesssim 10^{-10}$ Hz.

6 Conclusion

An experiment measuring spin precession frequencies of overlapping ensembles of ^{85}Rb and ^{87}Rb atoms contained within an evacuated, antirelaxation-coated vapor cell can be used to search for presently unconstrained anomalous long-range spin-mass couplings. Synchronous optical pumping with circularly polarized light is used to generate spin polarization transverse to an applied magnetic field and optical rotation of a linearly polarized probe beam is used to measure the ^{85}Rb and ^{87}Rb spin precession frequencies. The Earth is used as the source mass. The present statistical sensitivity of the apparatus to spin precession frequencies is 10^{-4} Hz in one second of integration, with a shot-noise-projected sensitivity exceeding this level by over two orders of magnitude. A variety of systematic errors are considered, and all known sources of error can be controlled at the 10^{-8} Hz level.

There are several promising and potentially more sensitive approaches to searching for long-range spin-mass couplings, including the use of spin-exchange-relaxation free (SERF) comagnetometers [57, 83, 84], ^{3}He/^{129}Xe free-precession comagnetometers [85], and liquid state nuclear-spin comagnetometers [86]. However, there are experimental challenges to applying each of these alternative approaches to a search for long-range spin-mass couplings. For example, it is potentially difficult to distinguish the coupling of spins to the local gravitational field from other lab-fixed backgrounds with a SERF comagnetometer [83], and magnetic field gradients may be an issue for liquid state nuclear-spin comagnetometers [86].

These same techniques can also be applied to search for long-range anomalous spin-spin interactions using polarized electrons in the Earth [87].

Acknowledgements. The authors are grateful to Dmitry Budker, Brian Patton, Szymon Pustelny, and Micah Ledbetter for invaluable discussions. Important early contributions to the experiment were made by Khoa Nguyen, L. Rene Jacome, Eric Bahr, Srikanth Guttikonda, Delyana Delcheva, and Lok Fai Chan. We are indebted to Mohammad Ali for technical work on several parts of the apparatus. This work was supported by the National Science Foundation under grants PHY-0652824 and PHY-0969666. Any opinions, findings and conclusions or recommendations expressed in this material are those of the authors and do not necessarily reflect those of the National Science Foundation.

References

[1] W.-T. Ni, Rep. Prog. Phys. **73**, 056901 (2010).
[2] I. Y. Kobzarev and L. B. Okun, Zh. Eksp. Teor. Fiz. **43**, 1904 (1962); Sov. Phys. JETP **16**, 1343 (1963).
[3] J. Leitner and S. Okubo, Phys. Rev. **136**(5B), 1542-6 (1964).
[4] F. W. Hehl and W.-T. Ni, Phys. Rev. D **42**, 2045 (1990).
[5] I. B. Khriplovich and A. A. Pomeransky, J. Exp. Theor. Phys. **86**, 839 (1998); Zh. Eksp. Teor. Fiz. **113**, 1537 (1998).
[6] A. J. Silenko and O. V. Teryaev, Phys. Rev. D **71**, 064016 (2005).
[7] F. W. Hehl, P. von der Heyde, G. D. Kerlick, and J. M. Nester, Rev. Mod. Phys. **48**, 393 (1976).
[8] I. L. Shapiro, Phys. Rep. **357**, 113 (2002).
[9] R. T. Hammond, Rep. Prog. Phys. **65**, 599 (2002).
[10] V. Alan Kostelecky, Neil Russell, and Jay D. Tasson, Phys. Rev. Lett. **100**, 111102 (2008).
[11] D. E. Neville, Phys. Rev. D **21**, 2075 (1980).
[12] D. E. Neville, Phys. Rev. D **25**(2), 573 (1982).
[13] S. M. Carroll and G. B. Field, Phys. Rev. D **50**(6), 3867 (1994).
[14] S. Ferrara, J. Scherk, and B. Zumino, Nucl. Phys. B **121**, 393 (1977).
[15] D. Atwood, C. P. Burgess, E. Filotas, F. Leblond, D. London, and I. Maksymyk, Phys. Rev. D **63**, 025007 (2000).
[16] D. Sudarsky, L. Urrutia, and H. Vucetich, Phys. Rev. Lett. **89**(23), 231301 (2002).
[17] T. Goldman, R. J. Hughes, and M. M. Nieto, Phys. Lett. B **171**, 217 (1986); T. Goldman, R. J. Hughes, and M. M. Nieto, Phys. Rev. D **36**, 1254 (1987); M. M. Nieto, T. Goldman, and R. J. Hughes, Phys. Rev. D **36** 3688 (1987); M. M. Nieto, T. Goldman, and R. J. Hughes, Phys. Rev. D **36** 3694 (1987); M. E. Ander, T. Goldman, R. J. Hughes, and M. M. Nieto, Phys. Rev. Lett. **60**, 1225 (1988).
[18] B. Ratra and P. J. E. Peebles, Phys. Rev. D **37**, 3406 (1988).
[19] C. Wetterich, Nucl. Phys. B **302**, 668 (1988).
[20] R. R. Caldwell, R. Dave, and P. J. Steinhardt, Phys. Rev. Lett. **80**, 1582 (1998).
[21] V. Flambaum, S. Lambert and M. Pospelov, Phys. Rev. D **80**, 105021 (2009).
[22] S. Mohanty, A. R. Prasanna, and G. Lambiase, Phys. Rev. Lett. **96**, 071302 (2006).
[23] T. A. Morgan and A. Peres, Phys. Rev. Lett. **9**(2), 79–80 (1962).
[24] I. Yu Kobzarev and L. B. Okun, Sov. Phys. JETP **16**, 1343 (1963).
[25] N. D. Hari Dass, Phys. Rev. Lett. **36**(8), 393-5 (1976).
[26] A. Peres, Phys. Rev. D **18**(8), 2739-40 (1978).
[27] K. I. MacRae and R. J. Riegert, Nuclear Physics B **244**, 513-22 (1984).
[28] B. Mukhopadhyaya and S. Sengupta, Phys. Lett. B **458**, 8-12 (1999).
[29] B. Mashhoon, Class. Quantum Grav. **17**, 2399–2409 (2000).
[30] G. Papini, Phys. Rev. D **65**(7), 077901 (2002).
[31] B. J. Venema, P. K. Majumder, S. K. Lamoreaux, B. R. Heckel, and E. N. Fortson, Phys. Rev. Lett. **68**, 135 (1992).
[32] B. R. Heckel, E. G. Adelberger, C. E. Cramer, T. S. Cook, S. Schlamminger, and U. Schmidt, Phys. Rev. D **78**, 092006 (2008).
[33] A. N. Youdin, D. Krause, Jr, K. Jagannathan, L. R. Hunter, and S. K. Lamoreaux, Phys. Rev. Lett. **77**, 2170 (1996).
[34] D. J. Wineland, J. J. Bollinger, D. J. Heinzen, W. M. Itano, and M. G. Raizen, Phys. Rev. Lett. **67**, 1735 (1991).
[35] G. Raffelt, Phys. Rev. D **86** 015001 (2012).
[36] J. E. Moody and F. Wilczek, Phys. Rev. D **30**, 130 (1984).
[37] B. A. Dobrescu and I. Mocioiu, J. High Energy Phys. **11**, 5 (2006).
[38] H. T. Janka, W. Keil, G. Raffelt, and D. Seckel, Phys. Rev. Lett. **76**, 2621 (1996).
[39] C. Hanhart, D. R. Phillips, and S. Reddy, Phys. Lett. B **499**, 9 (2001).
[40] J. Isern, E. García-Berro, S. Torres, and S. Catalán, Astrophys. J. **682**, L109 (2008); J. Isern, L. Althaus, S. Catalán, A. Córsico, E. García-Berro, M. Salaris, and S. Torres, arXiv:1204.3565.
[41] J. Isern, E. García-Berro, L. G. Althaus, and A. H. Corsico, Astron. Astrophys. **512**, A86 (2010); A. H. Córsico et al., arXiv:1205.6180.
[42] M. V. Balabas, T. Karaulanov, M. P. Ledbetter, and D. Budker, Phys. Rev. Lett. **105**, 070801 (2010).
[43] D. F. Jackson Kimball, L. R. Jacome, S. Guttikonda, E. J. Bahr, and L. F. Chan, J. Appl. Phys. **106**, 063113 (2009).
[44] D. Budker, W. Gawlik, D. F. Kimball, S. M. Rochester, V. V. Yashchuk, and A. Weiss, Rev. Mod. Phys. **74**, 1153 (2002).
[45] E. B. Alexandrov, M. Auzinsh, D. Budker, D. F. Kimball, S. M. Rochester, and V. V. Yashchuk, J. Opt. Soc. Am. B **22**, 7 (2005).
[46] D. Budker, V. Yashchuk, and M. Zolotorev, Phys. Rev. Lett. **81**, 5788, (1998).
[47] D. Budker, D. F. Kimball, S. M. Rochester, V. V. Yashchuk, and M. Zolotorev, Phys. Rev. A **62**, 043403 (2000).
[48] D. Budker, D. F. Kimball, S. M. Rochester, and V. V. Yashchuk, Phys. Rev. Lett. **85**, 2088 (2000).
[49] P. F. A. Klinkenberg, Rev. Mod. Phys. **24**, 63 (1952).
[50] S. Pustelny, D. F. Jackson Kimball, S. M. Rochester, V. V. Yashchuk, D. Budker, Phys. Rev. A **74**, 063406 (2006).
[51] S. Xu, S. M. Rochester, V. V. Yashchuk, M. H. Donaldson, and D. Budker, Rev. Sci. Instrum. **77**, 083106 (2006).
[52] K. L. Corwin, Z.-T. Lu, C. F. Hand, R. J. Epstain, and C. E. Wieman, Appl. Opt. **37**, 3295 (1998).
[53] V. V. Yashchuk, D. Budker, and J. Davis, Rev. Sci. Instrum. **71**, 341 (2000).

[54] D. Budker, D. F. Kimball, V. V. Yashchuk, and M. Zolotorev, Phys. Rev. A **65**, 055403 (2002).
[55] V. V. Yashchuk, D. Budker, W. Gawlik, D. F. Kimball, Yu. P. Malakyan, and S. M. Rochester, Phys. Rev. Lett. **90**, 253001 (2003).
[56] S. Pustelny, D. F. Jackson Kimball, S. M. Rochester, V. V. Yashchuk, W. Gawlik, and D. Budker, Phys. Rev. A **73**, 023817 (2006).
[57] M. Smiciklas, J. M. Brown, L. W. Cheuk, S. J. Smullin, and M. V. Romalis, Phys. Rev. Lett. **107**, 171604 (2011).
[58] M. Auzinsh, D. Budker, D. F. Kimball, S. M. Rochester, J. E. Stalnaker, A. O. Sushkov, and V. V. Yashchuk, Phys. Rev. Lett. **93**, 173002 (2004).
[59] D. Budker and M. V. Romalis, Nature Physics **3**, 227 (2007).
[60] D. Budker and D. F. Jackson Kimball, eds., Optical Magnetometry (Cambridge University Press, Cambridge, 2013).
[61] J. Nenonen, J. Montonen, and T. Katila, Rev. Sci. Instrum. **67**, 2397 (1996).
[62] S. K. Lamoreaux, Phys. Rev. A **60**, 1717 (1999).
[63] I. K. Kominis, T. W. Kornack, J. C. Allred, and M. V. Romalis, Nature **422**, 596 (2003).
[64] T. W. Kornack, S. J. Smullin, S.-K. Lee, M. V. Romalis, Appl. Phys. Lett. **90**, 223501 (2007).
[65] E. B. Alexandrov, M. P. Chaika, and G. I. Khvostenko, Interference of Atomic States (Springer, Berlin, 1993).
[66] M. Auzinsh, D. Budker, and S. Rochester, Optically Polarized Atoms: Understanding Light-Atom Interactions (Oxford University Press, Oxford, 2010).
[67] E. Arimondo, M. Inguscio, and P. Violino, Rev. Mod. Phys. **49**, 31 (1977).
[68] V. Acosta, M. P. Ledbetter, S. M. Rochester, D. Budker, D. F. Jackson Kimball, D. C. Hovde, W. Gawlik, S. Pustelny, and J. Zachorowski, Phys. Rev. A **73**, 053404 (2006).
[69] V. M. Acosta, M. Auzinsh, W. Gawlik, P. Grisins, J. M. Higbie, Derek F. Jackson Kimball, L. Krzemien, M. P. Ledbetter, S. Pustelny, S. M. Rochester, V. V. Yashchuk, and D. Budker, Optics Express **16**, 11423 (2008).
[70] K. Jensen, V. M. Acosta, J. M. Higbie, M. P. Ledbetter, S. M. Rochester, and D. Budker, Phys. Rev. A **79**, 023406 (2009).
[71] S. Pustelny, M. Koczwara, L. Cincio, and W. Gawlik, Phys. Rev. A **83**, 043832 (2011).
[72] I. I. Sobelman, Atomic spectra and radiative transitions (Springer-Verlag, Berlin, 1992).
[73] J. E. Stalnaker, D. Budker, S. J. Freedman, J. S. Guzman, S. M. Rochester, and V. V. Yashchuk, Phys. Rev. A **73**, 043416 (2006).
[74] W. Happer and B. S. Mathur, Phys. Rev. **163**, 12 (1967).
[75] B. S. Mathur, M. Tang, and W. Happer, Phys. Rev. **171**, 11 (1968).
[76] C. Cohen-Tannoudji and J. Dupont-Roc, Phys. Rev. A **5**, 968 (1972).
[77] M. V. Romalis and E. N. Fortson, Phys. Rev. A **59**, 4547 (1999).
[78] C. Y. Park, J. Y. Kim, J. M. Song, and D. Cho, Phys. Rev. A **65**, 033410 (2002).
[79] S. Haroche and C. Cohen-Tannoudji, Phys. Rev. Lett. **24**, 974 (1970).
[80] W. Happer and H. Tang, Phys. Rev. Lett. **31**, 273 (1973).
[81] M. Berry, Proc. R. Soc. London, Ser. A **392**, 45 (1984).
[82] J. M. Pendlebury, W. Heil, Yu. Sobolev, P. G. Harris, J. D. Richardson, R. J. Baskin, D. D. Doyle, P. Geltenbort, K. Green, M. G. D. van der Grinten, P. S. Iaydjiev, S. N. Ivanov, D. J. R. May, and K. F. Smith, Phys. Rev. A **70**, 032102 (2004).
[83] T. W. Kornack and M. V. Romalis, Phys. Rev. Lett. **89**, 253002 (2002).
[84] J. M. Brown, S. J. Smullin, T. W. Kornack, and M. V. Romalis, Phys. Rev. Lett. **105**, 151604 (2010).
[85] C. Gemmel et al., Phys. Rev. D **82**, 111901(R) (2010).
[86] M. Ledbetter, S. Pustelny, D. Budker, M. Romalis, J. Blanchard, and A. Pines, Phys. Rev. Lett. **108**, 243001 (2012).
[87] L. Hunter, J. Gordon, S. Peck, D. Ang, J.-F. Lin, Science **339**, 928 (2013).

www.ann-phys.org

adp

annalen der physik

WILEY-VCH

WILEY ONLINE LIBRARY

Early View publication on wileyonlinelibrary.com
(issue and page numbers not yet assigned;
citable using Digital Object Identifier – DOI)

Ann. Phys. (Berlin), 1–9 (2013) / DOI 10.1002/andp.201300039

annalen der physik

Original Paper

Mass measurements of singly and highly charged radioactive ions at TITAN: A new Q_{EC}-value measurement of ^{10}C

Anna A. Kwiatkowski[1,], Ankur Chaudhuri[1], Usman Chowdhury[1,2], Aaron T. Gallant[1,3], Tegan D. Macdonald[1,3], Bradley E. Schultz[1], Martin C. Simon[1], and Jens Dilling[1,3]*

Received 1 March 2013, revised 27 March 2013, accepted 11 April 2013
Published online 3 May 2013

Superallowed β-decay strengths or corrected $\mathcal{F}t$ values provide some of the most stringent limits for physics beyond the standard three-quark model. For this reason, the Q_{EC}-value ^{10}C has been measured and found to be 3468.31(51) keV with the TITAN Penning trap mass spectrometer. The facility is unique in coupling such an online spectrometer to a charge breeder, permitting a mass measurement of another superallowed β-emitter, ^{74}Rb, in the 8+ charge state. An overview of the TITAN facility and recent highlights are presented alongside the new Q_{EC}-value determination of ^{10}C.

1 Introduction

Measurements of the atomic mass, by way of the atomic binding energy, yield invaluable insight into the underlying nuclear structure, which in turn affects our understanding of nucleosynthesis, neutrino physics, and the standard model. Comparisons of measured and predicted mass values of neutron-rich calcium isotopes have showcased the role of three-body forces. Precise and accurate Q-value measurements for double β decay refine the search for neutrinoless double β decays. Among the most exacting limits on physics beyond the standard model have been achieved by studies of superallowed β decay.

The superallowed transition is attractive as its strength, or ft value, is nearly independent of nuclear-structure ambiguities and relies solely on the vector part of the weak interaction. Studies of superallowed β decay spanning several decades [1] have improved the up-down quark mixing element of the Cabbibo-Kobayashi-Maskawa (CKM) matrix V_{ud}, have provided the most stringent confirmation of the conserved vector current (CVC) hypothesis, have contributed to the most exacting test of the unitarity of the CKM matrix, and have reduced the limit on scalar currents. If the CVC hypothesis is correct, then the vector coupling constant G_V and therefore the "corrected" $\mathcal{F}t$ values should be identical. (The relation between G_V and the experimental ft requires radiative and isospin-symmetry-breaking corrections; see [1] for a detailed description.) If the maximum positron energy in the decay is Q, then the phase space factor is approximately proportional to Q^5, and the uncertainty δQ weighs five times more than any other parameter in the uncertainty of $\mathcal{F}t$ value. For this reason, a Penning trap Q_{EC}-value determination of ^{10}C was performed at TRIUMF's Ion Trap for Atomic and Nuclear science (TITAN) [2].

Penning trap mass spectrometry (PTMS) has become the leading technique for accurate and precise mass values [3]. It relies on the determination of the cyclotron frequency, from which the mass can easily be extracted. The technique is being advanced at TITAN with measurements on radionuclides with half lives as low as 9 ms [4] and on highly charged radioactive ions [5]. The latter can improve the precision, permit less beam time requirements [6], and improve the separation of isobars and low-lying isomers [7]. Fast measurement cycles and the use of highly charged ions (HCI) have allowed us to perform measurements despite the constraints due to short half lives and low yields. In this article, we present an overview of the TITAN facility and recent highlights including the new Q_{EC}-value determination of ^{10}C.

* Corresponding author E-mail: aniak@triumf.ca
[1] TRIUMF, 4004 Wesbrook Mall, Vancouver BC V6T 2A3, Canada
[2] Department of Physics and Astronomy, University of Manitoba, Winnipeg MB R3T 2N2, Canada
[3] Department of Physics and Astronomy, University of British Columbia, Vancouver BC, V6T 1Z1, Canada

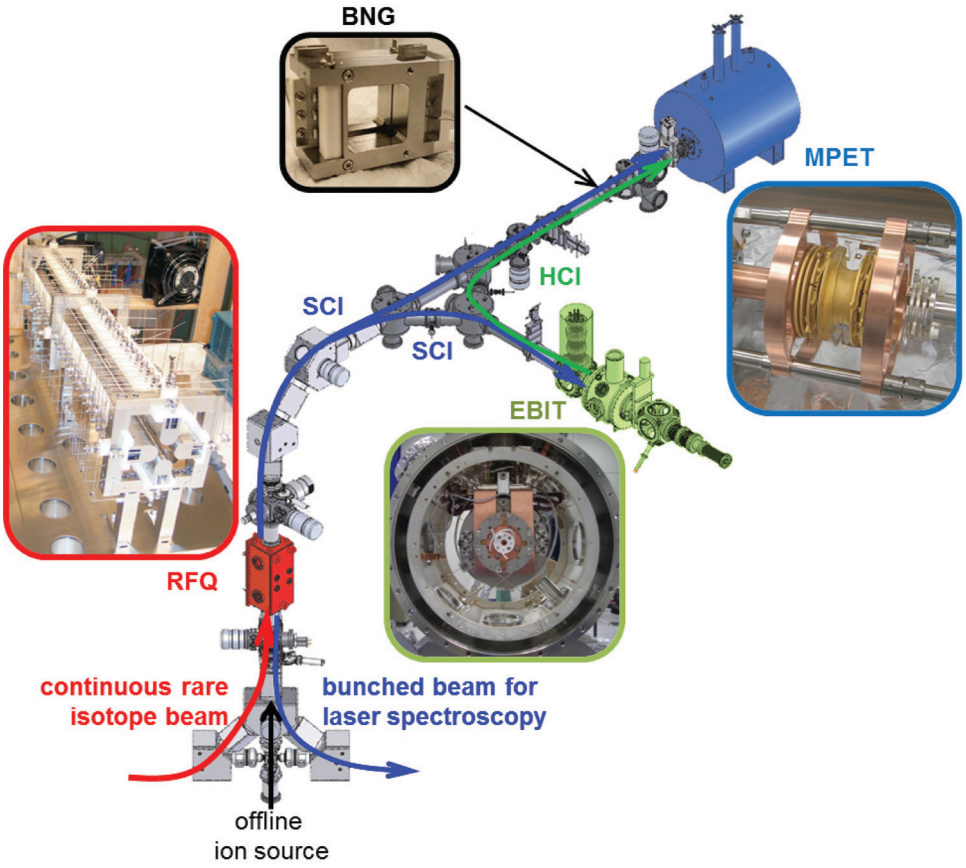

Figure 1 A schematic of the TITAN facility. The principle components are the radiofrequency quadrupole (RFQ) beam cooler and buncher, the electron beam ion trap (EBIT), the Bradbury-Nielsen gate (BNG), and the measurement Penning trap (MPET). The blue arrow indicates the path of singly charged ion (SCI) bunches. Reverse extraction from the RFQ directs cooled ion bunches to the collinear laser spectroscopy experiment. Forward extraction sends them to either the MPET for mass measurement or the EBIT for charge breeding. The green arrow indicates the path of highly charged ion (HCI) bunches.

2 The TITAN facility

TITAN is situated at TRIUMF's Isotope Separator and ACcelerator (ISAC) rare isotope production facility [8]. Radioactive ions are created by bombarding a thick ISOL target with 500-MeV protons at currents up to 100 μA. The radioisotopes diffuse out of the target and are ionized by surface ionization, FEBIAD [9], or TRIUMF's resonant ionization laser ion source (TRILIS) [10, 11]. A mass-separating magnet system (resolving power $\approx$2500) is used to eliminate any non-isobaric contaminants. The 20-keV beam is then transported to the TITAN experiment. Figure 1 shows a schematic of the TITAN beamline and the four principle components: the radiofrequency quadrupole (RFQ) beam cooler and buncher, the electron beam ion trap (EBIT), the Bradbury-Nielsen gate (BNG), and the measurement Penning trap (MPET). Each piece can be operated as a stand alone unit and optimized with an offline ion source.

2.1 The RFQ beam cooler and buncher

The TITAN RFQ [12, 13] accumulates, cools, and bunches the beam in a single-stage linear Paul trap filled with H_2 or He buffer gas. Accumulation is achieved by segmentation of the trapping structure in the axial direction to apply an appropriate DC gradient, and cooling is realized through collisions with the neutral buffer gas. The transverse RF field radially confines the ions for the duration of the trapping.

Two features are unique compared to beam cooler and bunchers at similar facilities like ISOLTRAP [14], JYFLTRAP [15], SHIPTRAP [16], and LEBIT [17]: its

digital RF driver and symmetric extraction capability. Ion trajectories are stable for certain combinations of RF frequency and amplitude given the RFQ's physical dimensions and the ion's mass-to-charge ratio m/q, which can vary by a factor of 30 at TITAN (from Li to Fr). Higher amplitudes increase the space charge limit and thus the ISAC beam acceptance (design limit 50π mm mrad transverse emittance). Consequently, the RF driver approach is to pair up and down MOSFET switches to generate a square wave for high RF amplitudes ($\leq$ 400 V_{pp}) over a broad frequency range, 0.2-1.2 MHz. The TITAN RFQ allows forward and reverse extraction. In the reverse extraction, the bunches are extracted from the injection side of the RFQ and directed to the collinear laser spectroscopy experiment [18]. In the forward direction, the bunched ions are transported at a variable energy, typically 2 keV, and delivered to subsequent ion traps, either the Penning trap or the EBIT for charge breeding prior to the mass measurement.

2.2 The electron beam ion trap

The TITAN EBIT [19, 20] was designed and built in collaboration with the Max-Planck-Institut für Kernphysik (MPI-K) for fast, efficient, and universal charge breeding. The positive ions are radially confined by the space charge of a high-current electron beam compressed by a strong magnetic field generated by a pair of superconducting Helmholtz coils. With field strengths as high as 6 T, the magnetic field also provides additional radial confinement of the highly charged ions (HCI). The potential applied to the trap electrodes axially traps the ions. Successive electron impact ionization produces higher charge states while the electron beam energy defines the maximum charge state achievable, which is Z dependent. The primary advantages of an EBIT over other charge breeders are the high charge states achievable and the narrow charge state distribution. The charge state distribution can be adjusted with an appropriate choice of electron beam energy and density to preferentially populate the desired charge state. The highest charge state created thus far at TITAN has been 33+ with ^{124}Cs and for a radioactive mass measurement 22+ with ^{71}Ge [21]. The design specifications of the TITAN EBIT can be found in Table 1.

The initial motivation to use HCI in Penning trap mass spectrometry (PTMS) was to boost the precision since $\delta m/m$ scales inversely with the charge state. This was demonstrated first in the mass measurement of $^{74}Rb^{8+}$ [5], as will be described below in more detail. Further experiments have been performed to investigate gains in beam purity. The separation of isobars and low-lying isomers with the ion of interest increases with the charge state, leading to better resolution in the Penning trap. A proof-of-principle experiment was performed to separate the 111-keV isomer in ^{78}Rb from its ground state [7], and the measured energy difference was found to be in agreement with earlier measurements. Another advance with HCI is threshold charge breeding for isobaric separation. The method was developed for the Q_{EC}-value measurement of ^{71}Ge [22], for which it was used in combination with TRILIS. Since a strong Ge beam required resonant laser ionization, the ISAC beam composition could be either a mono-isotopic beam of $^{71}Ga^{+}$ or a mixed beam of $^{71}Ga^{+}/^{71}Ge^{+}$ by blocking or not blocking the lasers respectively. The electron beam energy was tuned below the ionization potential of the Ne-like charge states $^{71}Ga^{21+}$ and $^{71}Ge^{22+}$; hence, the $^{71}Ga^{22+}$ and $^{71}Ge^{23+}$ states could not be produced. The time-of-flight mass filter (sec. 2.3) was adjusted to select the 21+ charge state when the lasers were blocked and the 22+ charge state when the lasers were not. As a result, mono-isotopic and mono-isoelectronic ion bunches were captured in MPET, allowing a clean determination of the Q_{EC}-value. Our result determined unambiguously that the Q_{EC}-value cannot be the source of the calibration discrepancy [23] observed in the measured-to-predicted event rate ratios at the solar neutrino experiments SAGE [24, 25] and GALLEX [26–28].

Table 1 TITAN EBIT maximum design specifications.

Parameter	Design Limit
Magnetic field	$\leq$6 T
Electron beam energy	$\leq$70 keV
Electron beam current	$\leq$5 A
Estimated max current density	$\sim 10^4$ A/cm^2

2.3 m/q Selection

Contaminants always pose a challenge at online facilities operating with a moderate resolution separator. A Bradbury-Nielsen gate (BNG) [29] was installed immediately upstream of the Penning trap. The desired m/q is selected by its time of flight (TOF) from either the RFQ or the EBIT. A BNG places two sets of evenly spaced wires parallel to each other. Equal but opposite polarity voltages are applied to each set of wires, deflecting ions with undesired m/q ratios. When the ions with the desired

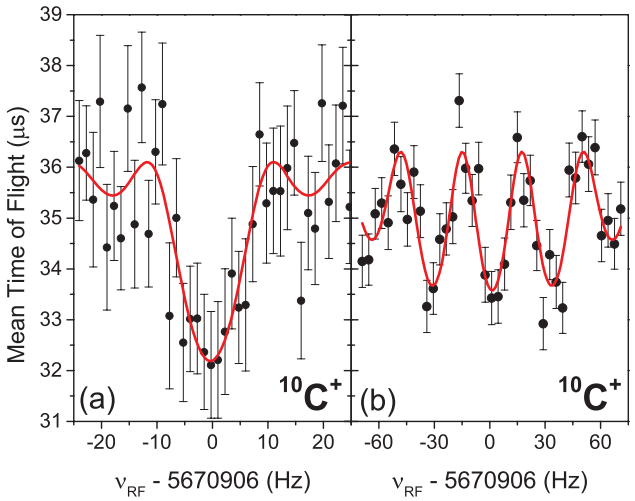

Figure 2 Resonances of $^{10}C^+$, in which the average time of flight is plotted for the excitation frequency ν_{RF}. (a) The conventional excitation scheme was used, in which the RF is applied continuously over the excitation time, here $T_{RF} = 76$ ms. (b) A Ramsey excitation scheme of 8-21-8 ms was implemented, where two 8-ms pulses of RF are separated in time by 21 ms. The solid curves are fits of the theoretical line shape [34, 36] to the data. The center of the resonance occurs at the cyclotron frequency, $2\pi\nu_c = q/m \cdot B$, from which the mass of an ion can easily be extracted.

m/q approach, all wires are placed on ground, allowing the ions to reach MPET.

2.4 The measurement Penning trap

The TITAN measurement Penning trap (MPET) [30, 31] consists of a pair of hyperbolic end caps and a hyperbolic ring electrode. The potential difference across these electrodes creates a weak electrostatic quadrupole field for axial confinement while a strong 3.7 T superconducting solenoidal magnetic field provides radial confinement. PTMS relies on the determination of the cyclotron frequency $2\pi\nu_c = q/m \cdot B$, where B is the magnetic field strength. At TITAN the time-of-flight ion-cyclotron-resonance (TOF-ICR) method [32, 33] has been adopted to accommodate the short half-lives of the radioactive ions. Ions are trapped, driven continuously at an RF frequency ν_{RF} near ν_c for the duration T_{RF}, and extracted from MPET. Their TOF to an MCP detector outside the magnetic field is recorded as a function of ν_{RF}. When $\nu_{RF} = \nu_c$, the ions experience a dramatic increase in energy, which can be observed as a decrease in the TOF. A typical resonance is shown in Fig. 2a. The width of the resonance $\Delta\nu_{FWHM}$ depends solely on T_{RF} [33] and is independent of q/m or B. The statistical uncertainty can be reduced by a factor of 2-3 by using the Ramsey method of separated RF fields [34, 35], in which the excitation is applied as two pulses separated by a waiting period. A resonance of $^{10}C^+$ excited with a Ramsey scheme is shown in Fig. 2b, where two 8-ms RF pulses were separated by a 21-ms waiting period (denoted as 8-21-8 ms in this article).

The measurement precision [37] can be described by

$$\frac{\delta m}{m} = \frac{\kappa m}{qBT_{RF}\sqrt{N}} \tag{1}$$

where $\sqrt{N}$ is a statistical factor, T_{RF} is the excitation time, and κ is a setup-specific parameter close to 1. The charge state can be increased up to Z+ (i.e. a bare ion) with a possible enhancement in the precision by a factor up to Z. Unfortunately, the remaining variables offer perhaps 2-3 times improved precision and are limited by other factors: The statistical factor is limited by the yield of the radionuclide and the length of beam time. The magnetic field must meet strict requirements for uniformity in the trapping region. And, the excitation time cannot greatly exceed the radionuclide's half life. At present, typical precisions of TITAN mass measurements are $\sim 10^{-8}$ for HCI and SCI, but can reach as low as 10^{-9}.

To extract the mass from the cyclotron frequency requires precise calibration of the magnetic field. Cyclotron frequency measurements of the radioactive ion is interleaved with those of a stable ion with a well known mass. Therefore, the primary experimental result is the ratio of their cyclotron frequencies, which can be related to their masses by

$$R = \frac{\nu_{c,ref}}{\nu_c} \cdot \frac{q}{q_{ref}} = \frac{m}{m_{ref}} \tag{2}$$

where the subscript *ref* refers to the reference ion. Typically, the reference ion is chosen to have its mass number and charge state as close to (if not the same) as the radioactive ion to minimize sources of systematic uncertainty.

3 Results and discussion

3.1 New Q_{EC}-value determination of the superallowed β-emitter ^{10}C

The $^{10}C^+$ and $^{10}B^+$ ions were produced by bombarding a NiO target with 500-MeV protons ($i = 20$ μA). The

$^{10}C^+/^{10}B^+$ ratio was roughly 1:20. The ions were cooled with He buffer gas and bunched in the RFQ, and then they were sent directly to MPET as SCI. Prior to the cyclotron frequency determination, dipole cleaning [38] was applied to remove one species from MPET since simultaneous storage of ions may cause a shift in the measured frequency [39]. Resonances were taken with conventional (single RF pulse) excitation ($T_{RF} = 27$, 37, 76 ms) and Ramsey excitation (8-21-8 ms) schemes. Typical resonances are shown in Fig. 2.

The cyclotron frequency ratio was determined to be 0.999 608 973(55). Relativistic and mass-dependent effects canceled as both ion species had the same A/q and experienced the same electric and magnetic forces. The drift in the magnetic field was monitored, and nonlinear temporal field changes were negligible (0.04 ppb/h [31]) compared to the statistical uncertainty since $^{10}B^+$ measurements were typically separated by $\leq$40 minutes. Two steps were taken to account for the effects of ion-ion interactions [39]. First, we only considered ion bunches with one detected ion although the average detection rate was 1/bunch for $^{10}B^+$ and 0.05/bunch for $^{10}C^+$. Second, to be conservative, we performed a so-called count class analysis [40] for $^{10}B^+$; however, statistics were too low for $^{10}C^+$ to do a count class analysis. Instead, we compared the cyclotron frequency determined with one detected $^{10}C^+$ per bunch to that with all detected ions per bunch. The difference in the ratios was added in quadrature to the statistical uncertainty.

The cyclotron frequency ratio of $^{10}B^+$ to $^{10}C^+$ can be related to the Q_{EC}-value:

$$Q_{EC} = (R-1)(M_B - m_e) \tag{3}$$

where the subscript B refers to the daughter $^{10}B^+$ and m_e is the electron mass. In eq. (3), we have used that both ions are singly charged and neglected the difference in electron binding energies ($\approx$3 eV [41]). We find $Q_{EC} = 3648.34(51)$ keV. As can be seen in Table 2, our value agrees within 1σ with the two most recent measurements [42, 43], upon which the Atomic Mass Evaluation 2012 (AME12) is based [44].

The slight increase in the ^{10}C Q_{EC}-value by the Penning trap mass measurements compared to earlier reactions data [1, 44] resurrects the possibility of scalar currents [43] by raising the ^{10}C $\mathcal{F}t$ value just outside the error bars from the average of all other $\mathcal{F}t$ values. However, as the uncertainty in its $\mathcal{F}t$ value is dominated by the uncertainty in the branching ratio [1], an improved measurement in the ^{10}C branching ratio is required as well as a higher ^{14}O $\mathcal{F}t$ value to confirm the presence of scalar currents.

Table 2 A comparison of Q_{EC}-value measurements of ^{10}C. Note that the authors of AME12 [44] increased the central value in ref. [42] by 10 eV and inflated its error to 0.70 keV in their evaluation although the original values are tabulated.

Method	Q_{EC} (keV)	Ref.
$^{10}C(p,n)^{10}B$	3647.95(12)	[42]
Penning trap	3648.12(8)	[43]
AME12	3648.064(69)	[44]
Penning trap	3648.34(51)	this work

3.2 Use of HCI for Q_{EC}-value determinations of superallowed β emitters

While low-Z superallowed β-emitters are more sensitive to the presence of scalar currents (if they exist), those with high Z allow one to better distinguish between conflicting nuclear models since the isospin-symmetry-breaking correction δ_C scales as Z^2. The heaviest of all superallowed β emitters is ^{74}Rb, whose mass was measured at TITAN [5]. By charge breeding to the 8+ charge state and using the Ramsey excitation scheme, TITAN achieved a comparable precision ($\delta m/m = 10^{-7}$) to ISOLTRAP in less than half the time. With the weighted average of the TITAN and ISOLTRAP mass values, the uncertainties of the Q_{EC}-value and δ_C now contribute roughly the same weight to the uncertainty of the $\mathcal{F}t$. Further reductions in ^{74}Rb δQ could be made by measuring the Q_{EC}-value directly, as was done for ^{10}C, and to charge breed to higher charge states, for example to $\approx$27+.

Generally speaking the advent of PTMS has substantially improved our knowledge of superallowed β decay with its superior accuracy and precision compared to the earlier charge exchange measurements. As reaction-based experiments are susceptible to different sources of systematic error, our confidence is increased for cases of agreement between them and PTMS. On the other hand, the consistent disagreement of a series of reaction-type measurements [45] led to their rejection in the most recent survey of superallowed β emitters (see [1] and the detailed discussion therein). The increasing precision of the Penning-trap results has matched and now often surpasses that of reaction-based measurements. Over the past decade, PTMS has played a crucial role in reducing the uncertainty of $\mathcal{F}t$ values, and yet gains can still be made.

Fast beam preparation, purity of trapped ions, and T_{RF} play crucial roles in reducing δQ. As demonstrated

for ^{74}Rb, HCI can permit the same achievable precision with shorter T_{RF} or less ions than SCI. This offers a distinct advantage for superallowed β emitters close to the driplines which usually suffer poor production rates and/or short half lives. In addition to increasing the separation of isobaric and isomeric contamination from the ion of interest, charge breeding breaks up molecular ions in the EBIT; simultaneously trapped contaminant ions may shift the measured cyclotron frequency [39]. Since charge breeding can be performed in a few milliseconds, even the shortest-lived superallowed β emitters can be charge bred: ^{74}Rb ($T_{1/2} = 65$ ms), ^{70}Br ($T_{1/2} = 79$ ms), and ^{66}As ($T_{1/2} = 96$ ms). The additional time does not necessarily lengthen the total beam preparation time substantially. It should be noted that the advantages offered by HCI can be tempered by efficiency losses due to the charge breeding process [6], e.g. non-unity breeding into the desired charge state and decay losses. The $q\sqrt{N}$ dependence in eq. (1) dictates that these losses must be less than a factor of q^2 for charge breeding to be favorable. Nonetheless as the first PTMS experiment with radioactive HCI, the ^{74}Rb mass measurement opened the door to this previously unexplored opportunity.

3.3 Investigations of the *r*-process near $A \approx 100$

Medium- to heavy-mass nuclides approaching the limits of nuclear existence typically suffer low production rates, making them more difficult to be studied. Unfortunately, these very nuclides are often expected to take part in the rapid neutron capture (*r*-) process if close to the neutron dripline or in the rapid proton capture (*rp*-) process if close to the proton dripline [46, 47]. These processes are believed to be responsible for the production of elements heavier than iron and may occur in core collapse supernova explosions and X-ray bursts respectively. Mass measurements assist in determining the energetically allowed pathways. Neutron-rich Rb isotopes around $A = 100$ lie along the *r*-process path [48], and their mass uncertainties were of order 10-100 keV or simply unknown [49]. By charge breeding $^{94,97-98}$Rb isotopes and neighboring $^{94,97-99}$Sr isotopes to the 15+ charge state, TITAN determined their masses with uncertainties less than 4 keV and deviations up to 11σ from the accepted values, which were mostly determined with β-endpoint energies. A global mass evaluation in the region was performed and used to predict the final abundances in a parameterized fully dynamic *r*-process model based on [50], which includes high-entropy winds. The small TITAN mass uncertainties eliminated fluctuations in the predicted final abundances for $A = 90$-100. Mainly due to the large deviations, our measurements significantly changed the composition and affected abundances as light as $A = 70$. Our calculation also shifts the *r*-process path toward more neutron-rich nuclei.

The TITAN mass values and other mass measurements from ISOLTRAP [51, 52] and JYFLTRAP [53–55] form a consistent map of the mass surface of nuclides near $A = 100$ and far from the valley of stability. The unusual topography illuminates the nuclear shape transition from $N = 59$ to $N = 61$. The strong deformation of the ground state extends from Kr to Tc ($Z = 36$-43).

3.4 Understanding the role of three-body forces in neutron-rich K and Ca isotopes

Deformation and other interesting nuclear structure can be revealed by unusual features in the mass surface. Among exotic nuclides, expected magic numbers may disappear and new ones may appear [56], such as those expected at $N = 32$, 34 in neutron-rich Ca isotopes [57]. TITAN scientists pursued mass measurements of neutron-rich K and Ca isotopes in order to verify this prediction [58, 59]. Our values revealed several deviations with accepted values [49], as much as 10σ for ^{49}K and as large as 1.7 MeV for ^{52}Ca. Consequently the $N = 28$ shell gap (as measured by the three-point binding energy difference) is 1 MeV stronger than previously believed [58]. The measured slope of the two-neutron separation energy flattened dramatically for $N = 30$-32.

Ca isotopes are particularly useful to theorists, possessing two doubly magic stable isotopes, which act as calibrations of theoretical predictions, serve as closed cores for construction of nuclear-shell-model wavefunctions, and provide benchmarks for predictions. Calculations were performed using chiral effective field theory with two approaches, the coupled-cluster method [60] and consistent calculations using many-body perturbation theory [59]. Both approaches required the inclusion of three-body forces to achieve good agreement with the experimental data.

4 Summary and outlook

All of the mass measurement campaigns we have described are being continued at TITAN. For neutron-rich Ca isotopes, we plan to measure strength of the predicted $N = 34$ subshell closure and to elucidate the role of three-body forces. An extension of mass measurements of neutron-rich Rb and Sr isotopes will not only aid

r-process predictions but also provide the first empirical values for $A \geq 100$ in Rb and $A \geq 103$ in Sr. Among the superallowed β emitters, we have newly measured the Q_{EC}-value of ^{10}C and confirmed the value determined at JYFLTRAP [43]. The slightly enhanced $\mathcal{F}t$ value hints at non-zero scalar currents, but confirmation requires a reduction in the branching ratio and a higher $\mathcal{F}t$ value in ^{14}O. We plan to measure the latter, which is the only superallowed β emitter not yet measured via PTMS. We also would like to reduce the uncertainties in the Q_{EC}-values of ^{66}As and ^{70}Br, whose uncertainties are prohibitively large to contribute meaningfully to a test of the CVC hypothesis. They are also well suited to distinguish between conflicting evaluations of δ_C due to their large Z like ^{74}Rb.

As demonstrated in the mass measurement of ^{74}Rb, the precision in PTMS can be improved by charge breeding the radionuclides. Systematic studies with HCI at the ppb level will be performed to establish the accuracy of the TITAN Penning trap mass spectrometer with HCI in the same manner as was done for SCI [31]. Confirmation of the accuracy of HCI at this level and improved vacuum (to avoid charge exchange of HCI with residual background) will clear the way for a new class of online mass measurements which, when combined with Ramsey excitation, may offer up to two orders of magnitude improved precision versus conventional SCI-TOF-ICR. This gain can be invaluable for tests of fundamental interactions, like the CVC hypothesis and the unitarity of the CKM matrix. For nuclear structure and astrophysics, the experimental precision with SCI suffices; nonetheless, highly charged radionuclides may reduce beam time requirements, permitting faster mass cartography or the same precision despite low production rates and very short half lives. Furthermore, the charge breeding process better separates low-lying isomers or nearby isobars from the ion of interest as shown for ^{78}Rb^{8+} and ^{71}Ge^{21+}. It can also be used to improve beam purity like with threshold charge breeding. TITAN has established the merit of PTMS with charge bred radionuclides, and future experiments with HCI are highly promising.

5 Acknowledgements

We thank the ISAC beam development and delivery groups for facilitating this experiment. We also thank C. Andreoiu, S. Ettenauer, K.G. Leach, A. Lennarz, M.R. Pearson, and V.V. Simon for their support and many fruitful discussions. This work has been supported by the Natural Sciences and Engineering Research Council (NSERC) of Canada and the National Research Council (NRC) of Canada through TRIUMF. A.T.G. acknowledges support from the NSERC CGS-D and T.D.M from NSERC CGS-M.

Key words. mass and binding energy, Penning trap, electroweak theory, nuclear structure.

References

[1] J. C. Hardy and I. Towner, Phys. Rev. C **79**(5), 055502 (2009).
[2] J. Dilling, P. Bricault, M. Smith, and H. J. Kluge, Nucl. Instrum. Meth. B **204**, 492–496 (2003).
[3] K. Blaum, J. Dilling, and W. Nörtershäuser, Phys. Scripta **T152**, 014017 (2013).
[4] M. Smith, M. Brodeur, T. Brunner, S. Ettenauer, A. Lapierre, R. Ringle, V. Ryjkov, F. Ames, P. Bricault, G. Drake, P. Delheij, D. Lunney, F. Sarazin, and J. Dilling, Phys. Rev. Lett. **101**(20), 202501 (2008).
[5] S. Ettenauer, M. C. Simon, A. T. Gallant, T. Brunner, U. Chowdhury, V. V. Simon, M. Brodeur, A. Chaudhuri, E. Mané, C. Andreoiu, G. Audi, J. R. Crespo López-Urrutia, P. Delheij, G. Gwinner, A. Lapierre, D. Lunney, M. R. Pearson, R. Ringle, J. Ullrich, and J. Dilling, Phys. Rev. Lett. **107**(27), 272501 (2011).
[6] M. C. Simon et al., Phys. Scripta accepted.
[7] A. Gallant, M. Brodeur, T. Brunner, U. Chowdhury, S. Ettenauer, V. Simon, E. Mané, M. Simon, C. Andreoiu, P. Delheij, G. Gwinner, M. Pearson, R. Ringle, and J. Dilling, Phys. Rev. C **85**(4), 044311 (2012).
[8] M. Dombsky, D. Bishop, P. Bricault, D. Dale, A. Hurst, K. Jayamanna, R. Keitel, M. Olivo, P. Schmor, and G. Stanford, Rev. Sci. Instrum. **71**(2), 978 (2000).
[9] P. G. Bricault, F. Ames, M. Dombsky, F. Labrecque, J. Lassen, A. Mjos, G. Minor, and A. Teigelhöfer, Rev. Sci. Instrum. **83**(2), 02A914 (2012).
[10] J. Lassen, P. Bricault, M. Dombsky, F. Izdebski, J. P. Lavoie, M. Gillner, T. Gottwald, F. Hellbusch, A. Teigelhöfer, A. Voss, and K. D. A. Wendt, AIP Conf. Proc. **1099**(1), 769–773 (2009).
[11] J. Lassen, P. Bricault, M. Dombsky, J. P. Lavoie, M. Gillner, T. Gottwald, F. Hellbusch, A. Teigelhöfer, A. Voss, and K. D. A. Wendt, AIP Conf. Proc. **1104**(1).
[12] M. Smith, L. Blomeley, P. Delheij, and J. Dilling, Hyperfine Interact. **173**(1-3), 171–180 (2006).
[13] T. Brunner, M. J. Smith, M. Brodeur, S. Ettenauer, A. T. Gallant, V. V. Simon, A. Chaudhuri, A. Lapierre, E. Mané, R. Ringle, M. C. Simon, J. A. Vaz, P. Delheij, M. Good, M. R. Pearson, and J. Dilling, Nucl. Instrum. Meth. A **676**, 32–43 (2012).
[14] A. Kellerbauer, G. Bollen, J. Dilling, S. Henry, F. Herfurth, H. J. Kluge, E. Lamour, R. Moore, C. Scheidenberger, S. Schwarz, G. Sikler, and J. Szerypo, Nucl. Phys. A **701**(1-4), 565–569 (2002).
[15] A. Nieminen, J. Huikari, A. Jokinen, J. Äystö, J. Billowes, P. Campbell, and E. Cochrane, Hyperfine Interact. **127**(1/4), 507–510 (2000).

[16] M. Block, D. Ackermann, D. Beck, K. Blaum, M. Breitenfeldt, A. Chauduri, A. Doemer, S. Eliseev, D. Habs, S. Heinz, F. Herfurth, F. P. Heßberger, S. Hofmann, H. Geissel, H. J. Kluge, V. Kolhinen, G. Marx, J. B. Neumayr, M. Mukherjee, M. Petrick, W. Plass, W. Quint, S. Rahaman, C. Rauth, D. Rodriguez, C. Scheidenberger, L. Schweikhard, M. Suhonen, P. G. Thirolf, Z. Wang, and C. Weber, Eur. Phys. J. A **25**(S1), 49–50 (2005).

[17] T. Sun, S. Schwarz, G. Bollen, D. Lawton, R. Ringle, and P. Schury, Eur. Phys. J. A **25**(S1), 61–62 (2005).

[18] E. Mané, A. Voss, J. A. Behr, J. Billowes, T. Brunner, F. Buchinger, J. E. Crawford, J. Dilling, S. Ettenauer, C. D. P. Levy, O. Shelbaya, and M. R. Pearson, Phys. Rev. Lett. **107**(21), 212502 (2011).

[19] G. Sikler, J. R. Crespo López-Urrutia, J. Dilling, S. Epp, C. J. Osborne, and J. Ullrich, Eur. Phys. J. A **25**(S1), 63–64 (2005).

[20] A. Lapierre, M. Brodeur, T. Brunner, S. Ettenauer, A. Gallant, V. Simon, M. Good, M. Froese, J. Crespo López-Urrutia, P. Delheij, S. Epp, R. Ringle, S. Schwarz, J. Ullrich, and J. Dilling, Nucl. Instrum. Meth. A **624**(1), 54–64 (2010).

[21] D. Frekers, M. C. Simon et al., submitted to Phys. Lett. B.

[22] M. C. Simon, J. C. Bale, U. Chowdhury, B. Eberhardt, S. Ettenauer, A. T. Gallant, F. Jang, A. Lennarz, M. Luichtl, T. Ma, D. Robertson, V. V. Simon, C. Andreoiu, M. Brodeur, T. Brunner, A. Chaudhuri, J. R. Crespo López-Urrutia, P. Delheij, D. Frekers, A. Grossheim, G. Gwinner, A. A. Kwiatkowski, A. Lapierre, E. Mané, M. R. Pearson, R. Ringle, B. E. Schultz, and J. Dilling, Rev. Sci. Instrum. **83**(2), 02A912 (2012).

[23] V. N. Gavrin, V. V. Gorbachev, E. P. Veretenkin, and C. B. T., Gallium experiments with artificial neutrino sources as a tool for investigation of transition to sterile states, 2011, arXiv:1006.2103v2 [nucl-ex].

[24] W. Hampel, J. Handt, G. Heusser, J. Kiko, T. Kirsten, M. Laubenstein, E. Pernicka, W. Rau, M. Wojcik, Y. Zakharov, R. Ammon, K. Ebert, T. Fritsch, D. Heidt, E. Henrich, L. Stielglitz, F. Weirich, M. Balata, M. Sann, F. Hartmann, E. Bellotti, C. Cattadori, O. Cremonesi, N. Ferrari, E. Fiorini, L. Zanotti, M. Altmann, F. V. Feilitzsch, R. Mößbauer, S. Wänninger, G. Berthomieu, E. Schatzman, I. Carmi, I. Dostrovsky, C. Bacci, P. Belli, R. Bernabei, S. d'Angelo, L. Paoluzi, M. Cribier, J. Rich, M. Spiro, C. Tao, D. Vignaud, J. Boger, R. Hahn, J. Rowley, R. Stoenner, and J. Weneser, Phys. Lett. B **447**(1-2), 127–133 (1999).

[25] F. Kaether, W. Hampel, G. Heusser, J. Kiko, and T. Kirsten, Phys. Lett. B **685**(1), 47–54 (2010).

[26] J. Abdurashitov, V. Gavrin, S. Girin, V. Gorbachev, T. Ibragimova, A. Kalikhov, N. Khairnasov, T. Knodel, V. Kornoukhov, I. Mirmov, A. Shikhin, E. Veretenkin, V. Vermul, V. Yants, G. Zatsepin, Y. Khomyakov, A. Zvonarev, T. Bowles, J. Nico, W. Teasdale, D. Wark, M. Cherry, V. Karaulov, V. Levitin, V. Maev, P. Nazarenko, V. Shkol'nik, N. Skorikov, B. Cleveland, T. Daily, R. Davis, K. Lande, C. Lee, P. Wildenhain, S. Elliott, and J. Wilkerson, Phys. Rev. C **59**(4), 2246–2263 (1999).

[27] J. Abdurashitov, V. Gavrin, S. Girin, V. Gorbachev, P. Gurkina, T. Ibragimova, A. Kalikhov, N. Khairnasov, T. Knodel, V. Matveev, I. Mirmov, A. Shikhin, E. Veretenkin, V. Vermul, V. Yants, G. Zatsepin, T. Bowles, S. Elliott, W. Teasdale, B. Cleveland, W. Haxton, J. Wilkerson, J. Nico, A. Suzuki, K. Lande, Y. Khomyakov, V. Poplavsky, V. Popov, O. Mishin, A. Petrov, B. Vasiliev, S. Voronov, A. Karpenko, V. Maltsev, N. Oshkanov, A. Tuchkov, V. Barsanov, A. Janelidze, A. Korenkova, N. Kotelnikov, S. Markov, V. Selin, Z. Shakirov, A. Zamyatina, and S. Zlokazov, Phys. Rev. C **73**(4), 045805 (2006).

[28] J. Abdurashitov, V. Gavrin, V. Gorbachev, P. Gurkina, T. Ibragimova, A. Kalikhov, N. Khairnasov, T. Knodel, I. Mirmov, A. Shikhin, E. Veretenkin, V. Yants, G. Zatsepin, T. Bowles, S. Elliott, W. Teasdale, J. Nico, B. Cleveland, and J. Wilkerson, Phys. Rev. C **80**(1), 015807 (2009).

[29] T. Brunner, A. R. Mueller, K. O'Sullivan, M. C. Simon, M. Kossick, S. Ettenauer, A. T. Gallant, E. Mané, D. Bishop, M. Good, G. Gratta, and J. Dilling, Int. J. Mass Spectrom. p. S1387380611003770 (2011).

[30] M. Brodeur, V. L. Ryjkov, T. Brunner, S. Ettenauer, A. T. Gallant, V. V. Simon, M. J. Smith, A. Lapierre, R. Ringle, P. Delheij, M. Good, D. Lunney, and J. Dilling, Int. J. Mass Spectrom. **310**, 20–31 (2012).

[31] M. Brodeur, T. Brunner, C. Champagne, S. Ettenauer, M. Smith, A. Lapierre, R. Ringle, V. L. Ryjkov, G. Audi, P. Delheij, D. Lunney, and J. Dilling, Phys. Rev. C **80**(4), 044318 (2009).

[32] G. Gräff, H. Kalinowsky, and J. Traut, Z. Phys. A-Hadron Nucl. **297**(1), 35–39 (1980).

[33] G. Bollen, R. B. Moore, G. Savard, and H. Stolzenberg, J. Appl. Phys. **68**(9), 4355 (1990).

[34] M. Kretzschmar, Int. J. Mass Spectrom. **264**(2-3), 122–145 (2007).

[35] S. George, K. Blaum, F. Herfurth, A. Herlert, M. Kretzschmar, S. Nagy, S. Schwarz, L. Schweikhard, and C. Yazidjian, Int. J. Mass Spectrom. **264**(2-3), 110–121 (2007).

[36] M. König, G. Bollen, H. J. Kluge, T. Otto, and J. Szerypo, Int. J. Mass Spectrom. **142**(1-2), 95–116 (1995).

[37] G. Bollen, Nucl. Phys. A **693**(1-2), 3–18 (2001).

[38] G. Bollen, S. Becker, H. J. Kluge, M. König, R. Moore, T. Otto, H. Raimbault-Hartmann, G. Savard, L. Schweikhard, and H. Stolzenberg, Nucl. Instrum. Meth. A **368**(3), 675–697 (1996).

[39] G. Bollen, H. J. Kluge, M. König, T. Otto, G. Savard, H. Stolzenberg, and G. Audi, Phys. Rev. C **46**(6), R2140–R2143 (1992).

[40] A. Kellerbauer, K. Blaum, G. Bollen, F. Herfurth, H. J. Kluge, M. Kuckein, E. Sauvan, C. Scheidenberger, and L. Schweikhard, Eur. Phys. J. D **22**(1), 53–64 (2003).

[41] R. A. Dragoset, A. Musgrove, C. W. Clark, and W. C. Martin, NIST periodic table: Atomic properties of elements, February 2012, National Institute of Standards and Technology, Gaithersburg, MD, Available at [http://www.nist.gov/pml/data].

[42] P. Barker and P. Amundsen, Phys. Rev. C **58**(4), 2571–2573 (1998).
[43] T. Eronen, D. Gorelov, J. Hakala, J. C. Hardy, A. Jokinen, A. Kankainen, V. S. Kolhinen, I. D. Moore, H. Penttilä, M. Reponen, J. Rissanen, A. Saastamoinen, and J. Äystö, Phys. Rev. C **83**(5), 055501 (2011).
[44] G. Audi, M. Wang, A. Wapstra, F. Kondev, M. MacCormick, X. Xu, and B. Pfeiffer, Chinese Phys. C **36**(12), 1287–1602 (2012).
[45] H. Vonach, P. Glässel, E. Huenges, P. Maier-Komor, H. Rösler, H. Scheerer, H. Paul, and D. Semrad, Nucl. Phys. A **278**(2), 189–203 (1977).
[46] G. Wallerstein, I. Iben, P. Parker, A. M. Boesgaard, G. M. Hale, A. E. Champagne, C. A. Barnes, F. Käppeler, V. V. Smith, R. D. Hoffman, F. X. Timmes, C. Sneden, R. N. Boyd, B. S. Meyer, and D. L. Lambert, Rev. Mod. Phys. **69**(4), 995–1084 (1997).
[47] M. Wiescher, H. Schatz, and A. Champagne, Philos. T. R. Soc. A **356**, 2105–2136 (1998).
[48] P. A. Seeger, W. A. Fowler, and D. D. Clayton, Astrophys. J. Suppl. S. **11**, 121 (1965).
[49] G. Audi, A. Wapstra, and C. Thibault, Nucl. Phys. A **729**(1), 337–676 (2003).
[50] C. Freiburghaus, J. F. Rembges, T. Rauscher, E. Kolbe, F. K. Thielemann, K. L. Kratz, B. Pfeiffer, and J. J. Cowan, Astrophys. J. **516**(1), 381–398 (1999).
[51] P. Delahaye, G. Audi, K. Blaum, F. Carrel, S. George, F. Herfurth, A. Herlert, A. Kellerbauer, H. J. Kluge, D. Lunney, L. Schweikhard, and C. Yazidjian, Phys. Rev. C **74**(3), 034331 (2006).
[52] S. Naimi, G. Audi, D. Beck, K. Blaum, C. Böhm, C. Borgmann, M. Breitenfeldt, S. George, F. Herfurth, A. Herlert, M. Kowalska, S. Kreim, D. Lunney, D. Neidherr, M. Rosenbusch, S. Schwarz, L. Schweikhard, and K. Zuber, Phys. Rev. Lett. **105**(3), 032502 (2010).
[53] U. Hager, T. Eronen, J. Hakala, A. Jokinen, V. Kolhinen, S. Kopecky, I. D. Moore, A. Nieminen, M. Oinonen, S. Rinta-Antila, J. Szerypo, and J. Äystö, Phys. Rev. Lett. **96**(4), 042504 (2006).
[54] S. Rahaman, U. Hager, V. V. Elomaa, T. Eronen, J. Hakala, A. Jokinen, A. Kankainen, P. Karvonen, I. D. Moore, H. Penttilä, S. Rinta-Antila, J. Rissanen, A. Saastamoinen, T. Sonoda, and J. Äystö, Eur. Phys. J. A **32**(1), 87–96 (2007).
[55] U. Hager, A. Jokinen, V. V. Elomaa, T. Eronen, J. Hakala, A. Kankainen, S. Rahaman, J. Rissanen, I. Moore, S. Rinta-Antila, A. Saastamoinen, T. Sonoda, and J. Äystö, Nucl. Phys. A **793**(1-4), 20–39 (2007).
[56] O. Sorlin and M. G. Porquet, Prog. Part. Nucl. Phys. **61**(2), 602–673 (2008).
[57] S. Zhu, R. V. F. Janssens, B. Fornal, S. J. Freeman, M. Honma, R. Broda, M. P. Carpenter, A. N. Deacon, E. Jackson, B. P. Kay, T. Lauritsen, C. J. Lister, P. F. Mantica, T. Otsuka, D. Seweryniak, J. F. Smith, D. Steppenbeck, and X. Wang, Phys. Rev. C **80**(2), 024318 (2009).
[58] A. Lapierre, M. Brodeur, T. Brunner, S. Ettenauer, P. Finlay, A. T. Gallant, V. V. Simon, P. Delheij, D. Lunney, R. Ringle, H. Savajols, and J. Dilling, Phys. Rev. C **85**(2), 024317 (2012).
[59] A. T. Gallant, J. C. Bale, T. Brunner, U. Chowdhury, S. Ettenauer, A. Lennarz, D. Robertson, V. V. Simon, A. Chaudhuri, J. D. Holt, A. A. Kwiatkowski, E. Mané, J. Menéndez, B. E. Schultz, M. C. Simon, C. Andreoiu, P. Delheij, M. R. Pearson, H. Savajols, A. Schwenk, and J. Dilling, Phys. Rev. Lett. **109**(3), 032506 (2012).
[60] G. Hagen, M. Hjorth-Jensen, G. R. Jansen, R. Machleidt, and T. Papenbrock, Phys. Rev. Lett. **109**(3), 032502 (2012).

www.ann-phys.org

adp

annalen der physik

WILEY-VCH

WILEY ONLINE LIBRARY

Early View publication on wileyonlinelibrary.com
(issue and page numbers not yet assigned;
citable using Digital Object Identifier – DOI)

Ann. Phys. (Berlin), 1–9 (2013) / DOI 10.1002/andp.201300044

annalen der physik

Review Article

State of the art in the determination of the fine structure constant: test of Quantum Electrodynamics and determination of h/m_u

Rym Bouchendira[1], *Pierre Cladé*[1], *Saida Guellati-Khélifa*[1,2,*], *Francois Nez*[1], *and Francois Biraben*[1]

Received 1 March 2013, revised 25 March 2013, accepted 9 April 2013
Published online 28 May 2013

The fine structure constant α has a particular status in physics. Its precise determination is required to test the quantum electrodynamics (QED) theory. The constant α is also a keystone for the determination of other fundamental physical constants, especially the ones involved in the framework of the future International System of units. This paper presents Paris experiment, where the fine structure constant is determined by measuring the recoil velocity of a rubidium atom when it absorbs a photon. The impact of the recent improvement of QED calculations of the electron moment anomaly and the recent measurement of the cesium atom recoil at Berkeley will be discussed. The opportunity to provide a precise value of the ratio h/m_u between the Planck constant and the atomic mass constant will be investigated.

1 Introduction

Since its discovery at the beginning of the 20^{th} century up to nowadays, the fine structure constant α remains one of the most fascinating fundamental constants, as it is dimensionless. Currently it plays a central role in the Physics of the 21^{st} century by testing the most accurate theories such as quantum electrodynamics (QED) [1–3], testing the stability of fundamental constants $(\dot{\alpha}/\alpha)$ (for example see review by J.P. Uzan [4]) but also in a practical way in the proposed redefinition of the international system of units (SI) [5].

The name of the fine structure constant derives from the Sommerfeld model [6]. It was intended to explain the fine structure of the hydrogen spectral lines, unaccounted for in the Bohr model. The Sommerfeld model combines the theory of relativity with the Bohr model. The constant α appears in the velocity of the electron (v_e) on its first orbit around the proton ($v_e = \alpha \times c$, where c is the velocity of light). The expression for α is:

$$\alpha = \frac{e^2}{4\pi\epsilon_0\hbar c} \tag{1}$$

where e is the charge of the electron, ϵ_0 the vacuum permittivity and $\hbar = h/2\pi$ in which h is the Planck constant.

The Sommerfeld model failed because it didn't take into account the spin of the electron. Nevertheless the constant introduced in this model is still relevant in the Dirac model which combines relativity and quantum mechanics [7]. This model predicts the existence of the positron and the spin of the electron! In 1947 a new effect from which the value of α can be deduced was discovered: the vacuum quantum fluctuations which contribute to the splitting of $2S_{1/2}$ and $2P_{1/2}$ energy levels in hydrogen (now usually called the Lamb shift) [8, 9] and also contribute to the anomaly of the gyromagnetic factor of leptons [10, 11].

Indeed the modern understanding of α is that it sets the scale of the electromagnetic interaction. Consequently many experiments in which a charged particle interacts with an electromagnetic field can be used to determine α. In 1998, the experiments considered by the CODATA task group on fundamental constants to give the best estimate of the fine structure constant value ranged from solid state physics and atomic physics to quantum electrodynamics [12].

As shown in figure 1, the current most precise determination of the fine structure constant comes mainly from two methods.

* Corresponding author E-mail: guellati@spectro.jussieu.fr
[1] Laboratoire Kastler Brossel, Ecole Normale Supérieure,Université Pierre et Marie Curie, CNRS, 4 place Jussieu, 75252 Paris Cedex 05, France
[2] Conservatoire National des Arts et Métiers, 292 rue Saint Martin, 75141 Paris Cedex 03, France

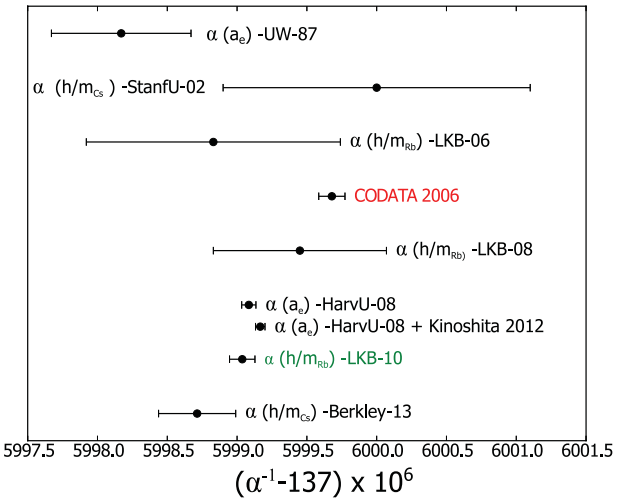

Figure 1 The most precise determinations of the fine structure constant. The value labelled $\alpha(h/m_{\mathrm{Cs}})$ is calculated using the value of the Compton frequency of cesium atoms measured by Muller's group [13]. The values labelled $(\alpha(a_{\mathrm{e}}) - \mathrm{UW} - 87)$ and $(\alpha(a_{\mathrm{e}}) - \mathrm{HarvU} - 08)$ are deduced from the experimental values of the electron moment anomaly a_{e} performed respectively by Dehmelt at the University of Washington [14] and Gabrielse at Harvard university [2].

The first method combines the measurement of the electron magnetic moment anomaly a_{e} and QED perturbation theory. The value of α is determined by comparing the experimental value of a_{e} with :

$$a_{\mathrm{e}} = A_1 \times \frac{\alpha}{\pi} + A_2 \times \left(\frac{\alpha}{\pi}\right)^2 + A_3 \times \left(\frac{\alpha}{\pi}\right)^3 + A_4 \times \left(\frac{\alpha}{\pi}\right)^4 + \ldots\ldots \quad (2)$$

$$+ a_{\mathrm{e}}\left(\frac{m_{\mathrm{e}}}{m_\mu}, \frac{m_{\mathrm{e}}}{m_\tau}, \mathrm{weak}, \mathrm{hadron}\right) \quad (3)$$

Thus in the QED model a_{e} is expressed as a power series of α and an additive term which takes into account the contributions due to the muon, the tau, the weak and hadronic interactions. The coefficients A_i are finite and dimensionless constants calculated by using Feynman diagrams [3].

The second one, introduced by the group of S. Chu at Stanford university [15], is based on the measurement of the ratio h/m_{X}, between the Planck constant h and the atomic mass m_{X}. This ratio is related to α by

$$\alpha^2 = \frac{2R_\infty}{c}\frac{A_r(\mathrm{X})}{A_r(\mathrm{e})}\frac{h}{m_{\mathrm{X}}} \quad (4)$$

The Rydberg constant R_∞ is known with an accuracy of 5×10^{-12} [16–18]. The uncertainty on the relative mass of the electron $A_r(\mathrm{e})$ and the relative atomic mass $A_r(\mathrm{X})$ are respectively 4.4×10^{-10} [19] and less than 10^{-10} for Rb and Cs [20, 21]. Using an atom interferometer and Bloch oscillations, we have performed in 2010 a determination of the ratio h/m_{Rb}. The value $\alpha(h/m_{\mathrm{Rb}})$ that has been deduced is the most precise value obtained using this method [1].

The comparison of these two determinations is one of the most precise test of QED. It is so accurate that one can think, in a near future, of using these lab-size experiments to check theoretical predictions tested up to now only on particle accelerators (for example the existence of internal structure of the electron [22]).

For many years, the main contribution to the determination of α_{CODATA} has been the one derived from the anomaly of the gyromagnetic factor of the electron $(\alpha(\mathrm{a_e}))$ which is strongly dependent on complex QED calculations. Nowadays the uncertainties of $\alpha(\mathrm{a_e})$ and $\alpha(\mathrm{Rb})$ are in the same order of magnitude. This makes the CODATA adjustment more reliable.

This reliability is essential for the redefinition of the SI which will rely on the values of fundamental constants [23–25]. In the proposed redefinition, the Planck constant will have a fixed value in SI units [5]. In order to link the microscopic definition to the macroscopic Kilogram, two kinds of experiments are competitive. The first one, the watt balance measures the ratio h/M between the Planck constant and a macroscopic standard mass M [26–28]. In the current SI, it gives a determination of h. In the future SI, it will give the measurement of a macroscopic mass. The second experiment is the Avogadro project, which directly determines the ratio M/m between a macroscopic mass (the mass of a silicon sphere) and a microscopic mass (the mass of the atom of silicon) [29]. In the current SI, it gives a determination of the (unified) atomic mass constant m_{u} defined according to $m_{\mathrm{u}} = m(^{12}\mathrm{C})/12$, or the Avogadro constant. The ratio h/m_{u} provides therefore a direct comparison between the two experiments. Its precise determination has a major interest in metrology. Whereas the photon-recoil measurement, combined with the appropriate relative atomic mass measurement, gives a determination of the ratio h/m_{u}, other values of α can be converted into h/m_{u} using the formula:

$$\frac{h}{m_{\mathrm{u}}} = \frac{\alpha^2 c A_r(\mathrm{e})}{2R_\infty} \quad (5)$$

We emphasize that the ratio h/m_u becomes identified with Avogadro Planck constant as:

$$N_A h = \frac{h}{m_u}\frac{M(^{12}C)}{12} \tag{6}$$

where $M(^{12}C) = 12\times10^{-3}$ kg/mol is the carbon molar mass and N_A is the Avogadro constant. The product hN_A is in the current SI, equivalent to the ratio h/m_u. It seems to us more relevant to consider h/m_u in the framework of the redefinition of the kilogram. In the future SI of units, the Avogadro constant N_A, which is used by the chemists to quantify and identify an amount of substance with atoms and molecules, will be fixed. This will break the link between atomic masses and molar masses. Consequently $M(^{12}C)$ will no longer be equal to 12 g/mol, but will be determined from equation (6) using the ratio h/m_u.

In the proposed new International Systems of Units, many others physical constants, that are set by the CODATA will have a fixed value. The constant α will be a keystone of the proposed SI, as many of the remaining constants will depend strongly on its knowledge (such as the vacuum permeability μ_0, the von Klitzing constant R_K, ...) [5].

The next and largest section of this paper will be devoted to the experiment in Paris. This experiment started in 1998 and was entirely renewed in 2008. In the last part, we will discuss the role of the various determinations of α. We will focus on the test of QED calculations and on the impact on the redefinition of the Kilogram.

2 Determination of the ratio h/m_{Rb}

2.1 Principle

The ratio h/m_{Rb} is deduced from the measurement of the recoil velocity v_r of an atom when it absorbs a photon ($v_r = \hbar k/m$ with $\hbar$ the reduced Planck constant, k the wave vector and m the mass of atoms). This measurement is performed by combining a Ramsey-Bordé atom interferometer [30] with the Bloch oscillations technique. Bloch oscillations have been first observed in atomic physics by the groups of Salomon and Raizen [31–33]. The atoms are shed with two counter-propagating laser beams whose frequency difference is swept linearly. One can then consider that the atoms are placed in a standing wave which is accelerated when the frequency difference between the two laser beams is swept. The atoms experiment an inertial force in a periodic optical potential. This system is analogous to the BO of an electron in a solid submitted to an electric field. Another point of view is to consider that the atoms undergo a succession of Raman transitions which correspond to the absorption of one photon from a beam and a stimulated emission of another photon to the other beam. The internal state is unchanged while the atomic velocity increases by $2\times v_r$ per oscillation. The Doppler shift due to this velocity variation is periodically compensated by the frequency sweep and the atoms are accelerated. For 87-rubidium atoms the Doppler shift induced by a variation of velocity of $2\times v_r$ is 30 kHz, the number of Bloch oscillations performed by the atoms is set precisely by the frequency sweep. In our previous work we demonstrated that BO is a very efficient process in terms of photon momentum transfer [34].

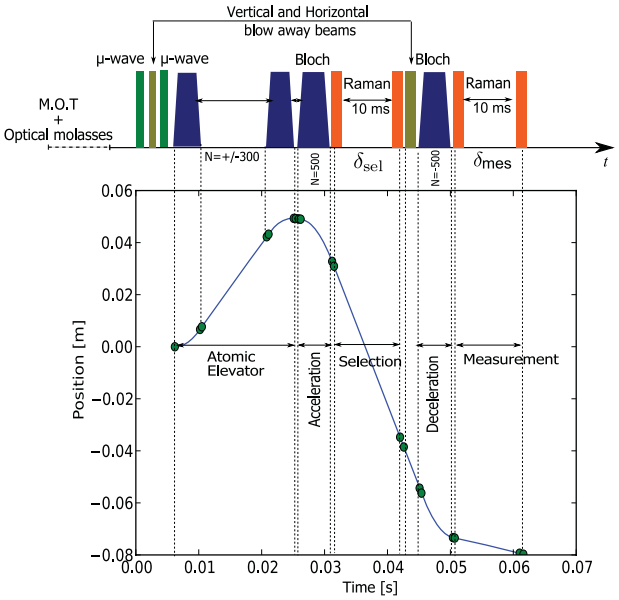

Figure 2 The pulses timing sequence and atomic trajectory during the measurement procedure.

The timing sequence of the experiment is depicted in figure 2. The 87-rubidium atoms are first cooled in a magneto-optical trap and optical molasses in the $F = 2$ hyperfine level. A μ-wave excitation is used to select atoms in $F = 2, m_F = 0$: we apply a vertical magnetic field of 7 μT, a first μ-wave excitation pulse transfers atoms from $F = 2, m_F = 0$ to $F = 1, m_F = 0$ Zeeman sub-level. The blow-away laser beam cleans the $F = 2$ hyperfine level. The atoms in $F = 1, m_F = 0$ are returned to $F = 2, m_F = 0$ using a second μ-wave pulse. In order to increase the interaction area, we apply an atomic elevator to displace the atoms toward the lower or the upper side of the vacuum chamber. The atoms are accelerated and then decelerated by the means of two Bloch pulses delayed by 10.3 ms. Each one transfers to the atoms

$600 \times v_r$ during 4.6 ms in a given direction. The atomic elevator carries 30% of the atoms, which represents the whole proportion of the atoms which fit in the first Brillouin zone.

We then start the measurement procedure by accelerating the atoms with 500 BO in 5.6 ms (for details see [35, 36]). The velocity of the atoms is measured by using a Ramsey-Bordé atom interferometer performed by two pairs of $\pi/2$ pulses. The delay T_R between two $\pi/2$ pulses is 10 ms and the duration of each pulse is $\tau = 600\mu s$. The laser pulses induce a Doppler sensitive Raman transition between the hyperfine levels $F = 2$ and $F = 1$, thus the velocity is measured in terms of frequency. The first pair of $\pi/2$ pulses transfers the resonant velocity class from $F = 2$ to $F = 1$. We then shine a resonant laser beam ($F = 2 \longrightarrow F' = 3$ transition) to push away atoms remaining in $F = 2$ before coherently accelerating atoms in $F = 1$ with 500 BO. The final velocity of the accelerated atoms is measured with a second pair of $\pi/2$ pulses by transferring atoms from $F = 1$ to $F = 2$. The population in each hyperfine level is measured with a time of flight technique. The fringe pattern which represents the final velocity distribution is obtained by scanning the frequency of the Raman lasers during the final $\pi/2$ pulses.

2.2 Experimental setup

A two-dimensional magneto-optical trap (2D-MOT) produces a slow atomic beam (about 10^9 atoms/s at a velocity of 20 m/s) which loads during 250 ms a three-dimensional magneto-optical trap. Then a σ^+-σ^- molasses generates a cloud of about 2×10^8 atoms in the $F = 2$ hyperfine level, with a 1.7 mm radius and at a temperature of 4 μK. The 2D-MOT cell is a glass cell separated from a UHV-chamber by a differential pumping tube which is also the aperture for the output slow beam. The cooling and pumping lasers are interference-filter-stabilized external-cavity diode lasers (IF-ECL) [37], both lasers are amplified in the same tapered amplifier. The frequency of the cooling beam is actively controlled by using the beatnote signal with the pumping beam, itself locked on a suitable rubidium crossover line. The Raman lasers are also IF-ECL diode lasers. The two diode lasers are phase-locked using a synthesized frequency referenced to a cesium atomic clock. As shown in figure 3, the synthesized frequency results from a mixing of a fixed frequency (6.84 GHz), a frequency ramp to compensate the fall of atoms in the gravity field (25 kHz/s) and the probe frequency. The probe frequency is switched between δ_{sel} and δ_{meas} using two independent synthesizers, where δ_{sel} and δ_{meas} are the frequency differences between the two Raman beams respectively during the first and the second pairs of $\pi/2$ pulses of the atom interferometer. The Raman beams are blue-detuned by 125 GHz from the 87-Rubidium D2 line. The Bloch beams originate from a 2.5 W Ti:sapphire laser. The output laser beam is split into two paths, each of which passes through an AOM to adjust the frequency offset and amplitude before being injected into a polarization maintaining fibre. The depth of the generated optical lattice is $45E_r$ (E_r is the recoil energy) for an effective power of 150 mW seen by the atoms. The optical scheme of the Bloch and the Raman beams is described in detail in [1, 35]. The frequencies of one Raman laser and the Bloch laser are stabilized onto a same ultra-stable Zerodur Fabry-Perot cavity, itself stabilized on the $5S_{1/2}(F = 3) \longmapsto 5D_{3/2}(F = 5)$ two-photon transition of 85-rubidium [38] (short term). On the long term, these frequencies are precisely measured by using a femtosecond comb referenced to the cesium clock. As the measurement of the ratio h/m_{Rb} is performed in terms of frequency, it is thus directly connected to the cesium standard.

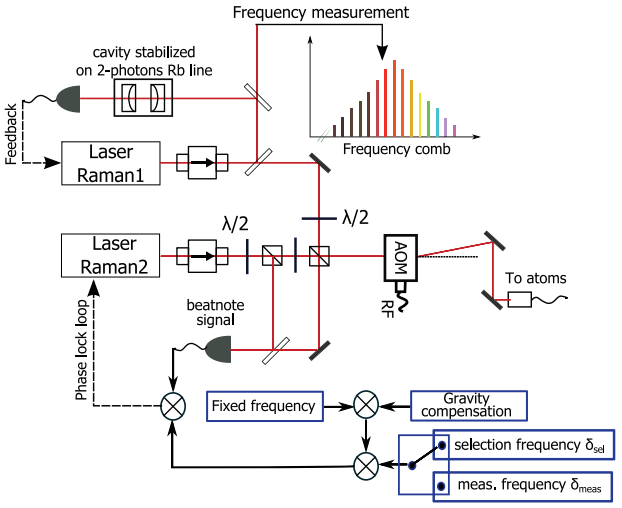

Figure 3 The optical setup of the Raman beam used to perform the atomic interferometer. The two laser diodes are stabilized using an interference-filter-stabilized extended cavity. They are phase locked. The frequency of one Raman laser is stabilized on an ultra-stable cavity and measured with a femtosecond comb.

The vacuum chamber is supported by an active vibration isolation platform. The residual acceleration is reduced by a factor of 100 above 10 Hz. However, vibrations remain one of the main limitations in the sensitivity of the atom interferometer.

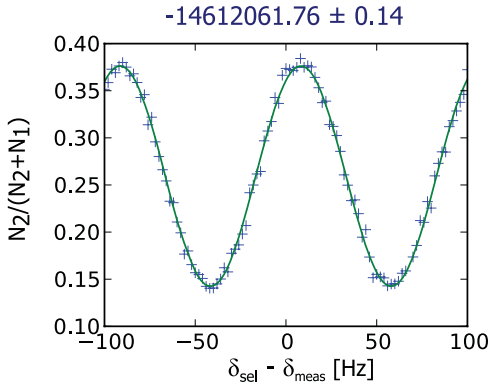

Figure 4 The quantity $N_2/(N_2+N_1)$ versus the frequency difference between the two pairs of $\pi/2$ pulses, where N_2 and N_1 represent respectively the populations in hyperfine levels $F=1$ and $F=2$. The spectrum is recorded with 100 points during 1 min. The measured position of the central fringe is indicated above the spectrum.

2.3 Results

In figure 4 we show a typical fringe pattern obtained with 100 points during 1 min. The central fringe is determined with an uncertainty of 0.14 Hz corresponding to the relative uncertainty of 10^{-8} on the Doppler shift $(\delta_{sel}-\delta_{meas})$ induced by 500 BO.

A value of h/m_{Rb} is obtained by recording four spectra obtained under different conditions to cancel systematic errors and then using:

$$\frac{\hbar}{m_{Rb}} = \frac{1}{4}\sum_{Spectra}\frac{2\pi\,|\delta_{sel}-\delta_{meas}|}{2Nk_B(k_1+k_2)} \tag{7}$$

where k_1 and k_2 are the wave-vectors of the Raman laser beam, k_B is the wave-vector of the Bloch laser beams and N the number of Bloch oscillations.

Two spectra allow to get rid of the change in velocity due to the free fall of atoms in the gravity field. They are obtained by accelerating the atoms alternatively upward and downward. The difference between the results eliminate gT, where T is the spacing time between the two pairs of Raman $\pi/2$ pulses. Otherwise for each initial acceleration, we record two other spectra by exchanging the direction of the Raman beams ($\vec{k_1}$ and $\vec{k_2}$) in order to cancel the parasitic level shifts due to the Zeeman effect and the light shifts. Typically a set of 4 spectra is obtained with the parameters shown on table 1. In this table, $N_{elev}(1)$ and $N_{elev}(2)$ represent the number of BO used to perform the atomic elevator (we first accelerate the atoms with $N_{elev}(1)$ BO then we stop them using $N_{elev}(2)$ BO). N_{up} and N_{down} are respectively the number of BO for the upward and downward acceleration. The two last lines of this table give the result of the fit of the central fringe and the corresponding uncertainty. Each column gives the parameters for one spectrum. We deduced the value of h/m_{Rb} with a relative uncertainty of 5×10^{-9} (2.5×10^{-9} on α).

Figure 5 shows a set of 170 determinations of the ratio h/m_{Rb} recorded for about 15 hours. The standard deviation on the mean value is 4.4×10^{-10}, with a $\chi^2/(n-1)=1.05$. We have evaluated the autocorrelation function using the approach described in reference [39]. The result is reported in the inset, there is no correlation between the successive measurements.

2.4 Systematic effects

The systematic effects are summarized in the table 2.

The main systematic effect comes from the Gaussian profile of the laser beams. The atoms experience an effective wave-vector determined by the gradient of the laser phase along the propagation axis z :

$$k_{eff} = \frac{d\phi}{dz} = k - \frac{2}{k}\left[\frac{1}{w^2} - \frac{r^2}{w^4} + \frac{k^2r^2}{4R^2}\right] \tag{8}$$

where r is the radius of the atomic cloud, w the waist of the laser and R, the curvature radius.

This formula includes both contributions of the Gouy phase and the wave front curvature. The geometrical parameters of the laser beams have been carefully measured with a Shack-Hartmann wave-front analyser. The alignment of the laser beams is ensured by controlling the coupling between the two optical fibres. The maximum angle error is estimated to 40 μrad. As shown in figure 6-A, this value has been confirmed by considering the deviation of the ratio h/m_{Rb} versus the angle between the upward and the downward Bloch beams (see figure 6-B). The experimental protocol allows to cancel a large part of the level shifts (Zeeman and light shift). This cancellation is performed in three ways: between the selection and the measurement Raman pulses, between the upward and downward trajectories, and when the Raman beams direction is changed. The vacuum chamber is enclosed in a double magnetic shield, we have precisely evaluated the residual magnetic field along the interaction area using Zeeman sensitive Raman transitions. The correction on α due to the second order Zeeman shift is estimated to 4×10^{-10}. The light shift is mainly due to the expansion of the atomic cloud between the selection step and the measurement step and

Table 1 Typical experimental parameters for the determination of one value of h/m_{Rb}.

$N_{\mathrm{elev}}(1)$	-300	-300	$+300$	$+300$
$N_{\mathrm{elev}}(2)$	$+300$	$+300$	-300	-300
N_{up}	$+500$	$+500$	-500	-500
N_{down}	-500	-500	$+500$	$+500$
Raman beams direction	$+1$	-1	$+1$	-1
$(\delta_{sel} - \delta_{meas})$(Hz)	15567824.42	-15567822.07	-14612062.24	14612067.77
Uncertainty on the central fringe	0.15	0.16	0.13	0.16

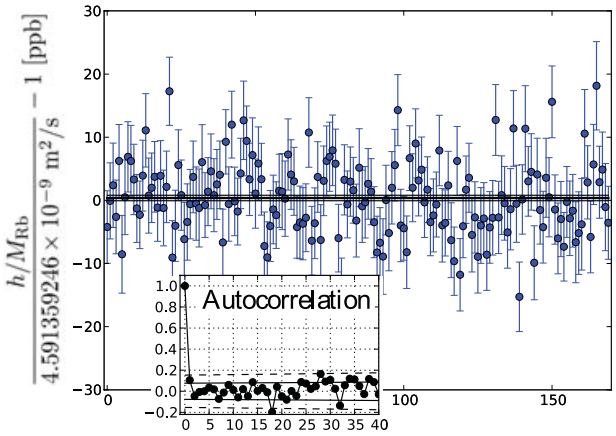

Figure 5 A selection of 170 measurements of the ratio h/m_{Rb} obtained during 15 hours integration time. The inset shows the autocorrelation function of these measurements. The solid and the dashed lines represent the 1σ and 2σ standard deviations of the autocorrelation function.

the unbalance of the laser intensity when we exchange the direction of the Raman beams.

The density of the atomic cloud after the μ-wave selection and the elevator sequence is about 2×10^8 atoms/cm^3. The correction due to the index and the mean-field effects is estimated to 10^{-10} with a conservative uncertainty of 2×10^{-10}(see [36]). Compared to the measurements made in 2008, the effect of the background vapour is now negligible (a few parts per 10^{-11}), thanks to the differential pumping in the double-cell design. Finally the deduced value of the fine structure constant is :

$$\alpha^{-1}(h/m_{\mathrm{Rb}}) = 137.035999044(90) \quad [0.66\mathrm{ppb}] \qquad (9)$$

This value is slightly different from that published in [1], where we have used the value of the rubidium mass determined by B. J. Mount et al. [21]. To obtain the result of equation (9), we have used the mean value between the mass values published in references [20] and [21].

Table 2 Systematic effects and relative uncertainty in part per 10^{10} on the determination of α^{-1}.

Laser frequencies		**1.3**
Beams alignment	-3.3	3.3
Wave front curvature and Gouy phase	-25.1	3.0
2nd order Zeeman effect	4.0	3.0
Gravity gradient	-2.0	0.2
Light shift (one photon transition)		0.1
Light shift (two photon transition)		0.01
Light shift (Bloch oscillation)		0.5
Index of refraction atomic cloud		
and atom interactions		2.0
Global systematic effects	-26.4	5.9
Statistical uncertainty		2.0
Rydberg constant and mass ratio		2.2
Total uncertainty		6.6

3 Discussion

The experiments which provide the values of the fine structure constant summarized in figure 1 can be used in two different ways. On the one hand, they can be seen as a test of QED calculations of the electron moment anomaly a_{e}. These very difficult calculations have been performed by the group of Kinoshita and Nio. They have recently calculated for the first time the

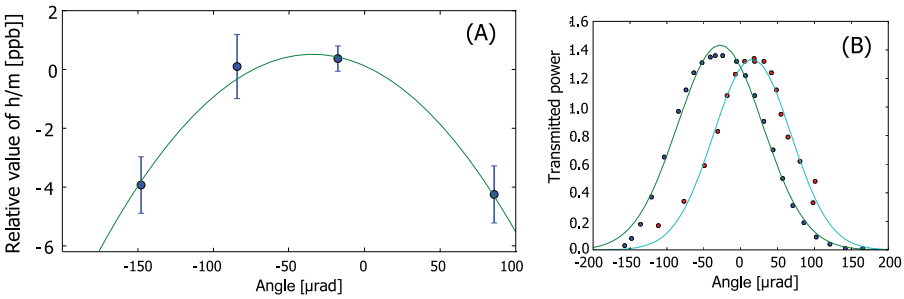

Figure 6 The statistical uncertainty on the measurement of the ratio h/m_{Rb} is sufficient to evaluate the deviation of some experimental parameters. (A): deviation of the misalignment angle between the Bloch beams. (B) Retro-reflection in the optical fibre versus the misalignment angle (green curve : Bloch beams, blue curve : Raman beams).

fifth coefficient of equation (3) and improved the uncertainty on the fourth one. For the test of QED only two data are involved: the experimental value of $a_{\mathrm{e}}(\mathrm{Exp})$ $(1159652180.73(28)\times10^{-12}$ [0.28ppt]) achieved by the group of Gabrielse and the one predicted by the theory, $a_{\mathrm{e}}(\mathrm{Theory})$. The latter is computed using $\alpha(h/m_{\mathrm{Rb}})$ as input data. The disagreement between the experimental and theoretical values of a_{e} is:

$$a_{\mathrm{e}}(\mathrm{Exp}) - a_{\mathrm{e}}(\mathrm{Theory}) = -1.09(0.83) \times 10^{-12} \qquad (10)$$

The upper part of figure 7 shows the comparison between the current values of a_{e}. The accuracy of the value of $\alpha(h/m_{\mathrm{Rb}})$ is sufficient to test the contributions due to the muon and hadrons in the theoretical value of a_{e}. The lower part shows the relative contributions to the electron anomaly of the different terms in Equation (3).

On the other hand, these experiments provide a way to investigate the impact of the measurements of α and the ratio h/m on the redefinition of the kilogram. Recently the group of H. Muller at the university of California, Berkeley, published a new measurement of the Compton frequency of the cesium atom $h/m_{\mathrm{Cs}}c^2$ [13]. Because c has an exact value, this is equivalent to a measurement of h/m that can be compared to ours (see table 3).

Reference [13] highlights the impact of such measurements on the proposed redefinition of the SI of units. The interpretation of the aforementioned work needs to be clarified: in the redefinition planned by the CGPM in 2015, the definition of the second will stay the same and the kilogram will be defined by fixing the value of the Planck constant h. This definition will be based on fundamental constants and therefore the resolution of the CGPM explicitly relies on the CODATA for the new definition [23].

The main challenge for the redefinition of the Kilogram, and the main reason why this redefinition has been delayed for several years, is the lack of a reliable link between the microscopic and macroscopic masses. This link is established with a relative uncertainty of 3 $\times10^{-8}$ [28] and with a large discrepancies between the different methods (watt balances and Avogadro project). One can notice that the recently measured value of the Avogadro constant [29], which is the most accurate input datum for the kilogram redefinition, is midway between the watt-balance values [40, 41].

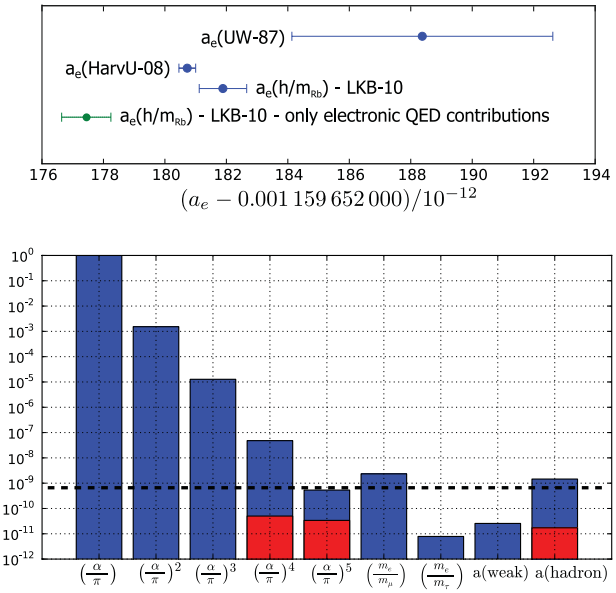

Figure 7 Upper figure: comparison of the measurements of the electron moment anomaly ($a_{\mathrm{e}}(\mathrm{UW}-87)$ and $a_{\mathrm{e}}(\mathrm{HarvU}-08)$) with the theoretical value obtained using $\alpha(h/m_{\mathrm{Rb}})$. The green point is obtained without the last term of equation (3). The lower figure in blue, relative contributions to the electron anomaly of the different terms of equation (3), in red their uncertainties. The dashed line corresponds to the relative uncertainty on the value of $\alpha(h/m_{\mathrm{Rb}})$.

Table 3 The values of the fine structure constant and the ratio h/m_u deduced from the experiments of Harvard, Berkeley and Paris.

	h/m_u [$m^2\,s^{-1}$]	α^{-1}
Harvard university	3.9903127118(26)$\times 10^{-7}$ [0.65 ppb]	137.035999173(35) [0.25 ppb]
Berkeley university	3.990312738(16)$\times 10^{-7}$ [4.0 ppb]	137.03599872(28) [2.0 ppb]
LKB	3.9903127193(50)$\times 10^{-7}$ [1.2 ppb]	137.035999044(90) [0.66 ppb]

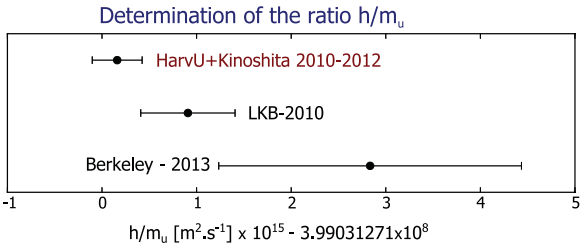

Figure 8 Determinations of the ratio h/m_u deduced from the measurement of the rubidium recoil and Compton frequency of the cesium atom. The most precise determination comes from the value of the fine structure constant given by the experimental value of the a_e measurement and QED calculations.

As for the CODATA, the recent measurement of Berkeley is strictly equivalent to an h/m_u measurement. While it contributes to the reliability of the determination of h/m_u by providing a determination below 10^{-8}, unfortunately it will not contribute that much to the CODATA (and therefore to the redefinition of the SI) because its uncertainty is too large (see Figure 8, in which is also included the value obtained from α(HarvU), assuming the exactness of QED calculations).

The ratio h/m_u will have an important role after the redefinition of the SI. As mentioned in reference [42] *This would yield a value for the mass of the atom in SI units, i.e. kilograms, without making reference to the prototype kilogram artefact as is now necessary.* Therefore, there is a strong motivation to continue to improve the uncertainty on h/m_u as much as possible, until competing methods are obviously superior.

This uncertainty will then be comparable to the ones of the comparison between atomic masses and therefore uncertainties of atomic masses in SI will be the same as in the atomic mass unit (AMU).

The watt balance and h/m measurement are similar in the sense that both measure a ratio between the Planck constant and a mass (or the Compton frequency of a given mass). The watt balance does indeed provide a measurement of the ratio h/Mg (g is the gravity acceleration, M a macroscopic mass). The atomic analogue is closely related to the period $\hbar k/mg$ of Bloch oscillations of atoms in a periodic lattice (k is the wave vector of the Bloch beam). Based on this idea, we have proposed in 2006 to measure the local gravity in the watt balance site using Bloch oscillations in a quasi-stationary optical lattice. This method gives a possibility to realize a link between h/M and h/m_u [43].

4 Conclusion

In this paper we have presented the details of our recent experimental setup. The fine structure constant is determined with a relative uncertainty of 6.6×10^{-10}. Taking account of the recent improvement of QED calculations, we deduce a theoretical value of the electron moment anomaly. The comparison with the experimental value of a_e realized by the group of Gabrielse at Havard university provides the most stringent test of QED.

In the future we plan to improve the accuracy on h/m_{Rb} and therefore on α, by increasing the sensitivity of the atom interferometer (velocity sensor) and by reducing the systematic effect due to the Gouy phase and the wave-front curvature. A new project is currently in progress in our group. It consists on a new experimental setup based on evaporatively cooled atoms. We plan to implement on this setup an atom interferometer based on large momentum beam splitters [44].

This experiment is supported in part by IFRAF (Institut Francilien de Recherches sur les Atomes Froids), and by the Agence Nationale pour la Recherche, FISCOM Project-(ANR-06-BLAN-0192).

Key words. Fine structure constant, electron moment anomaly, atom interferometry, Bloch oscillations, Quantum electrodynamics test, atomic mass unit.

References

[1] R. Bouchendira, P. Cladé, S. Guellati-Khélifa, F. Nez, and F. Biraben, Phys. Rev. Lett. **106**, 080801 (2011).
[2] D. Hanneke, S. Fogwell, and G. Gabrielse, Phys. Rev. Lett. **100**, 120801 (2008).

[3] T. Aoyama, M. Hayakawa, T. Kinoshita, and M. Nio, Phys. Rev. Lett. **109**, 111807 (2012).
[4] J. P. Uzan, Living Rev. Relativity **14**, 2 (2011).
[5] I. M. Mills, P. J. Mohr, T. J. Quinn, B. N. Taylor, and E. R. Williams, Phil. Trans. R. Soc. A. **369**, 3907 (2011).
[6] A. Sommerfeld, Annalen der Phyisk **17**, 1 (1916).
[7] P. A. M. Dirac, Proc. Soc. Lond. A **117**, 610 (1928).
[8] W. L. Jr and R. C. Retherford, Phys. Rev. **72**, 241 (1947).
[9] W. E. L. Jr and R. Retherford, Phys. Rev. **79**, 549 (1950).
[10] J. Schwinger, Phys. Rev. **73**, 416 (1948).
[11] P. Kusch and H. M. Foley, Phys. Rev. **74**, 351 (1948).
[12] P. Mohr and B. Taylor, Rev. Mod. Phys. **72**, 351 (2000).
[13] S. Y. Lan, P. C. Kuan, B. Estey, D. English, J. M. Brown, M. A. Hohensee, and H. Müller, Science **339**, 554–557 (2013).
[14] R. V. Dyck, P. Schwinberg, and H. Dehmelt, Phys. Rev. Lett. **59**, 26 (1987).
[15] A. Wicht, J. Hensley, E. Sarajlic, and S. Chu, Physica Scripta **T102**, 82 (2002).
[16] P. J. Mohr, B. N. Taylor, and D. B. Newell, Reviews of Modern Physics **80**, 633–730 (2008).
[17] T. Udem, A. Huber, B. Gross, J. Reichert, M. Prevedelli, M. Weitz, and T. W. Hänsch, Phys. Rev. Lett. **79**, 2646–2649 (1997).
[18] C. Schwob, L. Jozefowski, B. de Beauvoir, L. Hilico, F. Nez, L. Julien, F. Biraben, O. Acef, J. J. Zondy, and A. Clairon, Phys. Rev. Lett. **82**, 4960–4963 (1999).
[19] P. J. Mohr, B. N. Taylor, and D. B. Newell, Rev. Mod. Phys. **84**, 1527–1605 (2012).
[20] M. P. Bradley, J. V. Porto, S. Rainville, J. K. Thompson, and D. E. Pritchard, Phys. Rev. Lett. **83**, 4510–4513 (1999).
[21] B. J. Mount, M. Redshaw, and E. G. Myers, Phys. Rev. A **82**, 042513 (2010).
[22] G. Gabrielse, D. Hanneke, T. Kinoshita, M. Nio, and B. Odom, Phys. Rev. Lett. **97**, 030802 (2006).
[23] R. adopted by the General Conference on Weights and M. (24th meeting) (17-21 October 2011).
[24] C. J. Bordé, Phil. Trans. R. Soc. A. **363**, 2177–2201 (2005).
[25] I. M. Mills, P. J. Mohr, T. J. Quinn, B. N. Taylor, and E. R. Williams, Metrologia **43**, 227–246 (2006).
[26] B. P. Kibble, I. A. Robinson, and J. H. Belliss, Metrologia **27**, 173 (1990).
[27] R. L. Steiner, R. Liu, P.T. Olson, and D.; IEEE. Trans. Instrum. Meas. **56**, **592** (2007).
[28] E. R. Williams, R. L. Steiner, D. B. Newell, and P. T. Olsen, Phys. Rev. Lett. **81**, 2404–2407 (1998).
[29] B. Andreas, Y. Azuma, G. Bartl, P. Becker, H. Bettin, M. Borys, I. Busch, M. Gray, P. Fuchs, K. Fujii, H. Fujimoto, E. Kessler, M. Krumrey, U. Kuetgens, N. Kuramoto, G. Mana, P. Manson, E. Massa, S. Mizushima, A. Nicolaus, A. Picard, A. Pramann, O. Rienitz, D. Schiel, S. Valkiers, and A. Waseda, Phys. Rev. Lett. **106**, 030801 (2011).
[30] C. J. Bordé, Phys. Lett. A **140**, 10–12 (1989).
[31] M. B. Dahan, E. Peik, J. Reichel, Y. Castin, and C. Salomon, Phys. Rev. Lett. **76**, 4508 (1996).
[32] E. Peik, M. B. Dahan, I. Bouchoule, Y. Castin, and C. Salomon, PRA **55**, 2989 (1997).
[33] S. R. Wilkinson, C. F. Bharucha, K. W. Madison, Q. Niu, and M. G. Raizen, Phys. Rev. Lett. **76**, 4512–4515 (1996).
[34] R. Battesti, P. Cladé, S. Guellati-Khélifa, C. Schwob, B. Gémaud, F. Nez, L. Julien, and F. Biraben, Phys. Rev. Lett. **92**, 253001 (2004).
[35] M. Cadoret, E. de Mirandes, P. Cladé, S. Guellati-Khelifa, C. Schwob, F. Nez, L. Julien, and F. Biraben, Phys. Rev. Lett. **101**, 230801 (2008).
[36] P. Cladé, E. de Mirandes, M. Cadoret, S. Guellati-Khélifa, C. Schwob, F. Nez, L. Julien, and F. Biraben, Phys. Rev. A **74**, 052109 (2006).
[37] X. Baillard, A. Gauguet, S. Bize, P. Lemonde, P. Laurent, A. Clairon, and P. Rosenbusch, Optics Communications **266**, 609–613 (2006).
[38] D. Touahri, O. Acef, A. Clairon, J. J. Zondy, R. Felder, L. Hilico, B. de Beauvoir, F. Biraben, and F. Nez, Optics Communications **133**, 471–478 (1997).
[39] T. J. Witt, Metrologia **44**, 201 (2007).
[40] P. Becker, Contemporary Physics **53**, 461–479 (2012).
[41] G. Mana and E. Massa, Rivista Del Nuovo Cimento **35**, 353 (2012).
[42] P. J. Mohr, Metrologia **45**, 129 (2008).
[43] F. Biraben, M. Cadoret, P. Clade, G. Geneves, P. Gournay, S. Guellati-Khelifa, L. Julien, P. Juncar, E. de Mirandes, and F. Nez, METROLOGIA **43**, L47–L50 (2006).
[44] P. Cladé, S. Guellati-Khélifa, F. Nez, and F. Biraben, Phys. Rev. L **102**, 240402 (2009).

www.ann-phys.org

adp

annalen der physik

WILEY-VCH

WILEY ONLINE LIBRARY

Early View publication on wileyonlinelibrary.com
(issue and page numbers not yet assigned;
citable using Digital Object Identifier – DOI)

Ann. Phys. (Berlin), 1–12 (2013) / DOI 10.1002/andp.201300060

annalen der physik

Review Article

CPT symmetry tests with cold $\overline{\mathrm{p}}$ and antihydrogen

Yasunori Yamazaki[1,*] *and Stefan Ulmer*[2,**]

Received 17 March 2013, revised 14 April 2013, accepted 14 April 2013
Published online 17 May 2013

Precision comparisons of the properties of particles and their corresponding antiparticles are highly relevant because the Standard Model of elementary particle physics, a local, Lorentz-invariant field theory, is necessarily symmetric with respect to the combined CPT operation. This symmetry defines exact equality between the fundamental properties of particles and their anti-images. Any measured and confirmed violation constitutes a significant challenge to the Standard Model. Recent results of different CPT-tests are summarized, with emphasis to the high-precision measurement of the magnetic moment of the proton and the antiproton, as well as the precision investigation of antihydrogen ground state hyperfine splitting.

1 Introduction

Symmetries are an essential concept in modern physics particularly in the Standard Model (SM), and are categorized into global and local symmetries, which are related to conservation laws and forces, respectively [1]. Charge conjugation (C), parity operation (P), and time reversal (T) are the components of discrete symmetry transformations. The CPT symmetry, simultaneous application of all three transformations, is supposed to be the most fundamental symmetry in physics. Actually, it's conservation is theoretically guaranteed by local quantum field theories constructed on a flat space-time, which fulfil the condition of Lorentz invariance and unitarity [2]. Considering the fact that P [3], CP [4], and T [5] have already been found to be violated, the CPT symmetry is the last one still evading our pursuit. If some of the conditions which back-up CPT are not satisfied, the symmetry might be violated, *e.g.*, when space-time is curved by the gravitational interaction, and/or, non-local interactions play a role. It is noted, that the physical origin of the violations of P and CP symmetries in weak interactions is not yet understood in detail [6].

1.1 Gravitational interaction

The Planck mass m_{Pl} given by $\sqrt{\hbar c/G}(\sim 10^{19}\mathrm{GeV/c^2})$ is the critical mass of a particle, which in itself becomes a black hole, where $\hbar$ is the Planck constant divided by 2π, c the speed of light, and G the gravitational constant[3]. When we consider influences of the gravitational interaction on a physics system in question, a possible measure for CPT violation could be the ratio of the particle mass (m) involved in the system and the Planck mass, *i.e.*, $\delta_m = m/m_{Pl}$. The corresponding energy of the Planck mass is far too high to be accessible by accelerator techniques known until now[4], and will probably never be reached even in the distant future. It would therefore make sense to reconsider our strategy in studying the fundamental laws of nature not only by pushing to higher and higher energy, but instead by adopting a softer and humbler way with higher sensitivity. We call such a complementary approach as *listen to the whisper of nature*. For the proton (p)/antiproton ($\overline{p}$) system, $\delta_m = m_{\mathrm{p}/\overline{\mathrm{p}}}/m_{Pl} \sim 10^{-19}$, which corresponds to $m_{p/\overline{p}}c^2\delta_m \sim 10^{-19}$GeV. Although this quantity looks extremely small, in terms of a frequency it corresponds to ∼10 kHz, which might be resolvable, depending on the physical quantities targeted.

1.2 Non-local interaction

Another condition which might violate CPT is a non-local interaction. Actually, the string theory is in its

* Corresponding author E-mail: yasunori@riken.jp
** E-mail: stefan.ulmer@cern.ch
[1] RIKEN, Atomic Physics Laboratory, 2-1 Hirosawa, Wako, Saitama, 351-0198, Japan
[2] RIKEN, Ulmer Initiative Research Unit, 2-1 Hirosawa, Wako, Saitama, 351-0198, Japan

[3] This is really huge, comparable to the mass of a bacteria

[4] The highest energy from the largest accelerator (LHC) is $\sim 10^4$GeV in the center of mass frame, corresponding to $\sim 10^8$GeV in the laboratory frame. Even in the case of cosmic rays, it can be as high as 10^{11}GeV.

nature non-local, which may provide some proactive prediction to violate CPT [7]. Other Lorentz invariant non-local CPT violating models are proposed and discussed in [8, 9].

1.3 SME

The Standard Model Extension (SME), developed and extended considerably by Kostelecky and his colleagues, is constructed by adding possible CPT violating interactions artificially to the standard CPT conserving Lagrangean of the SM. Based on this approach physical quantities sensitive to CPT violation are discussed[5] [10–12]. One of the main statements of the SME is, that CPT violation should be tested by comparing quantities with respect to an absolute energy scale, not by comparing relative accuracies. In general, it would not make much sense to compare different quantities with relative accuracies[6].

1.4 Relation with Big Bang

The Big Bang scenario is quite successful and powerful in explaining various astronomical observations such as Hubble's law, cosmic microwave background radiation, abundance of primordial elements, galactic evolution and distribution, *etc.* On the other hand, it is still a mystery how matter survives escaping full annihilation with antimatter, because it is generally assumed that the same amount of matter and antimatter existed at the early stage of the hot universe. One interesting idea is that the universe might be a patchwork consisting of distinct regions of matter and antimatter still keeping the same amount of both, and we are just located on one of the matter patches. If this is the case, the universe as a whole is symmetric with respect to matter and antimatter. However, in this scenario the amount of annihilation near regional matter-antimatter boundaries is not negligible, and the observed cosmic γ ray spectrum would be considerably distorted, depending on the size of the patches. Actually, possible energy spectra were simulated as a function of the patch size. By comparing astronomical observations with these simulations, it was concluded that the size of the patch should be comparable to the size of the entire universe. This is considered to be rather unlikely, and thus, a matter-antimatter symmetric universe is unfavored [13]. The most recognized model to explain the matter dominant universe was proposed by Sakharov. It requires (1) baryon number non-conserving processes, (2) C- and CP violation, and (3) interactions far from thermal equilibrium conditions [14]. Although the CP symmetry is experimentally found to be violated for neutral mesons, which qualitatively supports the idea of Sakharov, the level of violation which is known is by far too small to explain the amount of matter observed in the present universe. Considering these facts, although speculative, CPT violation might be another possibility to drill a hole in the mystery of the matter dominant universe (see *e.g.*, refs. [8, 15, 16]).

2 Experiments to test CPT Symmetry

An important consequence of the CPT symmetry is that the mass, the total lifetime, the absolute values of the charge and the magnetic moment of an antiparticle should be exactly the same as those of the corresponding particle[7]. In addition, the spectroscopic properties of a complex anti-particle such as antihydrogen should again be exactly the same as those of the corresponding complex particle such as hydrogen. These facts provide potential schemes to test the CPT symmetry. Particularly when the particle is stable, observation time can be infinitely long, and accordingly, the mass/energy of particle conjugates in question can potentially be determined with arbitrarily high precision. In usual high precision measurements, experimental results are compared with predictions of precise and reliable theories taking into account all known interactions trying to find some finite deviations. Once successful, the residue can be attributed to a hidden interaction and/or to some important dynamics which need to be considered. In the case of CPT symmetry tests, the taste of the experiment can be qualitatively different from other high precision experiments described above, because detailed theoretical predictions are NOT necessary. As soon as a difference between matter and antimatter is observed, CPT violation is automatically confirmed. The research can be done purely experimentally, *i.e.*, the CPT test is performed and concluded in a model independent way. On the other

5 The SME also suggests sidereal-variation tests in the matter sector.

6 For example, as shown in table 1, the relative precision of 1S-2S transition of hydrogen is reported to be $\Delta\nu_{exp}/\nu \sim 4.2 \times 10^{-15}$. If the hydrogen mass is used in the denominator, this quantity may become $\Delta h\nu_{exp}/mc^2 \sim 4.2 \times 10^{-23}$

7 This does not necessarily exclude a possibility that the lifetime of a specific decay channel can be different between the paired particle and antiparticle

hand, no quantitative predictions are available from theory, and thus, experimentalists need to fix various experimental parameters as the physical quantities to be measured as well as their precision in a blind way, employing their full intuitions and sixth sense. In the following subsections, experiments on (K^0, $\overline{K}^0$), p/$\overline{p}$ and H/$\overline{H}$ are summarized and discussed, with special emphasis on p/$\overline{p}$ magnetic moments and H/$\overline{H}$ ground state hyperfine splittings.

2.1 K^0, $\overline{K^0}$

As is well-known, research on K^0 and $\overline{K^0}$ revealed for the first time that the CP symmetry is violated, which was one of the key findings to ignite theory to predict a three generation quark model [17]. At the same time, the CPT symmetry was reported to be verified with an accuracy as high as $|m(K^0) - m(\overline{K^0})|/m(K) < 6 \times 10^{-19}$ [18]. Although this is often cited as the most stringent test of the CPT symmetry, there is still a reservation on the way how it is discussed. In terms of energy, $|m(K^0) - m(\overline{K^0})|c^2 < 4.0\text{x}10^{-19}$GeV is obtained. Kobayashi *et al.* discussed that this small value just implies that CPT violating interaction, if any, is very weak compared to the strength of QCD. Considering the fact that $m(K^0) \neq m(\overline{K^0})$ requires both CP and CPT violations, it is more appropriate to compare the strength of possible CPT violation to the strength of CP violation [19]. Actually, the CP violation level of K^0 and $\overline{K^0}$ is $\mathrm{Im}(m_{12}) \sim 1.1 \times 10^{-17}$GeV, *i.e.*, the CPT violation could still be as large as a few % of the CP violation [20]. It is also noted that the accuracy above is comparable to the level of possible violation related with the gravity discussion (see Sec.1). It is evident that the experiments should be done with higher accuracy and also complementary experiments are necessary.

2.2 $\overline{p}$ and $\overline{H}$ related experiments

Proton (p) and antiproton ($\overline{p}$), as well as hydrogen (H) and antihydrogen ($\overline{H}$) are all stable, and thus meet the requirements to be observed for macroscopic time-scales and thus, perform high resolution spectroscopy.

Table 1 shows several comparisons of properties of conjugated particles such as the mass, the charge, and the g-factor for (e^-, e^+) and (p, $\overline{p}$). As a reference, some information of (μ^-, μ^+), (p, e^-), and (n, $\overline{n}$) conjugates is given as well. It is seen, that the CPT symmetry of these particles with respect to mass and charge has already been tested to the level of $10^{-8} \sim 10^{-9}$, corresponding to $\sim 10^{-9}$GeV for p/$\overline{p}$ and $\sim 10^{-12}$GeV for e^-/e^+. The g-factor of the (p, $\overline{p}$) pair is known with a precision of $4.4 \cdot 10^{-6}$. Actually, the g-factor measurements of an isolated proton [21] or an antiproton [22] just became possible very recently (See Sec. 3.2).

Table 1 Differences of mass, charge, and g-factor between electron and positron, and between proton and antiproton [18, 21, 38].

	$\frac{\lvert m_m - m_a\rvert}{m}$	$\frac{\lvert q_m + q_a\rvert}{\lvert q\rvert}$	$\frac{\lvert g_m + g_a\rvert}{\lvert g\rvert}$
e^- vs e^+	$< 8\times10^{-9}$	$< 4\times10^{-8}$	$(-0.5 \pm 2.1) \times 10^{-12}$
p vs $\bar{p}$	$< 2\times10^{-9}$	$< 2\times10^{-9}$	$< 5\times10^{-6}$
μ^- vs μ^+			$< (-0.11 \pm 0.12) \times 10^{-8}$
p vs e^-		$< 1 \times 10^{-21}$	
n vs $\bar{n}$	$(9 \pm 6) \times 10^{-5}$	–	–

Table 2 Spectroscopic properties of hydrogen.

	experiments (Hz)	$\frac{\Delta\nu_{exp}}{\nu}$	$\frac{\lvert\nu_{th} - \nu_{exp}\rvert}{\nu}$
ν_{1S-2S}	2,466,061,413,187,035 (10)	4×10^{-15}	1×10^{-11}
ν_{HF}	1,420,405,751.7667 (9)	6×10^{-13}	$(3.5 \pm 0.9) \times 10^{-6}$

Table 2 shows spectroscopic properties of the hydrogen atom, which are among the most precisely known quantities in atomic physics. The 1S-2S and ground state hyperfine transitions are experimentally determined with the fascinating precision of $\sim 4 \times 10^{-15}$ ($\sim$ 10 Hz) and $\sim 6 \times 10^{-13}$ ($\sim$1mHz), respectively [23]. On the other hand, as shown in Table 2, for the 1S-2S transition the theoretical accuracy is limited to 10^{-11} (10 kHz) and in case of the ground state hyperfine splitting to 10^{-5} (10 kHz). Once a $\overline{H}$ beam is available, an experiment can be conducted which would beat the limit of theoretical precision by two orders of magnitude. In the non-relativistic framework, the 1S-2S transition energy of hydrogen is given by

$$\frac{3}{4}\frac{m_e}{2}\frac{m_p}{m_e + m_p}(\alpha c)^2, \tag{1}$$

where m_e and m_p are the electron and proton masses, respectively, and α the fine structure constant defined by $\left(\frac{q_e q_p}{4\pi\epsilon_0 \hbar c}\right)^2$, where q_e and q_p are the electron and proton charges, respectively, ϵ_0 the vacuum dielectric constant, and c the speed of light. The electron mass defines the transition frequency at leading order, while the proton mass contributes at the level of 10^{-3}. Taking relativistic

and QED effects into account brings shifts at the 10 ppm level. The present theoretical limit of 10^{-11} is due to the ambiguity on the proton charge radius[8]. In the case of the ground state hyperfine transitions, it originates from the interaction between the magnetic moments of the proton and the electron, *i.e.*, this effect increases with the overlap of proton and electron wave-functions, like in the case of S states, particularly 1S state. The transition frequency between the singlet (F=0) and the triplet (F=1) states of hydrogen in its ground state is given by

$$\nu_{HF} = \frac{8}{3}\left(\frac{m_p}{m_p + m_e}\right)^3 \frac{m_e}{m_p}\frac{\mu_e}{\mu_B}\frac{\mu_p}{\mu_N}\frac{m_e(\alpha^2 c)^2}{h} \tag{2}$$

which approximates the proton as a point-like particle. Here μ_e and $\mu_B (= q_e\hbar/2m_e)$ are the magnetic moments of electron and the Bohr magneton, respectively, and μ_p and μ_N are the magnetic moments of proton and nucleon, respectively. The hyperfine transitions are directly proportional to the magnetic moment of proton as well as to that of electron. Thus, from a measurement of the ground state hyperfine splitting of $\overline{\mathrm{H}}$ an independent value for the magnetic moment of $\overline{\mathrm{p}}$ is obtained (see also section 3. 2). This is in contrast with 1S-2S transition, where the electron mass primarily determines the transition energies. Considering that μ_e/μ_B is -1.0011596521811 and μ_p/μ_N is 2.7928473565, the observed transition frequency can be reproduced with a precision of 10^{-5}, which is further improved to $3.5{\cdot}10^{-6}$ when the charge and magnetization radius of proton is taken into account. Again, the prediction level is limited by the uncertainty of charge and magnetization distribution of the proton [24]. Considering the fact that the 1S-2S transition and the hyperfine transitions are both reproduced by the CPT conserving theories to the level of 10 kHz, any experiment which aims for the discovery of the CPT violation should exceed this accuracy. Until now, it is not known which transition (*i.e.*, 1S-2S or hyperfine) is more sensitive for the CPT symmetry test. However, in the first order perturbation theory of the SME, in case of the 1S-2S transition the CPT violating energy shift cancels exactly. Thus, higher sensitivity to CPT violation is expected in case of the hyperfine transition [10]. In addition, a beam-based hyperfine transition experiment has higher potential to reach better resolution than 1S-2S transition of trapped $\overline{\mathrm{H}}$. It is noted that the hyperfine transition measurements of $\overline{\mathrm{H}}$ and magnetic moment

[8] The charge radius extracted from the pμ^- Lamb shift measurement [24] is reported to be 5σ away and smaller than the currently accepted CODATA value.

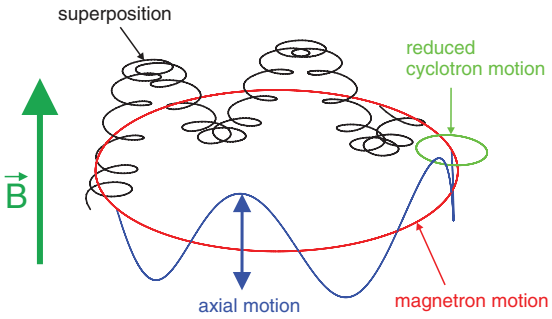

Figure 1 Trajectory of a single particle in a Penning trap, which is a superposition of three uncoupled harmonic oscillators.

measurement of the bare $\overline{\mathrm{p}}$ yield complementary and important information on the magnetic moment of $\overline{\mathrm{p}}$, since the hyperfine transition reflects the magnetization distribution inside $\overline{\mathrm{p}}$ probed by a positron and the spin transition frequency of bare $\overline{\mathrm{p}}$ reflects the overall magnetic moment probed by a macroscopic external magnetic field.

3 Precision Investigation of the Proton and the Antiproton

3.1 (Anti)proton charge and mass

The charge-to-mass ratios q/m of the p and the $\overline{\mathrm{p}}$ were compared with a fractional precision of $9{\cdot}10^{-11}$, which corresponds to $(q/m)_p/(q/m)_{\bar{p}} = -0.99999999991(9)$ [25]. Assuming $q_p = q_{\bar{p}}$, the accuracy in energy is about 0.08 eV. This fascinating test of the CPT symmetry was reported by the TRAP collaboration, which compared the free cyclotron frequencies $\nu_c = qB/(2\pi m)$ of an H^--ion and a single antiproton stored in a cryogenic Penning trap setup. Such a trap is a superposition of a homogeneous magnetic field B in the axial direction and an electrostatic quadrupolar potential. The trajectory of a particle stored in such a superposition of electric and magnetic fields is shown in Fig. 1.

It can be described as the superposition of three uncoupled harmonic oscillators, one at the *modified cyclotron frequency* ν_+, which is ν_c slightly modified by the trapping potential, another at the *axial frequency* ν_z, and a third one at the *magnetron frequency* ν_-. The free cyclotron frequency is obtained by measuring ν_+, ν_z and ν_-, and application of the so called invariance theorem [26]

$$\nu_c^2 = \nu_+^2 + \nu_z^2 + \nu_-^2. \tag{3}$$

The eigenfrequencies are measured non-destructively via image current detection. To achieve this high precision measurement several pioneering techniques were invented, as catching of antiprotons from the CERN Low Energy Antiproton Ring (LEAR) [27], electron cooling of antiprotons [28], and trapping of a single antiproton for arbitrarily long time [29].

In addition to these experiments, high precision laser spectroscopy of exotic $\bar{p}\mathrm{He}^+$ atoms has achieved impressive progress. These experiments allow for the measurement of the antiproton related Rydberg constant, which is proportional to $m_{\bar{p}} q_{\bar{p}}^2 q_e^2$. Thus, by combining the results of laser spectroscopy with the measured charge-to-mass ratio, the mass and the charge of the antiprotons can be extracted independently, and compared with those of the proton. Recently, Hori *et al.* reported on an agreement of both values at the sub-ppb level [30]. It is an amazing fact that once the used laser spectroscopy techniques slightly improve, the mass of the antiproton can be determined with higher accuracy than that of the proton. It is noted that in order to extract mass and charge of antiprotons, the experimentally obtained transition frequencies have to be compared with challenging theoretical three body calculations. For CPT tests at even higher precision, theoretical methods have to be improved significantly.

3.2 (Anti)proton magnetic moment

Among the numerous comparisons of different fundamental particle properties, one quantity has not yet been compared with high precision: the magnetic moment of the proton μ_p and the antiproton $\mu_{\bar{p}}$. Here, $\mu_{p,\bar{p}} = g_{\mathrm{p}/\bar{\mathrm{p}}}/2 \cdot q_{\mathrm{p}/\bar{\mathrm{p}}}\hbar/(2m_{\mathrm{p}/\bar{\mathrm{p}}})$, where $g_{\mathrm{p}/\bar{\mathrm{p}}}$ is the Landé g-factor, and $q_{p/\bar{p}}/m_{p,\bar{p}}$ the (anti)proton charge-to-mass ratio. The magnetic moment of the proton is known with a fractional accuracy of $8.2{\cdot}10^{-9}$ [31]. This value is based on hyperfine spectroscopy data of an atomic hydrogen maser in a magnetic field, from which the magnetic moment ratio of the proton and the electron bound in atomic hydrogen $\mu_{\mathrm{p}}(\mathrm{H})/\mu_{\mathrm{e}}(\mathrm{H})$ was extracted at that level. The g-value of the free proton

$$g_{\mathrm{p}} = g_{\mathrm{e}} \cdot \frac{\mu_{\mathrm{p}}(\mathrm{H})}{\mu_{\mathrm{e}}(\mathrm{H})} \cdot \frac{g_{\mathrm{p}}}{g_{\mathrm{p}}(\mathrm{H})} \cdot \frac{g_{\mathrm{e}}(\mathrm{H})}{g_{\mathrm{e}}} \cdot \frac{m_{\mathrm{p}}}{m_{\mathrm{e}}} \tag{4}$$

is calculated, where the g-factor of the electron g_{e}, and the proton-to-electron mass ratio $m_{\mathrm{p}}/m_{\mathrm{e}}$ are known at a level of $2.8 \cdot 10^{-13}$ [32] and $7.3 \cdot 10^{-10}$ [33], respectively. The theoretical correction terms $g_{\mathrm{p}}/g_{\mathrm{p}}(\mathrm{H})$ and $g_{\mathrm{e}}(\mathrm{H})/g_{\mathrm{e}}$ are reviewed in [34, 35] and are also known at the level $< 10^{-9}$, resulting in [36]

$$g_{\mathrm{p}} = 5.585694713(46), \tag{5}$$

limited by the experimental precision achieved in the hydrogen-maser experiment [31]. In contrast, the magnetic moment of the antiproton is only known with moderate precision. Currently two collaborations, a part of ATRAP and BASE, are pushing their efforts to measure the (anti)proton magnetic moment with sub-ppb precision. These experiments are based on spectroscopy with single particles stored in a Penning trap at 4 K. A major step towards this goal was achieved in 2011. Spin flips of a single trapped proton were observed for the first time [21, 37]. Recently, diSciacca *et al.* (ATRAP) reported on a $4.4{\cdot}10^{-6}$ measurement of the antiproton magnetic moment [22], which corresponds to a 680-fold improvement of the formerly best value [39]. In this experiment the particle's magnetic moment was measured in units of the nuclear magneton μ_N

$$\frac{\mu_{\bar{p}}}{\mu_N} = \frac{g}{2}\frac{e_{\bar{p}}/m_{\bar{p}}}{e_p/m_p} = \frac{\nu_L}{\nu_c}. \tag{6}$$

by determination of the free cyclotron frequency ν_c, and the spin precession frequency $\nu_L = g/2 \cdot \nu_c$ of a single antiproton. While the measurement of ν_c is straight forward [40], the determination of the spin precession frequency ν_L is a major challenge. It is based on the application of the continuous Stern-Gerlach effect, which has already been applied in the widely recognized $g-2$ comparisons of the electron and the positron [41]. However, these measurements involved magnetic moments at the level of the *Bohr magneton*. In contrast the magnetic moments of the proton/antiproton system are at the level of the *Nuclear magneton*, which is about 660 times smaller. This complicates the (anti)proton magnetic moment measurement significantly. A magnetic inhomogeneity

$$\vec{B} = B_0\vec{e}_z + B_2\left((z^2 - \rho^2/2)\vec{e}_z - z\rho\vec{e}_\rho\right). \tag{7}$$

is superimposed to the Penning trap, where B_2 characterizes its strength. This adds a spin dependent magnetic potential $\Phi_M = \pm\mu B_2 z^2$ to the axial electrostatic potential, and consequently, the axial oscillation frequency becomes spin dependent. Compared to a *magnetic moment-down* particle, a *magnetic moment-up* particle has a lower oscillation frequency ν_z. Thus, the determination of the spin eigenstate is reduced to a non-destructive frequency measurement. The spin

precession frequency ν_L is determined by the following sequence: first the axial frequency is measured, and subsequently a spin flip is driven by a magnetic radio-frequency drive with field vector $\vec{b}_{\mathrm{rf}}$ perpendicular to B_0 at a frequency ν_{rf}, which is close to the Larmor frequency ν_L. Afterwards the axial frequency is measured again. The detection of an axial frequency shift indicates a spin quantum jump. By repeating this sequence for several 100 times and different drive frequencies ν_{rf}, the spin flip probability is obtained as a function of ν_{rf}. From the well understood line-shape the Larmor frequency can be extracted with high precision. However, the axial frequency shift induced by an (anti)proton spin flip, is

$$\delta\nu_{\mathrm{z,SF}} = \frac{\mu B_2}{2\pi^2 m\nu_z}, \tag{8}$$

which is for typical experimental parameters ($\nu_z \approx$ 600 kHz to 1 MHz) in the order of a few hundred nHz$\cdot B_2$. Thus, to obtain a clearly detectable spin flip induced axial frequency jump, a very strong B_2 (300000 T/m^2) has to be used [21, 38]. Under these extreme conditions a spin quantum jump shifts the axial frequency by about 150 mHz to 200 mHz out of 600 kHz to 1 MHz.

The strong magnetic inhomogeneity constitutes a major challenge. In addition to the spin magnetic moment it couples as well the radial magnetic moments of the cyclotron mode and the magnetron mode to the axial frequency, which is shifted by

$$\Delta\nu_z(n_+, n_-) = \frac{h\nu_+}{4\pi^2 m_{\mathrm{p}}\nu_z}\frac{B_2}{B_0}\cdot\left(\left(n_+ + \frac{1}{2}\right) + \frac{\nu_-}{\nu_+}\left(n_- + \frac{1}{2}\right)\right), \tag{9}$$

where n_+ and n_- are the quantum numbers of the modified cyclotron and the magnetron mode, respectively. A cyclotron quantum jump $\Delta n_+ = \pm 1$ corresponds to a radial energy change of $\Delta E_+ = \pm 74$ neV and causes an axial frequency shift of $\Delta\nu_z = \pm 68$ mHz. A transition of the magnetron quantum number $\Delta n_- = \pm 1$ leads to $\Delta\nu_z = \pm 49\,\mu$Hz. Changes of both radial quantum numbers $\Delta n_\pm = \pm 1$ are due to easily driven electric dipole transitions. Spurious electrical field noise with amplitudes in the order of only a few 10 nV$\cdot$m$^{-1}\cdot$Hz$^{-1/2}$ cause fluctuations of ν_z, which are large enough to avoid the unambiguous detection of single (anti)proton spinflips. However, with the axial frequency stability reached by the two experiments [21, 38] it was possible to measure the (anti)proton magnetic moment in the strong B_2 by means of a statistical detection technique. Once spin flips are driven, the corresponding axial frequency shifts

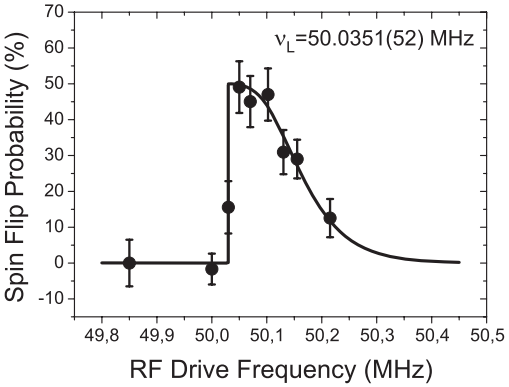

Figure 2 Larmor resonance curve measured with a single trapped proton.

$\delta\nu_{\mathrm{z,SF}}$ add up to the axial frequency fluctuation Ξ_{back}, which is defined as the rms-value of the difference of two subsequent axial frequency measurements $\nu_{z,i+1} - \nu_{z,i}$, in a statistical way

$$\Xi_{\mathrm{SF}} \approx \sqrt{\Xi^2_{\mathrm{back}} + P_{SF}\delta\nu^2_{z,SF}}. \tag{10}$$

By measuring Ξ_{SF} for different drive frequencies ν_{rf}, the spin flip probability $P_{SF}(\nu_{\mathrm{rf}})$ is obtained as well. The result of the first Larmor resonance curve ever measured with this technique [21] is shown in Fig. 2. The asymmetry of the resonance curve is easy to understand. While a spin flip is driven, the particle is in contact with the axial detection system, which leads to Boltzmann distributed fluctuations of the particle's axial energy E_z. As a consequence the Larmor frequency fluctuates since

$$\nu_L(E_z) = \nu_{L,0}\left(1 + \frac{B_2}{B_0}\frac{E_z}{2\pi^2 m\nu_z^2}\right), \tag{11}$$

and thus, the resonance is a convolution of the unperturbed spin transition-line with the asymmetric Boltzmann profile $w(E_z) = \frac{1}{kT_z}\exp(-E_z/(k_B T_z))$, where T_z is the temperature of the axial detection system. From a best fit to these data ν_L is obtained with 100 ppm precision. With an improved apparatus BASE obtained meanwhile a Larmor frequency resolution of $1.8{\cdot}10^{-6}$ [42], while the Harvard group reached a precision of $1.7{\cdot}10^{-6}$ [38]. For the determination of the g-factor, the cyclotron frequency is measured by using the same principle as in the case of the Larmor line, but with an electrical dipole drive tuned to the modified cyclotron frequency. The drive amplitude is chosen weak enough to avoid a significant increase of E_+, but it clearly affects the axial frequency fluctuation as a function of the drive frequency.

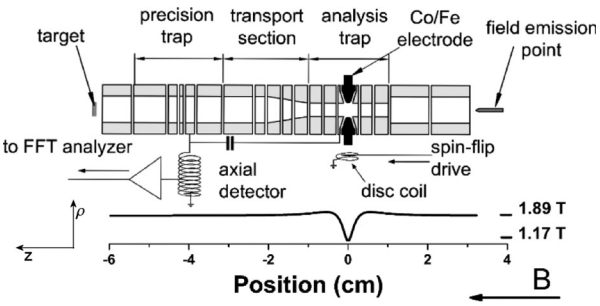

Figure 3 Schematic of a double Penning trap setup [21]. The system consists of two Penning traps which are connected by transport electrodes. The central ring electrode of the analysis trap is made of ferromagnetic material. The lower graph shows the magnitude of the magnetic field along the *z*-axis. For further details see text.

Again ν_+ is obtained from a best fit and

$$g/2 = 2.792\,849\,(25) \tag{12}$$

is extracted. The precision of this value is limited by the cyclotron frequency determination [42]. However, another order of magnitude can be gained easily by more accurate sampling of the cyclotron resonance line. This strategy was applied by di Sciacca *et al.*, who obtained [38]

$$g/2 = 2.792\,846\,(7). \tag{13}$$

By further improvement of the experimental setups the results of the statistical detection method may be improved by another order of magnitude, but as a matter of principle a limit is set by the strong magnetic bottle which produces an unavoidable line-width. To reach even higher precision, a group at Mainz developed the elegant double-trap method [43], in which the precision frequency measurements and the detection of the spin state are separated to two traps: a precision trap (PT) with a very homogeneous magnetic field, and an analysis trap (AT) with the strong superimposed magnetic inhomogeneity. Such a setup is shown in Fig. 3. The two traps are connected by transport electrodes. Voltage ramps applied to these electrodes are used to shuttle the particle between the traps. A magnetic moment measurement starts with the determination of the spin state in the analysis trap. Subsequently the particle is transported to the precision trap, where the cyclotron frequency is measured, while a spin flip drive is injected to the trap. Afterwards the particle is transferred back to the AT and the spin state is analyzed again. This measuring sequence is very similar to the *g*-factor measurement which has already been described above, with one major difference: Spin flips are driven in a magnetic field which is about a factor of 100000 more homogeneous than in the analysis trap. This reduces the line-shape dramatically and boosts experimental precision. This method has been applied successfully in experiments for the high precision determination of the magnetic moment of the electron bound to hydrogen-like ions [44, 45], for precise tests of bound state quantum electrodynamics. In these experiments precisions at the level of 0.5 ppb were achieved. The successful application of this method to measure the magnetic moment of the antiproton would provide a 1000-fold improved test of the CPT symmetry with baryons.

To apply this technique, single spin flip resolution is required, *i. e.*, it is crucial to clearly identify the spin eigenstate of the particle in the analysis trap. So far this was not possible due to the limited axial frequency stability, but recently important progress towards a first application of this technique has been reported [46]: single spin flips were clearly resolved for the first time with a significantly improved apparatus and the application of an elegant Bayesian analysis. The spin state of a single trapped proton was identified with a fidelity of about 90 %. Based on these results BASE demonstrated the application of the double Penning-trap method [47] for the first time, which paves a path to measure the magnetic moment of both, the proton and the antiproton, with ppb precision.

4 Precision Spectroscopy of Antihydrogen

4.1 $\overline{\mathrm{H}}$ synthesis and manipulation

Synthesis of antihydrogen ($\overline{\mathrm{H}}$) atoms has been intensively studied in the last decades [48, 49] to make stringent tests of the CPT symmetry via high precision spectroscopy either of the 1S-2S transition [50, 51] or of ground state hyperfine transitions [52–54]. Recently, studies on the gravitational interaction of antimatter ($\overline{\mathrm{H}}$) and matter (the earth), the so-called weak-equivalence principle, were also proposed [55, 56]. The cold antihydrogen research celebrated the first milestone in 2002, when ATHENA and ATRAP successfully synthesized cold $\overline{\mathrm{H}}$ atoms in a uniform magnetic field [57, 58]. Both groups aimed for 1S-2S high precision laser spectroscopy, and accordingly the next critical step was to prepare ultracold $\overline{\mathrm{H}}$ atoms (< 1 K) in the low-field-seeking states and to trap them in the Ioffe-Pritchard trap or a variant of it having minimum B field configurations [59, 60]. $\overline{\mathrm{H}}$ atoms were not really controlled, and the synthesis was only confirmed by annihilation signals, *i.e.*, it was a

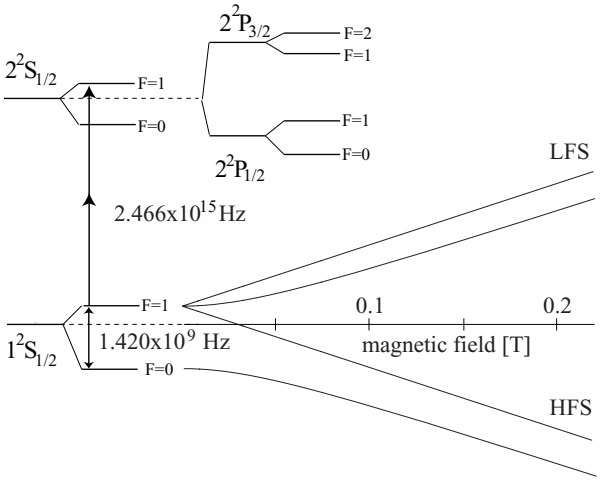

Figure 4 Frequency diagram of 1S-2S and ground state hyperfine transitions together with the variation of hyperfine levels as a function of magnetic field.

kind of archaeological approach, which confirmed that $\overline{H}$ atoms existed some time before the detection of their annihilation. After several years of experimental developments, ALPHA realized the second milestone in 2010, the success of trapping 39 $\overline{H}$s [61]. Just one month later, the ASACUSA-CUSP group reported on the successful synthesis of $\overline{H}$ atoms in a non-uniform magnetic field, a so-called cusp trap, which was a major step to extract an $\overline{H}$ beam to a field-free region for high precision microwave spectroscopy. This is essential for high resolution microwave spectroscopy of $\overline{H}$ hyperfine transitions [62] (see Sec 4.2). In 2011, ALPHA succeeded in trapping antihydrogen atoms for more than 1000s [63]. In presence of a magnetic field, the ground state hyperfine levels of $H/\overline{H}$ split into four sub-states, as shown in Fig. 4. Two of them become higher with increasing magnetic field, *i.e.*, they are attracted towards lower magnetic fields, and are named as *low-field seeking (LFS) states*. The other two levels are lowered, *i.e.*, they are attracted towards high magnetic fields, and are named *high-field seeking (HFS) states*. Figure 4 also shows, that the potential energy corresponding to the magnetic field difference of 0.2 T amounts to ∼3GHz. In other words, even for a magnetic trap with a magnetic field difference of 1 T, the trap depth is only about 0.7 K (∼ 14GHz).

4.2 Cusp trap scheme to extract $\overline{H}$ for microwave spectroscopy

For high resolution microwave spectroscopy, a weak and uniform magnetic field is essential. In order to make this practically feasible, a potential scheme had been invented employing a pair of anti-Helmholtz coils [52], which is called the cusp trap scheme. This opens for the first time a path to realize high precision microwave spectroscopy of antihydrogen ground state hyperfine transitions [52, 62]. Figure 5 shows a conceptual drawing of the experimental setup, which consists of the unique cusp trap (the combination of superconducting anti-Helmholtz coils and a stack of multiple ring electrodes (MRE)), a microwave cavity, a sextupole magnet, and an $\overline{H}$ detector. The cusp trap provides the minimum B field configuration still maintaining axially symmetric magnetic and electric fields, which enables stable manipulation of both $\overline{p}$s and e^+s such as trapping, cooling, compression, and mixing [64, 65]. Further, once $\overline{H}$ atoms are formed by mixing $\overline{p}$ and e^+ in the cusp trap, $\overline{H}$ atoms in low-field-seeking (LFS) states are preferentially focused along the cusp trap axis whereas those in high-field-seeking (HFS) states are strongly defocused, resulting in the formation of an intensity-enhanced spin-polarized $\overline{H}$ beam [52]. The microwave cavity is installed downstream of the cusp trap along the beam line in a weak, highly uniform magnetic field, which is carefully shielded from parasitic stray fields. A preliminary simulation revealed that the spin-polarization of a 50 K $\overline{H}$ beam amounts to about 30 % [66]. The microwave induces hyperfine transitions from LFS to HFS states when the microwave frequency matches with one of transition frequencies. The sextupole magnet sorts out $\overline{H}$ atoms in HFS states from those in LFS states. By recording the antihydrogen signal as a function of the drive frequency applied to the microwave cavity, the hyperfine structure becomes accessible. Figure 6(a) schematically shows the central part of the setup. It consists of the $\overline{p}$ catching trap [67], the e^+ accumulator, the cusp trap, and the 3D track detector to monitor $\overline{p}/\overline{H}$ annihilation near the cusp trap.

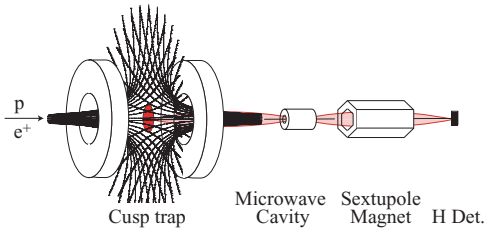

Figure 5 A conceptual experimental setup for the ground-state hyperfine transition measurements of $\overline{H}$ atoms with the cusp trap (see the text for more details).

Antiprotons of 5.3 MeV from the Antiproton Decelerator (AD) at CERN are extracted into the ASACUSA area, slowed down to ∼120 keV by a radio frequency

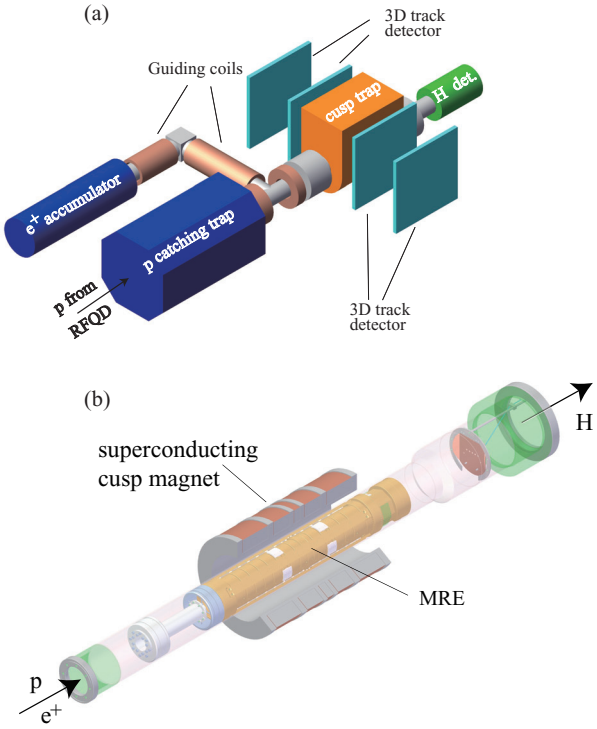

Figure 6 (a) A schematic drawing of the present experimental setup, which consists of the $\overline{\mathrm{p}}$ ($\overline{\mathrm{p}}$) catching trap, the compact positron (e^+) accumulator, the cusp trap for $\overline{\mathrm{H}}$ synthesis, the 3D track detector, and the $\overline{\mathrm{H}}$ detector downstream of the cusp trap. (b) The central part of the cusp trap, which consists of a superconducting solenoid coils, a cryogenic UHV bore tube, and an MRE installed in the bore tube.

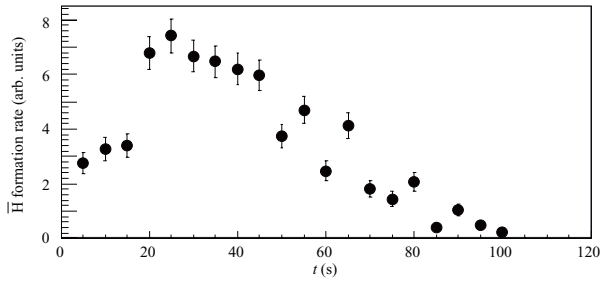

Figure 7 The number of field-ionized antihydrogen atoms accumulated in the field ionization trap. For this measurement the trap was opened every 5 s.

quadrupole decelerator (RFQD). Subsequently they are injected into the $\overline{\mathrm{p}}$ catching trap. Typically, $\sim 10^6\overline{\mathrm{p}}$s are accumulated and electron-cooled. The $\overline{\mathrm{p}}$ cloud is then radially compressed [68] which ensures efficient particle transfer to the cusp trap. Figure 6(b) shows the central part of the cusp trap structure, which consists of superconducting coils (B_{max}=2.7 T), a UHV cryogenic bore tube (6K), an MRE at the center of the coils. Figure 7 shows an example of the $\overline{\mathrm{H}}$ intensity variation since the start of the mixture of $3\times10^5\overline{\mathrm{p}}$s in 3×10^6 positrons [62]. The number increased in the first 30 s and then slowly decreased in the next 80 s yielding totally 70 events per mixture. The total number of $\overline{\mathrm{H}}$ atoms in high Rydberg states was estimated to be about 7×10^3 per mixture.

As already mentioned in section 2.2, from a measurement of the ground state hyperfine transition frequency at the ppm level together with an independent measurement of the magnetic moment of the antiproton at the same level (see section 3.2), constraints on antiproton substructure are obtained.

4.3 $\overline{\mathrm{H}}$ trapping for 1S-2S spectroscopy

In contrast to the beam concept applied in ASACUSA, ALPHA and ATRAP plan to perform spectroscopy with trapped antihydrogen atoms. Figure 8 (a) schematically shows the central part of the ALPHA setup used to synthesize and trap $\overline{\mathrm{H}}$ atoms [61]. The octupole coil provides a strong magnetic field gradient in the radial direction, and the pair of mirror coils produce a field gradient in the axial direction. A magnetic bottle is formed by the combination of these fields, which is an Ioffe-Pritchard type trap but employing an octupole coil instead of a usually used quadrupole. The magnetic field difference is about 0.7T, which can trap antihydrogen at temperatures up to 0.5 K. It is noted that the azimuthal uniformity of the usual Ioffe-Pritchard trap near the magnetic field axis is poor, which results in an instability in storing $\overline{\mathrm{p}}$s and positrons, the ingredients of antihydrogen. In order to match the interaction energy of $\overline{\mathrm{p}}$s and e^+ sensitively, so that potentially colder antihydrogen is synthesized, a so-called auto-resonance scheme had been employed. This can exclusively induce a center of mass motion, which doesn't affect the internal temperature of the $\overline{\mathrm{p}}$ cloud [69].

When the antihydrogen synthesis reactions are more or less over (about 1s after the mixing started), $\overline{\mathrm{p}}$s and positrons are cleaned up by applying voltages on the MRE. Then, the octupole coil and the pair of mirror coils are quenched to open the magnetic bottle. As soon as the magnetic bottle is opened, trapped $\overline{\mathrm{H}}$s are released, if any, and annihilate hitting the inner-wall of the MRE near the magnetic bottle. The red inverted triangles, the blue triangles, and the green circles in Fig. 8(b) shows such events as functions of the annihilation position and the time of annihilation since the quench of the magnetic bottle. Different symbols correspond to different electric fields applied. As is seen, the annihilation

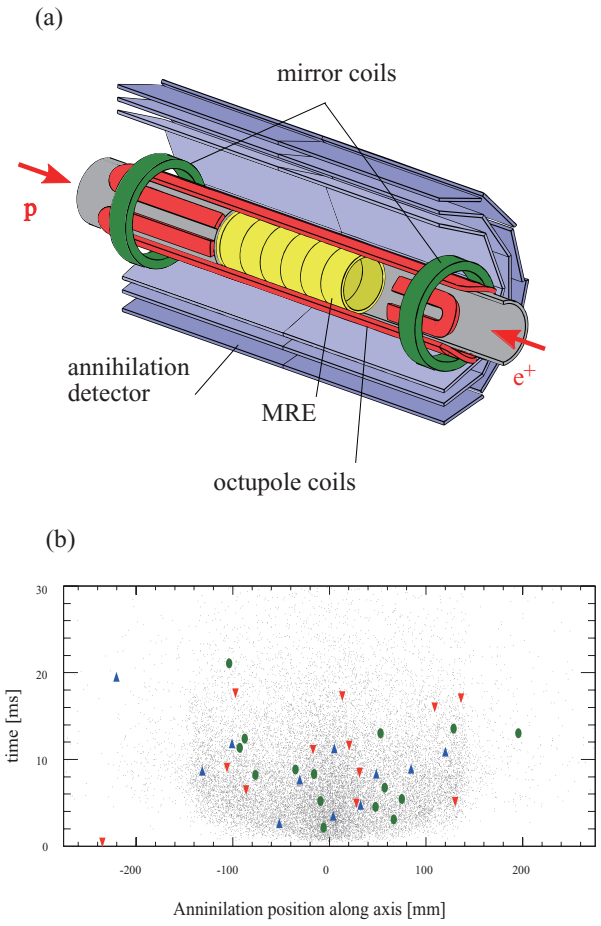

Figure 8 (a) A schematic drawing of antihydrogen synthesis and trapping region. The atom-trap magnets, the modular Si annihilation detector and some of the Penning trap electrodes are shown. An external solenoid (not shown) provides a 1 T magnetic field for the Penning trap. (b) Measured t-z distribution for annihilations obtained with no bias (circles), left bias (triangles), right bias (inverted triangles). The gray dots are from a numerical simulation of antihydrogen atoms at ground state. The simulated atoms have a maximum kinetic energy of 0.1 meV.

position did not depend on the electric field configurations. The fine gray dots in Fig. 8(b) show the results of simulation assuming antihydrogen atoms were trapped in the magnetic bottle. Repeating such runs, totally 38 trapped antihydrogen events were identified in 335 trials. The ATRAP collaboration also reported on successful trapping of $\overline{H}$ [70].

The next step is to laser-cool trapped $\overline{H}$s and to make laser spectroscopy. The Zeeman broadening due to magnetic field distribution in a magnetic bottle affects the spectroscopic resolution, which could amount to as high as 10^6 Hz. Donnan *et al.* reported that $\overline{H}$s can be cooled just by a one directional pulsed laser as low as 20 mK [71], which would improve resolution. Recently, hyperfine transitions of $\overline{H}$ trapped in a magnetic bottle have been successfully induced by a microwave drive in the right frequency range [72].

5 summary

In this article a brief motivation on tests of the CPT symmetry and their significance in physics was given. Particularly the experimental progress on tests with $\overline{p}$ and $\overline{H}$ was reviewed. Penning trap based experiments to measure the magnetic moments of a single proton and an antiproton have recently become possible, and in preamble experiments a precision in the order of 10^{-6} was achieved. The recently resolved single proton spin flips, and the first demonstration of the double Penning trap technique with a single proton are a major step towards another factor of 1000 improvement.

A cusp trap scheme for the efficient extraction of a spin-polarized $\overline{H}$ beam to a magnetic-field-free region has been developed. In the cusp antihydrogen atoms were synthesized successfully. This development allows for the first time a high precision ground state hyperfine spectroscopy of $\overline{H}$. By combining these quantities, constraints on the internal structure (magnetization distribution) of $\overline{p}$ are obtained, which constitutes another stringent test of the CPT symmetry. Successful trapping of $\overline{H}$ in a magnetic bottle has been demonstrated recently, which will soon allow first laser spectroscopy of the 1S-2S transition of antihydrogen atoms. Further cooling of trapped antihydrogen atoms would become an important issue to realize high resolution spectroscopy. Cold $\overline{H}$ research is now at a stage where first experiments to precisely investigate fundamental symmetries can start.

Key words. CPT symmetry, Antimatter, Fundamental Interactions.

Yasunori Yamazaki was a professor of the University of Tokyo from 1993 to 2011. In 1997, he was joint-appointed as a Chief Scientist of RIKEN, and then continues his carrier at RIKEN as a Distinguished Senior Scientist from 2011. He was the International Chairperson of ICPEAC from 2005 to 2007. He has been studying fundamental physics via antimatter as well as radiation biology via micro irradiation on living cells. He was awarded the Fellow of American Physical Society in 2011, 15th Matsuo Foundation

Hiroshi Takuma Memorial Award in 2011, and 52nd Toray Science and Technology Prize in 2012.

Stefan Ulmer received his PhD in 07/2011 at the University of Heidelberg for the first observation of spin flips with a single trapped proton. As a postdoctoral fellow he joined the ASACUSA CUSP collaboration and worked on the production of a polarized antihydrogen beam. Since 04/2012 he is leading a RIKEN initiative research unit as well as the international BASE collaboration at CERN, which intends to measure the magnetic moment of the antiproton with high precision.

References

[1] T. D. Lee and C. N. Yang, Phys. Rev. **98**, 1501 (1955).
[2] G. Lueders, Ann. Phys. **2**, 1 (1957).
[3] C. S. Wu, E. Ambler, R. W. Hayward, D. D. Hoppes, and R. P. Hudson, Phys. Review **105**, 1413 (1957).
[4] V. Fanti *et al.*, Phys. Lett. B **465**, 335 (1999).
[5] J. P. Lees *et al.*, Phys. Rev. Lett. **109**, 211801 (2012).
[6] K. P. Jungmann, AIP Conf. Proc. **793**, 18 (2005).
[7] see *e.g.*, A. Kostelecky, R. Potting, Nucl. Phys. B **359**, 545 (1991).
[8] M. Chaichian *et al.*, http://arxiv.org/abs/1210.0208.
[9] A. D. Dolgov and V. A. Novikov , JETP Letters **95**, 594 (2012).
[10] R. Bluhm, A. Kostelecky, and N. Russell, Phys. Rev. D **57**, 3932 (1998).
[11] R. Bluhm, A. Kostelecky, and N. Russell, Phys. Rev. Lett. **82**, 2254 (1999).
[12] A. Kostelecky and N. Russell, Rev. Mod. Phys. **83**, 11 (2011).
[13] A. G. Cohen, A. De Rujula, and S. L. Glashow, Astrophys. J **495**, 539 (1998).
[14] A. D. Sakharov, Sov. Phys. Usp. **34**, 392 (1991).
[15] A. D. Dolgov and Y. B. Zeldovich, Rev. Mod. Phys. **53**, 1 (1981).
[16] A. D. Dolgov, Physics of Atomic Nuclei **73**, 588 (2010).
[17] M. Kobayashi and T. Masukawa, Prog. Th. Phys. **49**, 652 (1973).
[18] J. Beringer *et al.*, (Particle Data Group), Phys. Rev. D **86**, 010001 (2012).
[19] M. Kobayashi and A. I. Sanda, Phys. Rev. Lett. **69**, 3139 (1992).
[20] I. I. Bigi, Nucl. Phys. A **692**, 227c (2001).
[21] S. Ulmer, C. C. Rodegheri, K. Blaum, H. Kracke, A. Mooser, W. Quint, and J. Walz, Phys. Rev. Lett. **106**, 253001 (2011).
[22] J. DiSciacca *et al.*, Phys. Rev. Lett. **110**, 130801 (2013).
[23] N. Ramsey, *Atomic hydrogen hyperfine structure experiments, in Quantum Electrodynamics* ed. T Kinoshita (*World Scientific* 1990), 673 (1990).
[24] R. D. Pohl *et al.* Nature **466**, 213 (2010).
[25] G. Gabrielse, A. Khabbaz, D. S. Hall, C. Heimann, H. Kalinowsky, and W. Jhe, Phys. Rev. Lett. **82**, 3198 (1999).
[26] L. S. Brown and G. Gabrielse, Phys. Rev. A **25**, 2423 (1982).
[27] G. Gabrielse *et al.*, Phys. Rev. Lett. **57**, 2504 (1986).
[28] G. Gabrielse *et al.*, Phys. Rev. Lett. **63** 1360 (1989).
[29] G. Gabrielse, D. F. Phillips, W. Quint, H. Kalinowsky, G. Rouleau, and W. Jhe, Phys. Rev. Lett **74**, 3544 (1995).
[30] M. Hori *et al.*, Nature **475**, 484 (2011).
[31] P. F Winkler, D. Kleppner, T. Myint, and F. G. Walther, Phys. Rev. A **5**, 83 (1972).
[32] D. Hanneke, S. Fogwell, and G. Gabrielse, Phys. Rev. Lett. **100**, 120801 (2008).
[33] T. Beier, H. Häffner, N. Hermanspahn, S. G. Karshenboim, H. -J. Kluge, W. Quint, S. Stahl, J. Verdù, and G. Werth, Phys. Rev. Lett. **88**, 011603 (2001).
[34] P. Mohr, B. Taylor, and D. Newell, Rev. Mod. Phys. **80**, 633 (2008).
[35] S. G. Karshenboim and V. G. Ivanov, Can. J. Phys. **80**, 1305 (2002).
[36] S. G. Karshenboim and V. G. Ivanov, Phys. Lett. B **566**, 27 (2003).
[37] R. Blatt, Nature **475**, 298 (2011).
[38] J. DiSciacca and G. Gabrielse, Phys. Rev. Lett. **108**, 153001 (2012).
[39] T. Pask, D. Barna, A. Dax, R. S. Hayano, M. Hori, D. Horvath, S. Friedreich, B. Juhasz, O. Massiczek, and N. Ono, Phys. Lett. B **678**, 55 (2009).
[40] S. Ulmer, K. Blaum, H. Kracke, A. Mooser, C. C. Rodegheri, W. Quint, and J. Walz, Phys. Rev. Lett. **107**, 103002 (2011).
[41] R. S. VanDyck, P. B. Schwinberg, and H. G. Dehmelt, Phys. Rev. Lett. **59**, 26 (1987).
[42] C. C. Rodegheri, K. Blaum, H. Kracke, S. Kreim, A. Mooser, W. Quint, S. Ulmer, and J. Walz, New J. Phys. **14**, 063011 (2012).
[43] H. Häffner, T. Beier, S. Djekic, N. Hermanspahn, H.-J. Kluge, W. Quint, S. Stahl, J. Verdù, T. Valenzuela, and G. Werth, Eur. Phys. J. D - At. Mol. Opt. Plas. Phys. **22**, 163 (2003).
[44] J. Verdù, S. Djekic, S. Stahl, T. Valenzuela, M. Vogel, G. Werth, T. Beier, H. Kluge, and W. Quint, Phys. Rev. Lett. **92**, 093002 (2004).
[45] S. Sturm *et al.*, Phys. Rev. Lett. **107**, 023002 (2011).
[46] A. Mooser, H. Kracke, K. Blaum, C. C. Rodegheri, W. Quint, S. Ulmer, and J. Walz, Phys. Rev. Lett. **110**, 140405 (2013).
[47] A. Mooser *et al.*, Phys. Lett. B. accepted (2013).
[48] G. Gabrielse, Adv. At. Mol. Opt. Phys. **50**, 155 (2005).
[49] M. Charlton *et al.*, Phys. Rep. **241**, 65 (1994).
[50] ATRAP Collaboration 1997 *Tech. Rep. SPSC-P-306, CERN, CERN-SPSC 97-8, Geneva.*
[51] ALPHA Collaboration 2005 *Tech. Rep. SPSC-P-325, CERN, CERN-SPSC 2005-006, Geneva*)

[52] A. Mohri and Y. Yamazaki, Europhys. Lett. **63** 207 (2003).
[53] ASACUSA Collaboration 2005 *Tech. Rep. SPSC-P-307 Add. 1, CERN-SPSC 2005-002, Geneva.*
[54] B. Juhász and E. Widmann, Hyperfine Interact **193**, 305 (2009).
[55] AEGIS Collaboration, *Tech. Rep. SPSC-P-334, CERN, CERN-SPSC 2007-017, Geneva*, (2007).
[56] sG. Chardin *et al., Proposal to measure the Gravitational Behaviour of Antihydrogen at Rest GBAR*, CERN-SPSC-P-342, (2011).
[57] M. Amoretti *et al.*, Nature **419**, 456 (2002).
[58] G. Gabrielse *et al.*, Phys. Rev. Lett. **89**, 213401 (2002).
[59] G. Gabrielse *et al.*, Phys. Rev. Lett. **100**, 113001 (2008).
[60] G. B. Andresen *et al.*, Phys. Lett. B **685**, 141 (2010).
[61] G. B. Andresen *et al.*, Nature **468**, 673 (2010).
[62] Y. Enomoto *et al.*, Phys. Rev. Lett. **105**, 243401 (2010).
[63] G. B. Andresen *et al.*, Nature Physics **7**, 558 (2011).
[64] H. Saitoh, A. Mohri, Y. Enomoto, Y. Kanai, and Y. Yamazaki, Phys. Rev. A **77**, 051403(R) (2008).
[65] A. Mohri, H. Saitoh, Y. Kanai, and Y. Yamazaki, *in Procs. 33rd EPS Conf. Plasma Phys.* (EPS, London, 2006), P-4. 067.
[66] The cusp trap can also confine cold H^- atoms in the LFS states with an efficient cooling mechanism. see *e. g.* T. Pohl, H. R. Sadeghpour, Y. Nagata, and Y. Yamazaki, Phys. Rev. Lett. **97**, 213001 (2006).
[67] N. Kuroda, H. A. Torii, K. Yoshiki Franzen, Z. Wang, S. Yoneda, M. Inoue, M. Hori, B. Juhãąsz, D. Horvãąth, H. Higaki, A. Mohri, J. Eades, K. Komaki, and Y. Yamazaki, Phys. Rev. Lett. **94**, 023401 (2005).
[68] N. Kuroda, H. A. Torii, M. Shibata, Y. Nagata, D. Barna, M. Hori, D. Horvath, A. Mohri, J. Eades, K. Komaki, and Y. Yamazaki, Phys. Rev. Lett. **100**, 203402 (2008).
[69] G B Andresen *et al.*, Phys. Rev. Lett. **106**, 025002 (2010).
[70] G. Gabrielse *et al.*, Phys. Rev. Lett. **108**, 113002 (2012).
[71] P. H. Donnan, M. C. Fujiwara, and F. Robicheaux, J. Phys. B **46**, 025302 (2012).
[72] ALPHA Collaboration, Nature **483**, 439 (2012).

www.ann-phys.org

adp

annalen der physik

WILEY-VCH

WILEY ONLINE LIBRARY

Early View publication on wileyonlinelibrary.com
(issue and page numbers not yet assigned;
citable using Digital Object Identifier – DOI)

Ann. Phys. (Berlin), 1–6 (2013) / DOI 10.1002/andp.201300062

annalen der physik

Rapid Research Letter

Frequency-comb spectroscopy of the hydrogen 1S-3S and 1S-3D transitions

Elisabeth Peters[1,2,*], *Dylan C. Yost*[1], *Arthur Matveev*[1], *Theodor W. Hänsch*[1,2], *and Thomas Udem*[1]

Received 18 March 2013, revised 17 April 2013, accepted 17 April 2013
Published online 17 May 2013

An observation of the 1S-3S and 1S-3D two-photon transitions in an atomic hydrogen beam using direct frequency-comb spectroscopy in a Doppler-free arrangement is reported. The measurements of these transition frequencies may be used for an improved determination of the Rydberg constant and the 1S Lamb shift and could shed light on the current discrepancy in the determination of the proton charge radius. Concurrently, a frequency comb well-suited for high-precision, Doppler-free spectroscopy in the deep ultraviolet (DUV) wavelength region is demonstrated.

1 Introduction

High-precision spectroscopy on simple atomic systems provides a powerful test of Quantum Electrodynamics (QED) since the energy levels of these systems can be calculated with high accuracy and compared with experiment. Two important parameters enter the theoretical description; the root-mean-square (rms) proton charge radius and the Rydberg constant. Assuming QED calculations are correct, these parameters can be determined if at least two transition frequencies in hydrogen or a hydrogen-like system are measured and therefore any additional measurements test the internal consistency of QED.

The 1S-2S two-photon transition frequency has long been known with the highest accuracy of any in hydrogen [1]. Therefore the conventional way to analyze the spectroscopic data has been to combine this frequency with other measured transitions that use the metastable $2S$ state as the ground state [2]. A more accurate way to determine the parameters entering the theoretical calculations became possible by using spectroscopic data from muonic hydrogen recently obtained by Pohl and co-workers [3, 4]. However, from these measurements it was found that the values for the proton charge radius and the Rydberg constant disagree from those obtained only with ordinary hydrogen by 4 combined standard deviations [4]. Moreover, the CODATA value, which takes elastic electron-scattering data into account, disagrees with the value obtained from muonic hydrogen by 7 combined standard deviations [5].

In general, the electron scattering experiments could provide a valuable and independent source of information on the proton size radius. Recent electron-scattering experiments performed at the Mainz Microtron MAMI [6] provide a value with an uncertainty of 1 % for the proton charge radius, which is in agreement with spectroscopic data of hydrogen. However, a reanalysis of the Mainz data [7] reveals a rms proton charge radius, which is consistent with the 10 times more accurate value deduced from the 2S-2P Lamb shift in muonic hydrogen measured by Pohl and co-workers [3]. Therefore, when considered together, the electron scattering data provides little insight into the discrepancy in the spectroscopic data. The energy levels of muonic hydrogen are $\sim 10^7$ times more sensitive to the proton charge radius so it seems unlikely that systematic effects in the muonic hydrogen data can explain the inconsistency. Some possible causes could be systematic effects overlooked in hydrogen measurements from the 2S ground state, or a limitation of QED. Therefore, high precision spectroscopy of hydrogen is currently very compelling.

The hydrogen spectroscopy from the 2S state to higher lying nS/D states has so far suffered from low 2S ground state population, high sensitivity to electric fields and velocity dependent systematic effects, since these measurements were carried out at room temperature. To circumvent these difficulties the Paris group has devised an experiment to measure the 1S-3S transition in hydrogen at 205 nm using a cw laser [8]. Conversely, we have

* Corresponding author E-mail: elisabeth.peters@mpq.mpg.de
[1] Max-Planck-Institut für Quantenoptik, Garching, Germany
[2] Ludwig-Maximilians-Universität, München, Germany

proposed using a 205 nm frequency comb and direct frequency comb spectroscopy (DFCS), which allows us to measure the 1S-3S as well as the 1S-3D transitions. The usability of a nonlinearly converted mode-locked laser for spectroscopy in the DUV wavelength region was first demonstrated by S. Witte on a two-photon transition at 212 nm in krypton using a Ramsey-type quantum interference scheme [9]. In this article, we report on the first observation of the 1S-3S and 1S-3D two-photon transitions in an atomic hydrogen beam at room temperature through DFCS in a Doppler-free arrangement.

It is difficult to produce cw radiation at 205 nm using nonlinear techniques because two limiting effects are observed; photochemical reactions on the nonlinear crystal faces and the photo-refractive effect [10]. However, a mode-locked laser, which can be described as a frequency comb source, offers a major experimental advantage. It features a high peak intensity and therefore greater nonlinear interactions and does not induce the photo-refractive effect. Thus, a deep ultraviolet frequency comb can, in general, be generated more efficiently than cw radiation. As an aside, using a KBBF crystal, which is capable for SHG down to 177 nm [11], two-photon transitions from the 1S ground state to higher nS/D states with $n > 3$ could be studied using a technique very similar to the one described here.

2 Direct Frequency Comb Spectroscopy

A pulse train emitted by a mode-locked laser is represented in the frequency domain by a comb of regularly spaced narrow frequency modes. The frequencies of these comb modes can be expressed as $\omega_m = \omega' + m\omega_r$, where ω' is the frequency of a single selected mode nearest to half the transition frequency, ω_r is the repetition rate of the laser and m an integer number [12]. To drive a two-photon transition with a frequency comb, the modes add pairwise to produce the transition energy $\hbar\omega_{eg}$ as shown in Fig. 1. By tuning ω' to half the transition frequency $\omega_{eg}/2$, all mode pairs which satisfy the relation $\omega_{eg} = \omega_m + \omega_{-m}$ contribute to the excitation rate. The same applies if the two-photon transition occurs exactly between two comb modes thus the signal repeats with half the repetition rate when scanning ω'. For Fourier-limited pulses, all frequency modes are properly phased and the excitation paths add up coherently. In this way, a pulsed laser drives a two-photon transition as efficiently as a cw laser and the width of a single frequency comb mode serves an analogous function to the cw laser linewidth in a determination of the achievable resolution [13–15]. Using chirped pulses for two-photon spectroscopy, though, will reduce the excitation rate but will not shift the center of the two-photon transition lines [16]. Furthermore, the AC-Stark shift is determined by the average power rather than by the peak power [17].

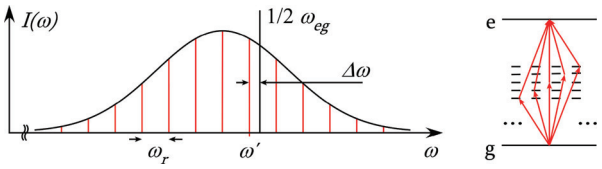

Figure 1 (online color at: www.ann-phys.org) Left: spectral envelope of the frequency comb used for two-photon excitation of the transition at ω_{eg}. One of the modes, ω' is picked to measure the detuning $\Delta\omega$, of which only values modulo ω_r are known without additional information. Right: on resonance ($\Delta\omega = 0$) pairwise addition of properly phased modes provides an efficient excitation of the atoms.

When driving a two-photon transition with a pulsed laser, the narrow Doppler-free signal originates from the region where two counter-propagating pulses overlap. This limits the interaction time of the atoms with the laser to the time-of-flight through the pulse overlap region. For collinear excitation this time-of-flight is given by the length of the pulse collision volume divided by the speed of the atoms, while for perpendicular excitation it is determined by the laser waist size. The finite interaction time gives rise to time-of-flight broadening, unless trapped ions or cold atoms are used. In the frequency domain, this effect may be described as residual Doppler broadening, since the Doppler shifts of the exciting comb lines do not cancel entirely away from ω'.

3 Experimental Setup

To produce a frequency comb at 205 nm wavelength, we frequency quadruple a mode-locked Ti:sapphire laser operating at 820 nm wavelength (Tsunami, Spectra Physics) as shown in Fig. 2. While this system was described in more detail elsewhere [18], here it is used with minor modifications. The Ti:sapphire laser provides Fourier-limited pulses of 1.3 ps pulse duration at 82 MHz repetition frequency with an average output power of 1.8 W. Around 10% of the output power is used to stabilize the laser to an external Fabry-Perot cavity (FPC) utilizing the radio-frequency (rf) side band technique [19]. A double-pass AOM in front of the FPC tunes the laser frequencies in order to scan over the hydrogen transition. This technique provides a stable frequency comb but no absolute frequency reference. The main part of the

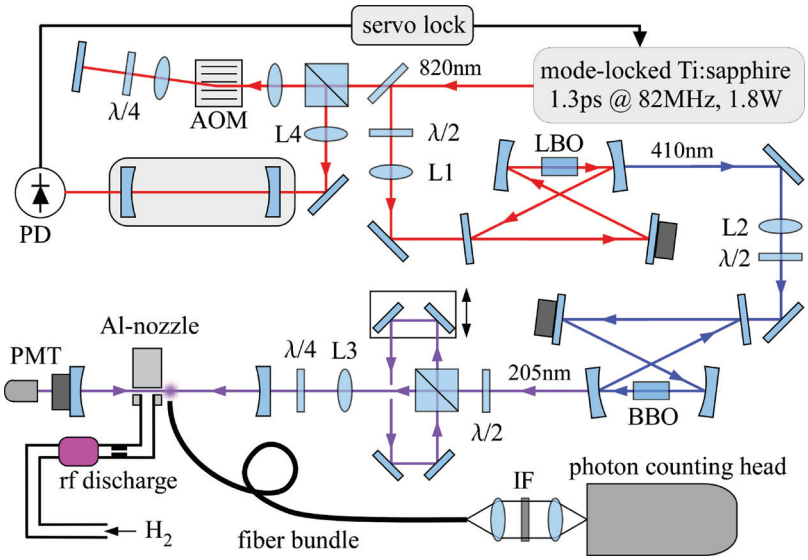

Figure 2 (online color at: www.ann-phys.org) Experimental setup for direct frequency comb spectroscopy of 1S-3S two-photon transition in hydrogen at 205 nm. AOM: acousto-optic modulator, PD: photo diode, PMT: photomultiplier tube, L1, L2, L3 and L4: mode matching lenses, IF: interference filter.

output power at 820 nm is mode matched into an enhancement cavity housing a LBO nonlinear crystal for resonantly enhanced second harmonic generation (SHG) at 410 nm. The 5 mm long crystal is anti-reflective (AR) coated for 820 nm and 410 nm wavelength and is cut at $\theta = 90$ deg and $\phi = 29.6$ deg for type I phase matching. The four mirror resonator length was chosen to filter every other comb mode out of the incident spectrum, i.e. its free spectral range (FSR) is twice the repetition rate of the mode-locked laser. In this way, we sacrifice half the incident laser power for larger FSR, which makes the resonator less sensitive to residual acoustic vibrations which cannot be compensated by the servo system and thus improves stability. Despite the lower circulating power, the SHG cavity is conversion loss dominated and we find experimentally that an input coupler with 94.8 % reflectivity is close to optimum for proper impedance matching. In this configuration, a conversion efficiency of 58 % can be achieved providing around 380 mW average power at 410 nm.

In the second conversion stage a BBO crystal is used to generate 205 nm light. The phase matching angle for this process is close to the cut-off. By cooling the 2 mm thin crystal to -10° C the phase matching cut-off is shifted to shorter wavelengths, which increases the nonlinear interaction. To avoid water condensation and photochemical reactions, the crystal is purged with a constant flow of dry oxygen away from the crystal surfaces. Despite cooling, the phase matching angle of BBO for SHG at 205 nm, $\theta = 86.4$ deg, is very close to the cut-off and the single pass conversion efficiency suffers. Using a similar enhancement cavity as is used in the first SHG stage, a conversion efficiency of around 3 % can be achieved providing 10 mW to 15 mW of output power at 205 nm, which is one order-of-magnitude higher than what has been achieved in cw regime [10].

The spectroscopy is carried out in an atomic beam formed by an aluminum nozzle. Atomic hydrogen is obtained by dissociating H_2 molecules in a rf discharge. A Teflon tube is used to guide the hydrogen atoms to the aluminum nozzle and the atoms leave the nozzle through two opposing orifices of 1 mm diameter. A linear enhancement resonator for the 205 nm frequency comb is constructed with two focusing mirrors such that the resonant radiation passes through the two orifices of the nozzle. The radius of curvature of the mirrors is 500 mm and with an FSR of 164 MHz this generates a 95 μm beam radius at the center of the cavity. With a reflectivity of 98 % and 93 % of the high reflective and input coupling mirror respectively, a power enhancement of 10 can be achieved. This provides around 100 mW of average power inside the spectroscopy resonator.

A delay arm utilizing a polarizing beam splitter cube in front of the spectrometer is used to produce two counter-propagating pulses in the cavity with orthogonal linear polarizations π/σ. A quarter-wave plate between the delay arm and the spectroscopy cavity alters the polarization to σ^+/σ^- which provides a more efficient excitation of the 1S-3S lines than with π/σ polarized light. This setup also allows to control the overlap positions of the pulses within the cavity by adjusting the delay length. For delays $\neq t_r/2$, where t_r is the time between two sequential pulses, there are two pulse collision points inside the resonator. By adjusting the delay to $t_r/2$ the pulse collision points overlap at the center of the spectroscopy resonator and the pulse repetition rate

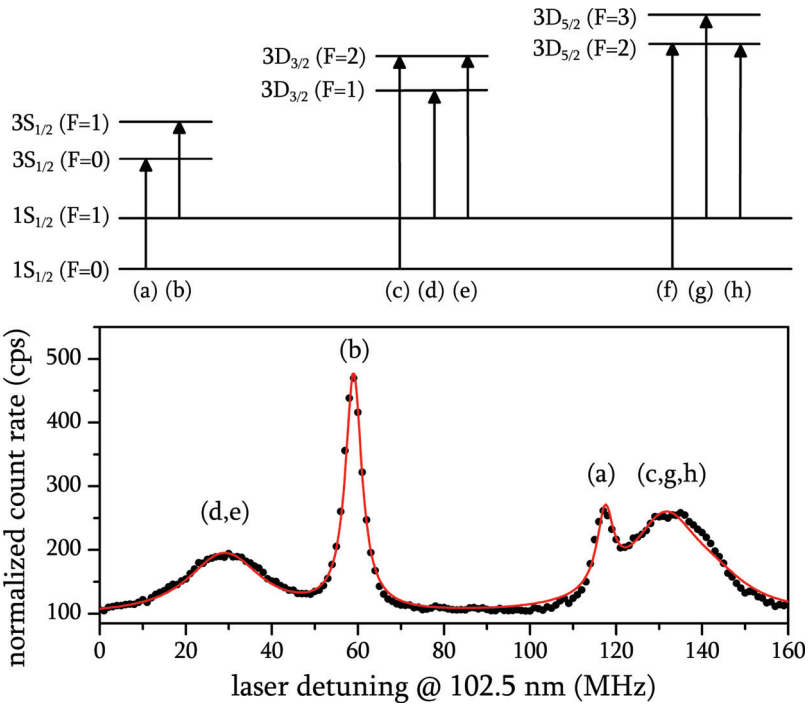

Figure 3 (online color at: www.ann-phys.org) Top: Level diagram showing the allowed transitions for σ^+/σ^- polarized light, according to the two-photon selection rules [20]. Bottom: Spectrum obtained by direct frequency comb spectroscopy of hydrogen at 205 nm wavelength with σ^+/σ^- polarized light. The frequency range is less than the full repetition rate so only 7 of 8 allowed transitions are observed. Full circles: experimental data, solid line: simulated spectrum.

as seen by the atoms is effectively doubled to 328 MHz. In this region collinear Doppler-free excitation of the 1S-3S transition takes place by means of absorption of two counter-propagating photons.

The excited 3S state decays via the 2P state emitting two subsequent fluorescence photons, a Balmer $H-\alpha$ at 656 nm and a Lyman $Ly-\alpha$ at 121 nm. A multi-mode fiber bundle (7 fibers, usable area of 83 %) is placed near the pulse collision position (≈ 0.5 mm distance) and collects the fluorescent 656 nm photons with no additional collection optics. This fiber bundle then transfers the radiation outside of the vacuum chamber. A telescope consisting of two $f = 25$ mm lenses images the fluorescence onto the cathode of a photon counting head (H10682-01, Hamamatsu) while a narrow bandwidth interference filter (FWHM: 1.5 nm) suppresses background light.

When using a pulsed laser for two-photon spectroscopy, all allowed transitions covered by the laser bandwidth are addressed. With a laser bandwidth of 140 GHz the 1S - $3D_{3/2}$ and 1S - $3D_{5/2}$ transitions, which lie 3 GHz and 4 GHz respectively above the 3S state, are also excited. Due to the nuclear spin of 1/2 all states split into two hyperfine components. According to the two-photon selection rules, transitions with $|\Delta F| \leq 2$ are allowed with the exception of $\Delta F : 0 \leftrightarrow 1$ which are forbidden [20]. This gives eight allowed components (see upper part of Fig. 3) which are excited as ω' is scanned and their spacings appear modulo the repetition rate.

4 Results and Discussion

The two-photon signal is recorded while shifting the comb spectrum in 1 MHz steps in order to scan over the atomic transition. For each frequency setting the PMT signal is integrated for 1 s. Fig. 3 shows an averaged spectrum over 15 individual scans (full circles) recorded at room temperature and a simulated spectrum taking time of flight broadening, quenching in stray electric fields and Zeeman splitting in stray magnetic fields into account (solid line). The frequency range in these plots is less than the full repetition rate so only 7 of 8 transitions are observed. For hydrogen atoms traveling with 2200 m/s through the 0.35 mm pulse collision volume, the time-of-flight broadening amounts to ≈ 4.5 MHz. This effect leads to a broadening of the 1S-3S lines from 1 MHz natural width to ≈ 4.6 MHz and of the 1S-3D from 10 MHz natural width to ≈ 11 MHz. However, in the recorded spectrum the 1S-3D linewidths are measured to be around 20 MHz. This might be explained by mixing of the $3D_{3/2}$ and the $3P_{3/2}$ states through a residual electric field [21]. As the electric field strength approaches a critical value of $E_c = 1.9$ V/cm the linewidth of the $3D_{3/2}$ and the $3P_{3/2}$ state saturates to 19.9 MHz for $E > E_c$. Considering photoelectron emission upon absorption of 205 nm light of the nozzle material, stray fields at the level of 2 V/cm in our interaction region are likely. In order to broaden the $1S-3S$ lines by a factor of 2, electric fields of about 12 V/cm would be

necessary. Splitting of the states with F $\neq$ 0 in a stray magnetic field leads to an additional broadening of the lines. In the experiment stray magnetic fields on the order of 0.1 mT could be measured in our interaction region, which broadens the $3D_{5/2}$ lines to around 20 MHz. For absolute frequency measurements, the interaction volume will need to be shielded against stray electric and magnetic fields to avoid these broadening and shifting mechanisms.

Fitting a theoretical curve to the experimental data with line centers, widths and amplitudes as free parameters allows a determination of the line center of the $1S_{1/2}$(F=1)-$3S_{1/2}$(F=1) transition (b) with an statistical uncertainty of 36 kHz. To improve the accuracy, in the future we can utilize a liquid helium flow cryostat to cool the atoms to 5.8 K. This will reduce time-of-flight broadening by a factor 7 below the natural linewidth and the remaining second-order Doppler shift by a factor 50 to 2 kHz.

For an absolute frequency measurement, the laser frequency of the probe laser needs to be linked to a frequency standard. For this purpose we plan to coherently phase lock the ps Ti:sapphire laser to a cavity-stabilized cw laser diode. This diode laser will, in turn, be referenced to a hydrogen maser via a fiber-laser frequency comb.

5 Conclusion

To conclude, we present the observation of the 1S-3S and 1S-3D two-photon transitions at 205 nm by means of Doppler-free direct frequency comb spectroscopy using a mode-locked ps laser. Through this we also demonstrate the suitability of a nonlinearly converted frequency comb for high-precision two-photon spectroscopy. A precise measurement would provide valuable information to the proton charge radius puzzle which arose from the 2S-2P Lamb shift measurement in muonic hydrogen [4].

Acknowledgements. The authors thank the hydrogen 1S-2S team and R. Pohl for insightful discussions and critically reading the manuscript. This work has been supported in part by the European Research Council (Advanced Investigator Grant 267854). D.Y. aknowledges support from the Alexander von Humboldt Foundation and T.W.H. from the Max Planck Foundation.

Key words. Two-photon spectroscopy, frequency-comb spectroscopy.

References

[1] C. G. Parthey, A. Matveev, J. Alnis, B. Bernhardt, A. Beyer, R. Holzwarth, A. Maistrou, R. Pohl, K. Predehl, T. Udem, T. Wilken, N. Kolachevsky, M. Abgrall, D. Rovera, C. Salomon, P. Laurent, and T.W. Hänsch Phys. Rev. Lett. **107**, 203001 (2011).

[2] B. de Beauvoir, C. Schwob, O. Acef, L. Jozefowski, L. Hilico, F. Nez, L. J. A. Clairon, and F. Biraben Eur. Phys. J. D **12**, 61–93 (2000).

[3] R. Pohl, A. Antognini, F. Nez, F. D. Amaro, F. Biraben, J. M. R. Cardoso, D. S. Covita, A. Dax, S. Dhawan, L. M. P. Fernandes, A. Giesen, T. Graf, T. W. Hänsch, P. Indelicato, L. Julien, C. Y. Kao, P. Knowles, E. O. L. Bigot, Y. W. Liu, J. A. M. Lopes, L. Ludhova, C. M. B. Monteiro, F. Mulhauser, T. Nebel, P. Rabinowitz, J. M. F. dos Santos, L. A. Schaller, K. Schuhmann, C. Schwob, D. Taqqu, J. F. C. A. Veloso, and F. Kottmann Nature **466**, 09250 (2010).

[4] A. Antognini, F. Nez, K. Schuhmann, F. D. Amaro, F. Biraben, J. M. R. Cardoso, D. S. Covita, A. Dax, S. Dhawan, M. Diepold, L. M. P. Fernandes, A. Giesen, A. L. Gouvea, T. Graf, T. W. Hänsch, P. Indelicato, L. Julien, C. Y. Kao, P. Knowles, F. Kottmann, E. O. L. Bigot, Y. W. Liu, J. A. M. Lopes, L. Ludhova, C. M. B. Monteiro, F. Mulhauser, T. Nebel, P. Rabinowitz, J. M. F. dos Santos, L. A. Schaller, C. Schwob, D. Taqqu, J. F. C. A. Veloso, J. Vogelsang, and R. Pohl Science **339**, 417 (2013).

[5] P. J. Mohr, B. N. Taylor, and D. B. Newell Rev. Mod. Phys. **84**, 1527–1605 (2012).

[6] J. C. Bernauer, P. Achenbach, C. A. Gayoso, R. Böhm, D. Bosnar, L. Debenjak, M. O. Distler, L. Doria, A. Esser, H. Fonvieille, J. M. Friedrich, J. Friedrich, M. G. R. de la Paz, M. Makek, H. Merkel, D. G. Middleton, U. Müller, L. Nungesser, J. Pochodzalla, M. Potokar, S. S. Majos, B. S. Schlimme, S. Širca, T. Walcher, and M. Weinriefer Phys. Rev. Lett. **105**, 242001 (2010).

[7] I. T. Lorenz, H. W. Hammer, and U. G. Meißner Eur. Phys. J. A **48**, 151 (2012).

[8] O. Arnoult, F. Nez, L. Julien, and F. Biraben Eur. Phys. J. D **60**, 243–256 (2010).

[9] S. Witte, R. T. Zinkstok, W. Ubachs, W. Hogervorst, and K.S. E. Eikema Science **307**, 400 (2005).

[10] S. Bourzeix, B. de Beauvoir, F. Nez, F. de Tomasi, L. Julien, and F. Biraben Opt. Commun. **133**, 239–244 (1997).

[11] X. Zhang, L. Wang, X. Wang, G. Wang, Y. Zhu, and C. Chen Opt. Commun. **285**, 4519–4522 (2012).

[12] T. Udem, R. Holzwarth, and T. W. Hänsch Nature **416**, 233–237 (2002).

[13] Y. V. Baklanov and V. P. Chebotayev Appl. Phys. **12**, 97–99 (1977).

[14] R. Teets, J. Eckstein, and T. W. Hänsch Phys. Rev. Lett. **38**, 760–764 (1977).

[15] J. N. Eckstein, A. I. Ferguson, and T. W. Hänsch Phys. Rev. Lett. **40**, 847–850 (1978).

[16] S. Reinhardt, E. Peters, T. W. Hänsch, and T. Udem Phys. Rev. A **81**, 033427 (2010).
[17] P. Fendel, S. D. Bergeson, T. Udem, and T. W. Hänsch Opt. Lett. **32**, 701–703 (2007).
[18] E. Peters, S. A. Diddams, P. Fendel, S. Reinhardt, T. W. Hänsch, and T. Udem Opt. Express **17**, 9183–9190 (2009).
[19] R. W. P. Drever, J. L. Hall, F. V. Kowalski, J. Hough, G. M. Ford, A. J. Munley, and H. Ward Appl. Phys. B **31**, 97–105 (1983).
[20] K. D. Bonin and T. J. McIlrath J. Opt. Soc. Am. B **1**, 52–55 (1984).
[21] H. A. Bethe and E. E. Salpeter, Quantum Mechanics of One- and Two-Electron Atoms (Dover, New York, 2008).